Multi-Frequency EDMR Studies of Light-Activated Paramagnetic Centers in μc-Si:H Thin-Film Solar Cells

Im Fachbereich Physik
der Freien Universität Berlin
eingereichte Dissertation von

Christoph Meier

Dezember 2013

1. Gutachter: Prof. Dr. Robert Bittl
2. Gutachter: Prof. Dr. Bernd Rech

Tag der Disputation: 21. März 2014

PUBLICATIONS

Parts of this thesis are already published and can be found in:

Christoph Meier, Jan Behrends, Christian Teutloff, Oleksandr Astakhov, Alexander Schnegg, Klaus Lips, Robert Bittl. *Multi-frequency EDMR applied to microcrystalline thin-film silicon solar cells*. Journal of Magnetic Resonance, 234 : 1 – 9, 2013.

Christoph Meier, Jan Behrends, Robert Bittl. *Electrical detection of Rabi oscillations in microcrystalline silicon thin-film solar cells*. Molecular Physics, 111 : 2683–2689, 2013.

Several results were presented in form of poster presentations and talks at different conferences and seminars (selection):

1. Christoph Meier. *Multi-frequency EDMR applied to microcrystalline thin-film silicon solar cells*. Workshop on "Spins as Functional Probes in Solar Energy Research", HZB, Berlin, Germany, 2013, talk.

2. Christoph Meier. *Microcrystalline Silicon: Orientation dependence of light-induced EDMR signals*. Royal Society of Chemistry ESR Conference, runners-up spot at the "JEOL Lecture", Manchester, Great Britain, 2012, talk.

3. Christoph Meier, Jan Behrends, Christian Teutloff, Matthias Fehr, Alexander Schnegg, Klaus Lips, Robert Bittl. *Spin-dependent transport in μc-Si:H thin-film solar cells*. EUROMAR 2011 and 8$^{\text{th}}$ European Federation of EPR Groups Meeting, Frankfurt/Main, Germany, 2011, poster (winner of the EUROMAR poster price).

4. Christoph Meier, Jan Behrends, Christian Teutloff, Matthias Fehr, Alexander Schnegg, Klaus Lips, Robert Bittl. *Silicon p-i-n solar cells investigated by multi-frequency EDMR*, Joint EUROMAR 2010 and 17th ISMAR Conference, Firence, Italy, 2010, poster.

ABSTRACT

This thesis presents a comprehensive study of paramagnetic centers in fully-processed microcrystalline silicon (μc-Si:H) thin-film solar cells. The heterogeneous material gives rise to a complex band structure with deep defects in the middle of the energy band gap as well as localized states close to the energy band edges. They can act as recombination centers and traps and, thereby, influence the charge transport of photogenerated charge carriers. Thus, they diminish the performance of the cell. To reduce the disadvantageous influence of the defect states on the cell efficiency, a detailed understanding of the charge transport processes via these states is necessary.
In this work, light-activated paramagnetic centers are studied with electrically detected magnetic resonance (EDMR) at various microwave frequencies. This technique combines electron paramagnetic resonance spectroscopy (EPR) with the photocurrent measurement in the solar cell, thus, delivering information about the transport processes and magnetic parameters of the involved defect states.
Multi-frequency EDMR at low temperatures reveals four paramagnetic states in μc-Si:H. Dangling bond (db) defects and holes in valence band tail (h) states are located in the disordered phase, whereas so-called CE and V states originate from the crystalline phase. The multi-frequency approach allows for a separation of field-dependent and -independent line widths. All EDMR signals are affected by line broadening due to spin-spin interaction, which could be used to estimate mean inter-spin distances of ≈ 0.5 nm for the V center and of $\approx 1-2$ nm for the remaining centers. Based on the strong spin-spin coupling and on transient nutation experiments the V signal could be correlated with a vacancy site in its excited triplet state. From the particular properties of the CE line it was concluded that the corresponding states are located in inversion layers and potential wells close to the conduction band of crystalline silicon.

KURZFASSUNG

Die vorliegende Arbeit ist eine umfassende Studie paramagnetischer Zentren in vollprozessierten Dünnschichtsolarzellen aus mikrokristallinem Silizium (μc-Si:H). Das heterogene Material führt zu einer komplexen Bandstruktur mit tiefen Defekten in der Mitte der Bandlücke und lokalisierten Zuständen in der Nähe von Leitungs- und Valenzbandkante. Diese können als Rekombinationszentren und Fallen wirken und beeinflussen damit den Ladungstransport photogenerierter Ladungsträger. Damit reduzieren sie die Solarzellleistung. Um diesen nachteiligen Einfluss der Defektzustände auf die Zelleffizienz zu verringern, bedarf es eines genauen Verständnisses der Ladungstransportprozesse entlang jener Zustände.
In dieser Arbeit werden licht-aktivierte paramagnetische Zentren mithilfe von elektrisch detektierter Magnetresonanz (EDMR) bei verschiedenen Mikrowellenfrequenzen untersucht. Diese Methode kombiniert Elektronenspinresonanzspektroskopie (EPR) mit der Photostrommessung in der Solarzelle und liefert damit Informationen über die Transportprozesse und die magnetischen Parameter der beteiligten Defektzustände.
Multifrequenz-EDMR bei tiefen Temperaturen bringt vier paramagnetische Zentren im μc-Si:H zu Tage. Dangling bond-Defekte (db-Defekte) und Löcher in Valenzbandausläuferzuständen (h-Zuständen) befinden sich in der ungeordneten Phase des Materials, wohingegen die sogenannten CE- und V-Zustände der kristallinen Phase entstammen. Der Multifrequenzansatz ermöglicht die Trennung feldabhängiger sowie feldunabhängiger Linienbreiten. Alle EDMR-Signale sind von Linienverbreiterungen durch Spin-Spin-Wechselwirkung betroffen, welche verwendet werden konnten, um mittlere Spinabstände von ≈ 0.5 nm für das V-Zentrum und $\approx 1-2$ nm für die verbleibenden Zentren zu bestimmen. Basierend auf der starken Spin-Spin-Kopplung und auf Messungen transienter Nutationen konnte das V-Signal mit einem Fehlstellendefekt in seinem angeregten Triplettzustand

korreliert werden. Aus den speziellen Eigenschaften der CE-Resonanz wurde geschlussfolgert, dass die dazugehörigen Zustände in Inversionsschichten und Potenzialsenken nahe des Leitungsbandes von kristallinem Silizium zu finden sind.

CONTENTS

1

INTRODUCTION

Thin-film solar cells bear the potential of converting solar energy at much lower costs than the well established wafer-based photovoltaic (PV) technology. The versatility and temperature robustness of thin-film PV modules resulted in a large gain in market share to about 15-20 % in the last years [1]. Among the various materials used in thin-film solar cells, hydrogenated amorphous silicon (a-Si:H) and hydrogenated microcrystalline silicon (μc-Si:H) play a key role. Both materials are compatible with the concept of third generation photovoltaics aiming at increasing device efficiencies while still using thin-film processes and abundant non-toxic materials [2]. Both materials can directly be deposited from the gas phase using low-temperature processes on inexpensive substrates and require only a fraction of the material that is necessary for crystalline silicon (c-Si) solar cells [3–6]. By choice of the deposition parameters a-Si:H and μc-Si:H can be produced with the same deposition equipment and can thus easily be combined in one device. This allows for the fabrication of tandem solar cells utilizing the different band gaps of a-Si:H and μc-Si:H and, consequently, a more efficient use of the solar spectrum.

Since the fabrication of the first a-Si:H solar cell in 1976 [7], the maximum conversion efficiencies increased steadily to more than 12 % for a-Si:H/μc-Si:H tandems [8, 9]. However, this value is well below the maximum efficiencies achieved with c-Si-based cells [10]. This gap is due to the inferior electrical properties of amorphous thin-film silicon as compared to its crystalline counterpart. Deep defects due to dangling bonds (db) and localized tail states in the band gap induced by strained bonds act as recombination

centers and traps, respectively, and thereby influence the charge transport of photogenerated charge carriers. They thus diminish the performance of the cell. Understanding these loss mechanisms on a microscopic level is a necessary prerequisite for the development of advanced cell concepts minimizing the detrimental influence of defect states on the cell performance.
Whenever a localized defect state is occupied by an odd number of electrons, it is paramagnetic and can be detected by electron paramagnetic resonance (EPR) spectroscopy. EPR can determine defect concentrations and thus allows for an optimization of a-Si:H and μc-Si:H deposition parameters [11]. Since the electron spin trapped in a defect state constitutes a sensitive probe for electron and nuclear spins in its vicinity, EPR and related multi-resonance techniques can deliver helpful information on defect structures in solar cell materials [12–14]. In particular a multi-frequency approach has recently proven successful for the investigation of the EPR parameters of dbs in a-Si:H [15].
Whether these paramagnetic defects are indeed involved in trapping and recombination processes can conveniently be analyzed when combining EPR with a photocurrent measurement. The resulting technique, electrically detected magnetic resonance (EDMR) [16], interferes with spin-dependent recombination or hopping rates and probes the resulting change in conductivity. EDMR employing continuous wave (cw) microwave (mw) excitation has been applied to thin-film silicon films and devices for a couple of years [17]. More recently the combination of electrical detection with pulsed mw excitation schemes was shown to provide new insight into charge carrier recombination and hopping transport in thin-film silicon devices [18, 19]. On the one hand, exploiting the time regime enabled the discrimination between spectrally overlapping EDMR signals associated with different spin-dependent processes in a-Si:H- and μc-Si:H-based solar cells [20, 21]. On the other hand, pulsed EDMR has paved the way for the application of sophisticated detection schemes known from mw-detected EPR [22–26].
In this work the successful multi-frequency EPR approach is combined with the electrical detection yielding *multi-frequency EDMR*. μc-Si:H thin-film p-i-n solar cells are studied at microwave frequencies ranging over 2 orders of magnitude from 3.5 to 263 GHz. It will be shown that in this way magnetic interactions with nearby electron and nuclear spins as well as the direct interaction with the external magnetic field can be separated and provide insights into the microscopic structure of the electron spin's environment. For example, spin-carrying nuclei like ^{1}H or ^{29}Si allow the assignment of

the paramagnetic centers to the crystalline or amorphous regions within the mixed-phase μc-Si:H material. The evaluation of electron spin dipolar couplings yields information about mean inter-spin distances. The g-value as a fingerprint property will help to characterize the different paramagnetic species.
The multi-frequency EDMR is not a specific EDMR experiment within the methodology of EDMR. Instead, multi-frequency EDMR extends the available mw frequency range for all EDMR experiments with the aim to make the specific experiments, like e.g. ENDOR, ESEEM or Rabi experiments even more powerful when performed at one or more appropriate microwave frequencies.
In addition to the magnetic parameters of the EPR-active centers, EDMR gives insights into the nature of the transport paths they are part of. The sensitive detection of conductivity reduction or enhancement under resonance conditions reveals which role the defects play within the device. Here, the enormous sensitivity of the EDMR current detection [27] allows the investigation of a broad range of semiconductor devices like pn-diodes, solar cells, LEDs or field effect transistors [17, 28–31] which are not accessible by EPR due to the complex device structure and the small number of spins.

This thesis describes a comprehensive study of thin-film μc-Si:H solar cells with multi-frequency EDMR. It is structured in the following way:

Chapter 2 gives an introduction of the theoretical background of EPR and EDMR methods. In the first part the interaction of a spin with an external magnetic field, the electron spin-spin interaction and the hyperfine interaction are described. In the context of spin-dependent processes involving two or more spins, the spin-spin interaction is of special relevance. It will be discussed in the limits of weak and strong coupling conditions to allow a precise interpretation of the EDMR results. The main aspects of electron paramagnetic resonance for this work are the coherent spin motion and the mechanisms of pulsed EPR. Finally, spin-dependent transport processes involving two as well as three spins and the underlying model (KSM model [32]) are described. They are the basis for the understanding of EDMR.

Chapter 3 presents the investigated thin-film solar cells, which were prepared at Forschungszentrum Jülich. Three different thin-film p-i-n cells are described which are made of microcrystalline and amorphous silicon. A special focus is put on the description of the EDMR setups at the different microwave frequencies. At microwave frequencies of 34 GHz and

below cavity-based setups are utilized, whereas at higher frequencies non-resonant setups are necessary. The EDMR setup at 94 GHz was developed in the framework of this work. Finally, the EDMR experiments are described in detail.

Chapter 4 introduces the approach of multi-frequency EDMR. The experiments are carried out on a μc-Si:H p-i-n solar cell with an n-a-Si:H layer at mw frequencies of 9.7 (X-band), 34 (Q-band) and 94 GHz (W-band). In this study we will answer the question if multi-frequency and high-frequency EDMR on disordered semiconductors like μc-Si:H are capable approaches regarding the spectral resolution of multi-component spectra, the separation between field-dependent and field-independent interactions and the resolution of line asymmetries.

Chapter 5 constitutes the heart of this work. Here a comprehensive EDMR study applied to a p-i-n solar cell completely made of μc-Si:H is presented. The EDMR spectrum is decomposed with the help of the signal dynamics measured by cw and pulsed EDMR techniques in Sec. 5.1. The multi-frequency EDMR investigation of the paramagnetic centers in this sample is described in Sec. 5.2. Two solar cells with intrinsic layers made of μc-Si:H with different ^{29}Si concentrations are studied to separate between the field-independent spin-spin and hyperfine interactions on the one hand and the field-dependent interactions on the other hand. In Sec. 5.3 ESEEM experiments are carried out in the complete range of the EDMR spectrum to get information about nuclei like hydrogen and silicon or the doping elements phosphorus and boron in the environment of the defects. In the end, Rabi nutation experiments are performed regarding two EDMR resonances. This allows to determine the spin quantum numbers of the paramagnetic centers and to look for the mutual spin partners of spin-dependent processes.

Chapter 6 delivers an overall discussions of all findings from chapters 4 and 5. Here, the microscopic environments of the defect states are described. Based on the EDMR results transport paths involving the different paramagnetic states are proposed. Afterwards, a schematic band diagram is presented which is consistent with all experimental results. Finally, the most relevant findings are summarized and an outlook for future work is given.

2

THEORY OF EPR AND EDMR

In this chapter we will present the theoretical background which is necessary for a detailed interpretation of the EDMR experiments applied to microcrystalline silicon solar cells. This chapter consists of three main parts. At the beginning we consider localized paramagnetic centers and their interaction with an external magnetic field as well as their couplings to neighboring nuclei and electrons in the material. This knowledge will help us to draw conclusions about the structure of the center´s microscopic environment from the experimental results. Then, we will comment on the concepts of EPR spectroscopy and spin manipulation. We will introduce the important aspects of the techniques, which will be used later. Finally, spin-dependent transport processes via localized centers are depicted. They are the basis for the detection a EPR-induced conductivity changes.

2.1 Spins in Magnetic Fields

The spin systems investigated in this thesis are characterized by paramagnetic species with the electron spin quantum number $S = 1/2$. These electron spins are in most cases coupled to nuclear spins with nuclear spin quantum number $I = 1/2$ primarily of silicon nuclei in the proximity. When the interspin distance of two different electron spins is small their spin-spin interactions has to be considered as well. Thus, for application of electron paramagnetic resonance (EPR) we need a detailed knowledge of the spin state and EPR transition energies of the systems $S = 1/2$ coupled to $I = 1/2$

as well as of the system ($S_1, S_2 = 1/2$) spin pairs interacting with a single nucleus $I = 1/2$.
Most studies presented here employ the method of electrically detected magnetic resonance (EDMR). Since detection of EDMR signals is based on spin-dependent processes of, in general, two electron spins coupled via spin-spin interactions [19], the subspecies consisting of pairs of interacting spins is picked out of the whole spin ensemble described above.
Hence, the following spin interactions have to be regarded: The Zeeman interaction given by the Hamiltonian $\mathcal{H}_{\mathrm{Z,i}}$ describes the interaction of the individual electron spin i with an applied external magnetic field. The nuclear spins in the sample are as well affected by this external field which is considered by the nuclear Zeeman term $\mathcal{H}_{\mathrm{NZ}}$. Further terms comprising interactions between different spins are the hyperfine interaction (HFI) term $\mathcal{H}_{\mathrm{HFI}}$ which describes the coupling of electron and nuclear spins and the exchange interaction as well as the dipolar coupling term $\mathcal{H}_{\mathrm{ex}}$ and $\mathcal{H}_{\mathrm{dd}}$, respectively. Both parts deal with the interaction of neighboring electron spins. Summarizing these yields the static spin Hamiltonian

$$\mathcal{H}_0 = \mathcal{H}_{\mathrm{Z,1}} + \mathcal{H}_{\mathrm{Z,2}} + \mathcal{H}_{\mathrm{NZ}} + \mathcal{H}_{\mathrm{HFI}} + \mathcal{H}_{\mathrm{ex}} + \mathcal{H}_{\mathrm{dd}}. \tag{2.1}$$

The individual interactions will be elucidated in the following (sections 2.1.1 to 2.1.5). Although spin systems of coupled electron spins are of special relevance with respect to the application of EDMR, single spins and their interactions are considered in a first step. In a second step, the spin partner is incorporated in the described theoretical concepts. In doing this, we will distinguish between weak and strong interspin couplings. Since the investigated paramagnetic species are located in a disordered solid state system, small site-to-site differences of magnetic parameters in the spin Hamiltonian $\mathcal{H}_0$ result in variations of energy levels. This aspect is illustrated in section 2.1.6.

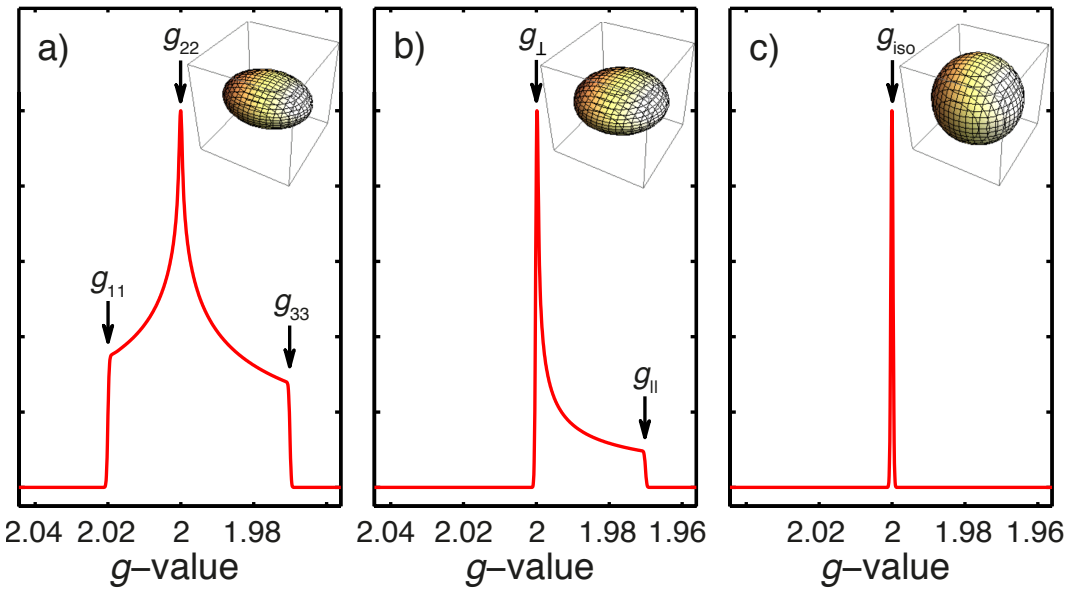

Figure 2.1: Simulation of EPR powder spectra for different symmetries of the g-matrix. The spectra were simulated with easyspin (an EPR toolbox) [33]. a) Rhombic symmetry. b) Axial symmetry. c) Cubic symmetry. For clarity, the displays have been normalized to equal maximum intensity. The insets show the ellipsoid representation of the respective g-matrices (the radii do not reflect the g_{ii}-values of the simulation).

2.1.1 The Electron Zeeman Interaction

The Zeeman interaction describes the interaction between the electron spin **S** and the external magnetic field **B** by

$$\mathcal{H}_Z = \beta_e \mathbf{B} \cdot \mathbf{g} \cdot \mathbf{S} \tag{2.2}$$

where β_e is the Bohr magneton and **g** the orientation-dependent 3×3 Zeeman interaction matrix, called *g-matrix*.
The g-matrix is characterized by three real matrix eigenvalues (g_{11}, g_{22} and g_{33}) and three Euler angles which describe the orientation of the g-matrix principal axes in the coordinate system of the paramagnetic defect.
In the general case we find $g_{11} \neq g_{22} \neq g_{33}$ (rhombic symmetry). For illustration this rhombic g-matrix can be described by an ellipsoid with three different radii g_{ii} (see the inset Fig. 2.1 a)). When $g_{11} = g_{22} \neq g_{33}$ one speaks of axial symmetry (inset Fig. 2.1 b)). The direction with $g_{33} = g_{||}$ constitutes a unique axis of the system. Measuring perpendicular to this unique axis

yields $g_{11} = g_{22} = g_{\perp}$. The ellipsoid looks like a zeppelin or a discus. Cubic symmetry is described by an isotropic g-value: $g_{\mathrm{iso}} = g_{11} = g_{22} = g_{33}$ (inset Fig. 2.1 c)). The ellipsoid becomes a sphere of radius g_{iso}.
In powder samples which consist of a big number of randomly oriented paramagnetic defects, all possible g-values contribute to the spectrum. A so-called *powder pattern* occurs. Examples of such powder patterns for all three symmetries are shown in Fig. 2.1 a) - c). The intensity profiles reflect the probability to find a defect of its particular orientation with respect to the magnetic field **B**.
The intrinsic spin angular momentum **S** of a free electron is associated with a g-factor $g_{\mathrm{e}} = 2.00232$. The free-electron g-value is expected in solid state or molecular systems in a non-degenerate electronic ground state as well, since the orbital angular momentum **L** is quenched. However, in a perturbative treatment spin-orbit interaction

$$\mathcal{H}_{\mathrm{LS}} = \lambda \mathbf{L} \cdot \mathbf{S} \tag{2.3}$$

admixes the ground state with other excited states and causes a small amount of **L** to appear in the true ground state connected with a shift of the g-value from g_{e}. The more important spin-orbit coupling is, the larger is the deviation of g from g_{e}. Since this g-value can be considered as a fingerprint property, it is often used to identify the considered paramagnetic center.

2.1.2 The Spin-Spin Interaction

When two electron spins are spatially sufficiently close to each other, they will interact (*spin-spin interaction*). This can happen via dipolar and exchange interaction. In this case the spin system comprises four spin states which can be expressed in two different representations dependent on the mutual spin-spin coupling strength: In the *uncoupled representation* they can be represented by simple product states:

$$|S_1, m_{S,1}\rangle \otimes |S_2, m_{S,2}\rangle = |m_{S,1}\rangle \otimes |m_{S,2}\rangle = \{|\uparrow\uparrow\rangle, |\uparrow\downarrow\rangle, |\downarrow\uparrow\rangle, |\downarrow\downarrow\rangle\}. \tag{2.4}$$

If the two electrons interact significantly, it is advantageous to combine

these configurations into combination states (*coupled representation*) because the system separates into a triplet state $S = 1$ with the substates

$$\begin{aligned} |T_+\rangle &= |\uparrow\uparrow\rangle \\ |T_0\rangle &= \frac{1}{\sqrt{2}}(|\uparrow\downarrow\rangle + |\downarrow\uparrow\rangle) \\ |T_-\rangle &= |\downarrow\downarrow\rangle. \end{aligned} \tag{2.5}$$

and a singlet state $S = 0$

$$|S\rangle = \frac{1}{\sqrt{2}}(|\uparrow\downarrow\rangle - |\downarrow\uparrow\rangle). \tag{2.6}$$

The Dipolar Interaction

The dipolar coupling arises from the classical dipole-dipole interaction of two magnetic moments. The classical interaction energy of two point dipoles $\boldsymbol{\mu}_1$ and $\boldsymbol{\mu}_2$ separated by the distance r (where the vector $\mathbf{r}$ points into the inter-spin direction) is:

$$U = \frac{\mu_0}{4\pi}\left[\frac{\boldsymbol{\mu}_1 \cdot \boldsymbol{\mu}_2}{r^3} - \frac{3(\boldsymbol{\mu}_1 \cdot \mathbf{r})\boldsymbol{\mu}_2 \cdot \mathbf{r})}{r^5}\right]. \tag{2.7}$$

The corresponding Hamiltonian operator of two interacting spins can be obtained by replacing $\boldsymbol{\mu}_i$ by $g_i\beta_e\mathbf{S}_i$ yielding

$$\mathcal{H}_{\mathrm{dd}} = \frac{\mu_0}{4\pi\hbar} g_1 g_2 \beta_e^2 \left[\frac{\mathbf{S}_1 \cdot \mathbf{S}_2}{r^3} - \frac{3(\mathbf{S}_1 \cdot \mathbf{r})\mathbf{S}_2 \cdot \mathbf{r})}{r^5}\right]. \tag{2.8}$$

Because the two electrons are coupled, it is more convenient to express $\mathcal{H}_{\mathrm{dd}}$ in terms of the total spin $\mathbf{S} = \mathbf{S}_1 + \mathbf{S}_2$:

$$\mathcal{H}_{\mathrm{dd}} = \mathbf{S}_1 \cdot \mathbf{D} \cdot \mathbf{S}_2 + \mathbf{S}_2 \cdot \mathbf{D} \cdot \mathbf{S}_1 = 2\mathbf{S}_1 \cdot \mathbf{D} \cdot \mathbf{S}_2 = \mathbf{S} \cdot \mathbf{D} \cdot \mathbf{S} \tag{2.9}$$

[34, 35] where $\mathbf{D}$ is the parameter matrix called zero-field splitting matrix containing the anisotropy of the dipolar interaction. In its principal axes system the dipolar matrix $\mathbf{D}$ is described by its diagonal elements D_{xx}, D_{yy}

and D_{zz}. Since $\mathbf{D}$ is traceless (Tr{$\mathbf{D}$} = 0) only two independent parameters D and E, are required. They are defined as $D = \frac{3}{2}D_{zz}$ and $E = \frac{1}{2}(D_{xx} - D_{yy})$ yielding

$$\mathbf{D} = \begin{pmatrix} -\frac{1}{3}D + E & & \\ & -\frac{1}{3}D - E & \\ & & \frac{2}{3}D \end{pmatrix}. \tag{2.10}$$

In the present study it is sufficient to consider axial symmetry ($E = 0$) of the dipolar interaction. The angular dependence of $\mathbf{D}$ can be obtained by calculating its matrix projections using the unit magnitude vector $\mathbf{n} = (\sin\theta\cos\phi, \sin\theta\sin\phi, \cos\theta)$ expressed in spherical polar coordinates:

$$d = \mathbf{n} \cdot \mathbf{D} \cdot \mathbf{n} = \frac{1}{3}D(3\cos^2\theta - 1) \tag{2.11}$$

where θ describes the angle between the direction of dipolar coupling and the magnetic field axis. Eqn. (2.8) can be evaluated in polar coordinates which, assuming the high-field approximation (Zeeman interaction is much more important than the dipolar interaction), delivers

$$\mathcal{H}_{dd} = d\left[S_{1z}S_{2z} - \frac{1}{4}(S_{1+}S_{2-} + S_{1-}S_{2+})\right] \tag{2.12}$$

[36] with

$$d = -\frac{\mu_0 g_1 g_2 \beta_e^2}{4\pi\hbar r^3}(3\cos^2\theta - 1) \tag{2.13}$$

and

$$d_\perp = \frac{\mu_0 g_1 g_2 \beta_e^2}{4\pi\hbar r^3}. \tag{2.14}$$

The r-dependence of $d_\perp$ is utilized to derive inter-spin distance from dipolar coupling strengths.

The Exchange Interaction

If the orbitals occupied by two electron spins have a significant overlap, the result is an exchange interaction. This purely quantum mechanical interaction has no classical counterpart but stems from the Coulomb interaction between the two unpaired electrons. The isotropic part of this interaction

(which is most important here) is represented by

$$\mathcal{H}_{\text{ex}} = J\mathbf{S}_1 \cdot \mathbf{S}_2 = JS_{1z}S_{2z} + \frac{1}{2}J(S_{1+}S_{2-} + S_{1-}S_{2+}) \tag{2.15}$$

[34, 35]. The energy levels of the singlet and triplet states are split apart by $\mathcal{H}_{\text{ex}}$. Whether the singlet or triplet state lies lower depends on the sign of J. The magnitude of J decreases with increasing inter-electron distance r so that $|J|$ is very small if the electrons are sufficiently far apart.

EPR Frequencies of a Pair of Coupled Electron Spins

The spin Hamiltonian of a pair of coupled spins within the high-field approximation can be written as:

$$\mathcal{H} = \mathcal{H}_{\text{Z}} + \mathcal{H}_{\text{ex}} + \mathcal{H}_{\text{dd}} \tag{2.16}$$

where

$$\mathcal{H}_{\text{Z}} = \omega_1 S_{1z} + \omega_2 S_{2z}$$

is the Zeeman interaction of the electron spins interacting with the applied magnetic field (along the z-axis). In the matrix representation of these three operators one finds for using the basis states given in set 2.4

$$\mathcal{H}_{\text{Z}} = \frac{1}{2}\begin{pmatrix} \omega_1+\omega_1 & 0 & 0 & 0 \\ 0 & \omega_1-\omega_2 & 0 & 0 \\ 0 & 0 & -(\omega_1-\omega_2) & 0 \\ 0 & 0 & 0 & -(\omega_1+\omega_2) \end{pmatrix}$$

$$\mathcal{H}_{\text{ex}} = \frac{J}{4}\begin{pmatrix} 1 & 0 & 0 & 0 \\ 0 & -1 & 2 & 0 \\ 0 & 2 & -1 & 0 \\ 0 & 0 & 0 & 1 \end{pmatrix} \quad \mathcal{H}_{\text{dd}} = \frac{d}{4}\begin{pmatrix} 1 & 0 & 0 & 0 \\ 0 & -1 & -1 & 0 \\ 0 & -1 & -1 & 0 \\ 0 & 0 & 0 & 1 \end{pmatrix}$$

Weak Coupling Limit In the weak coupling (wc) limit ($|J - \frac{1}{2}d| \ll |\omega_1 - \omega_2|$) one can ignore the off-diagonal terms in $\mathcal{H}_{\text{ex}}$ and $\mathcal{H}_{\text{dd}}$ so that the eigenvalues are the diagonal matrix elements of $\mathcal{H}$ and the eigenstates are simply the basic states:

$$\begin{aligned} E_1^{\mathrm{wc}} &= +\frac{1}{2}(\omega_1+\omega_2)+\frac{1}{4}(J+d) \qquad |1\rangle = |\uparrow\uparrow\rangle \\ E_2^{\mathrm{wc}} &= +\frac{1}{2}(\omega_1-\omega_2)-\frac{1}{4}(J+d) \qquad |2\rangle = |\uparrow\downarrow\rangle \\ E_3^{\mathrm{wc}} &= -\frac{1}{2}(\omega_1-\omega_2)-\frac{1}{4}(J+d) \qquad |3\rangle = |\downarrow\uparrow\rangle \\ E_4^{\mathrm{wc}} &= -\frac{1}{2}(\omega_1+\omega_2)+\frac{1}{4}(J+d) \qquad |4\rangle = |\downarrow\downarrow\rangle \end{aligned} \tag{2.17}$$

The frequencies of the allowed EPR transitions are therefore

$$\begin{aligned} E_{13}^{\mathrm{wc}} &= +\omega_1+\frac{1}{2}(J+d) \qquad E_{12}^{\mathrm{wc}} = +\omega_2+\frac{1}{2}(J+d) \\ E_{24}^{\mathrm{wc}} &= +\omega_1-\frac{1}{2}(J+d) \qquad E_{34}^{\mathrm{wc}} = +\omega_2-\frac{1}{2}(J+d) \end{aligned} \tag{2.18}$$

The spectrum in the weak coupling limit thus comprises a pair of doublets, centered at ω_1 and ω_2, with splitting $\omega_{ee} = |J+d|$. When $|J| \ll d$, this splitting is just $|d|$.

Strong Coupling Limit In the strong coupling (sc) limit, where $|J-\frac{1}{2}d| \gg |\omega_1-\omega_2|$ and $\omega_1 \approx \omega_2 \approx \omega$, the off-diagonal terms in in $\mathcal{H}_{\mathrm{ex}}$ and $\mathcal{H}_{\mathrm{dd}}$ result in complete mixing of $|\uparrow\downarrow\rangle$ and $|\downarrow\uparrow\rangle$ such that the eigenvalues and eigenstates are

$$\begin{aligned} E_1^{\mathrm{sc}} &= +\frac{1}{2}(\omega_1+\omega_2)+\frac{1}{4}(J+d) && |1\rangle = |\uparrow\uparrow\rangle \\ E_2^{\mathrm{sc}} &= -\frac{3}{4}J && |2\rangle = \frac{1}{\sqrt{2}}(|\uparrow\downarrow\rangle - |\downarrow\uparrow\rangle) = |S\rangle \\ E_3^{\mathrm{sc}} &= \frac{1}{4}J-\frac{1}{2}d && |3\rangle = \frac{1}{\sqrt{2}}(|\uparrow\downarrow\rangle + |\downarrow\uparrow\rangle) = |T_0\rangle \\ E_4^{\mathrm{sc}} &= -\frac{1}{2}(\omega_1+\omega_2)+\frac{1}{4}(J+d) && |4\rangle = |\downarrow\downarrow\rangle \end{aligned} \tag{2.19}$$

Only two allowed transitions $|1\rangle \leftrightarrow |3\rangle \leftrightarrow |4\rangle$ remain with frequencies

$$E_{13}^{\mathrm{sc}} = \omega+\frac{3}{4}d \qquad E_{34}^{\mathrm{sc}} = \omega-\frac{3}{4}d. \tag{2.20}$$

The spectrum consists of one doublet centered at ω and split by $\omega_{ee} = \frac{3}{2}|d|$.

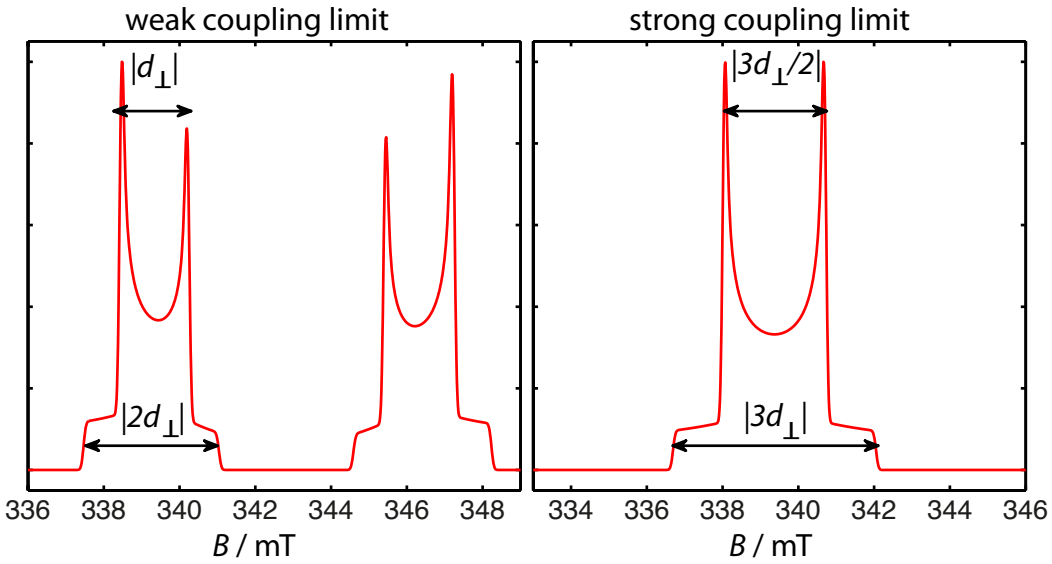

Figure 2.2: Dipolar spectra of powder samples. Left: Weak coupling case. Right: Strong coupling case. $d_\perp = -D/3$ and $d_\parallel = 2D/3$ with $D = 150$ MHz ≈ 5.4 mT. The spectra were simulated with easyspin (an EPR toolbox) [33].

Spectra of a Pair of Coupled Electron Spins We see that all allowed transitions in the weak as well as in the strong coupling case depend on d which itself is a function of θ describing the angle between the external magnetic field and the direction of dipolar coupling, as seen in Eq. (2.11). In the spectrum of a single crystal we thus observe a change of the doublet splitting as the crystal is rotated in the magnetic field. In the case of disordered solids, like the samples studied here, a random distribution of spin-spin orientations θ in the sample are expected giving rise to a powder spectrum. It is determined by the by the singularities $d_\perp = d(\theta = 90°) = -D/3$ and $d_\parallel = d(\theta = 0°) = 2D/3$ and the probability of finding a pair with orientation θ. Fig. 2.2 shows powder spectra of a pair of coupled spin in both limiting cases.

2.1.3 The Nuclear Zeeman Interaction

Analogous to the electron Zeeman interaction the nuclear Zeeman interaction describes the coupling of a nuclear spin I to the external field $\mathbf{B}$

$$\mathcal{H}_{\mathrm{NZ}} = -g_{\mathrm{n}}\beta_{\mathrm{n}}\mathbf{B}\cdot\mathbf{I}. \tag{2.21}$$

isotope	abundance/ %	spin I	g_n-value	ν_I/ MHz at 350 mT
^{1}H	99.985	1/2	5.59	14.90
^{11}B	80.2	3/2	1.79	4.78
^{17}O	0.038	5/2	-0.76	2.02
^{29}Si	4.67	1/2	-1.11	2.96
^{31}P	100	1/2	2.26	6.04

Table 2.1: Summary of the most important nuclei in this study. The list contains nuclei which can be found in hydrogenated microcrystalline Si solar cells with doping materials boron and phosphorus. ν_I demotes the nuclear Zeeman frequency.

where the quantum number I and the nuclear g_n are inherent properties of a nucleus [37]. β_n is the nuclear magneton which is three orders of magnitude smaller than the Bohr magnetic β_e of a free electron. The most important nuclei for this study are listed in table 2.1.

2.1.4 The Hyperfine Interaction

The interaction of a nuclear magnetic moment $\boldsymbol{\mu}_\mathrm{n} = g_\mathrm{n}\beta_\mathrm{n}\mathbf{I}$ with an electron magnetic moment $\boldsymbol{\mu}_\mathrm{e} = g_\mathrm{e}\beta_\mathrm{e}\mathbf{S}$ is given by

$$\mathcal{H}_\mathrm{HFI} = \frac{\mu_0}{4\pi\hbar^2} g_\mathrm{e} g_\mathrm{n} \beta_\mathrm{e} \beta_\mathrm{n} \mathbf{I} \cdot \left[\frac{\mathbf{L}}{r^3} - \frac{\mathbf{S}}{r^3} + 3\frac{\mathbf{r}(\mathbf{S}\cdot\mathbf{r})}{r^5} + \frac{8}{3}\pi\mathbf{S}\delta(\mathbf{r}) \right] \tag{2.22}$$

[36, 38]. This equation results from describing the behavior of an electron in the magnetic field produced by $\boldsymbol{\mu}_\mathrm{n}$. The first term in the bracket is the magnetic field caused by the electron orbital magnetic momentum $\mathbf{L}$. This is neglected in the coming considerations, since no significant contribution of $\mathbf{L}$ is expected [39]. The remaining terms describe the *electron nuclear magnetic dipole-dipole interaction*. The singular term is called the *Fermi contact interaction* which is only non-zero for electrons having a finite spin density $|\psi_e(r=0)|$ at the nucleus. The hyperfine interaction term can be written in a compact form as a sum of the isotropic Fermi contact interaction and the purely anisotropic part of the electron-nuclear dipole-dipole interaction:

$$\mathcal{H}_\mathrm{HFI} = \mathbf{S}\cdot\mathbf{A}\cdot\mathbf{I} = A_\mathrm{iso}\mathbf{S}\cdot\mathbf{I} + \mathbf{S}\cdot\mathbf{T}\cdot\mathbf{I} \tag{2.23}$$

with the isotropic coupling constant

$$A_{\text{iso}} = \frac{2}{3}\frac{\mu_0}{\hbar} g_{\text{e}}\beta_{\text{e}} g_{\text{n}}\beta_{\text{n}} |\psi_e(0)|. \tag{2.24}$$

Analogous to the dipolar electron spin-spin interaction (Eqn. 2.9), the traceless part of the electron nuclear dipole-dipole interaction can be expressed by the matrix

$$\mathbf{T} = \frac{\mu_0}{4\pi\hbar}\frac{g_{\text{e}}g_{\text{n}}\beta_{\text{e}}\beta_{\text{n}}}{r^3}\begin{pmatrix} -1 & & \\ & -1 & \\ & & 2 \end{pmatrix} \tag{2.25}$$

where r is the distance between the two spins. Again, one obtains the angular dependence

$$t = T(3\cos^2\theta - 1) \tag{2.26}$$

with θ the angle between the inter-spin direction and the external magnetic field and

$$T = \frac{\mu_0}{4\pi\hbar}\frac{g_{\text{e}}g_{\text{n}}\beta_{\text{e}}\beta_{\text{n}}}{r^3}. \tag{2.27}$$

The spin system $S = 1/2$ and $I = 1/2$, is connected with four possible spin states:

$$|S, m_S\rangle \otimes |I, m_I\rangle = \{|\uparrow_{\text{S}}\uparrow_{\text{I}}\rangle, |\uparrow_{\text{S}}\downarrow_{\text{I}}\rangle, |\downarrow_{\text{S}}\uparrow_{\text{I}}\rangle, |\downarrow_{\text{S}}\downarrow_{\text{I}}\rangle\} = \{|\uparrow\uparrow\rangle, |\uparrow\downarrow\rangle, |\downarrow\uparrow\rangle, |\downarrow\downarrow\rangle\}. \tag{2.28}$$

Assuming for example a small isotropic HFI in addition to a strong external magnetic field $\mathbf{B}(\parallel z-\text{axis})$ so that the high-field approximation is valid, the Hamiltonian can be simplified to

$$\begin{aligned} \mathcal{H}_{\text{Z}} + \mathcal{H}_{\text{NZ}} + \mathcal{H}_{\text{HFI}} &= g_{\text{e}}\beta_{\text{e}} B S_{\text{z}} - g_{\text{n}}\beta_{\text{n}} B I_{\text{z}} + A_{\text{iso}} S_{\text{z}} I_{\text{z}} \\ &= \omega_{\text{S}} S_{\text{z}} - \omega_{\text{I}} I_{\text{z}} + A_{\text{iso}} S_{\text{z}} I_{\text{z}} \end{aligned}$$

which yields the four energy levels

$$\begin{aligned} E_1 &= +\frac{1}{2}(\omega_{\text{S}} - \omega_{\text{I}}) + \frac{1}{4}A_{\text{iso}} & |1\rangle &= |\uparrow\uparrow\rangle \\ E_2 &= +\frac{1}{2}(\omega_{\text{S}} + \omega_{\text{I}}) - \frac{1}{4}A_{\text{iso}} & |2\rangle &= |\uparrow\downarrow\rangle \\ E_3 &= -\frac{1}{2}(\omega_{\text{S}} + \omega_{\text{I}}) - \frac{1}{4}A_{\text{iso}} & |3\rangle &= |\downarrow\uparrow\rangle \\ E_4 &= -\frac{1}{2}(\omega_{\text{S}} - \omega_{\text{I}}) + \frac{1}{4}A_{\text{iso}} & |4\rangle &= |\downarrow\downarrow\rangle \end{aligned} \tag{2.29}$$

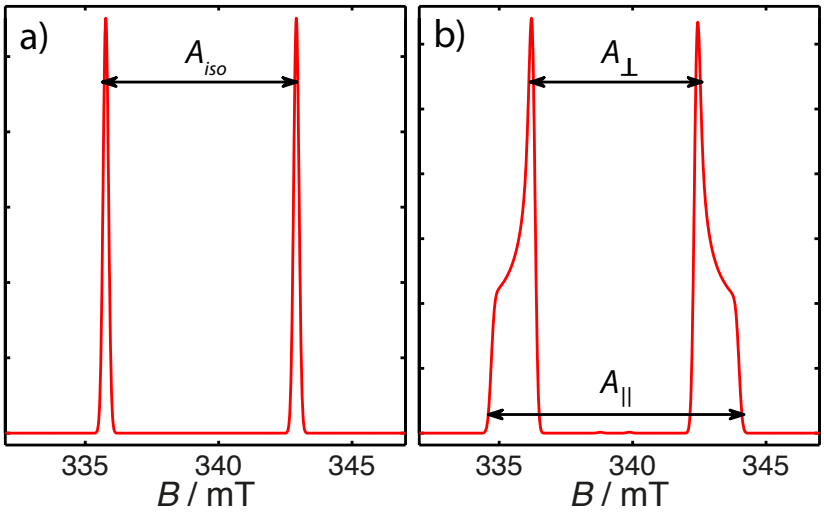

Figure 2.3: Simulated X-band spectra of an hyperfine coupled $S = 1/2$ plus $I = 1/2$ system. a) Only $A_{\text{iso}} = 200$ MHz contributes to the coupling. b) Here the HFI consists of $A_{\text{iso}} = 200$ MHz and $T = 30$ MHz. The spectra were simulated with easyspin (an EPR toolbox) [33].

The frequencies of the allowed EPR transitions ($\Delta m_S = \pm 1/2$) are therefore

$$\begin{aligned} E_{13} &= \omega_S + \frac{1}{2} A_{\text{iso}} \\ E_{24} &= \omega_S - \frac{1}{2} A_{\text{iso}} \end{aligned} \tag{2.30}$$

Hence, the spectrum consists of one doublet centered at ω_S and split by A_{iso}. This is shown in Fig. 2.3 a). This splitting is observed in solid crystal as well as in powder spectra, since it is orientation independent. Inclusion of the dipolar part introduces an additional θ-dependent splitting (since $A = A_{\text{iso}} + T(3\cos^2\theta - 1)$). An exemplary spectrum of a powder sample for this case is shown in Fig. 2.3 b). The intensity profile of the lines is caused by the the angular dependent dipolar part. The observed inner and outer edges are

$$A_\perp = A_{\text{iso}} - T \tag{2.31}$$

describing the smallest splitting and

$$A_\parallel = A_{\text{iso}} + 2T \tag{2.32}$$

describing the maximum splitting.

2.1.5 The Model System of $S = 1/2$ and $I = 1/2$ – Investigation of Hyperfine Interactions

The spin systems investigated in this thesis are in most cases composed of a coupled electron spin pair ($S_1, S_2 = 1/2$) and a single nuclear spin ($I = 1/2$). Nevertheless, it is advantageous to study first the simpler case of an electron spin $S_1 = 1/2$ coupled to a nuclear spin $I = 1/2$. Therefore, we give here a detailed discussion of this two-spin model system. In a second step, we extend this treatment to a coupled electron spin pair interacting with a nuclear spin by adding the exchange and dipolar interaction between the electrons under weak coupling conditions. Finally, the case of a strongly coupled electron spin pair plus a nuclear spin is considered.

Treatment of the System $S_1 = 1/2$ and $I = 1/2$

For an $S_1 = 1/2$, $I = 1/2$ system with a isotropic g-matrix and an anisotropic HFI the Hamiltonian is given by

$$\begin{aligned}\mathcal{H}_{01} &= \omega_{S1} S_{1z} + \omega_I I_z + \mathbf{S}_1 \cdot \mathbf{A} \cdot \mathbf{I} \\ &= \omega_{S1} S_{1z} + \omega_I I_z + a S_{1z} I_z + b S_{1z} I_x\end{aligned} \tag{2.33}$$

where the first and second term give the electron and nuclear Zeeman interaction. The two following terms are the secular and pseudo-secular parts of the hyperfine interaction. The pseudo-secular term $S_{1z} I_y$ as well as the terms in S_{1x} and S_{1y} can be very often neglected [37]. Furthermore,

$$a = A_\parallel \cos^2\theta + A_\perp \sin^2\theta \tag{2.34}$$

$$b = (A_\parallel - A_\perp) \sin\theta \cos\theta \tag{2.35}$$

where θ describes the angle between the electron-nuclear axis and the external magnetic field. In the product basis set 2.28 $\mathcal{H}_0$ is not diagonal. It can be diagonalized with the help of a unitary transformation [37] resulting in the set of eigenvectors

$$\begin{aligned}|1\rangle &= \cos(\eta_\alpha)\ |\uparrow\uparrow\rangle - \sin(\eta_\alpha)\ |\uparrow\downarrow\rangle \\ |2\rangle &= \sin(\eta_\alpha)\ |\uparrow\uparrow\rangle + \cos(\eta_\alpha)\ |\uparrow\downarrow\rangle \\ |3\rangle &= \cos(\eta_\beta)\ |\downarrow\uparrow\rangle - \sin(\eta_\beta)\ |\downarrow\downarrow\rangle \\ |4\rangle &= \sin(\eta_\beta)\ |\downarrow\uparrow\rangle + \cos(\eta_\beta)\ |\downarrow\downarrow\rangle\end{aligned} \tag{2.36}$$

The mixing angles η_α and η_β are given by

$$\tan 2\eta_\alpha = \frac{\frac{1}{2}b}{\frac{1}{2}a - \omega_\mathrm{I}} \qquad \tan 2\eta_\beta = \frac{\frac{1}{2}b}{\frac{1}{2}a + \omega_\mathrm{I}}. \tag{2.37}$$

One can see that b is responsible for the mixing of electronic and nuclear states. The energies corresponding to the eigenvectors $|1\rangle - |4\rangle$ are

$$\begin{aligned} E_1 &= \frac{\omega_{\mathrm{S1}}}{2} + \frac{1}{2}\omega_\alpha \\ E_2 &= \frac{\omega_{\mathrm{S1}}}{2} - \frac{1}{2}\omega_\alpha \\ E_3 &= -\frac{\omega_{\mathrm{S1}}}{2} + \frac{1}{2}\omega_\beta \\ E_4 &= -\frac{\omega_{\mathrm{S1}}}{2} - \frac{1}{2}\omega_\beta \end{aligned} \tag{2.38}$$

with

$$\omega_\alpha = \sqrt{(\frac{1}{2}a - \omega_\mathrm{I})^2 + \frac{1}{4}b^2} \qquad \omega_\beta = \sqrt{(\frac{1}{2}a + \omega_\mathrm{I})^2 + \frac{1}{4}b^2} \tag{2.39}$$

The transition frequencies are

$$\begin{aligned} E_{13} &= \omega_{\mathrm{S1}} + \frac{1}{2}(\omega_\alpha - \omega_\beta) \\ E_{14} &= \omega_{\mathrm{S1}} + \frac{1}{2}(\omega_\alpha + \omega_\beta) \\ E_{23} &= \omega_{\mathrm{S1}} - \frac{1}{2}(\omega_\alpha + \omega_\beta) \\ E_{24} &= \omega_{\mathrm{S1}} - \frac{1}{2}(\omega_\alpha - \omega_\beta) \end{aligned} \tag{2.40}$$

Without the anisotropy of the HFI ($a = A_\mathrm{iso}$ and $b = 0$) η_α and η_β become zero and we end up with the isotropic case in section 2.1.4. A energy level diagram and the corresponding transition frequencies are given in Fig. 2.4.

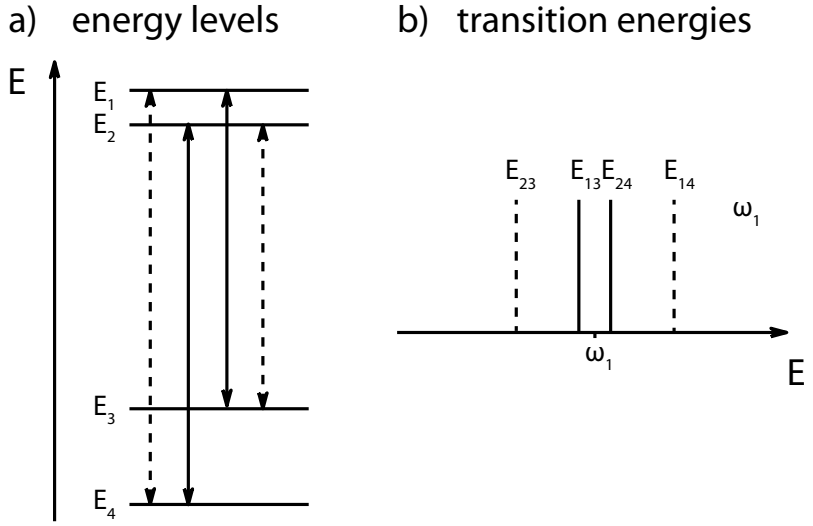

Figure 2.4: Spin system $S_1 = 1/2$ and $I = 1/2$ a) The energy level diagram for $a > 0, \omega_I > 0$ (as $g_n < 0$ for ^{29}Si nucleus) in the weak coupling limit ($\frac{1}{2}|a| < |\omega_I|$). b) Corresponding transition energies for the allowed (solid lines) and forbidden (dashed lines) EPR transitions.

A Weakly Coupled Spin Pair ($S_1, S_2 = 1/2$) Interacting with a Single Nucleus $I = 1/2$

In the case of a weakly coupled spin pair ($S_1, S_2 = 1/2$) interacting with a single nucleus $I = 1/2$ we have to add to the Hamiltonian $\mathcal{H}_{01}$ (Eqn. 2.33) the Zeeman interaction of the second electron and the two terms describing the exchange and dipolar interaction yielding

$$\mathcal{H}_{0wc} = \mathcal{H}_{01} + \omega_{S2} S_{2z} + J S_{1z} S_{2z} + d S_{1z} S_{2z}. \tag{2.41}$$

J is the strength of the exchange interaction (see Sec. 2.1.2), d is the strength of the axial dipolar coupling as introduced in Eqn. (2.13). Under conditions of weak coupling the nonsecular parts of the electron-electron interactions can be neglected [40]. The product basis $\{|\uparrow_{S1}\uparrow_I\rangle\ |\uparrow_{S2}\rangle, |\uparrow_{S1}\downarrow_I\rangle\ |\uparrow_{S2}\rangle, \dots\}$ is used. We write the states of electron 1 and the nucleus in one ket to emphasize the coupling of the nucleus to electron 1. The Hamiltonian $\mathcal{H}_{0wc}$ (wc = weak coupling) is diagonal in the electronic spin states but has off-diagonal elements connecting pairs of states with the same electron spin configuration but different nuclear spin orientations. Hence, the Hamiltonian must be diagonalized analogous to the two-spin system $S_1 = 1/2$, $I = 1/2$. This

results in eigenvectors

$$\begin{aligned}
|1+\rangle &= \cos(\eta_\alpha)\ |\uparrow_{S1}\uparrow_I\rangle\ |\uparrow_{S2}\rangle + \sin(\eta_\alpha)\ |\uparrow_{S1}\downarrow_I\rangle\ |\uparrow_{S2}\rangle \\
|1-\rangle &= -\sin(\eta_\alpha)\ |\uparrow_{S1}\uparrow_I\rangle\ |\uparrow_{S2}\rangle + \cos(\eta_\alpha)\ |\uparrow_{S1}\downarrow_I\rangle\ |\uparrow_{S2}\rangle \\
|2+\rangle &= \cos(\eta_\alpha)\ |\uparrow_{S1}\uparrow_I\rangle\ |\downarrow_{S2}\rangle + \sin(\eta_\alpha)\ |\uparrow_{S1}\downarrow_I\rangle\ |\downarrow_{S2}\rangle \\
|2-\rangle &= -\sin(\eta_\alpha)\ |\uparrow_{S1}\uparrow_I\rangle\ |\downarrow_{S2}\rangle + \cos(\eta_\alpha)\ |\uparrow_{S1}\downarrow_I\rangle\ |\downarrow_{S2}\rangle \\
|3+\rangle &= \cos(\eta_\beta)\ |\downarrow_{S1}\uparrow_I\rangle\ |\uparrow_{S2}\rangle + \sin(\eta_\beta)\ |\downarrow_{S1}\downarrow_I\rangle\ |\uparrow_{S2}\rangle \\
|3-\rangle &= -\sin(\eta_\beta)\ |\downarrow_{S1}\uparrow_I\rangle\ |\uparrow_{S2}\rangle + \cos(\eta_\beta)\ |\downarrow_{S1}\downarrow_I\rangle\ |\uparrow_{S2}\rangle \\
|4+\rangle &= \cos(\eta_\beta)\ |\downarrow_{S1}\uparrow_I\rangle\ |\downarrow_{S2}\rangle + \sin(\eta_\beta)\ |\downarrow_{S1}\downarrow_I\rangle\ |\downarrow_{S2}\rangle \\
|4-\rangle &= -\sin(\eta_\beta)\ |\downarrow_{S1}\uparrow_I\rangle\ |\downarrow_{S2}\rangle + \cos(\eta_\beta)\ |\downarrow_{S1}\downarrow_I\rangle\ |\downarrow_{S2}\rangle
\end{aligned} \tag{2.42}$$

The mixing angles are given by 2.37. The eigenenergies are

$$\begin{aligned}
E_{1\pm} &= +\frac{1}{2}(\omega_1+\omega_2) + \frac{1}{4}(J+d) \pm \frac{1}{2}\omega_\alpha \\
&= E_1^{wc} \pm \frac{1}{2}\omega_\alpha \\
E_{2\pm} &= +\frac{1}{2}(\omega_1-\omega_2) - \frac{1}{4}(J+d) \pm \frac{1}{2}\omega_\alpha \\
&= E_2^{wc} \pm \frac{1}{2}\omega_\alpha \\
E_{3\pm} &= -\frac{1}{2}(\omega_1-\omega_2) - \frac{1}{4}(J+d) \pm \frac{1}{2}\omega_\beta \\
&= E_3^{wc} \pm \frac{1}{2}\omega_\beta \\
E_{4\pm} &= -\frac{1}{2}(\omega_1+\omega_2) + \frac{1}{4}(J+d) \pm \frac{1}{2}\omega_\beta \\
&= E_4^{wc} \pm \frac{1}{2}\omega_\beta
\end{aligned} \tag{2.43}$$

where E_i^{wc} describes the energies of the weakly coupled electrons without an influence of a nuclear spin, as seen in Eqn. (2.17). One can see that in the case of two weakly coupled electron spins the secular term $bS_{1z}I_z$ leads to a mixing of the state $|\uparrow_{S1}\uparrow_I\rangle$ with $|\uparrow_{S1}\downarrow_I\rangle$ and $|\downarrow_{S1}\uparrow_I\rangle$ with $|\downarrow_{S1}\downarrow_I\rangle$. The second electron spin is not affected by HFI. Hence, the transitions E_{12} and E_{34} stay

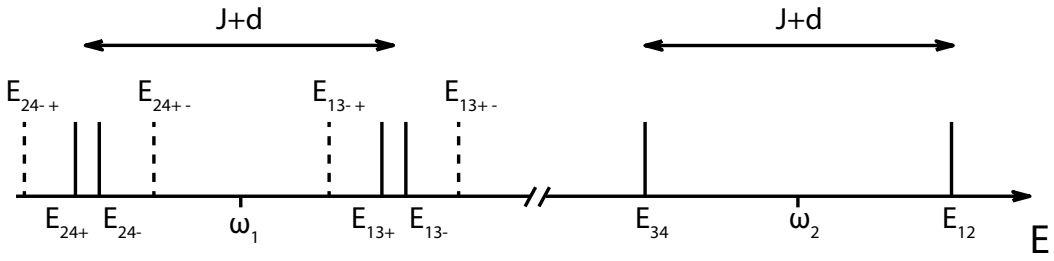

Figure 2.5: Weakly coupled spin pair ($S_1, S_2 = 1/2$) and a single nucleus $I = 1/2$. Transition energies for $a > 0, \omega_I > 0$ (as $g_n < 0$ for ^{29}Si nucleus) in the hyperfine weak coupling limit ($\frac{1}{2}|a| < |\omega_I|$) are shown. Solid lines symbolize the allowed and dashed lines the forbidden EPR transitions.

unchanged. The remaining transitions have the following energies:

$$\begin{aligned}
E_{13+} &= E_{13}^{wc} + \frac{1}{2}(\omega_\alpha - \omega_\beta) & E_{13-} &= E_{13}^{wc} - \frac{1}{2}(\omega_\alpha - \omega_\beta) \\
E_{13\pm} &= E_{13}^{wc} + \frac{1}{2}(\omega_\alpha + \omega_\beta) & E_{13\mp} &= E_{13}^{wc} - \frac{1}{2}(\omega_\alpha + \omega_\beta) \\
E_{24+} &= E_{24}^{wc} + \frac{1}{2}(\omega_\alpha - \omega_\beta) & E_{24-} &= E_{24}^{wc} - \frac{1}{2}(\omega_\alpha - \omega_\beta) \\
E_{24\pm} &= E_{24}^{wc} + \frac{1}{2}(\omega_\alpha + \omega_\beta) & E_{24\mp} &= E_{24}^{wc} - \frac{1}{2}(\omega_\alpha + \omega_\beta)
\end{aligned} \tag{2.44}$$

Again, E_{ij}^{wc} are given in Eqn. (2.18). The energy levels and corresponding transitions are depicted in Fig. 2.5

A Strongly Coupled Spin Pair ($S_1, S_2 = 1/2$) Interacting with a Single Nucleus $I = 1/2$

If the electron spins are strongly coupled, the non-secular terms of the electron-electron interaction can no longer be neglected. They have to be added to the Hamiltonian $\mathcal{H}_{0wc}$ giving

$$\mathcal{H}_{0sc} = \mathcal{H}_{0wc} + (\frac{J}{2} - \frac{d}{4})(S_{1+}S_{2-} + S_{1-}S_{2+}). \tag{2.45}$$

The "flip-flop" term is responsible for the state mixing of the electronic states $|\uparrow_{S1}\rangle\ |\downarrow_{S2}\rangle$ and $|\downarrow_{S1}\rangle\ |\uparrow_{S2}\rangle$. The eigenstates and eigenvalues of $\mathcal{H}_{0sc}$ in absence of a nucleus can be calculated delivering combined states and corre-

sponding energies [40, 41]:

$$\begin{aligned}
|1\rangle &= |\uparrow\uparrow\rangle \\
|2\rangle &= \frac{1}{\sqrt{2}}((\cos\phi + \sin\phi)\ |\uparrow\downarrow\rangle + (\sin\phi - \cos\phi)\ |\downarrow\uparrow\rangle) \\
|3\rangle &= \frac{1}{\sqrt{2}}((\cos\phi - \sin\phi)\ |\uparrow\downarrow\rangle + (\sin\phi + \cos\phi)\ |\downarrow\uparrow\rangle) \\
|4\rangle &= |\downarrow\downarrow\rangle
\end{aligned} \tag{2.46}$$

$$\begin{aligned}
E_1 &= +\frac{1}{2}(\omega_1 + \omega_2) + \frac{1}{4}(J + d) \\
E_2 &= \Omega - \frac{3}{4}J \\
E_3 &= -\Omega - \frac{1}{4}J - \frac{1}{2}d \\
E_4 &= -\frac{1}{2}(\omega_1 + \omega_2) + \frac{1}{4}(J + d)
\end{aligned} \tag{2.47}$$

with

$$\Omega = \sqrt{(-\frac{1}{2}J + \frac{1}{4}d)^2 + (\frac{\omega_1 - \omega_2}{2})^2} \tag{2.48}$$

and

$$\tan 2\phi = \frac{\frac{\omega_1 - \omega_2}{2}}{-\frac{1}{2}J + \frac{1}{4}d}. \tag{2.49}$$

Including the HFI part results in a not diagonal spin Hamiltonian, which is hard to diagonalize. Hence, an exact algebraic calculation of eigenstates and eigenvalues for the system of two strongly coupled electron spins ($S_1, S_2 = 1/2$) interacting with a single nuclear spin $I = 1/2$ is not possible. Thus, perturbation theory is utilized. In the present study the HFI energies are very small in comparison to 2Ω which is the energy separation between the states $|2\rangle$ and $|3\rangle$. Under these conditions the hyperfine terms connecting $|2\rangle$ and $|3\rangle$ can be considered as a perturbation. For the perturbation calculation the zero-order states $|j\rangle\ |\uparrow_\mathrm{I}\rangle, |j\rangle\ |\downarrow_\mathrm{I}\rangle, j = 1...4$ are used [40]. One finds the second-order correction to the energy of the states $|2\rangle$ and $|3\rangle$

$$\Delta E_{2\pm} = -\Delta E_{3\pm} = \frac{(\frac{1}{4}a^2 + \frac{1}{4}b^2)\cos^2 2\phi}{2\Omega}. \tag{2.50}$$

Hence, we obtain 8 energy levels:

$$\begin{aligned} E_{1\pm} &= +\frac{1}{2}(\omega_1+\omega_2)+\frac{1}{4}(J+d)\pm\frac{1}{2}\omega_\alpha \\ E_{2\pm} &= \Omega'-\frac{3}{4}J\pm\frac{1}{2}\omega_\gamma \\ E_{3\pm} &= -\Omega'-\frac{1}{4}J-\frac{1}{2}d\pm\frac{1}{2}\omega_\delta \\ E_{4\pm} &= -\frac{1}{2}(\omega_1+\omega_2)+\frac{1}{4}(J+d)\pm\frac{1}{2}\omega_\beta \end{aligned} \tag{2.51}$$

with

$$\Omega' = \Omega + \frac{(\frac{1}{4}a^2+\frac{1}{4}b^2)\cos^2 2\phi}{2\Omega} \tag{2.52}$$

and

$$\begin{aligned} \omega_\gamma &= \sqrt{(\frac{1}{2}a\sin 2\phi-\omega_I)^2+\frac{1}{4}b^2\sin^2 2\phi} \\ \omega_\delta &= \sqrt{(\frac{1}{2}a\sin 2\phi+\omega_I)^2+\frac{1}{4}b^2\sin^2 2\phi} \end{aligned} \tag{2.53}$$

The energy levels comprising the states $|1\rangle$ and $|4\rangle$ stay unchanged since the electronic states are the same as for the weak coupling case. The levels $E_{2\pm}$ and $E_{3\pm}$ are determined by perturbation calculation.

For $\phi = 0$ (strong coupling) the states $|\uparrow_{S1}\rangle\ |\downarrow_{S2}\rangle$ and $|\downarrow_{S1}\rangle\ |\uparrow_{S2}\rangle$ are completely mixed delivering the eigenstates

$$\begin{aligned} |1\rangle &= |\uparrow\uparrow\rangle \\ |2\rangle &= \frac{1}{\sqrt{2}}(|\uparrow\downarrow\rangle - |\downarrow\uparrow\rangle) \\ |3\rangle &= \frac{1}{\sqrt{2}}(|\uparrow\downarrow\rangle + |\downarrow\uparrow\rangle) \\ |4\rangle &= |\downarrow\downarrow\rangle \end{aligned} \tag{2.54}$$

For complete mixing we find that

$$\omega_\gamma = \omega_I \qquad \omega_\delta = \omega_I$$
$$\Delta E_{2\pm}(\phi=0) = -\Delta E_{3\pm}(\phi=0) = \frac{\frac{1}{4}a^2+\frac{1}{4}b^2}{-J+\frac{1}{2}d} \approx 0 \quad .$$

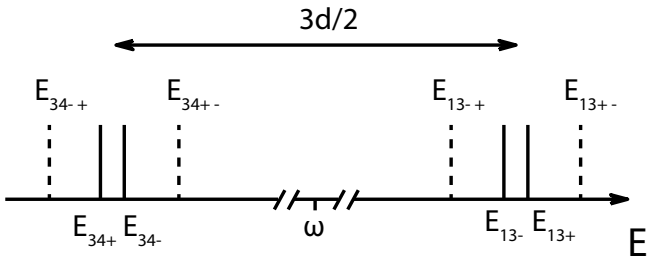

Figure 2.6: Strongly coupled spin pair ($S_1, S_2 = 1/2$) and a single nucleus $I = 1/2$. Transition energies for $a > 0, \omega_I > 0$ (as $g_n < 0$ for ^{29}Si nucleus) in the hyperfine weak coupling limit ($\frac{1}{2}|a| < |\omega_I|$) are shown. Solid lines symbolize the allowed and dashed lines the forbidden EPR transitions.

Thus we get the eigenvalues

$$\begin{aligned} E^{sc}_{1\pm} &= E^{sc}_1 \pm \frac{1}{2}\omega_\alpha \qquad & E^{sc}_{2\pm} &= E^{sc}_2 \pm \frac{1}{2}\omega_I \\ E^{sc}_{3\pm} &= E^{sc}_3 \pm \frac{1}{2}\omega_I \qquad & E^{sc}_{4\pm} &= E^{sc}_4 \pm \frac{1}{2}\omega_\beta \end{aligned} \tag{2.55}$$

where E^{sc}_i are the energy levels of a strongly coupled electron spin pair (see Eqn. (5.3)). The transition energies which are illustrated in Fig. 2.6 are

$$\begin{aligned} E_{13+} &= E^{sc}_{13} + \frac{1}{2}(\omega_\alpha - \omega_I) \qquad & E_{13-} &= E^{sc}_{13} - \frac{1}{2}(\omega_\alpha - \omega_I) \\ E_{13\pm} &= E^{sc}_{13} + \frac{1}{2}(\omega_\alpha + \omega_I) \qquad & E_{13\mp} &= E^{sc}_{13} - \frac{1}{2}(\omega_\alpha + \omega_I) \\ E_{34+} &= E^{sc}_{34} + \frac{1}{2}(\omega_I - \omega_\beta) \qquad & E_{34-} &= E^{sc}_{34} - \frac{1}{2}(\omega_I - \omega_\beta) \\ E_{34\pm} &= E^{sc}_{34} + \frac{1}{2}(\omega_I + \omega_\beta) \qquad & E_{34\mp} &= E^{sc}_{34} - \frac{1}{2}(\omega_I + \omega_\beta) \end{aligned} \tag{2.56}$$

with E^{sc}_{ij} given in Eqn. (2.20). We see that the energy levels of both EPR transitions $|1\rangle \leftrightarrow |3\rangle \leftrightarrow |4\rangle$ are affected by HFI under strong coupling conditions. The energy levels experience an additional splitting by sums and differences of ω_α, ω_β and ω_I.

2.1.6 Inhomogeneous Broadening of EPR Resonance Lines

Spectral lines are classified in homogeneously and inhomogeneously broadened lines. Homogeneous line broadening for a set of spins occurs when all these spins see the same net magnetic field and have the same spin Hamil-

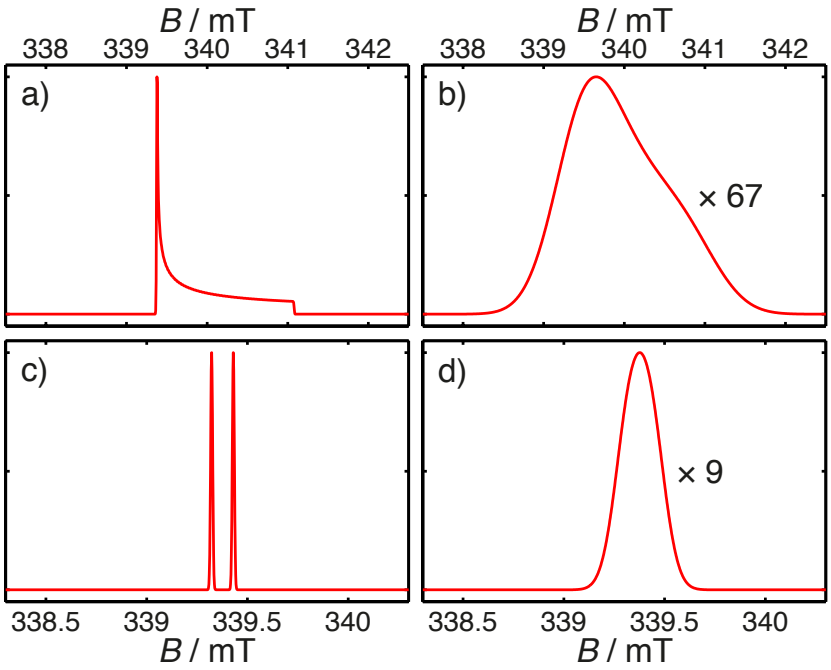

Figure 2.7: Unbroadened EPR spectra (left) compared to inhomogeneously broadened EPR spectra (right). a) Axial powder pattern with $g_\perp = 2.00$ and $g_\parallel = 1.99$. b) Additional broadening induced by g-strain of $\Delta g = 0.005$. c) EPR spectrum with resolved HFI of $A_{\text{iso}} = 3$ MHz. d) Adding g-strain of $\Delta g = 0.001$ washes out the resolved splitting. The intensities in b) (in d)) are multiplied by a factor of 67 (a factor of 9) relative to the spectrum in a) (in c)) to obtain equal maximum amplitudes.

tonian parameters. Such a set is called *spin packet*. The resulting line shape is usually a Lorentzian profile. Examples of sources of homogeneous broadening are fluctuating fields originating from electron and nuclear spin flips.

By contrast, in the inhomogeneous case the line broadening mechanism distributes the resonance frequencies over a finite range due to varying spin Hamiltonian parameters. The spectrum consists of a superposition of individual spin packets each slightly shifted in frequency from the others. In most cases this results in Gaussian line shapes. The following sources of broadening are relevant in disordered solid state systems as investigated in the work [35]:
Unresolved hyperfine structures occur in EPR spectra when the number of hyperfine components from nearby nuclei is so large that no distinct HFI splittings are observed. Hence one detects the envelope of a multitude of lines.

Anisotropic interactions are another source of inhomogeneous broadening. In randomly oriented solid state systems anisotropic hyperfine interaction gives a distribution of different local fields. Anisotropic Zeeman interaction causes a distribution of field/ frequency resonance conditions. Dipolar interactions with other paramagnetic centers in the environment give rise to line broadening, since they may impose a random local field at a given unpaired electron, arising from dipolar fields from other electron spins.
In disordered solid state systems the inhomogeneity in the local magnetic environment of the individual spin probe gives rise to site-to-site variations of magnetic parameters. Such structural site-to-site variations can leads to a distribution of g-values (*g-strain*), of hyperfine coupling strengths (*A-strain*) or of dipolar coupling strengths (*D-strain*).
In Fig. 2.7 the influence of inhomogeneous line broadening is illustrated using the example of g-strain. Effects of line broadening not only wash out distinct spectral structure, but also lead to a strong reduction of line intensities (and with this of the data quality), as indicated in the figure by the given scaling factors.

2.2 Electron Paramagnetic Resonance

In this section the interaction of spins with electromagnetic radiation is shortly described. Beside the macroscopic and microscopic static magnetic fields lifting the spin's energy level degeneracy (described in the preceding section), the interaction with oscillating magnetic fields (or photons) constitutes the second main pillar of EPR. This interaction is responsible for the absorption and emission of microwave radiation during magnetic dipole transitions which allows a comprehensive characterization of the spin system. In this section we focus on the key topics relevant in this work. First, the phenomenon of spin resonance is outlined (section 2.2.1). Second, the coherent motion of different spin systems during microwave irradiation is described (section 2.2.2). The distinct properties of spin dynamics help to get information about the spin quantum numbers of the investigated paramagnetic centers or the processes they are involved in. Third, the spin manipulation by pulsed microwave radiation is illustrated (section 2.2.3). Single pulses as well as sophisticated pulse sequences are important tools for measuring EPR and EDMR field sweep spectra or for the investigation of the microscopic environment of the paramagnetic centers. Their mechanics

are briefly described.

2.2.1 Principle of Electron Paramagnetic Resonance

As seen in the preceding section, a spin in an environment containing further nuclear and electron spins is affected by many different interactions. They cause additional energy level shifts and splittings resulting in a complex multi-level system. Transitions between these levels can be induced when the energy of the electromagnetic radiation $h\nu$ matches the energy level difference of the addressed transition ΔE:

$$E_\mathrm{i} - E_\mathrm{j} = \Delta E = h\nu. \tag{2.57}$$

For an isolated spin $S = 1/2$ ($g = g_\mathrm{e}$) only influenced by Zeeman interaction with an external magnetic field of strength $B = 340$ mT the transition between the states $m_\mathrm{S} = \pm 1/2$ is in resonance at the microwave frequency $\nu \approx 9.5$ GHz. The EPR spectrum then consists of a single line. An EPR spectrum can be obtained by either changing the energy splitting (by sweeping the external field) continuously during irradiation with a constant frequency radiation or by sweeping the frequency so that the resonance condition is met for all accessible transitions. In many cases the magnetic field sweep is preferred to detect EPR spectra.
Of special interest in this study are experiments in different magnetic field regimes (at different mw frequencies), since there are field-dependent (Zeeman interaction) and field-independent (spin-spin-) interactions. They dominate the EPR spectra at high and low external magnetic fields, respectively. Hence, by choice of a distinct field regime one of both groups of interactions can be preferentially studied. At sufficiently high fields field-independent contributions can be neglected which often leads to a gain of spectral resolution. Fields and frequencies applied in this work are given in Tab. 2.2. An exemplary simulated spectrum of two overlapping EPR signals is shown in Fig. 2.8.

2.2.2 Coherent Spin Motion

The application of an oscillating external magnetic field $\mathbf{B}_1(\mathrm{t})$ to a paramagnetic species of spin $S = 1/2$ with non-degenerate m_S energy levels in-

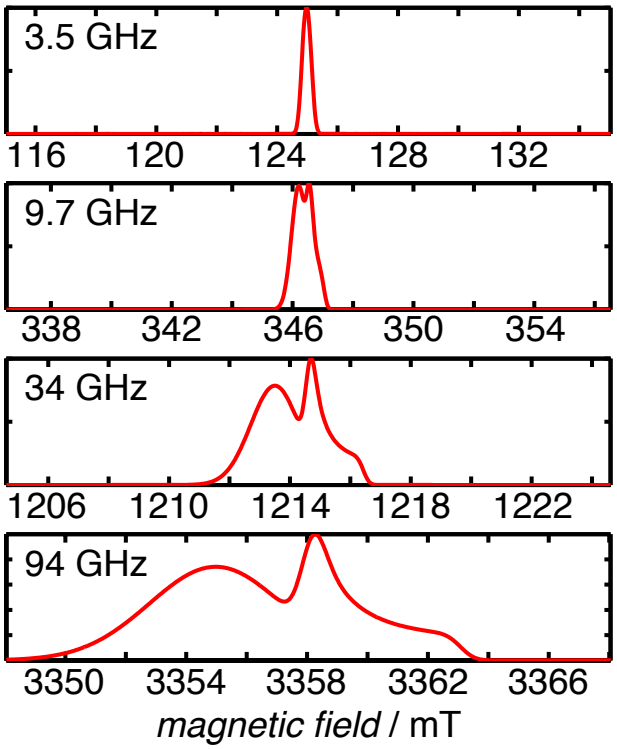

Figure 2.8: Simulation of EPR spectra in different field regimes. The spectrum consists of two independent paramagnetic species which partly overlap. The Zeeman interaction dominates at high fields/frequencies (resolution of g-matrix and broadening by g-strain). Unresolved HFI washes out any resolution at low fields.

duces magnetic dipole transitions. The corresponding time-dependent spin Hamiltonian $\mathcal{H}_1(t)$ is described by

$$\mathcal{H}_1(t) = g\beta_e \mathbf{S} \cdot \mathbf{B}_1(t). \tag{2.58}$$

In a frame of the rotating magnetic field $\mathbf{B}_1(t)$, also called a rotating Bloch sphere representation, the radiation amplitude behaves like a constant magnetic field vector so that the Hamiltonian becomes time-independent:

$$\mathcal{H}_1 = g\beta_e \mathbf{S} \cdot \mathbf{B}_1 = g\beta_e B_1 S_x = \omega_1 S_x \tag{2.59}$$

(assuming that $\mathbf{B}_1 \parallel \mathbf{x}$-axis). This aspect is described in more detail in Sec. 2.2.3. Transitions take place between spin states fulfilling the selection rule

EPR frequency/ GHz	frequency band	magnetic field/ mT ($g = 2$)
3.5	S	120
9.5	X	340
34	Q	1200
94	W	3360
263		9400

Table 2.2: Overview of microwave frequency bands and corresponding magnetic fields used in this work.

$\Delta m_S = \pm 1$, since

$$\langle S, m_S | S_x | S, m'_S \rangle = \frac{1}{2} \langle S, m_S | (S_+ + S_-) | S, m'_S \rangle \tag{2.60}$$

is only different from zero, when $m'_S = m_S \pm 1$. Under the influence of resonant microwave excitation of amplitude $2B_1$ the transitions between neighboring energy levels m_S and $m_S + 1$ of the spin S is driven with the *Rabi nutation frequency*

$$\Omega(m_S, m_S + 1) = \frac{g\beta_e B_1}{\hbar} \sqrt{S(S+1) - m_S(m_S+1)}. \tag{2.61}$$

For a spin $S = 1/2$ with $m_S = \frac{1}{2}, -\frac{1}{2}$ the nutation frequency is $\Omega^{S=1/2} = \frac{g\beta_e B_1}{\hbar} = \omega_1$. In the case of $S = 1$ there are three possible m_S-values: $m_S = -1, 0, +1$. For both transitions $\Delta m_S \pm 1$ one finds identical frequencies: $\Omega^{S=1} = \sqrt{2}\frac{g\beta_e B_1}{\hbar} = \sqrt{2}\omega_1$.

Considering a pair of electron spins ($S_1 = 1/2, S_2 = 1/2$), the Hamiltonian describing the interaction between the spins and the electromagnetic radiation is given by

$$\mathcal{H}_1 = g\beta_e(\mathbf{S_1} + \mathbf{S_2}) \cdot \mathbf{B}_1 = \omega_1(S_{1x} + S_{2x}). \tag{2.62}$$

Here it is necessary to distinguish two different scenarios: The selective excitation of one spin of the pair as well as the non-selective excitation where both spins are in resonance at the same time.
When the Larmor separation between both spin partners is larger than the mw field ($\hbar\Delta\omega \gg g\beta_e B_1$), only the spin S_1 is manipulated by the mw radiation (selective excitation). Spin S_2 is not affected. In this case the Hamil-

tonian reduces to $\mathcal{H}_1 = \omega_1 S_{1x}$. This is nothing else then the excitation of a single spin delivering the nutation frequency $\Omega = \omega_1$.
When both spins are excited simultaneously ($\hbar\Delta\omega \ll g\beta_e B_1$), the full Hamiltonian (Eqn. 2.62) has to be regarded. The transition matrix element

$$\langle S_1, m_{S,1}|\langle S_2, m_{S,2}|\omega_1(S_{1x} + S_{2x})|S_1, m_{S,1}+1\rangle|S_2, m_{S,2}+1\rangle \tag{2.63}$$

can be written in the form

$$\omega_1(\langle S_1, m_{S,1}|S_{1x}|S_1, m_{S,1}+1\rangle + \langle S_2, m_{S,2}|S_{2x}|S_2, m_{S,2}+1\rangle) \tag{2.64}$$

since independent angular momenta of different independent sets of eigenfunctions commute ($[S_{1x}, S_{2x}]_- = 0$). Thus, the nutation frequency $\Omega = 2\omega_1$ is expected. This behavior is referred to as *spin locking behavior*.

An alternative way to calculate the coherent spin dynamics of ensembles of spins and spin pairs makes use of temporal evolution of the density matrix [42, 43]. The time dependence of the density matrix ρ is given by the Liouville- von Neumann equation

$$\frac{d\rho}{dt} = -i\,[\mathcal{H}(t), \rho(t)] \tag{2.65}$$

with $\mathcal{H} = \mathcal{H}_0 + \mathcal{H}_1(t)$. $\mathcal{H}_0$ comprises the spin-spin interaction as well as the Zeeman interaction of both spins, $\mathcal{H}_1(t)$ describes the interaction with the microwave field (see Eqn. 2.62).
For the EDMR results presented in this work it is of special interest to look at the temporal development of the populations in the spin and spin pair states, since they directly influence the EDMR observable. Recently it was illustrated in a detailed application of this density matrix approach [43], that the single spin states $|\uparrow\rangle$ and $|\downarrow\rangle$ as well as the states $|\uparrow\uparrow\rangle$ and $|\downarrow\downarrow\rangle$ of the spin pair under selective excitation conditions are populated and depopulated with the frequency ω_1, whereas the populations in the spin pair states $|\uparrow\uparrow\rangle$ and $|\downarrow\downarrow\rangle$ under non-selective excitation oscillate with $2\omega_1$. This is in full agreement with the transition matrix element results obtained above.
In addition to these results, we consider the oscillation frequency of the populations of the spin $S = 1$ states. The detailed calculation of this frequency regarding the transition $m_S = -1 \leftrightarrow m_S = 0$ is given in appendix 7.1. One finds the oscillation frequency $\Omega = \sqrt{2}\omega_1$.
In the EDMR studies presented in the upcoming chapters Rabi nutation

frequencies constitute an important source of information about the spin-dependent processes in the solar cells and the underlying paramagnetic centers.

2.2.3 Pulse EPR

Let us assume a spin ensemble with spins $S = 1/2$. The spin nutation excited by the oscillating magnetic field $\mathbf{B}_1(\mathrm{t})$ leads to an oscillation of the spin state populations and with this of the sample magnetization $\mathbf{M}$, since the magnetic moments $\boldsymbol{\mu}_\mathrm{i}$ of the single spins add up to a macroscopic magnetization $\mathbf{M} = \sum_i \boldsymbol{\mu}_\mathrm{i}$. This magnetization constitutes the observable in EPR and NMR experiments. The choice of a coordinate system rotating with ω_1 simplifies the description of the temporal behavior of $\mathbf{M}$. $\mathbf{B}_1$ is then constant in time. Irradiation with microwaves of amplitude B_1 for a short time leads to a rotation of $\mathbf{M}$ about $\mathbf{B}_1$ by an angle $\phi = \omega_1 t_\mathrm{p}$ where t_p is the length of the mw pulse. The flip angle ϕ is dependent on the length of the pulse t_p as well as on the nutation frequency ω_1 which in turn is determined by the mw field amplitude B_1.
For a pulse $\phi = \pi$ the magnetization $\mathbf{M}$ is fully inverted which corresponds to an inversion of the populations of the spin states $|\uparrow\rangle$ and $|\downarrow\rangle$. The spin manipulation by π-pulses constitutes the basic manipulation for EDMR experiments, since with that the relative spin orientation of spin pair partners can be altered. This is discussed further in Sec. 2.3.
Application of a $\pi/2$-pulse rotates $\mathbf{M}$ into the xy-plane giving rise to an EPR signal called *free induction decay (FID)*. Due to dephasing of the different spin-packets of a resonance line, $\mathbf{M}$ decays quite fast so that the EPR signal is hard to detect in many cases. Fortunately, applying sequences of pulses helps to overcome these problems. The spin echo sequence is the most prominent example.

The Electron Spin Echo Sequence

The dephasing process described above can be reversed by an additional pulse of length π applied after a certain pulse-interval time τ. This leads to a rephasing of the spin-packets. The same time τ after the π pulse a building up and decay of the initial magnetization is observed. This refocussed signal

is called *echo*. The pulse sequence can be described by

$$\frac{\pi}{2} \; - \; \tau \; - \; \pi \; - \; \tau \; - \; \text{echo}$$

where the first pulse is named *excitation pulse* and the second one *refocussing pulse*. This sequence was first described in NMR (1950) and is called *Hahn sequence* after its discoverer [44]. In EPR this technique was first used in 1958 [45]. The spin echo intensity is a measure of the number of spins manipulated by the pulse sequence at a distinct mw frequency and magnetic field. By recording the echo intensity versus the external magnetic field, the EPR spectrum of the spin system can be obtained.

Electron Spin Echo Envelope Modulations

The spin-echo signal measured as a function of the pulse-interval time τ decreases in height. This decrease is caused by irreversible spin-spin and spin-lattice relaxation processes which affect the amount of refocussed magnetization. In selected systems this decay is superimposed with a modulation. This effect was first measured and theoretically described by Mims [46, 47] and is named Electron Spin Echo Envelope Modulation (ESEEM). It arises from anisotropic hyperfine interaction. The modulation frequencies which are obtained by Fourier-transformation of the echo decay time trace contain information about neighboring nuclei coupled to the electron spin. It was shown in Sec. 2.1.5, that anisotropic HFI leads to a mixing of electronic and nuclear states. This is responsible for additional transitions ($\Delta m_S = \pm 1$ plus $\Delta m_I = \pm 1$) which are forbidden for isotropic HFI, but become weakly allowed for anisotropic HFI. The additional flipping of nuclear spins influences the rephasing of the electron spin echo in form of echo intensity modulation with characteristic nuclear frequencies. This modulation of the echo intensity I_{Echo} as function of the pulse-interval time τ is given by

$$I_{\text{Echo}} = 1 - \frac{K}{4}(2 - 2\cos\omega_\alpha\tau - 2\cos\omega_\beta\tau + \cos(\omega_\alpha + \omega_\beta)\tau + \cos(\omega_\alpha - \omega_\beta)\tau)$$

for a single electron spin $S = 1/2$ coupled to a nucleus $I = 1/2$ [37, 48]. The frequencies ω_α and ω_β are

$$\omega_\alpha = \sqrt{(\frac{1}{2}a - \omega_I)^2 + \frac{1}{4}b^2} \qquad \omega_\beta = \sqrt{(\frac{1}{2}a + \omega_I)^2 + \frac{1}{4}b^2}. \tag{2.66}$$

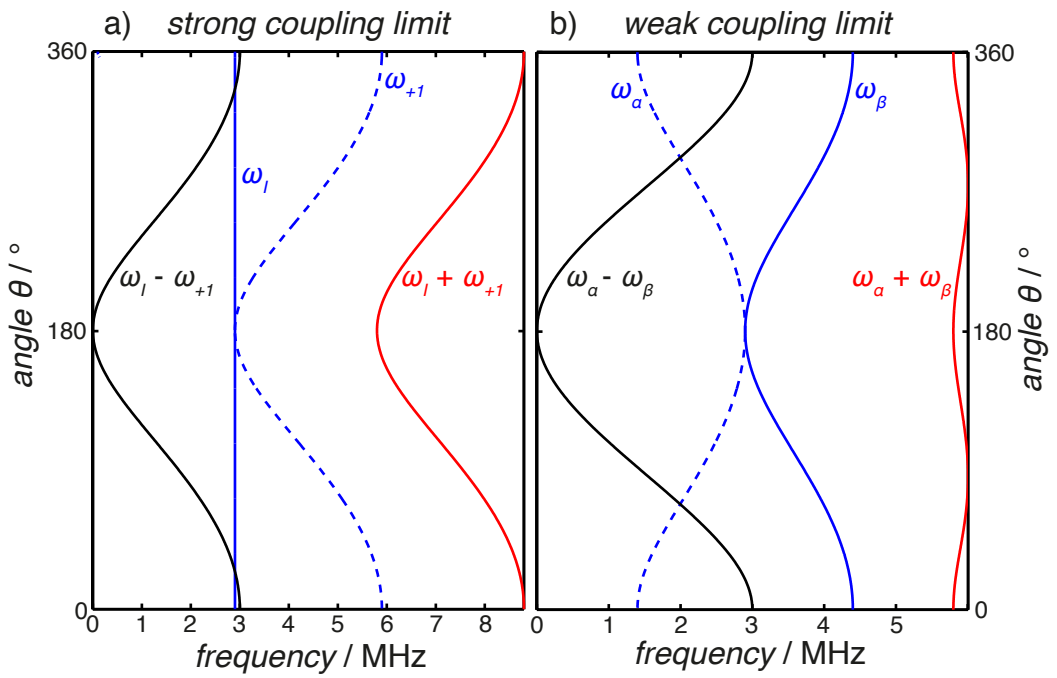

Figure 2.9: Angular dependence of two-pulse ESEEM transition frequencies of a spin pair ($S_1 = 1/2, S_2 = 1/2$) coupled to a single nuclear spin $I = 1/2$ ($\omega_\mathrm{I} = 2.9$ MHz). Hyperfine coupling parameters $A_\mathrm{iso} = 2$ MHz and $T = -1$ MHz were used for the calculation. a) Strong coupling limit ($S = 1$). The EPR transition $m_\mathrm{S} = +1 \leftrightarrow m_S = 0$ is considered. The transition frequencies ω_I, $\omega_{\pm1}$ (blue lines) and their sums (red) and differences (black) are illustrated. b) Weak coupling limit ($S = 1/2$). The transition frequencies ω_α, ω_β (blue lines) and their sum (red) and difference (black) are illustrated.

$$K = \left(\frac{b\omega_\mathrm{I}}{\omega_\alpha \omega_\beta} \right)^2 \tag{2.67}$$

is the modulation depth parameter. This frequency dependence is also valid to describe ESEEM data of weakly coupled electron spin pairs [40].
The τ dependence of the echo intensity for a spin pair in the strong coupling limit is described by

$$I_\mathrm{Echo} = 1 - \frac{K}{4}(2 - 2\cos\omega_\mathrm{I}\tau - 2\cos\omega_{\pm1}\tau + \cos(\omega_\mathrm{I} + \omega_{\pm1})\tau + \cos(\omega_\mathrm{I} - \omega_{\pm1})\tau)$$

with ω_{+1} for the transition $m_\mathrm{S} = +1 \leftrightarrow m_S = 0$ and with ω_{-1} for the transition $m_\mathrm{S} = 0 \leftrightarrow m_S = -1$, respectively. The frequencies $\omega_{\pm1}$ are given

by $\omega_{+1} = \omega_\alpha$ and $\omega_{-1} = \omega_\beta$.

$$K_{+1} = \left(\frac{b}{2\omega_\alpha}\right)^2 \qquad \text{and} \qquad K_{-1} = \left(\frac{b}{2\omega_\beta}\right)^2 \tag{2.68}$$

are the modulation depth parameters of both transitions [37, 40].
In both coupling limits the ESEEM data consist of 4 frequencies: There are ω_α, ω_β and their sums and differences in the weak coupling case. In the strong coupling case frequencies at ω_I, $\omega_{\pm1}$ and their sums and differences for the transitions $m_\mathrm{S} = \pm1 \leftrightarrow m_S = 0$ are expected. Since the hyperfine parameters a and b (see Sec. 2.1.5) depend on the angle θ between the direction of the external magnetic field and the electron-spin nuclear-spin coupling direction, all ESEEM frequencies except ω_I show angular dependence (see Fig. 2.9). For single crystal samples these distinct θ-dependent frequencies are clearly observed in ESEEM traces [49–51]. Contrary to that, solid state powder samples as the solar cells investigated here are affected by line averaging, since contributions of all angles θ are part of the spectrum. Provided that the HFI parameters are small compared to ω_I, ESEEM spectra of weakly coupled spin pairs interacting with a nucleus show frequencies around ω_I and $2\omega_\mathrm{I}$ as well as $\omega \approx 0$. ESEEM traces of strongly coupled spin pairs interacting with a nucleus $I = 1/2$ are therefore dominated by the θ-independent nuclear frequency ω_I. Additional (minor) contributions in the range $\omega \approx 0 - 3\omega_\mathrm{I}$ are expected.

2.3 Electrically Detected Magnetic Resonance

The aforegoing sections have shown that EPR facilitates to draw a precise picture of the microscopic environment of the studied paramagnetic centers. Hence, the investigation of charge carrier processes in working devices as solar cells, LEDs or transistors with means of EPR is strongly desirable to allow new helpful insights. However, the application of EPR is often not possible owing to the complexity of the device structure or the low detection sensitivity of this method.
An interesting approach to solve these problems is the combination of electron spin manipulation with the detection of a suitable sample observable. For example, observation of the change of the sample luminescence under spin manipulations is called optically detected magnetic resonance

(ODMR) [52–56]. Reaction-yield detected magnetic resonance (RYDMR) utilizes the spin-dependence of chemical reactions involving paramagnetic radicals [57, 58]. EDMR makes use of the influence of localized paramagnetic centers on the sample conductivity [16, 59, 60]. All these combined methods are characterized by their high sensitivity with respect to the sensitivity of standard EPR. The reason for the greater sensitivity is a quantum transformation of the spin-flip detection from direct absorption due to transitions between the Zeeman levels (quantum energy of a few tens of μeV) to transitions between different electronic states governed by spin-selection rules (quantum energy up to an order of 1 eV) [17].
Since the photocurrent plays a key role of solar cells' working principles, EDMR constitutes a convenient method to explore the charge carrier processes via localized states within these working devices. The principles of EDMR will be subject of the following sections. First, the well-established theory of spin pairs developed by Kaplan, Solomon and Mott (*KSM model*) will be introduced [32] (section 2.3.1). This theory describes the basic spin-dependent step which is part of and thereby governs different charge transport processes via localized states. In the following, the influence of this spin-dependent step on different charge transport mechanisms is illustrated (section 2.3.2) comprising hopping transport and recombination as the most important mechanisms in the present devices. It shows that spin-dependent processes including strongly coupled spin pairs have to be considered to explain some of the EDMR signatures. The respective models are described in section 2.3.3. Finally, similarities and differences between EPR and EDMR experiments are discussed in section 2.3.4.

2.3.1 The Spin Pair Model

The first quantitative model describing resonant changes $\Delta\sigma/\sigma$ of photoconductivity σ is the spin polarization effect considered by Lepine in 1972 [61] for the case of recombination of photo carriers with surface states in crystalline Si. In this model the spin-dependent recombination depends on the thermal polarization of charge carriers. Unfortunately, the predicted dependencies of the EDMR signal strength on the external magnetic field $\mathbf{B}$ and the temperature T could not be confirmed experimentally.
A series of further approaches to explain the phenomenon of EDMR were made [31, 62–65], but most of the models failed to predict correct magni-

tudes or correct dependencies on **B** and T.
In 1978 the KSM model was developed by Kaplan, Solomon and Mott [32] describing spin-dependent recombination in terms of an intermediate pair model where two spins in localized states form an exclusive spin pair from which they either recombine or dissociate. Whether the recombination step takes place or whether the pair dissociates is governed by the symmetry of the spin wave function of the two electron spins within this exclusive pair.
In the following we focus on the spin-dependent part of the recombination process described in the KSM model. This basic spin-dependent step is not only part of spin-dependent recombination [19, 32, 66] but also part of the spin-dependent hopping transport [67], which is observed in the samples studied here.
Let us assume two localized states (states A and B) sufficiently close to each other, which are both occupied by one electron forming a spin pair. A further assumption should be that the electron occupying state A has to transfer to state B. The spin state of the pair should be conserved during the transition process. A scheme of this transition is shown in Fig. 2.10.
In scenario 1 the spins in the states A and B are aligned antiparallel. The spin pair is in a singlet state ($S = 0$) and a transition of the electron from state A to state B is allowed. The spin-dependent step is completed when state B is doubly occupied. In a subsequent spin-independent step one electron leaves state B and the spin pair dissociates.
In scenario 2 both spins are aligned parallel and, hence, form a triplet state ($S = 1$). The transition is now forbidden [68]. When one of the two electrons jumps to a third state nearby, the spin pair is destroyed.

The Hamiltonian of a spin pair was already discussed in sections 2.1.2 and 2.1.5. We saw that the Hamiltonian in Eqn. (2.16) yields four eigenstates Eqn. 2.46. Two of them are pure triplet states ($|\uparrow\uparrow\rangle$ and $|\downarrow\downarrow\rangle$) independent of the mutual spin-spin coupling. The remaining two states are mixed states which can be expressed in terms of the singlet state $|S\rangle$ and the third pure triplet state $|T_0\rangle$:

$$\begin{aligned} |1\rangle &= |\uparrow\uparrow\rangle = |T_+\rangle \\ |2\rangle &= \cos\phi|S\rangle + \sin\phi|T_0\rangle \\ |3\rangle &= \cos\phi|T_0\rangle + \sin\phi|S\rangle \\ |4\rangle &= |\downarrow\downarrow\rangle = |T_-\rangle \end{aligned} \tag{2.69}$$

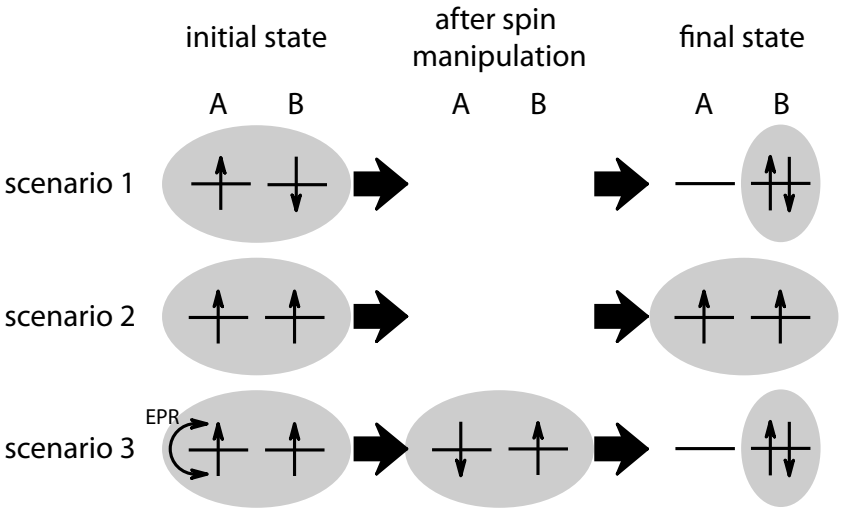

Figure 2.10: Principle of a spin-dependent transition based on the KSM model is described. The three different scenarios are explained in the text. The spin orientation is represented by arrows. Gray shaded areas highlight the exclusive spin pairs.

where

$$\phi = \frac{1}{2}\arctan\left(\frac{\frac{\omega_1-\omega_2}{2}}{-\frac{1}{2}J+\frac{1}{4}d}\right) \tag{2.70}$$

is a measure of state mixing. For $\phi = 0$ the spins are strongly coupled yielding $|T_0\rangle$ or $|S\rangle$ as appropriate eigenstates, whereas for $\phi = \pi/4$ the interspin coupling becomes zero and we obtain $|{\downarrow}{\uparrow}\rangle$ and $|{\uparrow}{\downarrow}\rangle$ as convenient states. The spin pair model describes transitions from any of the four pair states as solely dependent on the symmetry of the spin wave function. Thus, for pure singlet and triplet states distinct probabilities r_S and r_T can be assigned. In an intermediate coupling regime state mixing in the singlet and triplet eigenstates $|2\rangle$ and $|3\rangle$ occurs, which have different transition probabilities [67]

$$r_\mathrm{i} = r_\mathrm{S}|\langle i|S\rangle|^2 + r_\mathrm{T}|\langle i|T_0\rangle|^2 \tag{2.71}$$

dependent on ϕ, whereas the transition probabilities r_T of the triplet states $|T_+\rangle$ and $|T_-\rangle$ remain unchanged.
Due to the multiplicity $M = 2S+1 = 3$ for the spin quantum number $S = 1$ compared to $M = 2S+1 = 1$ for the $S = 0$, there is always a surplus of

spin pairs with triplet character even without an external magnetic field. This surplus is further enhanced by the long lifetimes of triplet pairs with respect to singlet pairs due to the different transition probabilities as well as by the spin polarization when high fields and low temperatures are applied. This fact constitutes the basis of the EDMR effect (see scenario 3 in Fig. 2.10): The resonant mw excitation of a single spin which is part of a pair in the states $|T_+\rangle$ or $|T_-\rangle$ alters the spin symmetry by creating states $|2\rangle$ or $|3\rangle$, and the initially forbidden transition becomes allowed. This activation of charge carrier transitions influences the sample conductivity dependent on the subsequent process and finally gives rise to a mw-induced current change which is the observable of an EDMR experiment.

2.3.2 The Spin-Dependence of Charge Transport

EDMR measures the mw-induced change of the sample photoconductivity σ_{ph}. The conductivity of an ideal semiconductor can be described by

$$\sigma = e\left[n_e\mu_e + n_h\mu_h\right] \tag{2.72}$$

consisting of an electron and a hole conductivity contribution. Here, e is the elementary charge. n_i and μ_i are the charge carrier concentrations and mobilities. The spin manipulation can influence n_i as e.g. in recombination processes as well as μ_i as in the case of hopping transport. Both examples of charge carrier processes are topic of the next sections.

Spin-Dependent Recombination

Spin-dependent recombination [61] was the first process investigated by EDMR. It can be observed in samples containing localized states in the band gap with significant energy differences via which charge carriers recombine. Disordered semiconductors comprising amorphous and microcrystalline silicon belong to these materials. They contain deep defects called *dangling bonds* in the middle of the mobility gap (band gap) [17, 69] which act as recombination centers.
The recombination process consists of two steps. First, an electron from a state in or near the conduction band tunnels into a deep energy state. Second, a hole from a state in or near the valence band is captured in this deep

defect state annihilating both carriers. Hence, recombination processes influence the electron as well as hole concentrations n_e and n_h.
In general, band-to-band recombination is spin-independent, whereas recombination via localized states is spin-dependent. Considering recombination via localized states the spin-dependence occurs when the deep defect is singly occupied (Fig. 2.11). Then the transition probability of an electron from a localized state near the conduction band depends on the spin configuration of both spins as described in Sec. 2.3.1. Changing the spin pair state by selective EPR manipulation of one spin, increases the singlet content of the spin pair which increases transition probability according to 2.71. Regarding an ensemble of spin pairs, this is, in turn, connected with a change of the sample conductivity

$$\Delta\sigma_{ph} = e\left[\Delta n_e \mu_e + \Delta n_h \mu_h\right]. \tag{2.73}$$

Since the charge carrier concentrations n_i decrease, the photoconductivity is reduced.
The dynamics of the spin pair ensemble is determined by the individual spin pairs whose evolutions depend on their pair Hamiltonian [19]. The dynamics of the pair ensemble can be described in terms of stochastic Liouville equation whilst taking into account stochastic processes like pair generation and annihilation as well as spin relaxation [19, 70]. The obtained time-dependent conductivity change $\Delta\sigma_{ph}(t)$ is a sum of exponential functions which depend on the spin pair generation, dissociation and recombination rates [19, 67].

Spin-Dependent Hopping Transport

Hopping transport processes can take place in networks of localized states of similar energies. Repetitive transitions (tunneling processes) of charge carriers from one localized state to another constitute charge carrier transport. Most of these tunneling events are spin-independent when the charge carrier jumps into an initially unoccupied state. But this process, again, can be spin-dependent as tunneling of an electron into a singly occupied state depends on the mutual spin orientation of both electrons. Spin manipulation increases the probability of tunneling processes into singly occupied states (see Sec. 2.3.1) and thus, increases the macroscopic sample mobility whereas the charge carrier concentration remains unchanged. The change

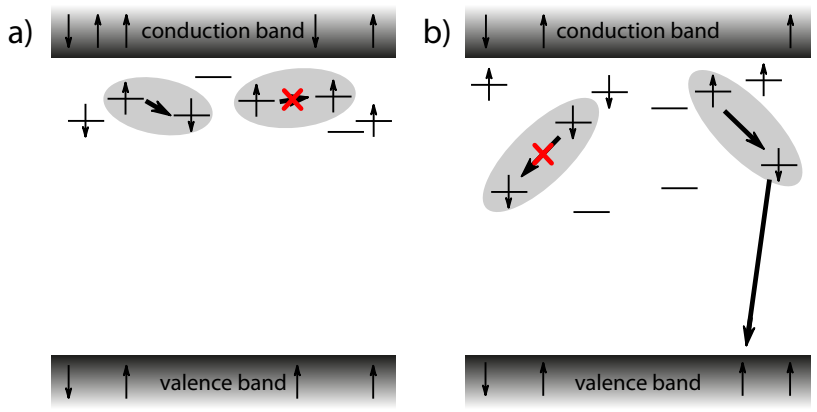

Figure 2.11: Mechanisms of spin-dependent charge transport. a) Spin-dependent hopping. b) Spin-dependent recombination. The spin orientation is represented by arrows.

of photoconductivity using Eqn. (2.72) for one type of carriers is given by

$$\Delta\sigma^{i}_{ph} = en_i\Delta\mu_i. \tag{2.74}$$

A spin-dependent hopping process was first mentioned by Kishimoto et al. [71] in their investigation of variable range hopping in amorphous Si-Au alloys.
Hopping transport channels were found in amorphous and microcrystalline silicon at low temperatures [21, 72] because under these conditions a significant part of the charge carrier transport takes place via localized states with energies close to the Fermi or quasi-Fermi level. In these disordered materials the localized states are found at the edges of the mobility gap. Hence, doping of the material to shift the Fermi level or optical excitation of charge carriers into the bands which then thermalize into the localized states is favorable for the observation of hopping transport.
Conduction band tail states are states spread over a range between 0 and 0.2 eV below the conduction (or mobility) band edge [73]. *Valence band tail states* are found 0-0.3 eV above the valence band edge. Since these states are energetically not well separated from the mobility band edges, the correlation energy U plays an important role. Hopping transport can only take place if U is smaller than the energetic distance of the involved singly occupied states from the energy band edge [74]. This is the case for amorphous silicon where U is in the range of 10 meV and 100 meV for conduction and valence

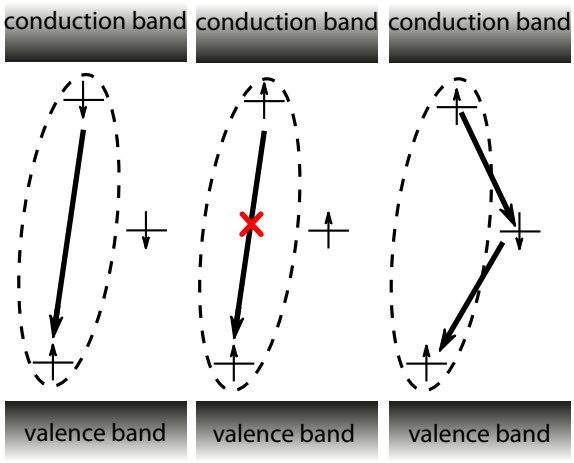

Figure 2.12: Spin-dependent processes involving three spins. The dashed lines mark a strongly coupled spin pair close to a single spin. Left: The spin pair is in a singlet state. The recombination can take place. Middle: The spin pair is in a triplet state, recombination within the pair is blocked. The single spin is aligned parallel to the strongly coupled spins, recombination via this defect is not allowed. Right: The spin pair is in a triplet state. The defect spin is aligned antiparallel with respect to the pair constituents, so that recombination via this state is allowed.

band tail states, respectively. Microcrystalline silicon is assumed to posses comparable properties.
The time evolution of the conductivity change for spin-dependent hopping $\Delta\sigma^{i}_{ph}(t)$ is developed analogously to the recombination model [19, 67] and is described in the literature [43, 67]. The transient conductivity change found there is in general a sum of exponential functions particularly dependent on the transition probabilities for the pure triplet states $|T_+\rangle$ and $|T_-\rangle$ and the mixed states $|2\rangle$ and $|3\rangle$. This transient behavior of the EDMR signal will be utilized in chapters 4 and 5 to distinguish between different transport paths in the sample.

2.3.3 Spin-Dependent Processes Involving three Spins

In the context of this thesis spin-dependent processes involving strongly coupled electron spins play an important role. Therefore an approach of spin-dependent processes which could include strongly coupled spin pairs is illustrated.

Electronic processes involving singlet ($S = 0$), doublet ($S = 1/2$) and triplet ($S = 1$) species are of considerable importance in the research field of magnetoresistence [75–79], optically detected magnetic resonance (ODMR) [80] and even EDMR [81, 82] to describe the observed phenomena. Hence, one finds various mechanisms involving triplets which could be relevant for the interpretation of spin-dependent processes in EDMR.
One interesting mechanism is called *triplet-exciton polaron quenching* [75] where a triplet (T) and a doublet (D) species interact which leads to a triplet deactivation with dissipation of electronic excitation energy or with excitation of the doublet species

$$T + D \leftrightarrow (TD) \rightarrow S_0 + D \ \ (\text{or } D^*) \tag{2.75}$$

[75, 78]. Within the field of EDMR studies, Vranch et al. [83] described a model for spin-dependent recombination based on a trapped electron-hole (e-h) pair in the proximity of a singly occupied P_b center which is based on the above mentioned mechanism. This system comprises three weakly coupled spins with $S = 1/2$ where the spin of the P_b center acts as an intermediator for the electron-hole recombination. This idea was continued by Behrends [43] to determine the dynamics of the recombination process of an e-h pair coupled to an additional spin and to correlate this process with the change of sample conductivity.
Following the concept in [43] the model is shortly described. Assuming a correlated e-h pair close to a deep defect state, which is singly occupied, this three spin system can exist in different spin configurations. When the electron-hole pair is in a singlet configuration (antiparallel spin orientation) the recombination process will take place regardless of the defect spin. For a spin pair in a triplet state (parallel spin orientation) the direct recombination step is less probable. However, the defect spin orientation becomes important: (i) For a defect spin aligned antiparallel to the e-h pair spins, the e-h pair electron can transfer to the defect state followed by a transition of the defect electron to the hole state which completes the recombination process. (ii) Is the defect spin aligned parallel to the spin pair a recombination via the defect state is improbable. Since case (ii) is connected with long life times, a surplus of this spin configuration builds up in the sample. Spin manipulation of the spin pair or the defect spin then results in shorter transition times giving rise to higher recombination probabilities.
Behrends [43] suggested that the energy released by the recombination step

can be transferred to the electron in the defect state through an Auger process which affects the sample conductivity. Hence, the electron is excited into the conduction band where it contributes to the sample conductivity. Indeed, Auger recombination at low temperatures has been reported for amorphous as well as crystalline silicon [84–86].
This three-spin process constitutes one possibility how strongly coupled spin pairs in triplet states coupled to a paramagnetic center nearby can influence the sample conductivity.

2.3.4 EDMR Experiments

It was shown that the main difference between EPR and EDMR experiments lies in the mode of detection. On the one side, spin coherences (which are connected with a precessing sample magnetization perpendicular to the spin quantization axis) are detected via emission of mw radiation in EPR. On the other side, changes of the spin pair singlet-to-triplet proportion (which is connected with populations of the single spin states) give rise to an altered sample conductivity in EDMR. Consequently, it is the easiest approach to transfer EPR pulse techniques to EDMR by adaption of the existing pulse sequence, so that populations instead of coherences are detected.

The FID experiment in EPR which excites spin coherences by the application of a $\pi/2$-pulse (the magnetization is turned by an angle $\pi/2$ with respect to the quantization axis) can be altered for EDMR just by applying a π-pulse instead. This spin manipulation allows to change the populations in the spin pair states $|T_+\rangle$, $|2\rangle$, $|3\rangle$ and $|T_-\rangle$ so that a change of conductivity is created [18]. Alternatively, the $\pi/2$-pulse of the FID experiment in EPR can be augmented by a further $\pi/2$-pulse separated by a waiting time τ yielding the sequence $\pi/2 - \tau - \pi/2$. When τ is incremented the FID signal decay can be scanned as function of the time as shown in Ref. [87]. In the limit of short τ the above mentioned π-pulse experiment is obtained.

Based on these ideas the spin echo sequences (see Sec. 2.2.3) can be adapted by adding a $\pi/2$ pulse which transfers the final spin coherences to populations for current detection. This approach indeed works well, as could be shown by Huebl et al. [22]. Several EPR techniques based of the spin echo sequences were adapted in this way for electrical detection, e.g. electrically detected ESEEM (ED-ESEEM) [25, 88] or electrically

detected electron-nuclear double resonance (ED-ENDOR) [24]. The details of the particular EDMR experiments for the present study and their special aspects will be subject of chapter 3.

3

MATERIALS AND METHODS

In this chapter the details about the experimental aspects of this work are described. This includes the utilized samples, the general instrumentation for the EPR experiments and the EDMR setups. Furthermore, the performed EDMR experiments are described in detail. The high quality microcrystalline Si thin-film solar cells which are studied here were prepared by the Forschungszentrum Jülich. The experiments at S-, X-, Q- and W-band were carried out at Freie Universität Berlin, whereas the measurements at 263 GHz were performed at Helmholtz-Zentrum für Materialien und Energie Berlin (HZB).
Among the topics presented below, a main focus of this thesis was extending EDMR to new frequency bands to study one type of solar cells or even one and the same cell within multi-frequency investigations.

3.1 Samples

The concept of Si thin-film solar cells constitutes a promising advancement of silicon photovoltaic technologies connected with smaller material consumption, reduction of production energy due to low temperature deposition as well as the possibility to fabricate solar cells on large areas. Nevertheless, the conversion efficiencies of single junction thin-film solar cells or thin-film cells made of a stack of amorphous and microcrystalline p-i-n structures [9, 89, 90] do by far not reach the efficiencies of cells made of crystalline silicon [10]. This is due to inferior electronic properties of the

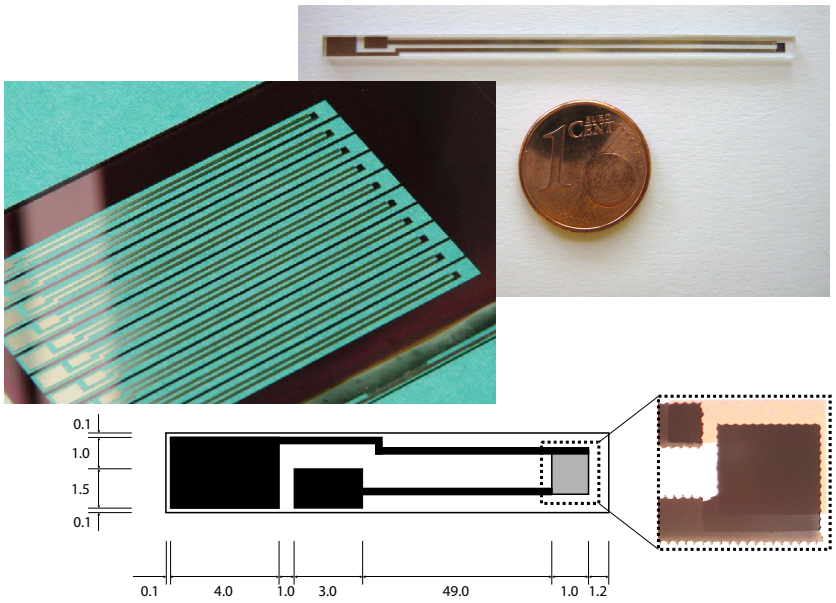

Figure 3.1: Design of the thin-film solar cells. Top: picture of a single solar cell with glass substrate, conduction lines and contact pads on the left as well as the active cell area on the right. Middle: The deposition takes place on a 10×10 cm^2 corning glass. The samples for EDMR are obtained by removing not needed material with laser scribing. Bottom: Contact geometries for the thin-film samples. Black parts indicate conduction lines and contact pads. The active area of the cells is shown in grey. A micrograph of this part is shown in the blow-ups on the right. All dimensions are given in millimeters.

disordered materials compared to the crystalline counterpart. Deep defects due to dangling bonds (db) and localized tail states in the band gap induced by strained bonds act as recombination centers and traps, respectively, and thereby influence the charge transport of photo-generated charge carriers. They thus diminish the performance of the cell.
EDMR allows us to manipulate charge carriers in these localized states of the solar cell material and thereby observe their influence on the charge carrier transport by measuring the current through the solar cell. With this method it is possible to directly investigate the state-of-the-art devices to get information about the role of defects and traps for the electronic properties of the device.
In this thesis thin-film μc-Si:H single junctions in a p-i-n configuration as described in Ref. [5, 6, 91] were studied. In order to perform the EDMR measurements the solar cells with a size of 1×1 mm^2 and a special contact configuration were prepared by laser scribing (see Fig. 3.1). The preparation

sequence and laser scribing procedure was presented in more details elsewhere [21, 92]. The total size of the samples for the EDMR investigations ($55.0 \times 2.9 \times 0.7$ mm^3) is limited by the cavity size of the setup at Q-band frequencies. The thickness of the metal back contact was reduced to avoid an influence on the microwave mode. Except for these adaptations, the deposition parameters of the solar cells were identical to those of the device grade cells. In the following sections the employed samples are described in detail.

3.1.1 μc-Si:H p-i-n Solar Cell with n-a-Si:H Layer

The thin-film solar cell studied in chapter 4 is a single junction p-i-n (p-μc-Si:H / i-μc-Si:H / n-a-Si:H) diode prepared in a superstrate configuration with a process developed for a high quality device [93]. The cell was deposited by plasma enhanced chemical vapor deposition (PECVD) at a plasma radio frequency of 13.56 MHz and at $T \approx 200$ °C on a texture-etched ZnO coated glass substrate (Corning 1737). The ZnO works as a transparent conductive oxide (TCO), so that the cell can be illuminated through the glass. This substrate supports the light-trapping together with the ZnO/Ag back contact. The boron doped p-layer serves as a nucleation layer for the subsequent μc-Si:H deposition. A silane concentration $SC = [SiH_4] / [H_2 + SiH_4]$ in the deposition feed gas of 0.84 % was chosen for the deposition of the intrinsic layer. The i-layer thickness was estimated to 1 μm and its crystallinity was determined to be $I_c \approx 65$ % according to Raman measurements [94]. The n-a-Si:H layer was doped with phosphorus.

3.1.2 μc-Si:H p-i-n Solar Cells

For a comparative multi-frequency EDMR study in chapter 5 two thin-film solar cells with different ^{29}Si contents in the intrinsic μc-Si:H layer were produced. Both cells were deposited at $T \approx 260$ °C on a glass substrate consisting of a stack with 800 nm texture-etched ZnO, boron-doped p-μc-Si:H, ≈ 1 μm intrinsic μc-Si:H absorber, phosphorus-doped n-μc-Si:H and ZnO with silver as a back contact.
For the first sample with an i-layer of natural Si isotope composition a silane gas with (natural) ^{29}Si content of 4.7% was used. The silane concentration in the hydrogen-silane gas mixture was $SC = 5\%$. This i-layer was deposited

with 94.7 MHz PECVD [5, 6] and had a crystalline volume fraction of $I_c = 52\%$. For the second sample a ^{28}Si enriched silane gas of high purity $> 99.9\%$ $^{28}SiH_4$ was used. The deposition at 80.7 MHz together with a silane concentration of $SC = 4\%$ led to an i-μc-Si:H crystalline volume fraction of $I_c = 74\%$.
For the n- and p-doped layers of both cells silane of natural Si isotope composition was utilized due to technical reasons. Nevertheless, the ^{29}Si concentration in the whole sample can be considered as strongly reduced, since the doped layers are thin ($\approx$ 30 nm thickness) in comparison to the intrinsic layer ($\approx 1\mu$m thickness).

3.2 EDMR Instrumentation

In the present thesis EDMR experiments comprising a very broad range of microwave frequencies were performed. The frequency spectrum extends from 3.5 GHz (S-band) via 9.7 GHz (X-band), 34 GHz (Q-band) to 94 GHz (W-band) and even 263 GHz. Within the scope of this work the EDMR setups were realized at S-, and W-band. The Q-band setup which was first used by Behrends [43] was refined. The following descriptions are divided into four parts. In the first part, the instrumentation to perform general EPR experiments are introduced. In the second part, we describe the EDMR setups which were realized in the form of cavity-based structures followed by information about the setups at high frequencies. Finally, the electrical detection for the EDMR is depicted.

3.2.1 General EPR Instrumentation

The EDMR experiments were carried out at different Bruker Biospin EPR spectrometers:

- S-band: For EDMR measurements at S-band a spectrometer of type Elexsys E680 equipped with a Super-S FT upgrade and a split ring resonator (ER4118S-MS5) was used. A 40 W solid-state amplifier generated π-pulses of down to $t_p \approx 60$ ns . The sample cooling was realized

by a Helium flow cryostat and a temperature controller 321 Autotuning from LakeShore.

- X-band: The X-band cw and pulse experiments were carried out on spectrometers of type Elexsys E580 and E680 utilizing dielectric ring resonators ER 4118X-MD5 (all measurements in chapter 4) and EN4118X-MD4 (chapter 5). Both resonators posses an optical access for sample illumination. With the help of a 1 kW TWT mw amplifier π-pulses down to $t_p \approx 20$ ns were generated. A CF935 cryostat and an ITC503 temperature controller from Oxford Instruments were taken for the cooling.
- Q-band: The Q-band spectrometer (type Elexsys E580) was equipped with a Super-Q FT upgrade. A home built probe head was used for the measurements. Together with an 0.5 W solid-state mw amplifier π-pulses down to $t_p \approx 70$ ns could be reached. The samples were, again, cooled by a CF935 cryostat and an ITC503 temperature controller.
- W-band: For experiments at W-band frequencies an Elexsys E680 spectrometer was available. The EDMR measurements were realized with the help of a non-resonant setup (see Sec. 3.2.3). The maximum available mw power of 0.4 W in this non-resonant setup yielded π-pulses of 500 ns. Low temperatures were reached utilizing a CF935 cryostat and an ITC503 controller.
- 263 GHz: At this mw frequency a spectrometer of type Elexsys E780 was available at HZB. EDMR experiments were performed in a non-resonant configuration. The 15 mW mw power allows π-pulses down to 1.5 µs. An ITC503 temperature controller and a Helium flow cryostat were used for the sample cooling.

All spectrometers are equipped with a microwave-pulse forming unit (MPFU) [95]. The unit consists of two arms (+x,-x), which deliver pulses of individual amplitude and phase.

3.2.2 EDMR at S-, X- and Q-band

At S-, X- and Q-band frequencies the sample was mounted in a mw resonator as for conventional EPR measurements (see Sec. 3.2.1). The sample consisting of the glass substrate, the thin solar cell and silver conduction

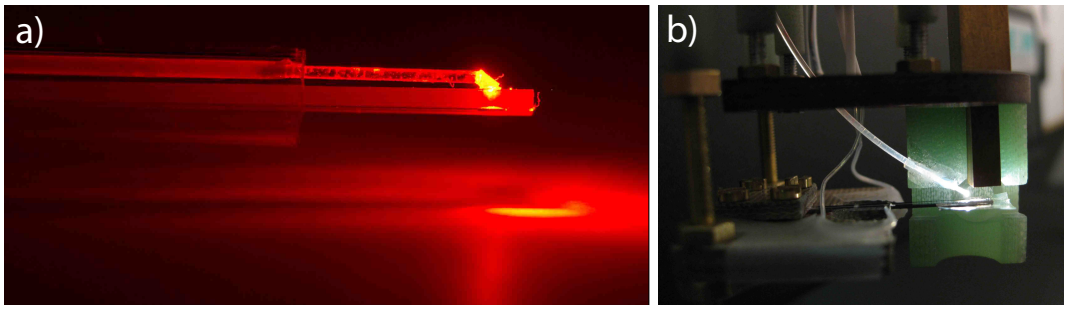

Figure 3.2: The setup for EDMR experiments is shown. a) Setup for S-, X- and Q-band. The glass substrate of the sample can be seen. Directly above, the quartz glass fiber is fixed with the rectangular micro prism at the end. The light is directly reflected onto the solar cell. b) W-band setup. On the right side the sample is placed underneath the mw wave guide. The green resin body is used to fix the glass fiber for illumination. In the middle the coax cables can be seen.

lines was glued on a copper board to stabilize the sample and to allow a reliable contacting. The conduction lines on the glass were connected with coaxial cables. This setup was built into a conventional sample rod used for EPR measurements so that the solar cell could be mounted precisely in the center of the mw resonator. At S- and X-band the diameter of the cavity access allowed for the use of 4 mm quartz glass tubes to protect the cell and to further concentrate the mw magnetic field B_1.
The mw resonators at X-band had an optical access so that the sample illumination could happen directly through this window. This was not possible at S- and Q-band. Thus, an alternative way of irradiation was necessary for EDMR experiments under illumination at these frequency bands. The existing setup was augmented with an optical fiber guided in the interior of the sample rod to the sample. At the end of the fiber a small rectangular prism of 0.7 mm edge length was fixed to reflect the radiation directly onto the active area of the solar cell. Fig. 3.2 a) shows a photograph of this setup and illumination via the fiber. This optical fiber setup yielded sufficient light intensities and photo currents in the solar cell. Furthermore, it allowed constant illumination conditions for arbitrary sample orientations in the resonator. This was an important advantage of the setup, since it made measurements as function of the orientation between sample and external magnetic field possible.
The magnetic field was calibrated at S-, X- and Q-band frequencies using a LiLiF standard with a known g-value of 2.002293(2) [96] as well as a N@ C_{60}

sample ($g = 2.00211(4)$ [97]).

3.2.3 EDMR at W-band and 263 GHz

At frequencies higher than Q-band an EDMR setup is much more difficult to implement in dielectric or fundamental mode resonators due to the smaller wave lengths. Lang et al. [98] were able to employ a commercial Bruker Teraflex EN 600-1021H resonator at 94 GHz allowing a sample diameter of 0.87 mm to investigate silicon field-effect transistors (active area of 160×40 μm^2, sample size $15.0\times0.5\times0.3$ mm^3).
Such a resonant setup could not be used here to investigate the solar cells already utilized for the lower frequency band experiments because the size of the previously chosen solar cells exceeded the allowed maximum sample dimensions of the resonant setups at 94 and 263 GHz. For this reason we used a non-resonant setup at both frequencies.

EDMR setup at W-band

At 94 GHz an existing probe head equipped with a mw resonator was modified. The cavity was removed and the sample placed underneath a mw transmission line consisting of an oversized rectangular (Q-band) waveguide, which was tapered down to W-band dimensions at the end. This non-resonant structure allowed for the insertion of several mm^2 large samples and convenient sample illumination. In an EDMR experiment the solar cell was illuminated by visible light (via an optical fiber) and microwave through the glass substrate (see Fig. 3.2b)). To increase the B_1 field at the sample the back side of it was covered with an additional reflective metallic layer. A BDPA (1,3-bisdiphenylene-2-phenylallyl) sample was used for transient nutation experiments to estimate possible B_1 inhomogeneity in this setup. It was deposited as a thin film on a glass substrate with a total film area larger than the active area of the solar cell. Nutations could be detected over several periods indicating small inhomogeneity effects.
The field axis calibration was done at W-band with the help of a small BDPA sample (g = 2.00264 [99]) fixed on the glass substrate of the solar cell next to the active area. Calibration measurements were performed for mw frequencies between 93.7 and 94.4 GHz to cover a sufficient field range.

EDMR setup at 263 GHz

At 263 GHz a wide sample space probe head was used which can work in a non-resonant and resonant configuration. The millimeter waves for the EDMR experiments were brought to the sample via a quasi-optical front-end positioned above the probe head and a tapered corrugated transmission line within the probe head. The large sample area of up to 3 mm in length and 4.5 mm diameter allowed to measure the solar cells.
The glass substrate of the sample was cut to a size of approximately 3×3 mm so that only the active area and short conduction lines for contacting were left over. This small sample was mounted on a Teflon cylinder. The conduction lines were contacted to coaxial cables which, again, were connected to plugs for current detection. The cylinder was then attached to a sample holder for vertical positioning of the sample. The illumination was realized with the help of a glass fiber which was guided to the sample within the probe head and finally bent to directly illuminate the solar cell.
For the magnetic field calibration a small piece of solid N@C_{60} was glued onto the glass substrate next to the active area of the cell so that the EPR spectrum of this standard sample with the well-known g-value of $g = 2.00211(4)$ [97] could be measured simultaneously with the EDMR spectrum.

3.2.4 Experimental Conditions and Current Detection

The EDMR experiments of the microcrystalline Si solar cells were carried out at low temperatures of 5 K (µc-Si:H p-i-n solar cells) and 10 K (µc-Si:H p-i-n solar cell with n-a-Si:H layer) under illumination. In Fig. 3.3 *I-V* curves of the investigated solar cells are shown at room temperature and $T = 10$ K. The low-temperature curves differ significantly from the room temperature curves. Furthermore, both cells labelled with (A) and (B) (in consistence with Ref. [21]) show differences in the *I-V* development at $U > 0$ V. The current increase of sample (A) is less pronounced compared to sample (B). This can be mainly attributed to the energy barrier between the n-a-Si:H and the µc-Si:H layer in sample (A) which is absent in cell (B) [21]. For the low-temperature EDMR measurements the cells were operated at $U = -1$ V reverse bias (indicated in Fig. 3.3 b)) to extract the photo-generated charge carriers from the device leading to photocurrents upto 20 µA dependent on the illumination conditions.

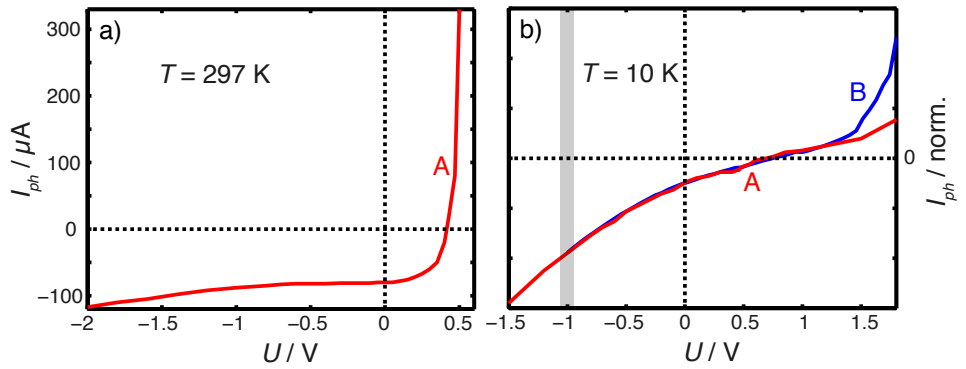

Figure 3.3: Current-voltage characteristics of the μc-Si:H p-i-n solar cell (B) and the μc-Si:H p-i-n solar cell with n-a-Si:H layer (A) under illumination. a) High-temperature *I-V* curve of sample A. b) Low-temperature *I-V* curve. The vertical line in the plot indicates the voltage used for all EDMR measurements. The curves are normalized to the short-circuit current I_{sc} at $U = 0$ V to compare their shape. The short circuit current was $I_{sc} = -1.6$ μA and $I_{sc} = -3.4$ μA for samples (A) and (B), respectively.

The microcrystalline Si solar cells were illuminated in all experiments at S-, X-, Q- and W-band by a stabilized DC driven halogen cold light source (P = 150 W) from Polytec. At 263 GHz a DC driven halogen lamp from Schott was used.

The low-noise detection of small currents in the solar cell constitutes the most critical part of the EDMR detection. For cw experiments we utilized a low-noise current/voltage converter DLPCA-200 produced by Femto Messtechnik GmbH, Berlin in combination with a battery-based constant voltage source (Stanford research SIM928). The output of the current/voltage converter was connected to the internal lock-in amplifier of the EPR spectrometer. For pulsed EDMR experiments a combined voltage source and current amplifier especially developed for transient photocurrent detection was used [21, 43]. It was produced by Elektronik Manufaktur Mahlsdorf, Berlin. The amplifier is designed in a symmetrical configuration so that the influence of external perturbations on the sample current can be minimized. The signal is amplified to a level that is suitable for the transient recorder in the Elexsys line of spectrometer (Bruker SpecJet).

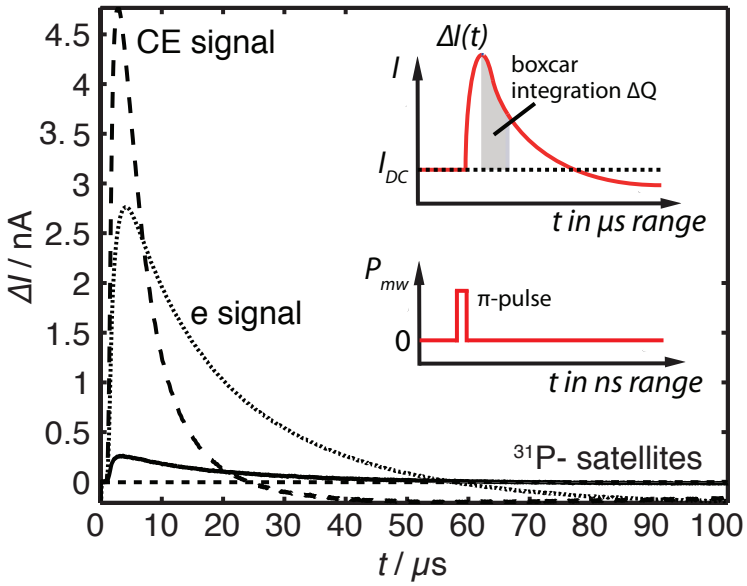

Figure 3.4: pEDMR current transients $\Delta I(t)$ of the µc-Si:H p-i-n solar cell with n-a-Si:H layer are illustrated. The underlying signals are described in detail in chapter 4. Inset: Scheme of pEDMR experiment. EDMR field spectra are generated by integrating over a certain time interval of the transient current response (digital boxcar integration). This is illustrated in Fig. 3.5.

3.3 EDMR Experiments

The π-Pulse Experiment

In π-pulse EDMR experiments the sample is subjected to short mw pulses at constant mw frequency while the magnetic field B is swept. Pulse lengths of $t_p > 100$ ns are chosen to avoid significant influence of spectral broadening due to the pulse excitation bandwidth. Under spin resonance conditions the rates of the spin-dependent transport processes change and a transient current response is measured (see Fig. 3.4). This change of rates is maximum for pulses with spin flip angle $\phi = \pi$. Directly after the pulse a rapid change of the current is detected due to the enhanced process rates as shown in Fig. 3.4. In the course of time the steady state is reestablished which is observed as an EDMR signal decay.
In Fig. 3.5 a complete 2-dimensional Q-band pEDMR data set is shown as an illustrative example. Digital boxcar integration of the current transients in fixed time intervals after the pulse yields the EDMR field spectra. The transients at specific field positions contain information about the dynam-

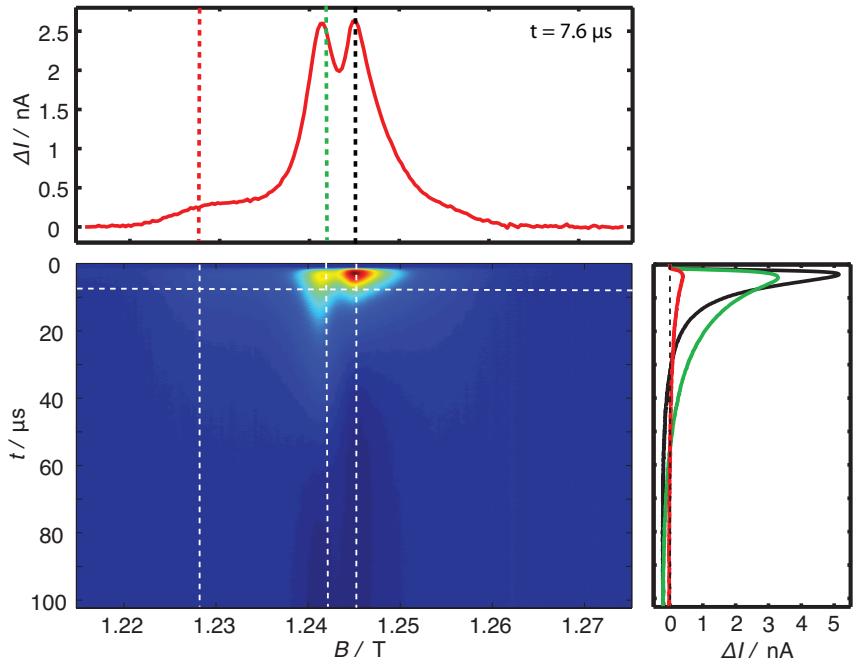

Figure 3.5: 2-dimensional Q-band pEDMR data set of the µc-Si:H p-i-n solar cell with n-a-Si:H layer. The transient current response of the sample is detected after the pulsed mw excitation as function of the magnetic field B. Two segments from the 2D date set are shown: (top) The field spectrum at $t = 7.6$ µs after the mw pulse (integration interval of 100 ns). (right) Current transients at three different field positions. The chosen time and field position in the 2D data set are marked by white vertical and horizontal lines.

ics of the underlying signal. The differences in signal dynamics will be employed to decompose multi-component spectra as described in Sec. 4.2.1.

Rabi Oscillation Experiments

The Rabi oscillation experiment is a constant-field experiment, in which the length of the applied mw pulse t_p is incremented in small time steps as shown in Fig. 3.6. The current response $\Delta I(t)$ following the pulse is integrated in a fixed interval yielding $\Delta Q(t_p)$. The integral ΔQ is detected as function of the pulse length t_p. An oscillating behavior is observed because the pulse lengths t_p is proportional to the spin flipping angle ϕ which, in turn, influences the signal amplitude.
This Rabi measurement is frequently used prior to pulse experiments to determine the correct pulse length t_p needed to flip the spins by a distinct

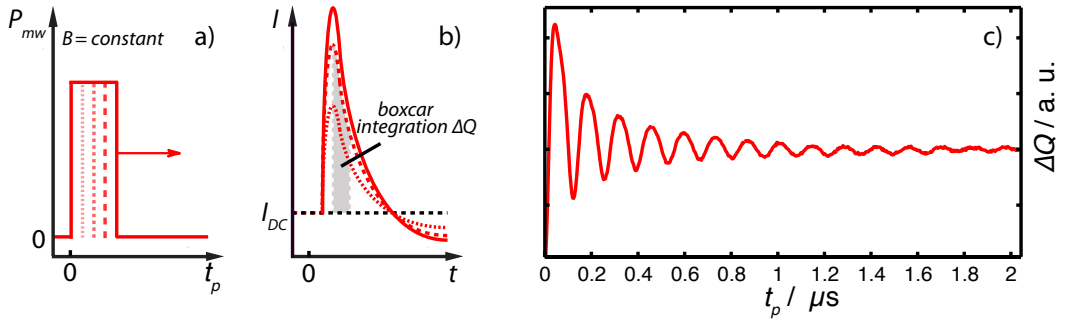

Figure 3.6: Rabi experiment: a) and b) At constant magnetic field B the mw pulse length t_p is incremented. At a fixed waiting time after the pulse the current response $\Delta I(t)$ is integrated yielding ΔQ. c) The integral ΔQ is plotted as a function of t_p revealing the oscillation behavior (example: CE signal of μc-Si:H p-i-n solar cell, see Sec. 5.4).

angle ϕ for the used mw power. Furthermore, this experiments allows to measure the mw B_1 field strength at the sample position.

Continuous Wave Experiments

In continuous wave (cw) EDMR experiments the sample is continuously subjected to mw radiation at a fixed frequency and intensity while the magnetic field B is swept. The observable is the current at a fixed voltage. When the resonance condition is fulfilled, spin-dependent recombination or hopping time constants change and thus alter the sample conductivity. The main advantage of cwEDMR is its sensitivity which is usually higher than for pEDMR. This is a consequence of the applied lock-in detection which increases the signal-to-noise ratio (SNR). In all cwEDMR measurements presented in this thesis, B was modulated in order to allow for phase-sensitive detection. In principle, a modulation of the mw frequency is possible as well. Due to the fact that the mw power in cwEDMR is much lower than in pEDMR experiments, power broadening of the resonance lines, which may severely distort pEDMR spectra, is of minor relevance in cwEDMR. The mw resonator is critically coupled to achieve a high cavity quality factor Q. In this way the high sensitivity in cwEDMR is reached without using high mw power. Conductive parts of the sample are generally disadvantageous for reaching high Q values. This problem becomes more serious, the higher the experiment temperature and the mw frequencies are.
cwEDMR can be used to extract line widths and g-values from the spec-

	$\pi/2$	π	$\pi/2$
step 1	+x	+x	+x
step 2	-x	+x	+x

Table 3.1: Phase-cycling steps of the electrically detected FSE sequence.

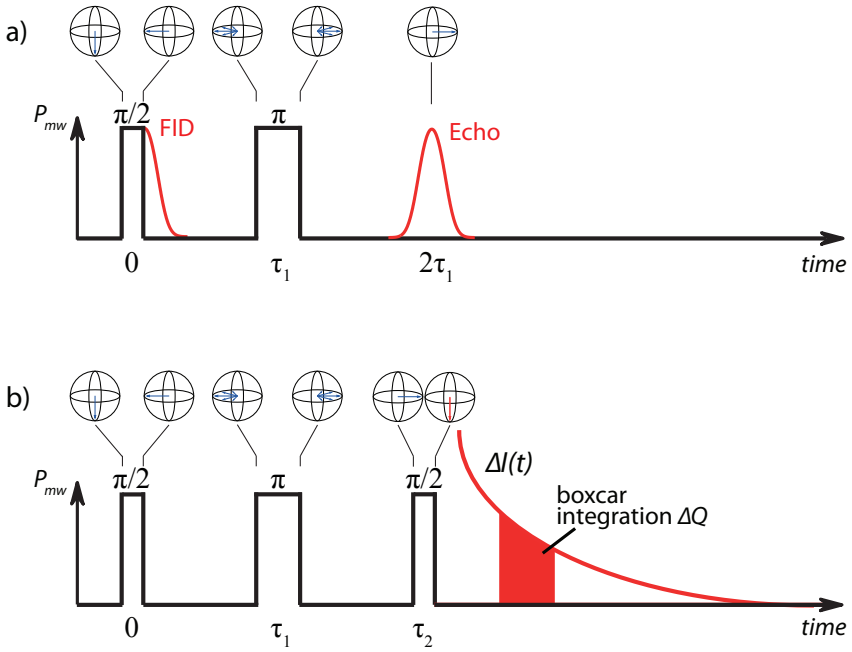

Figure 3.7: Spin echo pulse sequence in EPR and EDMR. The arrows in the spheres symbolize the sample magnetization and its manipulation. a) Spin echo experiment in EPR. b) Spin echo experiment in EDMR.

tra. Regarding extraction of information about the dynamics of the spin-dependent transport processes, cwEDMR is less capable, since it is a "quasi-static" experiment. But the high-frequency modulation of B yields a quadrature spectrum, and by adjusting the lock-in phase different processes having different time constants can be separated [100]. Thus, it is possible to decompose multi-component spectra, when the components are connected with processes of different time constants. This is utilized in Sec. 5.1.

Echo Experiments and ED-ESEEM

The field swept echo (FSE) experiment in EPR is based on the spin echo pulse sequence $\pi/2 - \tau_1 - \pi - \tau_2 -$ echo (see Fig. 3.7 a) and Ref. [44, 45]). At time $\tau_2 = 2\tau_1$ the spin echo signal is formed. The data are acquired

by integrating the complete spin echo in time. If the integration interval is chosen too small, *power broadening* effects appear [37]. The advantage of this technique is the independence of resonator dead-time effects in EPR and the versatile application in various pulse experiments. Repetition of the spin echo experiment at many field positions yields the FSE spectrum.

The FSE experiment is adapted for EDMR by adding a $\pi/2$ read out pulse at the time of echo formation to transfer the sample magnetization back to the "EDMR detection axis" (z-axis) (see Fig. 3.7 b) and Ref. [22]). Since the read out pulse takes over the task of echo integration, broadening effects occur when the read out pulse is shorter than the echo profile. The broadening can be reduced by using long read out pulses of low mw power. The transient current response $\Delta I(t)$ after this pulse sequence contains the current change due to the primary echo in addition to the current changes excited by each individual pulse (comparable to the signal in single-pulse experiments). In order to remove the part of the resonant current change, that is not due to the spin echo, the application of phase cycling steps is mandatory [37]. In the spin echo sequence for EDMR the phase of the initial pulse is cycled (+x,-x) as shown in Tab. 3.1. Hence, the phase cycle consists of two steps. In the first step, all pulse have the same phase yielding a net flip angle of $\phi = \pi/2 + \pi + \pi/2 = 2\pi$, so that a minimum echo-induced current response is measured. In the second step, the net flip angle yields $\phi = -\pi/2 + \pi + \pi/2 = \pi$ connected with a maximum echo-induced current response. The signals of the first and second phase-cycling step are subtracted yielding as difference only the current transient induced by the spin echo. Finally, integration of this current transient in time yields the electrically detected spin echo signal ΔQ.

The ED-ESEEM experiment which scans the echo modulations as function of time is based on the pulse sequence of the ED-FSE experiment. The inter-pulse delay τ_1 is incremented which leads to a shift of the echo position at $\tau_2 = 2\tau_1$ to later times. The position of the read out pulse as well as the start of data acquisition is incremented accordingly. Boxcar integration of the current response gives ΔQ which is detected as function of τ_1 yields the ED-ESEEM trace.

4

MULTI-FREQUENCY EDMR APPLIED TO N-A-SI:H / μC-SI:H P-I-N SOLAR CELLS

Pulsed EDMR applied to thin-film μc-Si:H solar cells already allowed many interesting insights in the spin-dependent transport processes via localized states in these devices [20, 21, 25, 43]. However, the investigations were often complicated by strongly overlapping signals at the commonly used X-band mw frequencies (9.7 GHz). Furthermore, it was often not possible to disentangle field-dependent and field-independent line widths by measurements at a single mw frequency.
To lift this restriction to only one mw frequency, Behrends started to install the EDMR on these samples at the higher Q-band frequency (34 GHz) in the framework of his thesis [43]. This work is continued here. Furthermore, an EDMR setup at W-band (94 GHz) is realized. This *multi-frequency EDMR* approach, which is routinely used in conventional EPR spectroscopy [15, 101], is applied to a single junction p-i-n (p-μc-Si:H / i-μc-Si:H / n-a-Si:H) diode, a sample which was already investigated in detail at X-band frequencies [20, 21]. Due to the signals from the μc-Si:H and the n-a-Si:H layers this solar cell is especially suitable to answer the questions connected with the benefit of the multi-frequency EDMR approach:

1. Is a gain in spectral resolution observed at high frequencies with respect to the spectra at X-band? Is it possible to separate field-independent hyperfine and spin-spin interactions from field-

dependent Zeeman interactions?

2. At X-band the signals from μc-Si:H solar cells showed symmetric profiles. Can measurements at high frequencies reveal an asymmetric profile e.g. due to g-anisotropy? g-anisotropy reveals important information about the paramagnetic states, contained in the distribution and canonical values of the electronic g-matrix.

3. Furthermore, recent X-band pEDMR studies on μc-Si:H solar cells assumed spin pair processes to be responsible for the observed spin-dependent transport processes. These processes do not depend on the equilibrium Boltzmann spin polarization. However, studies limited to one polarization regime may miss other important spin polarization dependent transport processes like e.g. recombination of electrons and holes in the conduction and valence bands with thermalized spin polarization [61], trapping of conduction electrons at ionized donors [102], spin-dependent scattering [103] or polarization transfer from donors to delocalized electrons [104]. In order to investigate the impact of these processes, EDMR experiments at different resonance fields and/or temperatures are required.

The present study is an extension of previous pEDMR work performed on μc-Si:H p-i-n thin-film solar cells [20, 21, 43]. Based on X-band pEDMR at cryogenic temperatures three resonances in the μc-Si:H pEDMR spectrum could be identified (Fig. 4.1). They stem from paramagnetic centers in the device, which contribute to spin-dependent charge carrier transport. Based on their g-value they were assigned to well-known paramagnetic states in the μc-Si:H and a-Si:H layers of the cell. First, a signal at $g_{\mathrm{CE}} = 1.9975(5)$ (CE signal) from shallow localized states in energetic proximity to the μc-Si:H conduction band. This signal could be further attributed to states within μc-Si:H grains by electrically detected ESEEM [25, 105]. Second, a resonance at $g_{\mathrm{e}} = 2.0049(5)$ (e signal) originating from n-a-Si:H conduction band tail states. Third, doublet signals of P donor states in n-a-Si:H. These signals are centered around $g_{\mathrm{P}} \approx 2.003(1)$ (P signal)) and exhibit a ^{31}P hyperfine splitting ($I = 1/2$, natural abundance 100 %) of ≈ 25 mT.
All three signals were assigned to spin-dependent hopping processes in the μc-Si:H and n-a-Si:H layers. Since the energetic position of the quasi Fermi levels under the experimental conditions used here is supposed to be in the range of the energy band tail states, electrical transport is strongly influenced by hopping of charge carriers along localized states. No indica-

tions for spin-dependent recombination via db states could be found in the EDMR spectra at low temperatures. Possibly the strong hopping signals superimpose a weaker db recombination signal. This hypothesis is consistent with the results of a previous study, where an EDMR recombination signal could only be found in purely microcrystalline p-i-n solar cells, but not in cells with amorphous p- and/or n-doped layers exhibiting strong EDMR signals from hopping transport via tail states [21]. However, at room temperatures a weak db signal was found in all spectra irrespective of the n- and p-layer material [43].
The experiments at high temperatures delivering particularly the dangling bond signal are relevant for studies on the fully processed cell. Nevertheless, the achievable SNR is small under these temperature conditions. Hence, the EDMR measurements on thin-film solar cells will be performed at cryogenic temperatures, since under these conditions the above mentioned paramagnetic species contribute to the EDMR spectra with a high signal-to-noise ratio (SNR), which is suitable for the further development of multi-frequency EDMR.

In the following the interesting results of the multi-frequency study on this sample are described and answers to the raised questions are given. These results gave rise to a recent publication in the *Journal of Magnetic Resonance* (see Ref. [106]).
After briefly describing the performed experiments, we present the results of the multi-frequency study. First, the experimental spectra are described followed by the explanation of the methods for the spectral deconvolution. Afterwards we determine precise g-values of the e and P signals and corroborate hyperfine interaction as the reason for the splitting of the P resonance and consider the line profile of the CE line making use of the decomposed spectra. We analyze the influence of field-dependent line broadening effects of the deconvoluted CE and e signals on the spectral resolution in the EDMR spectra. Finally, we discuss the effect of thermal spin polarization on the EDMR spectrum.

4.1 Experiment

We performed pulsed EDMR experiments utilizing Bruker Biospin spectrometers of type Elexsys E580 and E680 working at frequencies of 9.7, 34

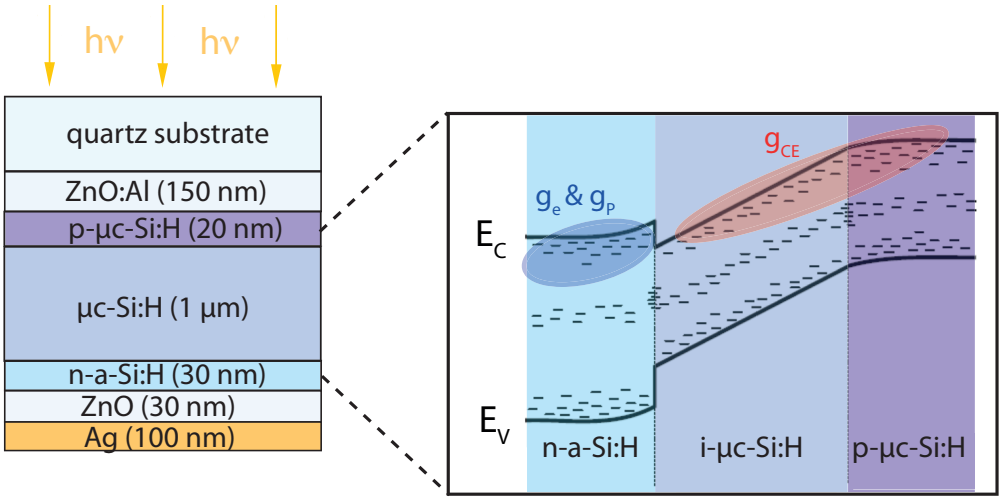

Figure 4.1: Left: layer structure of the µc-Si:H p-i-n thin-film solar cells. Right: schematic representation of the energy-band diagram at room temperature without illumination. The amorphous layer can be identified by the larger band gap. The detected signals are assigned to hopping transport via shallow conduction band tail states at a g-value of g_{CE} in the µc-Si:H regions and conduction band tail states at g_e as well as phosphorus donor states at g_P in the amorphous layer.

and 94 GHz (X-, Q- and W-band). The time-dependent conductivity change was measured after excitation with a mw π-pulse as a function of the static magnetic field while the resonance frequency was kept constant. At every field point current transients of up to 100 µs were recorded.
The measurements under illumination conditions were done at 10 K to benefit from the high signal-to-noise ratio (SNR). The cell was operated at 1 V reverse bias in X- and Q-band to extract the photo-generated charge carriers from the device leading to photocurrents between 4 and 8 µA dependent on the illumination conditions. Smaller light intensities due to the setup at W-band reduced the photocurrent at 1 V bias voltage and 10 K significantly (see Sec. 3.2.3). Hence we used here a higher voltage of 1.5 V (3.2 µA) and 5 K to further increase the detected spin-dependent response. The change of these parameters did not influence the spectral information but only led to a better SNR.
EDMR spectra were measured as function of mw power to optimize the signal intensity without affecting the line shape by broadening effects. At 9.7 GHz and 34 GHz π-pulses of 100 ns and 70 ns, respectively, where found

frequency	setup	π-pulses	B_1-field amplitude
9.7 GHz	ER 4118X-MD5	100 ns	178$\pm$12 μT
34 GHz	lab built resonator	70 ns	255$\pm$24 μT
94 GHz	non-resonant setup	500 ns	36$\pm$8 μT

Table 4.1: Overview of characteristic quantities of the different frequency bands. The π-pulse lengths and B_1-field amplitudes (B_1=$\frac{\Omega_{Rabi}}{\gamma}$) were determined by EDMR transient nutation experiments [107].

as optimum conditions. The maximum available mw power of 0.4 W in the non-resonant W-band setup yielded π-pulses of 500 ns (see table 4.1). Detailed information about the EDMR setups at the different frequencies and the π-pulse experiments are described in Chapter 3.

4.2 Results and Discussion

The EDMR spectra of the µc-Si:H solar cell at all three measurement frequencies are shown in Fig. 4.2. The center of the current integration windows was chosen such that the maxima at the two field positions indicated by vertical lines have equal intensity to show the differences in spectral resolution. At X- and Q-band an integration window of 100 ns in the transients recorded was used. Due to the reduced SNR of the transients at W-band an integration window of 7.45 µs width was chosen in order to achieve a sufficient SNR. The two main signal contributions are assigned to the CE resonance at $g \approx 1.998$ (dashed line) and the e resonance at $g \approx 2.005$ (dotted line). The P signal pair is not well resolved in these spectra as it is outside of the covered field range in X-band or buried under the stronger resonances at W-band. Only in the Q-band spectrum it can be observed as broad tails of the central lines.

4.2.1 Spectral Deconvolution

The basis for the analysis of the EDMR spectra at different frequencies and for the determination of field-dependent and field-independent line broadening effects is the knowledge of the line shapes and widths of the different signals. For the determination of these line parameters the X-band EDMR spectrum of the µc-Si:H solar cell was fitted with symmetric line profiles

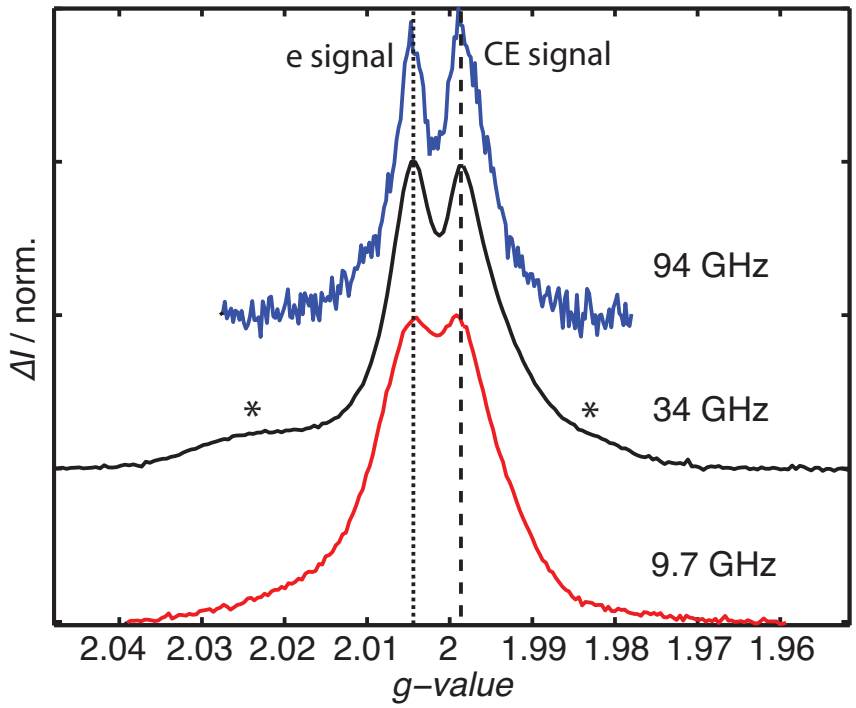

Figure 4.2: EDMR spectra of the µc-Si:H solar cell at 9.7, 34 and 94 GHz. The narrow signals are assigned to CE states ($g \approx 1.998$, dashed line) and e states ($g \approx 2.005$, dotted line). At 34 GHz the broad hyperfine satellites of phosphorus donors centered around $g \approx 2.004$ can be observed as broad shoulders (marked with asterisks).

[20, 21]. The CE and e signal were described by Lorentzian line shapes, the P satellites were approximated by a pair of Gaussian lines. These line shapes, especially the Lorentzian profiles, were chosen because they adequately fit the EDMR signals. However, we note that the Lorentzian line shape should not be interpreted as a result of homogeneous broadening. In a first step, the same fitting approach was applied to the X-, Q- and W-band data of our study as demonstrated examplarily in Fig. 4.3 a) for the Q-band data set. The fit yields the following results: The EDMR spectrum can be well described in the low field range up to $\approx$ 1245 mT by Lorentzian lines for the CE and e signals, respectively and one Gaussian line for the low-field P signal. At the high field side of the CE signal a significant deviation between experimental spectrum and fit is observed (marked in shaded red). This deviation can be reduced neither by changing the CE line position nor its line width. The high field side of this resonance is significantly broader than the low field side. This asymmetric CE line profile is found in the EDMR

spectra at all three frequency bands.

The fitting procedure based on symmetric fit functions is not sufficient to describe the spectrum consisting of partly asymmetric lines and to extract reliable parameters. Hence in a second step we use the time dependence of the pulsed EDMR signal transients to decompose the strongly overlapping signal contributions. Our approach is again demonstrated utilizing the Q-band data set and applied then also to the X- and W-band data.

Decay-Associated Spectra

The time dependence of the Q-band data set is shown in Fig. 4.3 b). Spectra extracted at different times after the mw-pulse by integrating over a time interval of 100 ns in the current transient are displayed. Starting from the maximum of current change at 3.7 μs after the mw-pulse the EDMR signal intensity decreases, changes sign and decays to zero for long times after the mw-pulse. This signal evolution is connected with different time constants over the spectrum: in the field range of the CE signal values of 4-5 μs and 14-16 μs are found, while in the range of the e and P resonances time constants of 8-9 μs and 24-27 μs dominate. Similar time constants for the e and P resonances are expected as these paramagnetic centers contribute to the same transport path [21]. The difference in the time behavior is used to separate the spectra into so-called decay-associated spectra (DAS) [108]. The EDMR spectrum is decomposed by approximating the current transients with the help of a fit function consisting of four exponential functions with time constants restricted to the above mentioned time intervals. Plotting the prefactors of the exponential functions connected with the four time constants in dependence on the magnetic field results in the DAS. Fig. 4.3 c) shows the DAS of the Q-Band data set. A clear separation regarding the e and P (shaded in grey), as well as the CE signal is seen. Nevertheless, the high-field satellite of the P pair overlapping with the strong CE line is not reproduced between 1245 and 1460 mT with the expected Gaussian line fitting well the low-field satellite. The reason is the high intensity of the CE line in comparison to the P signal in this field range as well as the relatively small difference in the time constants characterizing the different resonances. Hence we make use of further decomposition methods.

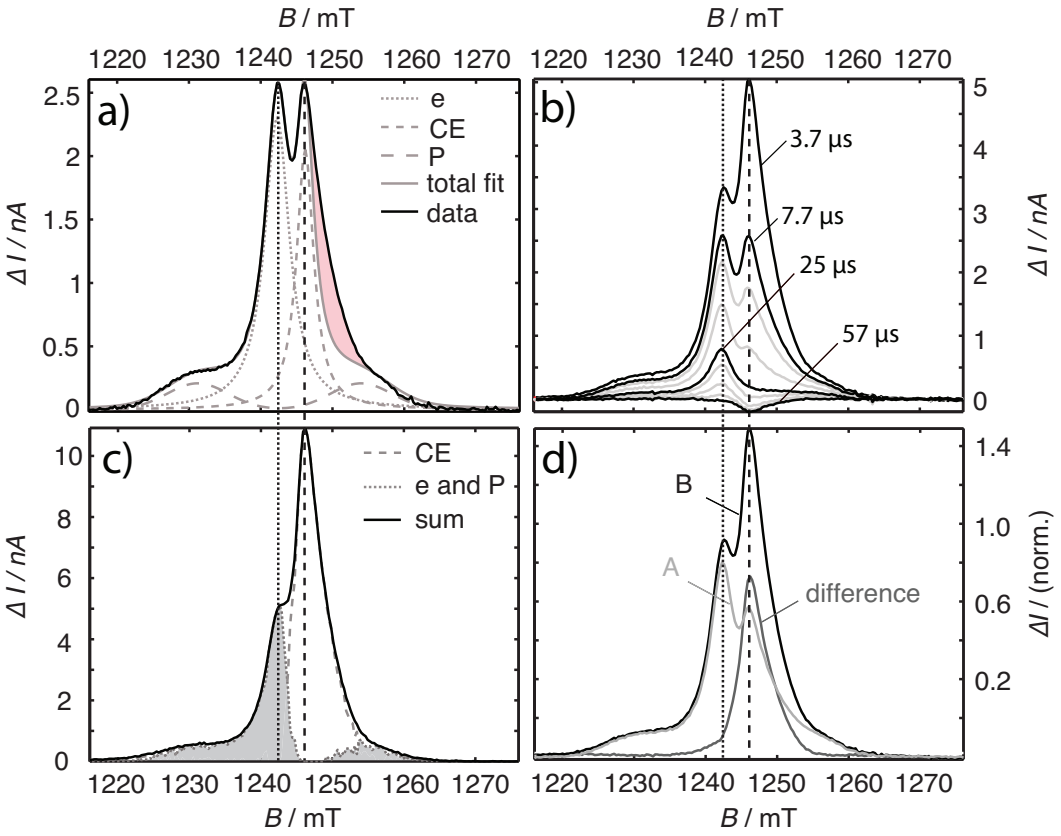

Figure 4.3: Deconvolution of the EDMR spectra demonstrated for the Q-band data set. a) shows the spectrum at t = 7.7 μs fitted by symmetric lines. On the high field side deviations between fit and spectrum are observed (marked in shaded red). b) shows the time dependence of the spectrum. At t = 7.7 μs the e and CE signals exhibit equal amplitudes. At $t \approx 25$ μs only the e and P signals contribute. At $t \approx 57$ μs solely the CE line is observed. c) shows the deconvolution into decay-associated spectra. The sum of the prefactors of the two exponential functions fitting the transients of the CE line (dashed line) on the one hand, and the transients of the e and P signals (dotted line, area shaded in grey) on the other hand are shown in dependence on the magnetic field. d) shows the decomposition of the spectrum by subtracting spectra A and B of different relative signal intensities. For details see Sec. 4.2.1.

Deconvolution Utilizing Signal Dynamics

As seen in the time dependence of the EDMR spectrum in Fig. 4.3 b), the CE signal decays faster and changes sign at roughly $t \approx 25$ µs. At this time this resonance does not contribute to the spectrum. Only the e and P signals show a contribution as they decay with larger time constants. Their contribution to the spectrum disappears at around $t \approx 57$ µs. Here only the CE signal (with inverted sign) is observed.

To precisely determine the time points of zero crossing of the e, P and CE lines for a detailed spectral analysis, the time behavior of the single contributions is calculated. This is achieved by fitting the Q-band EDMR spectrum at $t = 7.7$ µs in the low field range upto 1247 mT (near the maximum of the CE line) by three symmetric lines yielding a very good representation of the experimental spectrum in this field range (Fig. 4.3 a)). This fit is repeated for all time steps in the signal transients keeping the line widths and positions of all signals constant and solely fitting the varying amplitudes. The time dependent change of the line amplitudes as well as the zero intersection time points are obtained by this procedure.

Hence we are able to extract the individual signals from the X- and Q-band spectra with this method. A disadvantages of the approach is the low signal quality especially of the CE line as the SNR at $t \approx 57$ µs is already clearly reduced. Application of this method to W-band data yields decomposed spectra of low SNR. Hence an improved approach is suggested in the next section.

Deconvolution Utilizing Relative Signal Intensities

In order to improve the spectral deconvolution of the overlapping signal contributions we employed an additional approach making use of the different signal dynamics in an alternative way. The e and P signals have indistinguishable dynamics, which clearly deviate from CE signal dynamics. This leads on the one hand to different relative amplitudes of the CE signal compared to the e and P signals at different times and, on the other hand, to constant relative intensities of the e and P signals. The two previous deconvolution methods also clearly show that the low field part of the EDMR spectra below 1235 mT is exclusively due to the e and P resonances. Thus, a scaling of two spectra extracted at different times after the mw pulse to

identical intensity of the low-field P resonance immediately results also in identical intensity for the e resonance. This is shown for the Q-band data set in Fig. 4.3 d), where two spectra A and B with A integrated over the time interval between 3.7 μs and 29.9 μs and B between 3.65 μs and 3.75 μs are scaled to identical intensity in the low-field part. Subtraction of the spectra A and B removes the signal contributions of the P and e resonances and exclusively retains the CE resonance. The results for the CE resonance are in agreement with the previous results of the deconvolution methods, but show a significantly improved SNR, in particular in the case of the W-band data set.

The final decomposed spectra for the e and P signals and the CE signal at all three frequency bands are shown in Fig. 4.4 a) to c). The magnetic parameters that can be extracted for the individual signal contributions will be discussed in the next section starting with the e and P resonances.

4.2.2 Analysis of the e and P Resonances

The extracted e and P signals from the a-Si:H layer of the solar cell are given in Fig. 4.4 a). Fitting the spectra with symmetric Lorentzian lines for the e signal and two broad Gaussian lines for the P signal yields very good results (Fig. 4.4 b), table 4.2). The obtained g-values are g_e = 2.0050(3) and $g_P \approx 2.005(2)$ at X-band. At Q-band we get g_e = 2.0047(2) and g_P = 2.0041(5). The precision of the results is increased in this frequency band due to a high SNR of the spectrum and the larger Zeeman splitting. No further improvement of the g_e precision was achieved at W-band so far, as the SNR of the W-band spectrum is limited due to the small B_1 field strengths in the non-resonant setup. For the e resonance we obtain g_e = 2.0047(2). An asymmetry of the e signal cannot be resolved even at W-band. The P signal shows a low SNR at 94 GHz due to the weak intensity, which hampers the determination of the g-value. Using the results of the other frequency bands, the P signal pair at W-band is well described, yielding g_P = 2.004(1). The line width has a FWHM of $\Delta B_P \approx 12.4$ mT at X- and Q-band and 12(2) mT at W-band. The signal splitting of a_0 = 21.2(6) mT at X- and Q-Band, as well as a_0 = 21(3) mT at W-band is unchanged within errors at all measured frequencies. These obtained results of the P signal position, width and splitting are consistent for all three frequency bands with respect to the interpretation as hyperfine satellites.

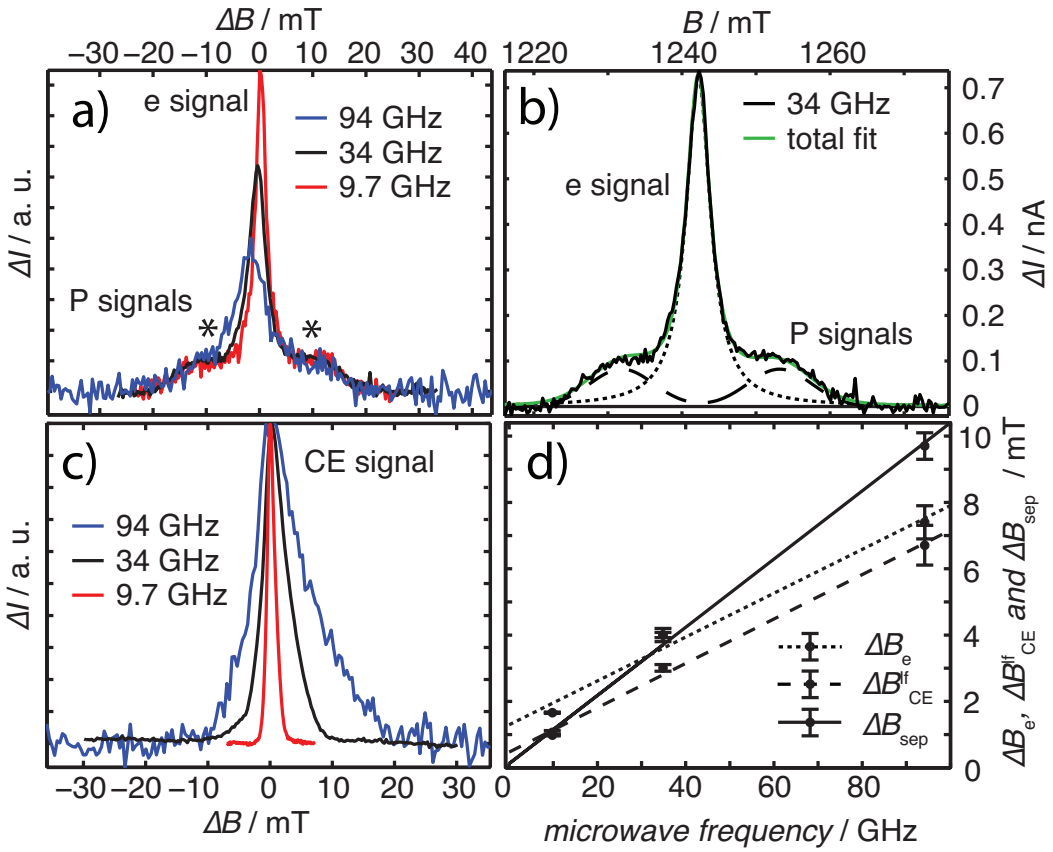

Figure 4.4: Spectral decomposition results achieved by methods described in Sec. 4.2.1. a) Narrow e signal (central line), together with P signals (marked with asterisks), extracted from signal dynamics (Sec. 4.2.1). Spectra are shifted in field relative to the center of the P doublet and normalized to P signal maxima. b) Q-band spectrum recorded at 25 µs, together with spectral fits to the e and P resonances (dotted and dashed lines, respectively). c) Deconvoluted CE resonances obtained from relative signal intensities (Sec. 4.2.1). Spectra are shifted in field relative to the center of the CE line and normalized to the signal maxima. d) CE and e signal line widths (FWHM). $\Delta B^{\mathrm{lf}}_{\mathrm{CE}}$ and ΔB_{e} and the spectral separation of both resonance lines ΔB_{sep} plotted against EDMR resonance frequencies. Dashed, dotted and solid lines represent fits to the respective parameters.

frequency	g_{CE}	g_{e}	g_{P}	ΔB_{P}	a_0
X-band	1.9988(3)	2.0050(3)	2.005(2)	12.4(6) mT	21.2(6) mT
Q-band	1.9984(2)	2.0047(2)	2.0041(5)	12.4(4) mT	21.2(6) mT
W-band	1.9988(2)	2.0047(2)	2.004(1)	12(2) mT	21(3) mT

Table 4.2: Results of the evaluation of the CE, e and P signals for all measured frequency bands. The g-values g_{CE} (g-value of line maximum), g_{e} and g_{P} as well as the P doublet line width ΔB_{P} (FWHM) and its splitting a_0 are given.

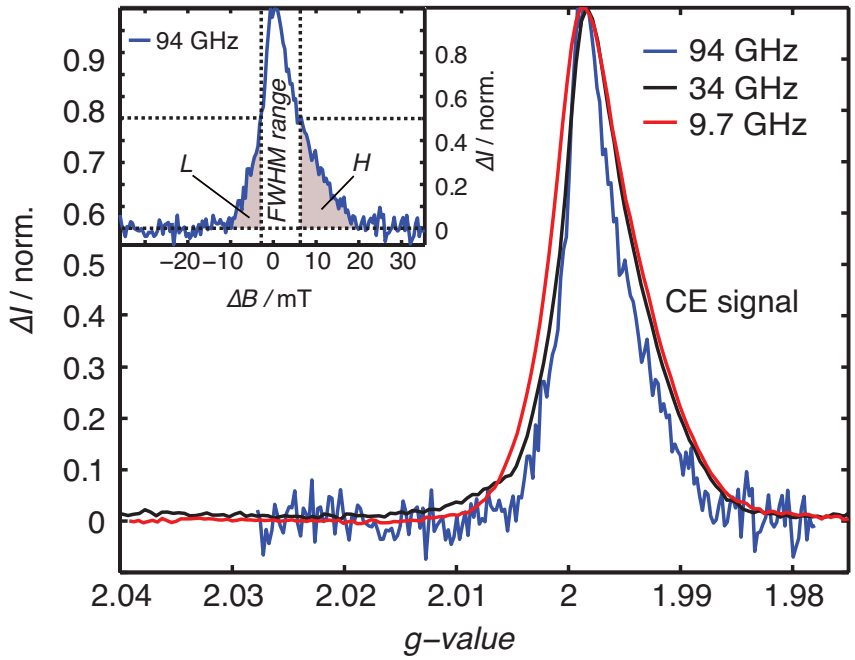

Figure 4.5: The extracted CE line at all three frequency bands is displayed on the g-value axis. In this picture the increased resolution of the asymmetry is seen. Inset: The degree of asymmetry of the CE profile (W-band spectrum) is determined by comparing the spectral contribution from the field intervals above (interval *H*) and below (interval *L*) the FWHM range of the line.

4.2.3 Asymmetry of the CE line

The CE resonance from the microcrystalline part of the sample could be extracted reliably from the EDMR spectra with the help of its dynamics despite the strong overlap with the e signal and the high field P satellite (Fig. 4.2). It reveals an asymmetric profile (Fig. 4.5), which is observed in all three frequency bands. The resonance with its signal maximum at $g = 1.9986(3)$ reaches g-values up to $g \approx 2.004$ on the low field side and down to $g \approx 1.988$ on the high field side. The integrated spectral intensities of the CE profile in the field ranges above (interval *H*) and below (interval *L*) the FWHM range of the line were compared to quantify the degree of asymmetry (Fig. 4.5, inset). The ratio $r = \frac{H}{L}$ yields 1.2, 1.3 and 1.8 for X-, Q- and W-band, respectively. The values clearly deviating from 1.0 indicate an asymmetric character at all measured frequencies, with the largest asymmetry seen at W-band.

The CE resonance is interpreted in the literature as originating from

the crystalline region of the μc-Si:H material. At first the CE states were assigned to free carriers in the conduction band of the crystalline grains [109–111]. Later on the states were attributed to shallow conduction band tail states in the Si crystallites acting as electron traps [112, 113]. However, the microscopic center associated with the CE resonance could not be unambiguously identified yet.

The asymmetric line profile with field-dependent high- and low-field line widths clearly shows a Zeeman interaction dominated line-broadening effect for the paramagnetic states giving rise to the CE resonance. It is important to note, however, that the particular line shape cannot be reconciled with an axial g-matrix under the assumption of an isotropic powder sample. Instead, it has been regarded before as being due to a superposition of two lines [114]. However, the magnetic parameters suggested in [114] do not fit our data set.

An asymmetric line profile can result from a non-isotropic distribution of paramagnetic centers. Possible candidates for such centers are dangling bonds at (internal) interfaces between amorphous and crystalline regions in the μc-Si:H layer. Given the fact that the crystalline regions exhibit a preferential orientation with respect to the substrate, the resulting *restricted* powder pattern will lead to an asymmetric line shape that differs from a *full* powder pattern expected for a purely isotropic distribution. However, a recent EDMR study on recombination in a-Si:H/c-Si heterostructures, which can be regarded as model systems for microcrystalline Si, has revealed an orientation dependent g-matrix with main values of $g_{\perp} = 2.008(1)$ and $g_{\parallel} = 2.001(1)$ for the paramagnetic centers located at the interface [115]. This g-value range clearly deviates from the g-values of the CE center. In consequence, an anisotropic distribution of paramagnetic states at internal a-Si:H/c-Si interfaces cannot be responsible for the CE line asymmetry.

Therefore, we suggest a different origin for the line shape, still assuming the CE resonance to arise from the crystalline part of the μc-Si:H material as inferred from previous EPR/EDMR investigations [25, 110, 116].

μc-Si:H contains small crystallites separated by amorphous material. These crystallites can be regarded as an ensemble of quantum structures. We assume that the g-value of a CE center located inside a Si nanocrystal depends on the respective crystal diameter. Following this idea, the CE line shape is governed by the size distribution of the Si nanocrystals. In

the following, we will evaluate whether the geometrical confinement due to the crystal sizes found in μc-Si:H may influence the CE *g*-value and thus provide a credible explanation for the CE line shape.

μc-Si:H deposited under similar conditions as the investigated sample contains crystallites with an average size between 7 and 14 nm [94, 117]. While it is impossible to prepare μc-Si:H comprising of only one particle size and to study the influence of the crystal size on the CE *g*-value directly, data is available on size-selected Si nanoparticles.

Ye et al. [118] studied resonant electron tunneling between c-Si nanocrystals of ≈ 10 nm diameter embedded in an amorphous SiO_2 matrix. They observed several aspects of quantum confinement. Electrons forming delocalized states in bulk semiconductor crystals that are invisible to most EPR techniques, may give rise to strong EPR signals when confined in nanostructures with reduced dimensionality. Nestle et al. [119] for example reported about electrons confined in $Si/Si_{1-y}C_y/Si$ quantum wells having a depth of 50 meV and well width of 6 nm. These paramagnetic centers were detected with EPR signals showing properties (e.g. *g*-value, temperature dependences) resembling those of CE centers [13]. Going to nanostuctures of varying size, Pereira et al. [120] found a clear change of the P hyperfine splitting of donors in phosphorus-doped c-Si nanocrystals in dependence of the particle size up to diameters >10 nm due to dielectric confinement. This is a consequence of the modified donor wavefunction localization.

Since the crystallite sizes in μc-Si:H are in the range of the above mentioned quantum structures, it is reasonable to assume an influence of confinement effects on the energy landscape of the structure and wavefunction localization of the CE centers. A modification of the electron wavefunction leads to a change of the spin orbital coupling, which has a direct influence on the *g*-value of the CE center. Hence we assume a dependence of the CE *g*-value on the crystalline grain size at least for a part of the grains. The line shape of the CE resonance then reflects the grain size distribution within the μc-Si:H material and not a powder pattern for a rhombic or axial *g*-matrix.

While we believe that a dependence of the CE *g*-value on the crystallite size seems plausible, we cannot quantify this effect yet. However, DFT techniques capable of calculating EPR parameters for localized states in thin-film silicon became available recently [115, 121, 122] and may be employed to study the *g*-value as function of the crystallite diameter.

4.2.4 Field-Dependence of the Spectral Resolution

At 9.7 GHz the e and CE resonances overlap strongly (Fig. 4.2). At 34 and 94 GHz the increased Zeeman splitting of the spin states results in a larger separation of both signals on the field axis, which is seen in the central part of the spectra. For a detailed evaluation of the gain in spectral resolution, the line width of the decomposed resonances in dependence on the mw-frequency was analyzed (Fig. 4.4 a) and c)). Therefore, the e line width ΔB_e at the three frequency bands was taken from the fit results of the decomposed e and P spectra (Fig. 4.4 a) and b)). As the CE profile is asymmetric, only the line width ΔB_{CE}^{lf} describing the low field side, relevant for the spectral resolution, is used.

In Fig. 4.4 d) the separation of the peak positions of the e and CE lines in field ΔB_{sep}, deduced from the X-, Q- and W-band measurements are plotted as a function of the mw frequency. ΔB_{sep} can well be fitted by a straight line as the g-values obtained for both species agree within error margins for all three frequency bands. The slope of the linear fit $\Delta g_{slope} = 0.0057(5)$ is in agreement with the average g-value difference $\Delta g_{sep} = g_e - g_{CE} = 0.0061(5)$ calculated from the g-values obtained at the three frequency bands.

Fig. 4.4 d) also shows the line width change of ΔB_{CE}^{lf} and ΔB_e in dependence of the mw frequency. The line width increases significantly with increasing observation frequency. The three measurements covering one order of magnitude in frequency can be fitted well by a linear function (dotted line for ΔB_e, dashed line for ΔB_{CE}^{lf}). This clearly demonstrates that the line width is dominated by field-dependent broadening. Two possible origins for field-dependent line broadening are i) g-anisotropy and ii) g-strain (site-to-site variations of the principal g-values, [123]). Investigations of paramagnetic centers in disordered silicon such as the dangling bond defect in amorphous silicon [12, 15] show that g-anisotropy and g-strain dominate the resonance spectrum at Q-band and higher frequencies whereas hyperfine interactions with ^{29}Si and ^{1}H are important at X-band and below.

Hence we consider the development of line widths in the X-, Q- and W-band spectra to deduce information about the field-dependent line width contribution Δg. A distinction between the two field-dependent broadening effects - g-anisotropy and g-strain - is impossible. Field-independent contributions, e.g. hyperfine couplings, are neglected at the frequencies used

here.

A rough value for Δg is obtained from the dependence of the line width on the resonance frequency as the slope s_i of the line width development is determined by:

$$s_\mathrm{i} = \frac{h}{\beta_\mathrm{e}} \frac{\Delta g_\mathrm{i}}{g_\mathrm{i}^2} \nu_0$$

[124] with the Planck constant h and the Bohr magneton β_e. On the basis of this relation $\Delta g_\mathrm{e} = 0.004(1)$ and $\Delta g_\mathrm{CE}^\mathrm{lf} = 0.0037(6)$ can be calculated for the e and CE resonances. These field-dependent contributions to the CE and e line widths are smaller than the g-value separation $\Delta g_\mathrm{sep} \approx 0.006$ of both resonances. This results in an increased spectral resolution at higher fields and frequencies which makes multi-frequency and especially high-frequency EDMR a powerful tool to obtain information about g-values, -anisotropy and -strain of paramagnetic centers in semiconductor devices.

4.2.5 Influence of Spin Polarization

The EDMR signals reported throughout this study are assumed to originate from spin-dependent transitions between two charge carriers where the symmetry of the spin pair governs the transition rate as described in Sec. 2.3. The signal resulting from such a *pair process* does not depend on the (thermal) polarization of the spins, i.e., the EDMR spectrum is supposed to be independent of temperature and magnetic field [32]. This is consistent with the X-, Q- and W-band spectra shown in Fig. 4.2, indicating that the same transport process is responsible for the EDMR signals for all frequency bands, although the spin polarization $p = \Delta N / N$ (the ratio between the difference ΔN in spin down concentration, $N_\downarrow$, and spin up concentration, $N_\uparrow$, and the total spin concentration $N = N_\downarrow + N_\uparrow$) changes considerably from 2.3 % at X-band (9.7 GHz, 10 K) to 42 % at W-band (94 GHz, 5 K). In particular, the dynamics of the signals attributed to e, P and CE states as well as the relative signal intensities remain nearly constant upon variation of the resonance frequency, whereas the resonance line shapes exhibit a pronounced field-dependence as shown in Fig. 4.4 c). Drastic changes of the EDMR spectra upon variation of p were observed e.g. for spin-dependent processes at the Si/SiO_2 interface [125]. Here, the authors detected a sign inversion of high-field EDMR signals associated with spin-dependent processes involving ^{31}P donor states near the Si/SiO_2 interface when the temperature was

varied between 3 and 12 K. This indicates a p-dependent process. In contrast, no evidence for the existence of p-dependent processes in μc-Si:H solar cells could be found under the experimental conditions used in the present study. This indicates that the hopping processes involving e, P and CE states reported in this study are surprisingly robust against changes in the thermal spin polarization over a wide range.

4.3 Summary

In this study light-induced EDMR signals of a single p-i-n μc-Si:H solar cell at mw frequencies between 9.7 and 94 GHz were investigated. With the help of deconvolution methods the different spectral components were separated and analyzed in detail.

The g-value of the e resonance could be determined precisely with Q- and W-band measurements. A signal asymmetry is not resolved even at W-band. The P signal pair splitting of ≈ 21 mT is constant at all measured frequencies, corroborating the reason for the signal doublet to be hyperfine interaction. The CE line profile shows an asymmetry at all three frequency bands, which is most pronounced at W-band. This particular line shape leads us to the suggestion that a size distribution of crystallites accommodating light-activated CE centers is responsible for a g-value distribution and hence for the CE resonance asymmetry. From the line width development of the e and CE lines in dependence on the mw frequency a field-dependent line width contribution of $\Delta g_{\mathrm{e}} \approx \Delta g_{\mathrm{CE}}^{\mathrm{lf}} = 0.004(1)$ could be deduced. The signal splitting of both resonances $\Delta g_{\mathrm{sep}} \approx 0.006$ is larger than the extracted field-dependent broadening, which results in a gain in resolution of EDMR spectra measured at high fields and frequencies. The fact that the EDMR spectra are almost independent of the resonance frequency indicates that the same spin polarization-independent transport process is responsible for the EDMR signals observed in X-, Q- and W-band.

The chosen approach of multi-frequency and especially high-frequency EDMR is thus an important tool to characterize paramagnetic centers involved in transport paths of the fully-processed thin-film solar cells. The precise magnetic parameters obtained can further be the fundament for structural identification of these paramagnetic centers by theoretical modeling. In order to study the paramagnetic centers (e.g. the CE center) in

microcrystalline silicon in more detail, the multi-frequency approach will be applied to a thin-film cell completely made of μc-Si:H in the next chapter.

5

INVESTIGATION OF μC-SI:H P-I-N SOLAR CELLS

In chapter 4 the application of multi-frequency EDMR to thin-film μc-Si:H solar cells showed the capability of this technique for the investigation of light-activated paramagnetic centers. This study revealed, among others, signals which were assigned to so-called conduction band tail states in amorphous silicon (*e states*, $g_e \approx 2.0048$) as well as in microcrystalline silicon (*CE states*, $g_{CE} \approx 1.998$). The signals of both centers do not only differ significantly in their g-value, but also in the high-field/high-frequency line profiles. The e signal is symmetric even at 94 GHz, whereas the CE signal shows a pronounced field-dependent asymmetry. A size distribution of crystallites accommodating light-activated CE centers was suggested as the reason for a g-value distribution and hence for the CE resonance asymmetry.

Summarizing these results shows that, despite the assignment to conduction band tail states in both cases, the magnetic properties of the states differ markedly. This means, that the microscopic structure of the CE center in the crystalline regions deviates significantly from that of the e centers in the amorphous material. Thus, this center and its interesting properties should be object of further investigations.

The sample used in the present chapter is, again, a thin-film solar cell in a p-i-n configuration. Now, all three layers consist of μc-Si:H material, since in this way the signals stemming from the a-Si:H layer can be removed from the spectra. It was shown by Behrends et al. [21, 43] that not only CE centers

give rise to a signal in the EDMR spectrum of the μc-Si:H solar cell. Also a signal due to dangling bond (db) defects was found. A broad signal covering a field range of 60 mT was observed as well and assigned to μc-Si:H conduction band tail states (called CH states).
All these signals have in common that they originate from the heterogenous microcrystalline structure. Hence, this chapter presents a comprehensive study of the different defect centers in μc-Si:H thin-film solar cells with the help of various EDMR techniques. This study appreciates in value based on many questions regarding the CE center and the additional light-activated paramagnetic centers in μc-Si:H. A selection of open questions is:

1. Since the CE centers are assumed to be accommodated in Si crystallites, how does the spin-dependent transport via neighboring CE centers take place? Is the CE center involved in further transport paths?

2. What is the nature of the EDMR-active center giving rise to the broad resonance line? Which interaction leads to the line width and which role does this center play in transport processes in the solar cell?

3. Why are phosphorus donor states and boron acceptor states not visible in the EDMR spectra? In which phase of the material do we find the doping atoms?

In the first section the EDMR spectrum of the light-activated paramagnetic centers is examined using continuous wave (cw) as well as pulse (p) EDMR. The different spectral contributions will be separated and assigned to the respective defects.
Second, the promising multi-frequency approach, which was established in chapter 4 will be applied to the sample to determine field-dependent and field-independent line widths. This approach is combined with the investigation of solar cells of controlled Si isotope concentration to distinguish between hyperfine (HFI) and spin-dipolar interactions.
Third, the microscopic environment of the defect states will be studied by electrically detected electron spin echo envelope modulation (ED-ESEEM). This technique gives information about spin-carrying nuclei like ^{29}Si or ^{1}H in the vicinity which are coupled to the defect.
Finally, transient nutation experiments are used to get further insights into spin pair coupling characteristics and the spin state of the centers which are responsible for the broad background resonance.

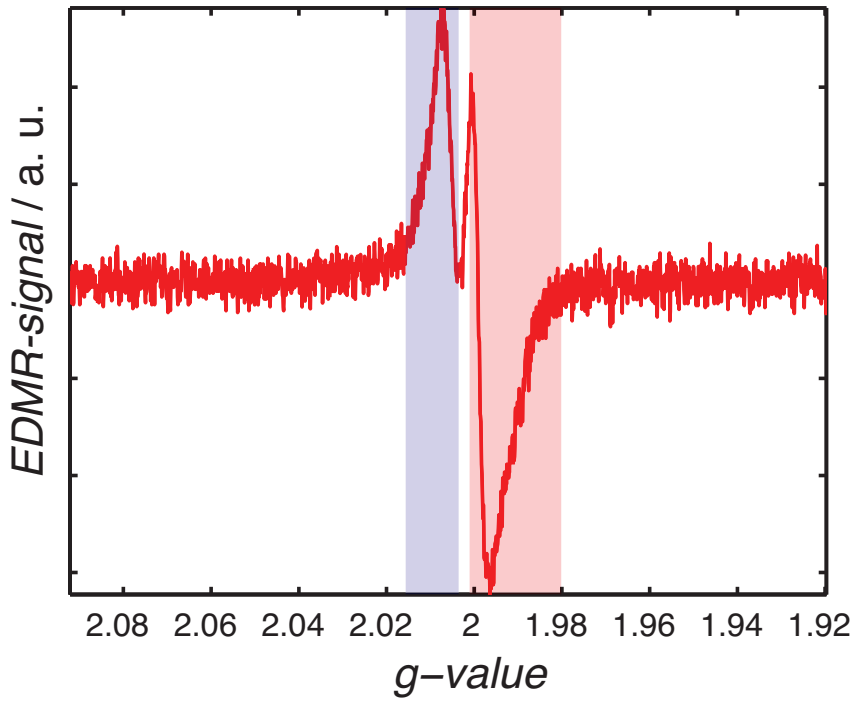

Figure 5.1: cw EDMR spectrum of µc-Si:H thin-film solar cell measured at 10 K. The spectrum consists of two main components at $g \approx 2.004$ (blue shaded area) and $g \approx 1.998$ (red shaded area).

5.1 Continuous Wave and Pulse Measurements

The EDMR spectrum of the thin-film microcrystalline Si solar cell is investigated in this section. Therefore continuous wave and pulse EDMR experiments are applied which enable a decomposition of the spectrum.

5.1.1 Continuous Wave Experiments

Continuous-wave EDMR experiments at low temperatures were performed to analyze the spectrum of the µc-Si:H thin-film solar cell. A first look on the cw EDMR spectrum reveals two overlapping resonances with centers at $g \approx 1.998$ and at $g \approx 2.004$ (Fig. 5.1). We chose two different approaches to obtain detailed information about all contributing signals.
On the one hand, spectra were measured as a function of the modulation phase because Dersch et al. [100] report about cw spin-dependent photoconductivity experiments on a-Si:H samples at different field modulation

phase settings [35] showing signals with different g-values and line shapes. They assigned this effect to be caused by separate spectral components with different process dynamics. This approach is especially interesting in combination with EDMR (in comparison to EPR), as the spin-dependent processes including different species of paramagnetic states can be connected with different time constants resulting in phase shifts. Hence, we expect to separate the contributing EDMR signals via their modulation phase dependence.
On the other hand, we performed experiments at various temperatures as there are reports about significant differences in the temperature dependences of paramagnetic dangling bond and CE centers in microcrystalline silicon [13, 110].

Modulation Phase Dependence

Spectra of ΔB = 30 mT width were measured at 10 K. The modulation phase ϕ_{mod} was varied in steps of $\Delta\phi_{\mathrm{mod}}$ = 30° to investigate the dependence of the EDMR signals on ϕ_{mod}. The modulation frequency was chosen to be ν_{mod} =10 kHz, the modulation amplitude was 0.2 mT. At $U = 1$ V reverse bias a photocurrent of $I_{\mathrm{ph}} = 14.2$ μA was obtained.
Two spectra at $\phi_{\mathrm{mod}} = 60°$ and $\phi_{\mathrm{mod}} = 150°$ are shown in Fig. 5.2 a) and b). The profile of both spectra is completely different, which is a hint for differences in the phase dependence of the individual signals. The spectra were fitted with a set of Voigtian lines to evaluate the data.
In a first step, the change of the spectral tails were analyzed for different modulation phases ϕ_{mod} because here the EDMR spectra are probably dominated by only one signal profile. It follows that at least three resonances contribute to the EDMR spectrum. Consequently, three lines at $g \approx 1.996$, $g \approx 2.002$ and at $g \approx 2.003$ were used to describe the modulating EDMR spectra. In the marginal regions fit and spectra show good accordance which can be seen in the upper part of Fig. 5.2 a) and b). The residuals show deviations in the central region, which is a hint for additional lines or asymmetric line profiles in the spectrum.
In a second step, five Voigtian lines were used to fit the EDMR spectra (shown in Fig. 5.2 c) and d)). These five lines do not yet have a physical meaning as they are only used to describe the spectra. In a least square fit procedure the line parameters (except the line amplitudes) were optimized for a first spectrum and transfered to fit to the other spectra, so that finally

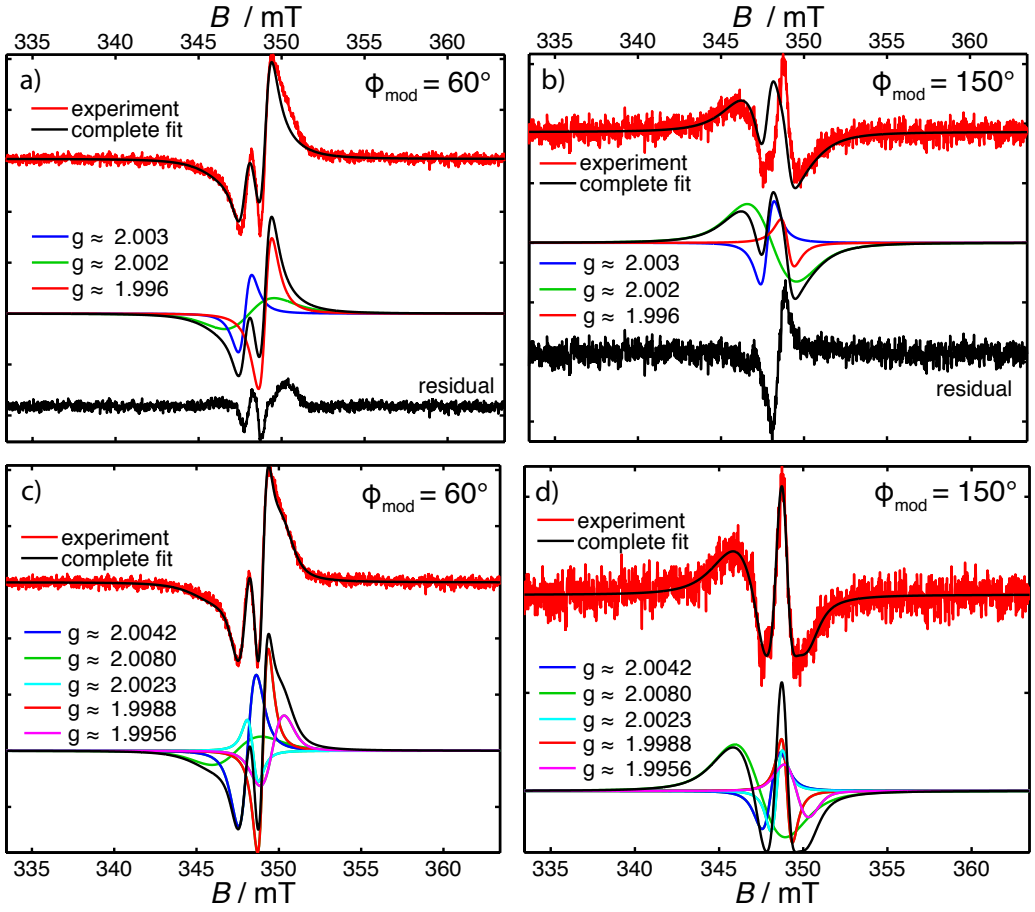

Figure 5.2: a) and b): cw EDMR spectra for $\phi_{\mathrm{mod}} = 60°$ (left) and 150° (right) are shown together with the fit result based on three lines. c) and d): the same cw EDMR spectra are shown now fitted with five lines. Spectrum and fit match well.

one set of line parameters was used to describe the complete data set. Only the line amplitude was a free parameter which delivers the modulation phase dependence of the EDMR signals. The results of that fit can be seen in Fig. 5.3. Here the signal line intensity is plotted as a function of the modulation phase ϕ_{mod}. All five lines show a sinoidal behavior of the line intensity. They can be summarized to three groups of phase behavior. Starting at small values of ϕ_{mod} the broad line at $g \approx 2.008$ (green squares) disappears at $\phi_{\mathrm{mod}} \approx 100°$. The narrow lines at $g \approx 2.0023$, $g \approx 1.9988$ and $g \approx 1.9956$ (all have triangular symbols) have zero amplitude at $\phi_{\mathrm{mod}} \approx 140°$. Finally, the resonance at $g \approx 2.0042$ (circles) does not contribute to the EDMR spectrum at $\phi_{\mathrm{mod}} \approx 160°$.

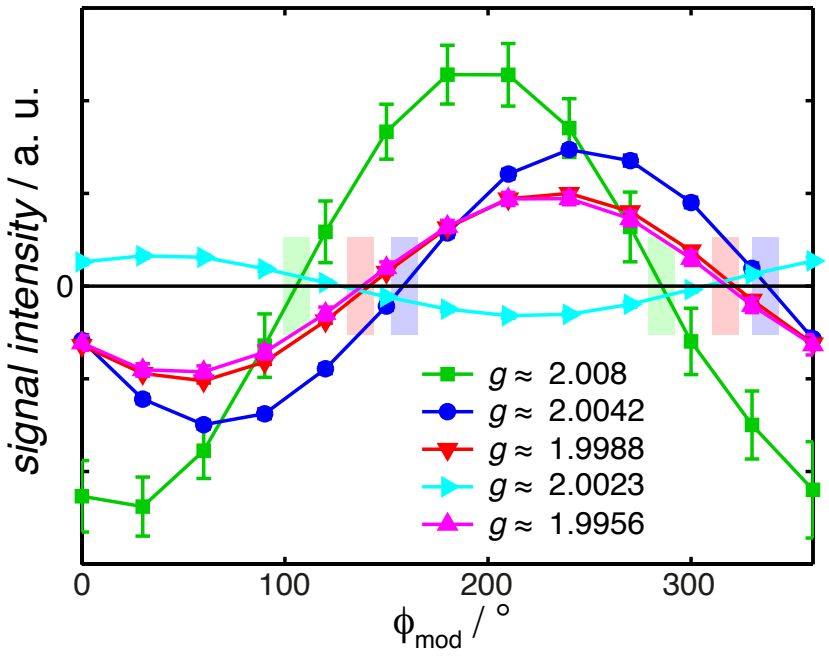

Figure 5.3: The intensity of the lines used for the fit procedure are shown as a function of the modulation phase ϕ_{mod}. The phase shifts of the lines are indicated by the colored boxes. The errors are estimated from the SNR of the cw data sets and are small compared to the used symbols except for the broad line at $g \approx 2.008$.

These three groups are interpreted as follows: The green line ($g \approx 2.008$) and the dark blue line ($g \approx 2.0042$) in Fig. 5.3 are independent lines with individual phase shifts and are therefore interpreted as individual signals. Here the g-value at $g \approx 2.008$ is in range of valence band tail states in amorphous silicon [21, 100, 126, 127] thus we denote that signal as *h signal* for the moment. The signal at $g \approx 2.0042$ is possibly due to a-Si:H conduction band tail states or db states in microcrystalline Si [100, 128–130] leading us to the preliminary name *e-db signal*. Further investigations will allow a profound interpretation of the detected resonances later. On the contrary, the three lines at small g-values (violet, red, light blue) show exactly the same phase shift thus probably belonging to one signal. The three lines only served to describe the asymmetric line profile at $g \approx 1.998$. The g-value and the line asymmetry point to the expected *CE signal*. In summary, the modulation phase analysis showed that the EDMR spectrum consists of three resonances at $g \approx 2.008$, $g \approx 2.004$ and $g \approx 1.998$.

No. of line	position	width / mT	signal position	line width/ mT
1	2.008	[2.94 4.42]	2.008(1)	4.1(4)
2	2.0042	[0.94 1.91]	2.0042(4)	1.54(5)
3	2.0023	[0.47 1.56]	-	-
4	1.9988	[0.35 1.65]	1.9976(4)	1.42(5)
5	1.9956	[1.65 1.39]	-	-

Table 5.1: Overview of the line parameters used for the fit of the modulation phase data sets and the resulting g-values and line widths of the EDMR signals. The line with No. 3 to 5 are finally summarized to one EDMR signal.

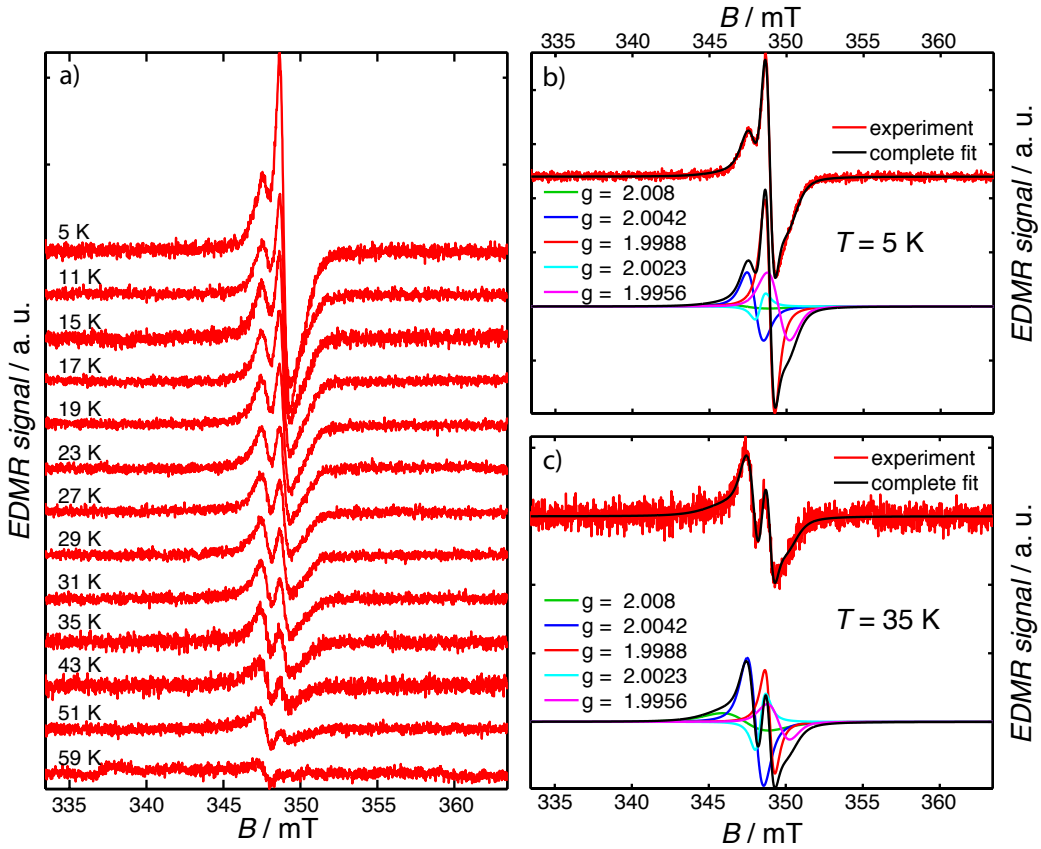

Figure 5.4: Temperature dependence of the EDMR spectrum. In a) raw data between 5 and 59 K are shown. b) and c) illustrate spectra at 5 and 35 K, respectively, together with fit results.

Temperature Dependence

Continuous wave experiments were performed in the range of 5 K to 59 K to investigate the temperature dependence of the EDMR spectrum. In this

temperature range the photocurrent I_{ph} of the cell (1 V reverse bias) increases from 13.3(1) μA to 41.7(1) μA. As in the experiments before the modulation frequency was chosen to be 10 kHz, the modulation amplitude was 0.2 mT and $\phi_{mod} = 60°$. An overview of the data is given in Fig. 5.4. In Fig. 5.4 a) the raw spectra are given. Fig. 5.4 b) and c) show the spectra at 5 K and 35 K as well as the five single fit functions and the complete fit. One can see that the EDMR spectrum decreases by increasing the temperature, so that it nearly vanishes at 59 K. The two example spectra furthermore make clear that the signals show individual temperature behavior. The spectra were approximated by the same set of five lines, which was already applied to the modulation phase spectra (see Tab. 5.1). The line parameters (position, line width, line shape) were kept constant, whereas the amplitudes were again the only free parameters. The results of this evaluation are shown in Fig. 5.5. Using the given data set, good fit results were reached in the complete temperature range.
At temperatures below 20 K the lines in the region of $g \approx 1.998$ dominate the spectrum (triangular symbols). Going to higher temperatures the intensities of the contributions at $g \approx 1.9956$ and 1.9988 strongly decrease, so that they disappears already at ≈ 50 K. Their temperature dependence is identical as shown in Fig. 5.5. The relatively small contribution of the line at $g \approx 2.0023$ (light blue) as well as the position directly in the middle of the spectrum do not allow to deduce a reliable temperature dependence. Nevertheless the mutual T and ϕ_{mod} behavior of the three lines underlines, that they belong to one EDMR signal (the CE signal). The components taken together result in a resonance with a g-value of g_{max} = 1.9976(4) at the position of maximum amplitude.
The e-db line at $g \approx 2.0042$ (circles) shows a weaker temperature dependence, clearly deviating from the behavior of the lines near $g \approx 1.998$. It can be detected at temperatures up to 59 K. The temperature dependence of the h signal at $g \approx 2.008$ (squares) is hard to extract, since the low SNR of the broad line results in big errors.

5.1.2 Single Pulse Experiments

With the help of cw EDMR experiments it was possible to obtain a good overview of the EDMR spectrum. These investigations are extended in a next step to single pulse EDMR experiments, as pulse experiments offer im-

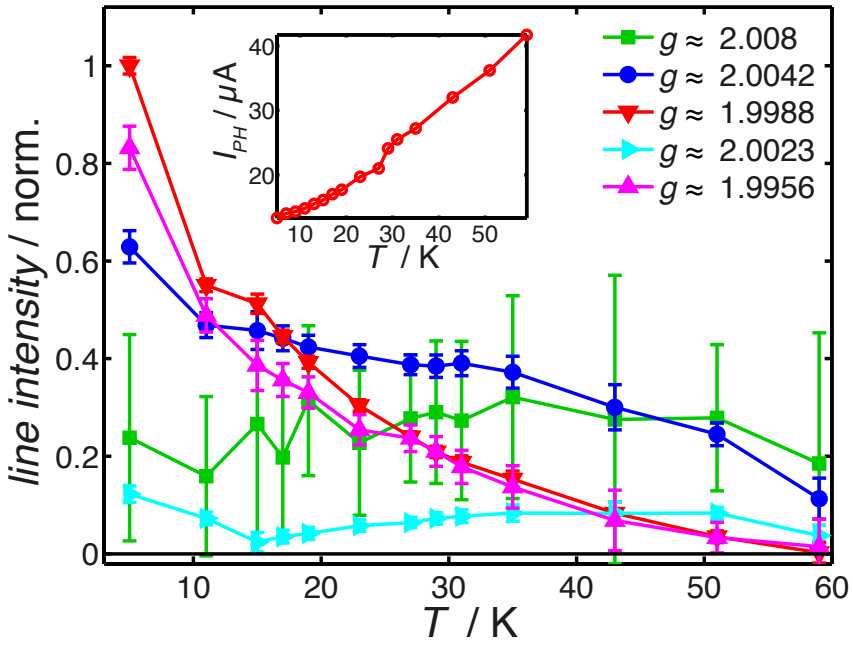

Figure 5.5: The intensities of the five lines used to fit the spectra are shown as function of the temperature. The errors indicated are estimated from the signal-to-noise ratio. This error of the h signal at $g = 2.008$ is large due to the high line width and small amplitude. Inset: Photocurrent I_{PH} of the cell at $U = 1$ V reverse bias as function of the temperature.

portant advantages to obtain more information about the detected signals. On the one side, cw experiments with lock-in detection are not suitable to resolve broad spectral components when small modulation amplitudes are used. Pulse EDMR techniques do not have this disadvantages. On the other side, the study of modulation phase dependencies allows only limited excess to signal time constants, whereas the transient current response after a pulsed mw excitation directly contains this information. Finally, single pulse experiments constitute the basis for pulse sequences as Hahn echo or stimulated echo experiments, which again are the basis for pulse techniques addressing electron-nuclear (ESEEM, ENDOR) or electron-electron interactions (ELDOR).

In the first part of this section performed X-band π-pulse EDMR experiments are evaluated. The spectra are deconvoluted to characterize the known as well as new contributions. In the second part the results are tested for reliability by application to pulse EDMR data measured at different light intensities.

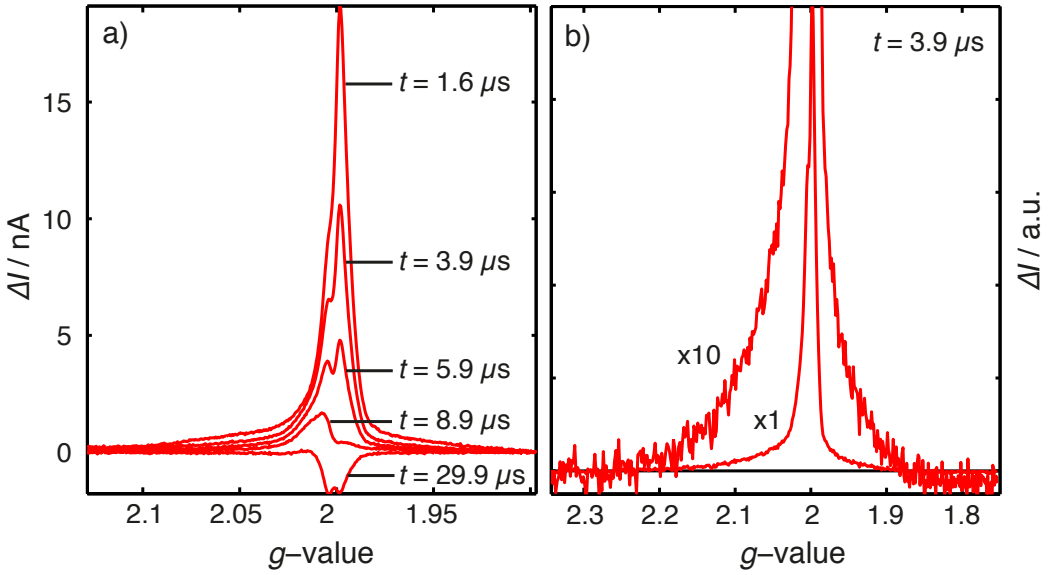

Figure 5.6: a) 40 mT broad field sweep spectra at different time points after the mw excitation. Three narrow lines can be identified. b) EDMR spectra with $\Delta B = 100$ mT. This field interval allows to display the complete width of the very broad signal at $g > 2$. For a better resolution of this line the spectrum is scaled by a factor of 10. At small g-values baseline distortions appear.

The Pulsed EDMR Spectrum

The field sweep π-pulse EDMR spectra at X-band were measured at $T = 5$ K using low power π-pulses of $t_p = 300$ ns length to avoid a significant pulse length broadening. Field ranges of $\Delta B = 40$ mT and in addition 100 mT were chosen to detect the complete spectrum. The cell was operated at $U = 1$ V reverse bias ($I_{ph} = 18.9(1)$µA). In Fig. 5.6 a) the EDMR spectra are shown at different time points after the mw excitation. Starting at $t = 1.6$ µs (maximum signal) the intensity of the spectrum decreases and becomes negative for large times. On the g-axis narrow features in the region around $g = 2$ are detected. Taking a closer look, the EDMR spectra at $t = 5.9$ µs and $t = 8.9$ µs reveal three lines as expected from the cw EDMR analysis. A very broad line centered at $g > 2$ can be observed (Fig. 5.6 b)), which was not visible in the cw data. It covers a range of approximately 50 mT. Despite the strong overlap of the resonances a spectral deconvolution is possible due to differences in the signal dynamics.

For the evaluation the methods described in chapter 4 were applied,

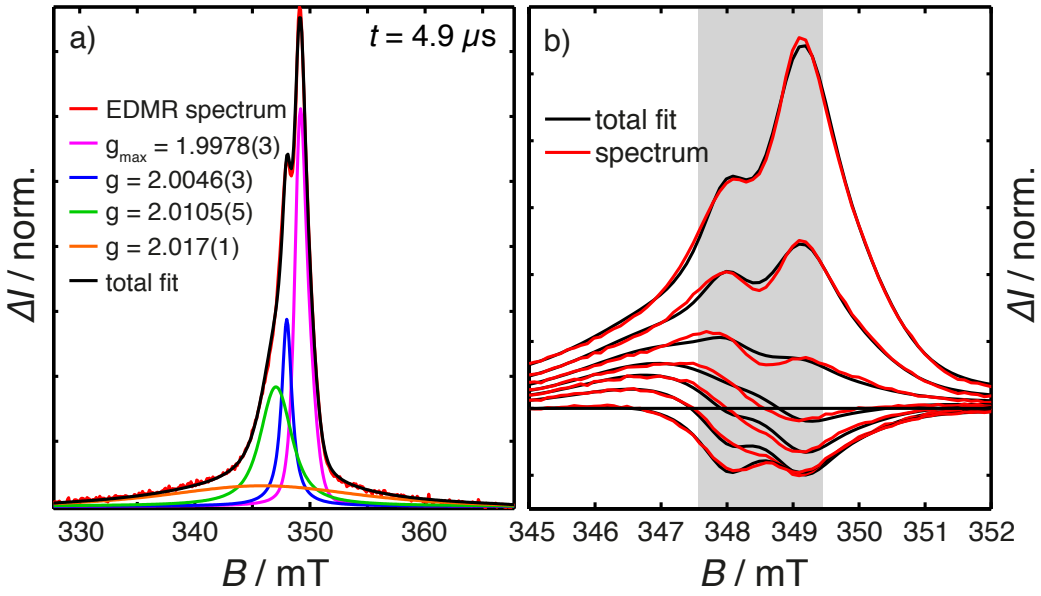

Figure 5.7: a) The EDMR spectrum at $t = 4.9\mu s$ is shown together with the single fit lines and the total fit. With the help of four lines the spectrum is well described. b) In the central region between 347.5 mT and 349.5 mT small discrepancies between fit and spectrum appear for a long time interval.

which make use of the individual signal dynamics. The analysis of these spectra here is complicated by the existence of at least three species with different time behavior, instead of two, as in the case of the n-a-Si:H/μc-Si:H solar cell (chapter 4). The parameters of the three narrow lines obtained from the analysis of the cw data in section 5.1.1 were used for the fit of the pulse spectra. The fit procedure consists of two steps.
In a first step these parameters were taken as starting conditions for the fit of a π-pulse spectrum at a fixed time after the mw excitation. The fit parameters line width and position were confined to intervals for each signal, whereas the amplitudes were completely free. Within this fitting process it was found that the line widths deduced from the cw EDMR data are slightly broader. Nevertheless, the parameters of the symmetric lines could be used. Only the asymmetric profile of the CE line obtained from the cw data was rejected. Instead, the isolated CE profile from chapter 4 was employed as the basic shape for the fit of the asymmetric line. The obtained results are given in table 5.3. An exemplary spectrum is shown in (Fig. 5.7 a)).
In the second step the values obtained so far where kept fixed and applied to the spectra at other time points. Only the signal amplitudes were used as free parameters. With four lines the EDMR spectra can be described very

assignment	g-value	Voigtian shape	line width
h center in a-Si:H	2.0105(5)	[1.57 2.48] mT	3.3(1) mT
db center in a-Si:H	2.0046(3)	[0.07 1.07] mT	1.1(1) mT
CE center in Si crystallites	1.9978(3)	asym. shape	1.4(1) mT
V center in µc-Si:H	2.017(1)	[11.4 11.4] mT	19(1) mT

Table 5.2: The final line parameters of the four signals deduced from the pEDMR data sets. For the assignment of the resonances to the paramagnetic centers see section 5.1.3.

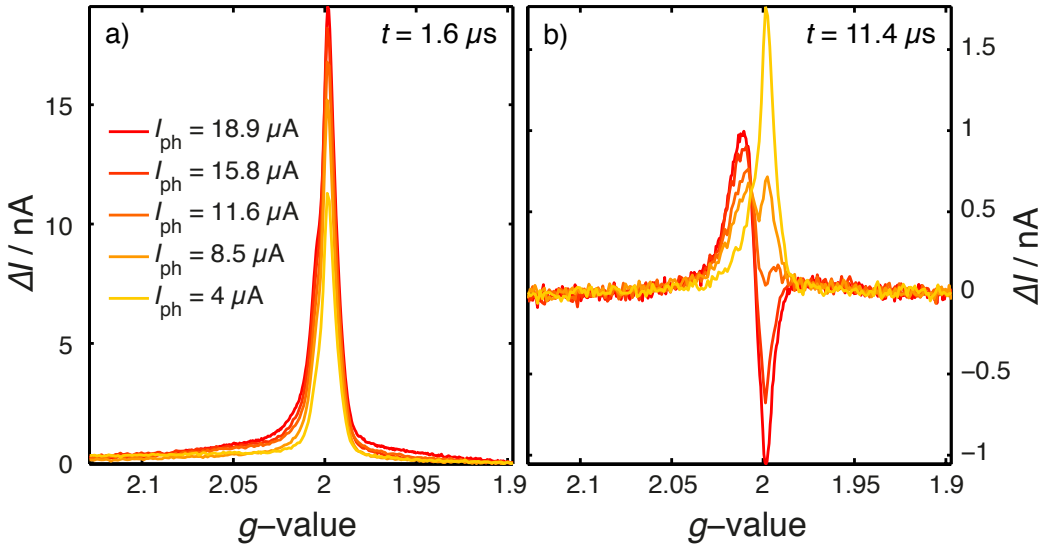

Figure 5.8: EDMR spectrum shown at a fix time after mw excitation as function of the light intensity. a) At $t = 1.6$µs a general decrease of the overall spectral intensity is visible. b) At $t = 11.4$µs significant light intensity dependent changes of the signals' dynamics lead to different shapes of the spectra.

well despite the strong overlap of the different components. Small deviations between spectrum and fit (shaded area in Fig. 5.7 b)) are only observed in the time interval $t = 6 - 12$µs. These deviations are probably caused by the different dynamics of the asymmetric line at $g = 1.9978(3)$ and the line at $g = 2.0046(3)$.

Dependence on Light Intensity

The measurements at varying light intensities were performed in the same way as the previous pulse experiments. By reduction of the light inten-

sity the photocurrent was decreased from the maximum value of $I_{ph} = 18.9(1)\mu A$ to $I_{ph} = 4.0(1)\mu A$. The EDMR spectra shown at two different times after the mw pulse illustrate on the one hand the decrease of the allover current response with decreasing I_{ph} (Fig. 5.8 a)) and on the other hand the change of the signal dynamics (Fig. 5.8 b)). This change delivers a large number of spectra, which consist of all four signals with different relative amplitudes and time behavior. With these data a reliability test of the line parameters (table 5.3) is possible. For this the extracted line properties were used to fit all spectra of this light intensity series. Again only the signal amplitudes were free parameters. All data sets can be described with the same parameter set. Small deviations between spectrum and fit are observed when the lines at $g = 1.9978(3)$ and at $g = 2.0046(3)$ contribute only with small amplitudes.
After this successful deconvolution procedure we have access to the dynamics of the deconvoluted single resonances via the time-dependent signal amplitudes (Fig. 5.9 a) to d)). In general, the current transients are characterized by an initial current increase (enhancing signal) followed by a current decrease (quenching signal). The steady decay of the fitted amplitudes without any artifacts is an indicator for a suitable choice of line properties. Sudden jumps of amplitudes would indicate a compensation of mismatches in the fit. The dynamics of the four signals can be classified in two manners: i) The transient behavior of the lines at $g = 1.9978(3)$ and at $g = 2.0046(3)$ (Fig. 5.9 a) and b)) can be summarized by an initial steep growth followed by a signal decline below zero until a lower limit clearly deviating from zero is reached. Finally, the signal decays back to zero for long times. Contrary to that, the time-dependence of the remaining signals at $g = 2.017(1)$ and at $g = 2.0105(5)$ in Fig. 5.9 c) and d) can rather be described by a sudden increase followed by a signal decay back to zero. A negative component is small in comparison to the initial maximum. ii) Comparing the transients within the first group (Fig. 5.9 a) and b)) one observes shorter time constants of the negative transient contribution at $g = 1.9976(3)$ and longer time constants at $g = 2.0046(3)$. The signal increase is connected with more or less equal rates. Comparing the transients at $g = 2.017(1)$ and at $g = 2.0105(5)$ from the second group, the later one shows clearly larger time constants, so that a possible negative contribution is not in the detection window.

The knowledge about the dynamics of the current response offers the possibility to find spectra consisting of a reduced number of signals. At the times highlighted by gray shaded boxes in Fig. 5.9 a) to d) the respective

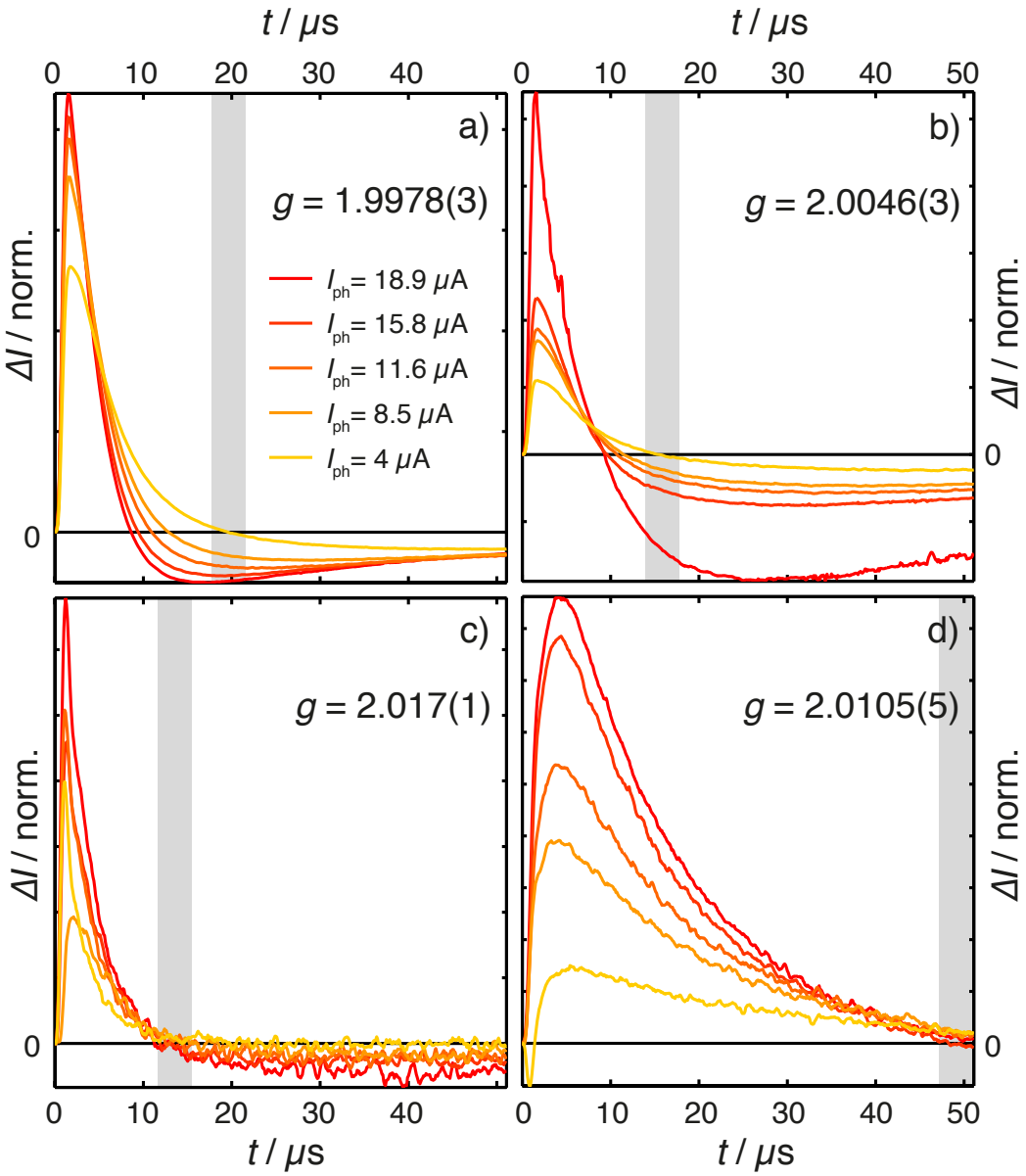

Figure 5.9: a) to d) The dynamics of the deconvoluted EDMR signals are displayed as function of the photocurrent. This dependency is obtained by plotting the fitted signal amplitudes as function of the time after the mw pulse. The gray areas mark the time interval of zero crossing of the respective EDMR signal for the case of $I_{\mathrm{ph}} = 4.0(1)\,\mu\mathrm{A}$. The spectra belonging to these times are shown in Fig. 5.10.

signals do not contribute to the EDMR spectrum. These simplified spectra are shown in Fig. 5.10. The g-values in the legend denote the components that do not contribute to the given spectrum. In summary, we could show

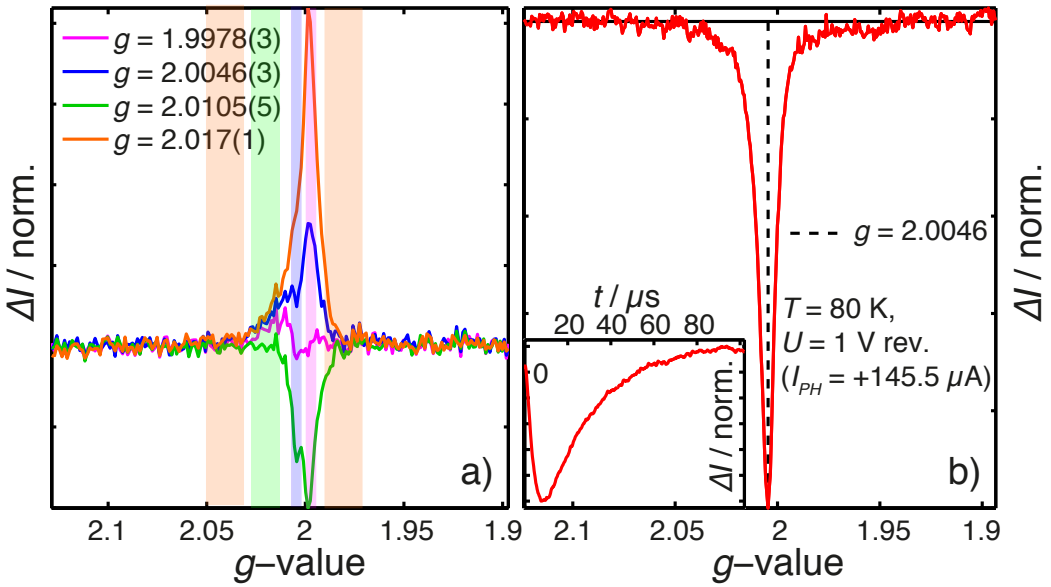

Figure 5.10: a) EDMR spectra of the data set at $I_{\mathrm{ph}} = 4.0(1)\,\mu\mathrm{A}$ are shown for four time points after mw excitation. The time points are chosen to map spectra consisting of only three signals, since the remaining one (with position at the g-value given in the legend) does not contribute due to its dynamics (see Fig. 5.9). b) EDMR spectrum measured at $T = 80$ K under reverse bias conditions. Here a single resonance at $g \approx 2.0046$ appears. Inset: transient current response at $g = 2.0046$.

that pEDMR data sets deliver a wealth of information to reliably decompose the total spectrum of overlapping lines into single resonances, whose properties can be further investigated.

5.1.3 Discussion

In this section continuous wave EDMR as well as pEDMR experiments were used to characterize the contributions to the spectrum. In the first part modulation phase and temperature dependencies were studied with cw EDMR. The cw spectra could be fitted unambiguously based on the different dependencies. Three species were identified. These signals were found in the pulse spectra as well. In addition, a broad component could be detected. The transient current response after the mw pulse allowed for a detailed deconvolution because the related time constants are characteristic for each signal. The deduced line parameters were corroborated by applying to additional spectra measured at different light intensities.

Comparing the cw and pulse line parameters shows that the narrow lines at $g \approx 2.004$ and $g \approx 1.998$ have similar g-values in both types of experiment. A discrepancy is observed for the third signal at high g-value. In the cw experiments $g = 2.008(1)$ is measured. The accuracy of this value is limited by the low SNR. The quality of the pEDMR data on the other hand allowed the deduction of $g = 2.0105(5)$, which is the more reliable value. The broad signal at $g = 2.017(1)$ was only found in pulsed experiments. Furthermore, one can see that the line widths from the cw results are larger than the line widths from the pEDMR experiments. The reason for this is probably the use of a too high cw mw power, which was a compromise between high SNR and reliable line parameters. We decided to use the pEDMR results for further evaluations, since the line parameters of all four signals could be extracted with good quality by this technique.
The obtained line properties are utilized in the following to assign the EDMR signals to the paramagnetic centers and to the corresponding spin-dependent processes.

CE Signal The EDMR line with the smallest g-value at $g \approx 1.9978(3)$ can be described with the asymmetric CE line profile which was extracted from the EDMR data of the μc-Si:H thin-film cell with n-a-Si:H layer in chapter 4. This is a clear hint for the assignment of this line to CE centers in the microcrystalline material. The g-value itself is indicative of this CE center in μc-Si:H [13, 21, 110, 129–131]. It is further supported by the characteristic T-behavior, which was found with the help of EPR studies [13].

db Signal The EDMR line parameters of $g \approx 2.0046(3)$ and 1.1 mT line width point to two paramagnetic centers found in microcrystalline and amorphous silicon. On the one hand, the μc-Si:H db center and on the other hand the a-Si:H conduction band tail state. As the sample has an amorphous volume fraction of 48% both interpretations are possible.
Following the interpretation of a conduction band tail state in a-Si:H, one finds $g \approx 2.0043$ ($\Delta B = 0.5 - 1.5$ mT dependent on doping conditions) [127], which is in agreement with the line parameters found here. These centers are observed in n-type as well as illuminated amorphous silicon [100, 128]. This finding fits to the existence of h centers in our spectra (see next paragraph) because they are observed in a-Si:H material, too.
Following the interpretation of a db state, one finds reports about so-called

db1 states at $g \approx 2.0052$ and db2 states at $g \approx 2.0043$, which are assigned to two independent defects located in different microscopic environments [13, 129, 130, 132]. For material deposited by the same methods as used for the investigated p-i-n solar cell, room temperature EPR measurements indeed show a composition of both lines [132]. A composition of two lines cannot be resolved here, but the g-value of 2.0046(3) could be the result of strongly overlapping db1 and db2 resonances. Behrends et al. found in µc-Si:H p-i-n solar cells a signal at $g \approx 2.0045(5)$ with 1.3(3) mT [21], which was assigned to db states in the microcrystalline silicon. The line parameters are similar to those found here, but the current response after a pulsed excitation is markedly different. It is negative directly after the pulse, which led to the interpretation of a db state participating in recombination processes.
We performed additional measurements at $T = 80$ K that show a single EDMR signal at $g \approx 2.0046$ of ≈ 1.5 mT width (Fig. 5.10 b)). The line properties again fit to the considered EDMR line. The important difference between both lines measured at 5 K and 80 K is the sign of the EDMR current change. The signal at 80 K shows a reduction of current in spin resonance with respect to the photo current (quenching signal) under reverse bias conditions, which is a hint for a recombination process. This process primarily takes place via deep defects like db centers, as they are efficient recombination centers.
In summary, we assign the considered EDMR line to db centers in the microcrystalline material. The time behavior of the current response at low T, which resembles that of the transport process rather than a recombination process is not yet understood. An overlap of EDMR signals caused by unlike paramagnetic centers (participating in different processes) is still possible.

h Signal The line at $g \approx 2.01$ is found as well in the cw as in the pulse EDMR spectra. In µc-Si:H p-i-n solar cells with p-a-Si:H layer a resonance at the same g-value is observed [21], but was assigned to come from hole centers in the amorphous layer and not from the µc-Si:H layers. The sample investigated here has no amorphous layers, but has an amorphous volume fraction of 48% where the hole centers could stem from. The g-value of the resonance serves in this case as a fingerprint. It is indicative for a valence band hole states (h states) found in amorphous silicon as shown in many reports [100, 126, 127]. We were unable to find reports about hole signals in microcrystalline Si with comparable line parameters.

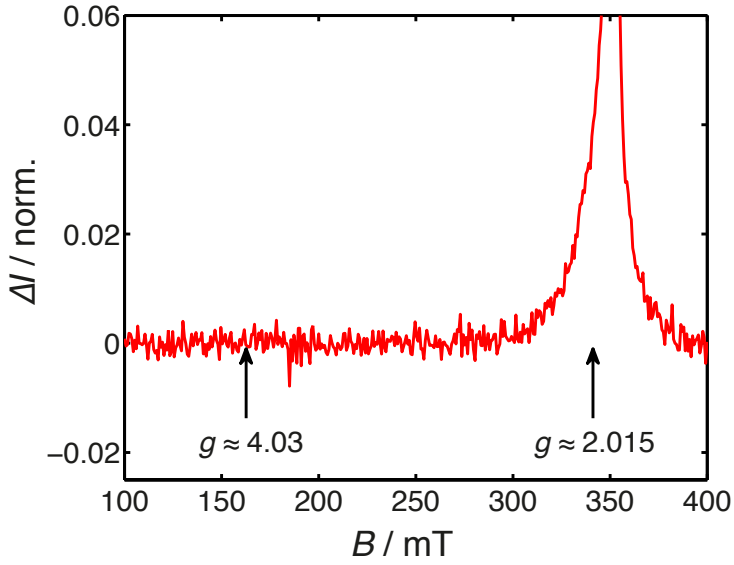

Figure 5.11: Field sweep EDMR spectrum of the p-i-n μc-Si:H solar cell. The sweep range was chosen to cover the ranges of the $\Delta m = \pm 1$ - transitions near $g = 2$ and the $\Delta m = \pm 2$ - transitions near $g = 4$. The spectrum is normalized but only the range of small intensities is shown to better resolve weak signals. Only around $g = 2$ the known spectrum is observed.

The assignment of the resonance to h states is supported by its modulation phase shift of $\approx 60°$ at a modulation frequency of $\nu_{\mathrm{mod}} = 10$ kHz with respect to the db signal observed in the cw experiments at 10 K. Dersch et al. [100] report about a resembling significant modulation phase shift of the hole signal in comparison to e and db signals in a-Si:H. This shift increased from 8° at 300 K ($\nu_{\mathrm{mod}} = 1$ kHz) to 15° at 150 K ($\nu_{\mathrm{mod}} = 1$ kHz) in that study and is explained by an increase of the process time constant with lower temperatures. The estimated time constant of 50 μs was much slower than the time constants of the e and db signals. The hole signal in the present study is as well connected with the slowest time constants in the pulse experiments (see Fg. 5.9) which corresponds to the modulation phase shift in the cw spectra. Hence, the resonance is assigned to hole centers in amorphous regions of the microcrystalline material.

V Signal In the EDMR study of Behrends et al. [21] a broad signal at high g-value in two of the considered sample structures was found (one of them is similar to the structure in the present work). This resonance exhibits a total width of roughly 60 mT, has an asymmetric shape and extents from

$g \approx 1.96$ to $g \approx 2.2$. By substitution of the doped layer material from a-Si:H to μc-Si:H in the p-i-n solar cell this signal was found to come from the p-doped and intrinsic microcrystalline layers. Furthermore, the EDMR current dynamics of this line resembles the dynamics of the line in our study.
In the EPR and ODMR literature three different paramagnetic species are described which give rise to broad resonance lines at $g > 2$.
First, a line at $g \approx 2.12 - 2.13$ of 50 mT width (FWHM) was found in boron doped μc-Si:H and thus attributed to acceptor states [113, 133]. These acceptor states are not observed here, because the g-value and the line width deviate significantly from our findings ($g = 2.017(1)$ of 19(1) mT width).
Second, investigations of doped and undoped μc-Si:H powder samples under dark and light conditions revealed a so-called CH signal at $g = 2.065 - 2.08$ ($\Delta B = 22.5 - 25$ mT), which shows properties like the CE signal in μc-Si:H [129]. This line is ascribed to trapped holes in valence band tail states in μc-Si:H. The central g-value and the width, again, deviate from our findings. An explanation of possible deviations of line widths is given by Feher et al. [134]. They report about EPR on p-doped c-Si and find that in absence of external compressive stress the hole signal from the valence band is not observed. By increasing the stress the line becomes narrow and can be detected. They explain this by the splitting of the valence band degeneracy by stress, which results in line narrowing for high stress because of a reduction of allowed EPR transitions. Hence, it is possible that hole signals in μc-Si:H are as well affected by small internal random strain due to imperfections and dislocations, which leads to broad lines. However, the g-value should stay unchanged. We conclude that the broad signal is not identical to these CH centers.
Third, ODMR measurements of μc-Si:H samples resolve a signal at $g = 2.016$ of 10 mT width at X-band [135, 136]. It was assigned to triplet excitons formed of strongly coupled electron spins. Broad lines of excitons observed in their triplet $S = 1$ state are also described in ODMR studies of a-Si:H ($g \approx 2.01$, ≈ 20 mT width) [137–140] and porous Si ($g \approx 2$, ≈ 50 mT width) [141]. The observation of forbidden $\Delta m = \pm 2$ -transitions is a characteristic property of triplet excitons in EPR. These signals are indeed found in the ODMR studies regarding amorphous materials.
The EDMR experiments of the present μc-Si:H sample, however, do not show a resonance at the half-field position (see Fig. 5.11). This does not mean that in the present case the $S = 1$ interpretation must be excluded because the $\Delta m = \pm 2$ transition of isolated paramagnetic centers in a triplet

$S = 1$ state does not alter the $|T_{+-}\rangle / |T_0\rangle$ proportion and with this the probability of intersystem crossing into the singlet ($|S\rangle$) state. Hence, this transition cannot give rise to an EDMR or ODMR half-field signal, whereas the $\Delta m = \pm 1$ transition is detected. This is possibly the case in microcrystalline silicon.
In the case of an interaction between triplets and paramagnetic centers nearby, the $\Delta m = \pm 2$ - transition leads to a spin-dependent process via the transition of the six-state manifold of the $S = 1/2$, $S = 1$ pair into a doublet ($S = 0$, $S = 1/2$) system [75, 76, 81, 82]. This could explain the detection of the half-field resonance in the ODMR studies of amorphous materials which are rich of defects.
For a reliable assignment of the broad signal to one of the mentioned or to a new paramagnetic center in the μc-Si:H material further investigations addressing the spin state of this center by Rabi nutation measurements or addressing the nuclear environment by ESEEM studies are necessary. On the basis of results which are described in the following sections the discussed signal will be called *V signal*.

5.1.4 Summary

Continuous wave and π-pulse EDMR experiments were employed in this section for a fundamental investigation of the μc-Si:H thin-film solar cell. At first, cw modulation phase and temperature dependent experiments were performed successfully to separate the different spectral components and to assign them to the underlying paramagnetic centers. Shifts in the modulation phase of the respective signals were observed based on variations in the time constants of the spin-dependent processes via different species of localized states. This allowed a decomposition of the spectrum into three different resonances. One of them showed an asymmetric line profile. The different temperature dependencies yielded a second approach to separate these three signal. The results corroborated the line parameters found in the modulation phase study.
In the second part, π-pulse EDMR experiments were applied to the same sample. The time behavior of the transient current response after the pulsed mw excitation at individual field positions was used to decompose the spectrum and to deduce g-values and line widths. The lines were assigned to conduction band tail states (*CE states*) in the crystalline regions,

to dangling bonds (*db states*) in the disordered phase of the material and to holes in valence band tail states (*h states*) probably in the amorphous parts. In addition, a very broad resonance was found but could not be assigned reliably yet. The signal which might be assigned to defects in a triplet state is called *V signal* here and will be discussed later.

5.2 Multi-Frequency EDMR Applied to Cells with i-Layers of Isotopically Controlled Si

The investigation of the thin-film solar cells is continued in this section. We applied a comprehensive multi-frequency study ranging from 3.5 GHz to 263 GHz to the samples. This approach was already introduced in chapter 4. Furthermore, two cells with intrinsic layers of different Si isotope compositions were studied. One sample has an intrinsic part with a natural isotope composition, the other sample's i-layer consists of ^{28}Si-enriched μc-Si:H.
The multi-frequency EDMR allows us to separate between field-dependent and field-independent line widths by measurements at various mw frequencies. In addition, we can distinguish between field-independent line width contributions caused by electron-nuclear interactions and electron-electron interactions by controlling the content of the spin-carrying isotope ^{29}Si.
We chose this approach to find answers to the following questions: How important is the influence of electron-nuclear (hyperfine) interactions on the line width of the EDMR resonances? Can conclusions be drawn regarding the localization of the electron wavefunctions? Does the CE line show the same asymmetric profile as in the multi-frequency study in chapter 4? How do the line profiles (widths, asymmetries) of the remaining three signals develop at higher mw frequencies and which conclusions are possible? Where does the large width of the broad line (called *V signal*) come from? These questions will be addressed within this section. Answering these would help to obtain a deeper understanding about defect structures in microcrystalline silicon, their microscopic surrounding and their role in transport processes within the device.

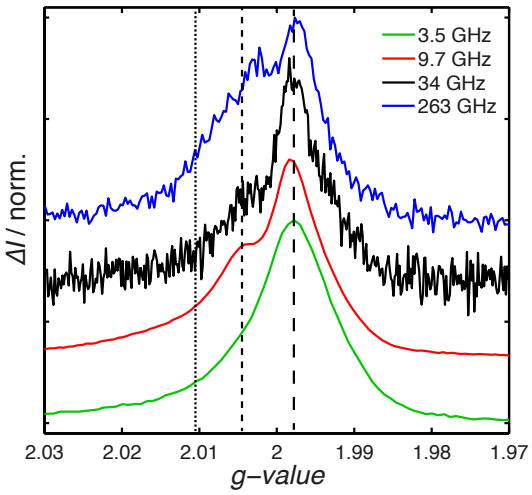

Figure 5.12: Normalized EDMR spectra of sample S_{nat}. The dashed lines mark the positions of the h signal at g_h = 2.0105, of the db signal at g_{db} = 2.0046 and of the CE signal at g_{CE} = 1.9978. The spectra are vertically shifted for better distinction.

Experiment

EDMR π-pulse experiments were applied to two different p-i-n thin-film solar cells. One cell with an intrinsic μc-Si:H layer of natural Si isotope abundance (called sample S_{nat}) and one sample with an i-layer made of ^{28}Si-enriched μc-Si:H material (sample S_{28}). The experiments were preformed in four frequency bands comprising mw frequencies between 3.5 GHz (S-band) and 263 GHz. The pulse length was chosen to be 300 ns for all measurements at S-, X- and Q-band to keep effects of excitation band width broadening small. At 263 GHz the shortest pulse length that could be generated was 1.5 μs. Field sweep spectra of 20 mT and 60 mT width at S-band, of 40 mT and 100 mT at X- and Q-band and 286 mT at 263 GHz were recorded to map the narrow and broad signals. The measurements were performed at $T = 5$ K. The cells were operated under reverse bias ($U = 1$ V) conditions resulting in photocurrents in the range of $I_{ph} = 5 - 9$ μA at S-band, $I_{ph} = 15 - 30$ μA at X-band, $I_{ph} = 1 - 2$ μA at Q-band, and $I_{ph} = 40$ μA at 263 GHz. The differences are due to the strong dependencies on the illumination conditions in the EDMR setups (see Sec. 3.2).

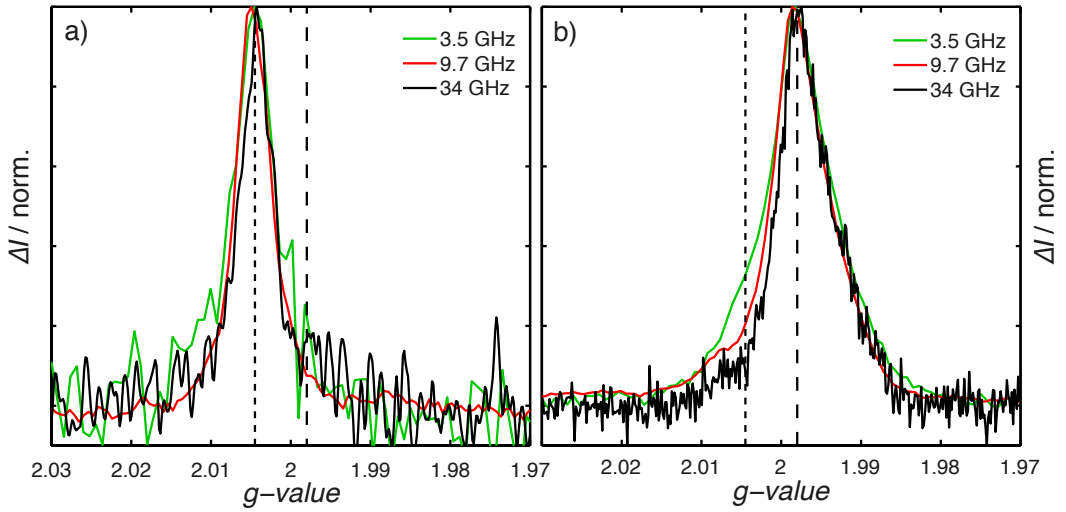

Figure 5.13: Decomposed EDMR spectra of sample S_{28}. The dashed lines mark the positions of the signals. a) The normalized db resonance. b) The normalized CE resonance. Further details about the spectral decomposition in the text.

Results

The sample S_{nat} was measured in all four frequency bands. The EDMR spectra shown in Fig. 5.12 are obtained by integrating the transient current response in time. Since the different illumination conditions in the setups influence not only the photo current of the cell but also the intensity of every EDMR signal, the 2D-spectra (like e.g. in Fig. 3.5) consist of resonances with different relative intensities. However, the spectra can be shown in a comparative way in Fig. 5.12 by choosing sufficient integration intervals yielding spectra with (nearly) equal relative db and CE line intensities. The spectra are shown in the frequency-independent g-axis representation. Hence, it is possible to indicate the line positions of the three narrow signals by vertical dashed lines at the characteristic g-values. The EDMR resonances strongly overlap. But the CE (g_{CE} = 1.9978) and db (g_{db} = 2.0046) lines can be clearly distinguished at the higher mw frequencies, whereas the h signal is hidden at 2.01 in the high g-value wing of the spectrum.
The π-pulse experiments of sample S_{28} were performed in S-, X- and Q-band. The spectra in Fig. 5.13 are shown in the g-value representation. The time constants of the db and CE signals differ considerably which allows for their separate illustration by a suitable choice of the integration intervals. The decomposition is responsible for the different signal-to-noise ratios.

In Fig. 5.13 a) the db resonance is shown. It appears as a symmetric line in all three frequency bands. Within the SNR the line width is unchanged on the g-axis which corresponds to a linear growth of the width as function of the mw frequency.
The CE line profile in Fig. 5.13 b) is asymmetric in all spectra. The profile at small g-values is identical for all measurements. In the range of $g \approx g_{\mathrm{db}}$ small contributions of the db signal overlap with the CE resonance.
The constant width of both lines on the g-value axis is clearly indicative for a field-dependent broadening mechanism.

Fit of the Multi-Frequency Data

In the following, the data given above are evaluated in detail. The aim of the evaluation is to find a set of line positions and widths of the different signals which fit all multi-frequency EDMR spectra. With this we are able to identify to field-dependent and field-independent broadening effects.
The fit of the data includes the prior knowledge of line parameters extracted in section 5.1.2. The characteristic g-values of the db, h and V signals define the line positions of the signals in all spectra. Furthermore, the isolated asymmetric CE line profile extracted from the multi-frequency EDMR spectra in chapter 4 is used here to describe the current CE line profile: Therefore, the isolated CE profiles at X- and Q-band frequencies (chapter 4) are displayed as a function of the g-value, since this is a frequency-independent representation. Then, these profiles are fitted. The result is an asymmetric fit function which is used to describe the CE line shapes of the current study. We decided to use the X-band fit function for the fit of the low frequency profiles (S- and X-band) and the Q-band fit function for the high frequency profiles (at Q-band and 263 GHz), since the CE profile is a composition of field-independent and field-dependent line width contributions which show different behavior at high and low mw frequencies. We make use of the Q-band instead of the W-band profile, as the Q-band data show a better SNR and thus more significant fit parameters.
The main task of this evaluation is to extract line widths of the individual signals from the EDMR spectra. In a first step, the spin-dependent current response after the pulsed mw excitation is integrated in appropriate time intervals yielding EDMR spectra. Such spectra show under optimum conditions, i.e. significantly different time behavior of the different species, signals dominated by one paramagnetic state. The line width of such signals

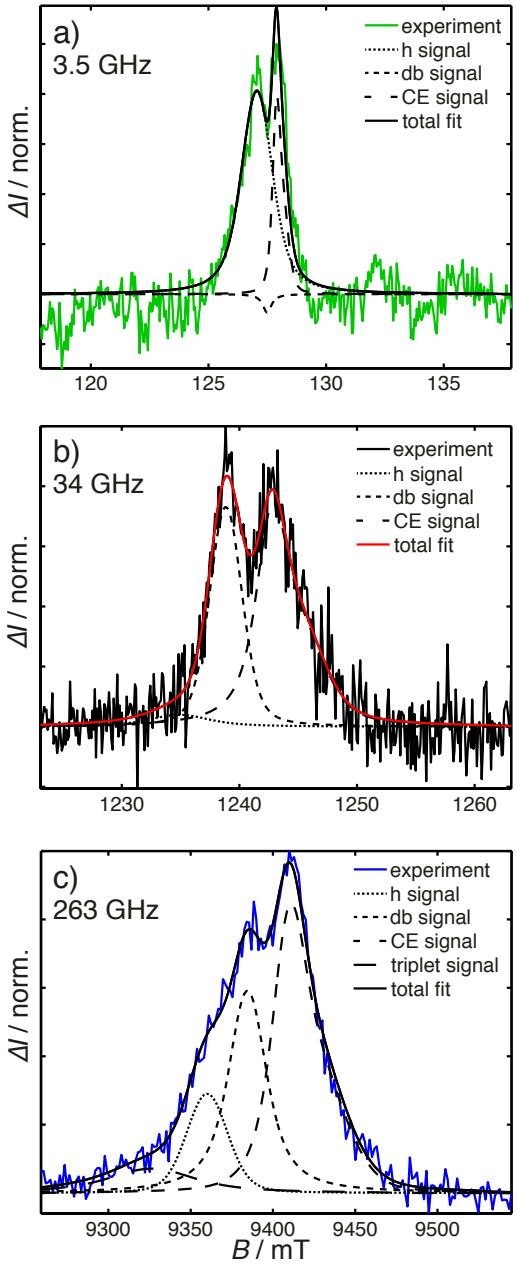

Figure 5.14: Examples of EDMR spectra at S-band, Q-band and 263 GHz used for determination of line widths. a) S-band S_{nat} spectrum showing mainly the CE and h signal. b) Q-band S_{28} spectrum consisting of the db and CE lines. c) 263 GHz S_{nat} spectrum showing four signals.

can then be determined reliably. Unfortunately, in most cases spectra showing two main contributions instead of one are obtained, which is due to similar time constants for some of the four spectral contributions.

In a second step, the obtained spectra are fitted with four line shapes such that best agreement between experimental spectrum and fit is achieved. Three Voigtian lines are used for the db, h and V signals as well as the asymmetric profile for the CE line. The line positions are defined by the g-values of the four EDMR signals. The line widths (restricted to certain intervals) as well as the amplitudes are the free parameters of the fit. Thus, fitting the spectra of all frequency band yields a set of frequency-dependent line widths for every EDMR signal.
Three different examples of fitted EDMR spectra are illustrated in Fig. 5.14. At S-band the integration of the S_{nat} EDMR data between 14.9 and 20.9 μs yields a spectrum mainly consisting of the CE and the h line (Fig. 5.14 a)). Here the S-band line width of the h signal is deduced. The signal dynamics of the Q-band EDMR data of sample S_{28} are convenient to extract spectra showing mainly the db and CE line. The spectrum of the integration interval between 33.9 and 50.9 μs shown here is taken for the deduction of the db line width (Fig. 5.14 b)). Due to the small light intensity available at Q-band, the db as well as the h signal contribute with only small intensities. Hence both line widths can only be deduced with larger uncertainty. Integration of the S_{nat} 263 GHz data between 2.9 and 3.9 μs results in an EDMR spectrum showing all signals with significant contribution. Usage of the asymmetric CE profile as well as the defined line positions of the other signals together with a fit of the line widths in a useful mT-range results in a good fit of the data as seen in Fig. 5.14 c).
The obtained parameter sets of the narrow db, CE and h signals for a particular frequency band can be applied to the spectra of both samples. Within the estimated errors no differences in line widths are observed. The line widths of the broad V signal cannot be transferred from sample S_{nat} to S_{28}, as they are different (see Fig. 5.17, inset). At S- and Q-band the V signal cannot be resolved in the S_{28} spectra due to the small SNR.
Summarizing, the fitting procedure yields four parameter sets describing the four observed EDMR resonances in the spectra of the samples S_{nat} and S_{28} at different mw frequencies. The CE line is well reproduced with the help of the line profile found in chapter 4. The db and the h signals are fitted by symmetric lines of growing line widths at g_{db} = 2.0046 and g_h = 2.0105. The V signal of sample S_{nat} is resolved at all four frequencies and can be described by a line of large width at S-band which further increases as function of the mw frequency. In the following, the results of this fitting procedure are described.

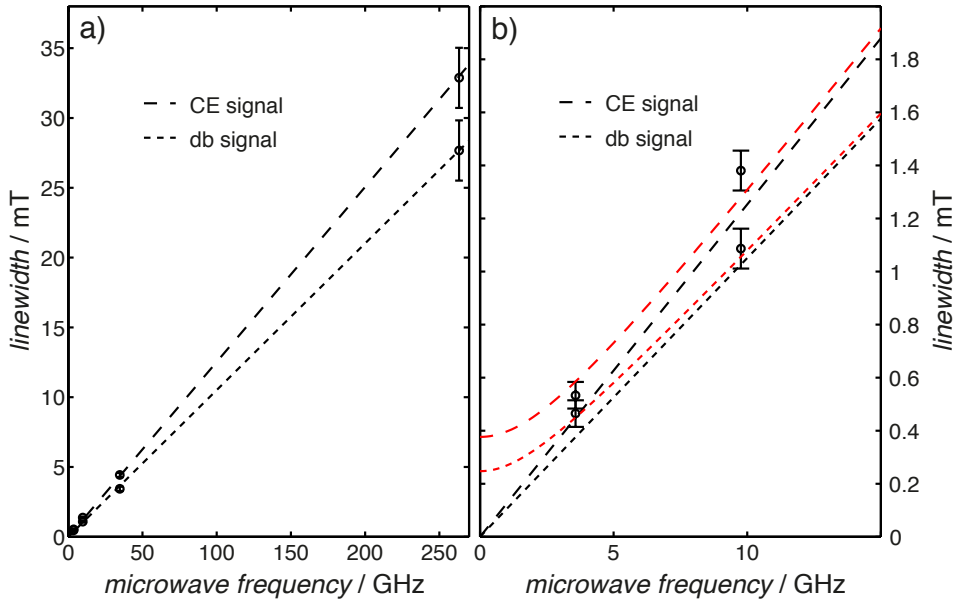

Figure 5.15: Frequency dependence of the S_{nat} CE and db line widths. The extracted widths (FWHM) are shown as data points, the extrapolations of the 263 GHz line widths down to 0 GHz as black lines. a) Frequency range $0 - 263$ GHz. b) The frequency range below 15 GHz is scaled up. The fit results based on Eqn. (5.2) are shown in red lines.

Evaluation of the db and CE Line Widths

The field-dependence of the db and CE line widths (FWHM) of sample S_{nat} are shown in Fig. 5.15 a). The widths increase significantly between the mw frequencies $\nu_0 = 3.5$ GHz and 263 GHz from ≈ 0.5 mT to ≈ 30 mT. The data points can be well described by a linear fit intersecting ≈ 0 mT at 0 GHz. This linearity is indication of a dominant field-dependent part to the line widths. This field-dependent line width is expressed by a g-value range Δg_i. It can be calculated from the slope s_i of the linear fit using

$$s_i = \frac{h}{\beta_e} \frac{\Delta g_i}{g_i^2} \nu_0 \tag{5.1}$$

[124] with the Planck constant h and the Bohr magneton β_e. The results are $\Delta g_{CE} = 0.0070(5)$ for the CE line and $\Delta g_{db} = 0.0059(5)$ for the db line.
The linear dependence of the line width is valid if the field-dependent contribution dominates. Towards low mw frequencies this line width decreases, so that the relative contribution of a field-independent line width grows. Let's assume a convolution of two Gaussian lines. One line has the

field-independent line width $\Delta B_{\mathrm{i}}^{\mathrm{FI}}$, the other one has the field-dependent line width $\Delta B_{\mathrm{i}}^{\mathrm{FD}}(B_0)$, which of course, is also frequency-dependent just by substituting B_0 by $\frac{h}{\beta_{\mathrm{e}} g_{\mathrm{i}}}\nu_0$ resulting in $\Delta B_{\mathrm{i}}^{\mathrm{FD}}(\nu_0)$. The total line width is given by

$$\Delta B_{\mathrm{i}}(\nu_0) = \sqrt{(\Delta B_{\mathrm{i}}^{\mathrm{FI}})^2 + (\Delta B_{\mathrm{i}}^{\mathrm{FD}}(\nu_0))^2}. \tag{5.2}$$

Such an approach in the literature which makes use of this fitting approach is given in Ref. [142]. In Fig. 5.15 b) the frequency range comprising the S- and X-band is shown. The trend of the field-dependent part $\Delta B_{\mathrm{i}}^{\mathrm{FD}}$ of the line widths is illustrated by extrapolating the 263 GHz value down to 0 GHz. It is apparent that the X- as well as the S-band widths lie above the extrapolation. This shows that field-independent contributions play a role at low ν_0. A fit based on Eqn. (5.2) was applied to the data points to take note of this. $\Delta B_{\mathrm{i}}^{\mathrm{FD}}$ was taken from the extrapolation. The results of the fit are displayed as red dashed lines. This fitting approach leads to an improved description of the data points and yields $\Delta B_{\mathrm{CE}}^{\mathrm{FI}} \approx 0.4$ mT as well as $\Delta B_{\mathrm{db}}^{\mathrm{FI}} \approx 0.25$ mT. The quality of these results would be increased significantly if more data points in the low frequency region would be available. This cannot be realized with resonators operating at a single microwave frequency as used here. An alternative approach could be the use of non-resonant designs [143, 144].

After the analysis of the db and CE line width behavior of sample S_{nat} we try to get information about the origin of the field-independent contributions $\Delta B_{\mathrm{CE}}^{\mathrm{FI}}$ and $\Delta B_{\mathrm{db}}^{\mathrm{FI}}$ and try to assign them to hyperfine or spin-spin-interactions by direct comparison of the S- and X-band spectra of the samples S_{28} and S_{nat}.
The spectra of both frequency bands are illustrated in Fig. 5.16. The integration intervals of the current response was chosen in a way to obtain comparable spectra mainly consisting of the db and CE resonances. The CE line is the main contribution in Fig. 5.16 a), whereas the db lines have the higher amplitudes in 5.16 b). At a first glance, the resonances of S_{nat} seem to have larger line widths. However, fitting the spectra of both samples with the deduced parameter set (which is identical for samples S_{28} and S_{nat}) shows that both spectra are well described (Fig. 5.16 c) and 5.16 d)). The impression of larger line widths is a result of different line intensities of the broad V signal (line width at S- and X-band: 10 mT and 19 mT) in the spectra of S_{nat} and S_{28}. Based on identical line widths of the db and CE signals from both samples we conclude that no influence of ^{29}Si hyperfine interaction on the line widths is observed within the achievable SNR. Hence, we

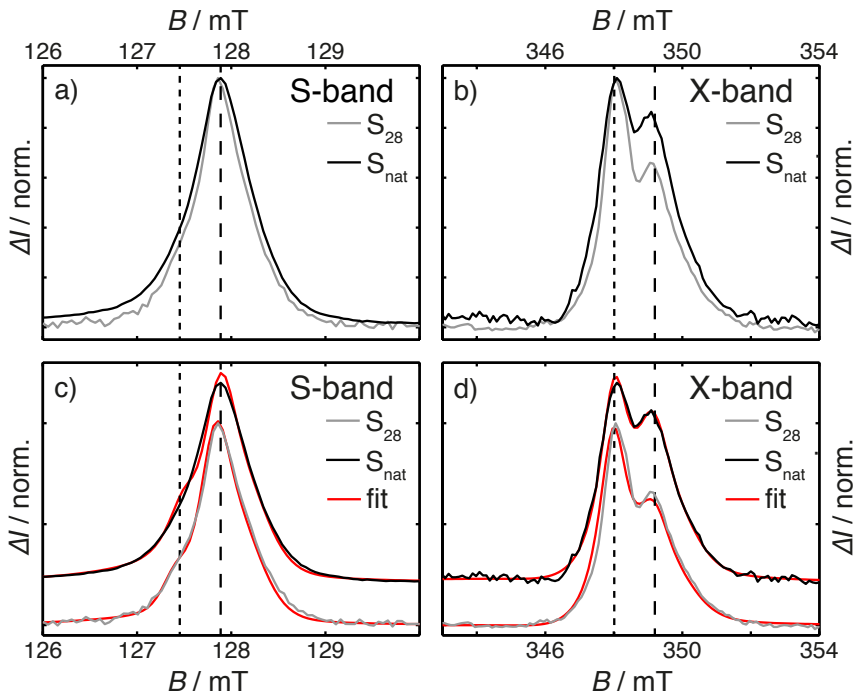

Figure 5.16: Comparison of spectra from samples S_{28} and S_{nat} differing in the i-layer Si isotope composition. The vertical dashed lines indicate the positions of the db and CE resonance. a) and c) Normalized S-band spectra of S_{28} and S_{nat}. b) and d) Normalized X-band spectra of S_{28} and S_{nat}. c) and d) Fit results of all four spectra (vertically shifted).

can assign the field-independent widths to spin-spin interactions.

Evaluation of the h and V Line Widths

The evolution of the h and V line widths as function of the mw frequency is illustrated in Fig. 5.17. The extracted line widths are error-prone, since the signals have broad profiles compared to their small line amplitudes.
Fig. 5.17 shows the development of the h signal line width. The line width of the 263 GHz measurement is used to illustrate the trend of the field-dependent width ΔB_h^{FD} between 0 and 263 GHz. Therefore we assume that the 263 GHz line width is affected only by a negligible part of field-independent width ΔB_h^{FI}. The calculation of Δg_h from the slope of this extrapolation yields $\Delta g_h = 0.0063(5)$. The widths at lower frequencies lie above the trend line. This is indicative for a significant contribution of ΔB_h^{FI}. ΔB_h^{FI} cannot be determined by fitting the data points with the fit function given in Eqn. (5.2), because the X- and Q-band line width seem to converge

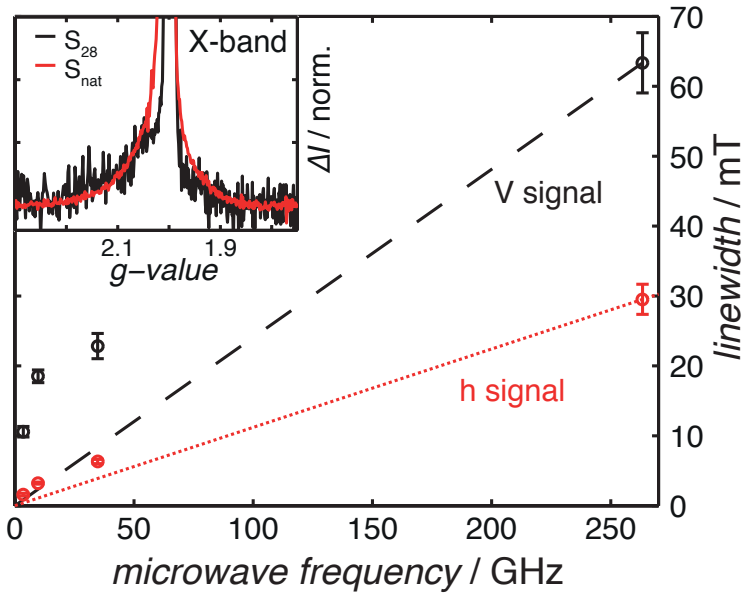

Figure 5.17: Frequency dependence of the h and V line widths (FWHM). The extracted widths as well as the extrapolation of the 263 GHz line width down to 0 GHz are shown. The inset illustrates the V signal in the X-band EDMR spectra of both samples S_{28} and S_{nat}.

to a value of $\Delta B_h^{FI} \approx 3$ mT, whereas the S-band width lies below this threshold. Thus we estimate ΔB_h^{FI} to be ≈ 2 - 3 mT.
Since the same line parameters are applicable to the h signals of both samples, the HFI of ^{29}Si can be ruled out as the reason for this broadening effect. Hence, considerable interaction of neighboring electron spins is assumed as source of the field-independent line broadening.
The proceeding decrease of the line width below 34 GHz could be connected with the influence of fast spin exchange, which can result in an averaging of the effect of dipolar broadening and thus in a reduction of the line width [145, 146]. A detailed understanding of this effect is still missing.
The V signal line width development of sample S_{nat} is illustrated in Fig. 5.17. We find line widths in the range of 10 - 20 mT when approaching low frequencies. This is indicative of a large field-independent contribution. The extrapolation of the 263 GHz line width down to zero yields a field-dependent line width of $\Delta g_V = 0.014(1)$ in the g-value representation. Probably, ΔB_V^{FI} is not negligible at 263 GHz. This results in a too large value of Δg_V which, however, gives a good orientation. The X- and Q-band line widths tend to a field-independent line width of 15 - 20 mT. Again, the S-band value is smaller as already observed for the h signal. Hence we roughly estimate

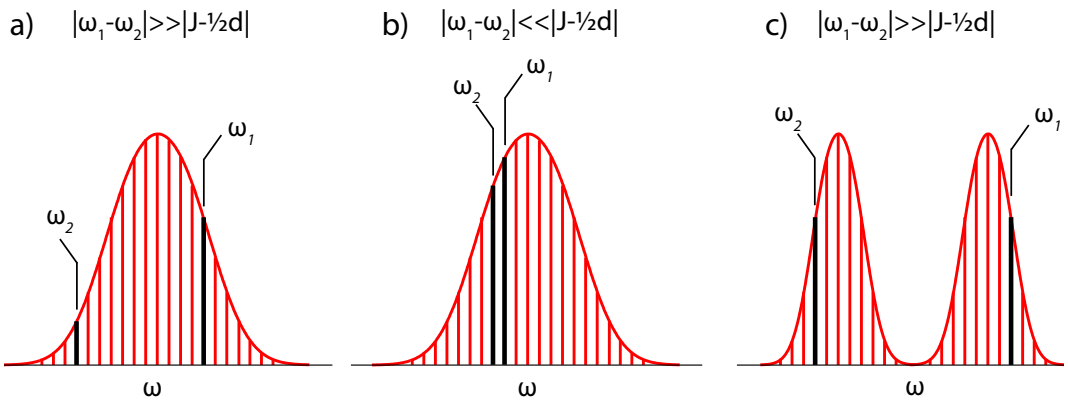

Figure 5.18: Illustration of the two coupling cases considered for the calculation of inter-spin distances. a) Spins are part of the same signal. Weak coupling case ($|J - \frac{1}{2}d| \ll |\omega_1 - \omega_2|$). b) Spins are part of the same signal. Strong coupling case ($|J - \frac{1}{2}d| \gg |\omega_1 - \omega_2|$). c) Spins are part of different signals. Weak coupling case ($|J - \frac{1}{2}d| \ll |\omega_1 - \omega_2|$).

$\Delta B_{\mathrm{V}}^{\mathrm{FI}}$ to be $\approx$ 10 - 20 mT. The line shape of the V signal differs for the samples S_{28} and S_{nat} as shown in the inset of Fig. 5.17. The V line of sample S_{nat} appears with a symmetric profile, whereas the line in the spectrum of S_{28} seems to be asymmetric or shifted to higher g-values. It is not possible to evaluate this aspects in detail, as the V resonance always overlaps with the remaining db, CE and h signals. Hyperfine satellites buried in the broad profile of the V signal could give rise to this discrepancy.
However, the line widths are comparable in both cases so that the main field-independent contribution to the line width is caused by strongly interacting electron spins. The frequency-dependent decrease of $\Delta B_{\mathrm{V}}^{\mathrm{FI}}$ is possibly owing to the influence of spin exchange which could result in a reduction of the detected line widths, as already supposed as explanation for the h line width behavior.

Determination of inter-spin distances

The field-independent line widths $\Delta B_{\mathrm{i}}^{\mathrm{FI}}$ resulting from electron-electron interactions can be related to mean inter-spin distances. In the following a simple model is described how the unresolved broadening can be used to calculate these inter-spin distances.
The basis to detect EDMR is the interaction of two spins in localized states sufficiently close together. The spins will interact via electron-dipolar cou-

pling. Since spin transitions between these localized states take place, wave function overlap and thus exchange interaction plays a role. This means that the spin system considered in this model only consists of coupled spins, uncoupled spins do not contribute. The inter-spin distances will be estimated based on the field-independent line widths $\Delta B_{\mathrm{i}}^{\mathrm{FI}}$ which is fully assigned to dipolar line broadening. However, an influence of the exchange interaction on $\Delta B_{\mathrm{i}}^{\mathrm{FI}}$ exists, but cannot be specified. That is why the calculated inter-spin distances constitute only rough values rather than precise mean distances.
For the determination of the distances from the field-independent line widths three different coupling scenarios have to be regarded. They are shown in Fig. 5.18. Spin-dependent transport processes can involve spins of the same kind giving rise to a single EDMR signal, like e.g. hopping via CE states. A scheme of the resonance line is illustrated in Fig. 5.18 a) and b) consisting of a distribution of narrow lines with slightly different resonance energies ω_{i}. This distribution can be due to unresolved HFI or g-strain. Dipolar broadening is not incorporated in the scheme.
When a spin-dependent hopping process takes place between two spins which significantly differ in there resonance energies (Fig. 5.18 a)) so that the Larmor separation $|\omega_1 - \omega_2|$ is large compared to the electron-electron coupling of both spins $|J - \frac{1}{2}d|$, one speaks about the weak coupling limit.
When a spin-dependent hopping process takes place between two spins which have nearly identical resonance energies (Fig. 5.18 b)) so that the Larmor separation $|\omega_1 - \omega_2|$ is small compared to the electron-electron coupling of both spins $|J - \frac{1}{2}d|$, one speaks about the strong coupling limit.
When a spin-dependent transport process takes place between two spins which are part of different signals, like e.g. hopping via a-Si:H conduction band tail states (e states) and phosphorus donor states (P states) (see chapter 4) the Larmor separation $|\omega_1 - \omega_2|$ is large compared to the electron-electron coupling of both spins $|J - \frac{1}{2}d|$ when the signals do not overlap. This is shown in Fig. 5.18 c). These conditions are considered as weak coupling conditions as well.
This means, dependent on the Larmor separation of the spins forming the EDMR spin pair, weak or strong coupling conditions apply. Since the Pake patterns under both conditions differ (see Fig. 2.2) and the their impact on the field-independent line width $\Delta B_{\mathrm{i}}^{\mathrm{FI}}$ is not known, the $\Delta B_{\mathrm{i}}^{\mathrm{FI}}$ will be evaluated assuming both cases. This comprises the CE signal, the h signal as well as the db signal resonance. The V signal which is connected with $\Delta B_{\mathrm{V}}^{\mathrm{FI}} \approx 10 - 20$ mT will be evaluated assuming the strong coupling limit. In

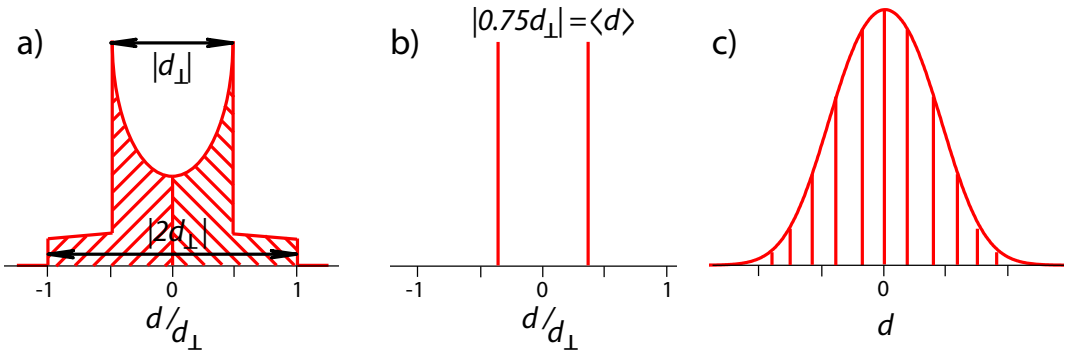

Figure 5.19: a) A powder pattern of a dipolar spectrum called Pake pattern is shown for the case of weak coupling. The positive and negative branches are shaded. b) Doublet $D(r, \langle d \rangle)$ of average splitting determined from Pake pattern (a). c) Variation of spin-spin distances leads to a distribution $M(\langle d \rangle)$ of doublet spectra $D(r, \langle d \rangle)$.

the following, the calculation of the inter-spin distances from the line width $\Delta B_{\mathrm{i}}^{\mathrm{FI}}$ is presented.

Weak coupling case Two unpaired electron spins located in neighboring localized states and separated by distance r are assumed to be weakly coupled ($|J - \frac{1}{2}d| \ll |\omega_1 - \omega_2|$) to each other through electron-electron dipolar interaction. The considered dipolar coupling Hamiltonian is given by Eqn. (2.8):

$$\mathcal{H}_{\mathrm{dd}} = \frac{\mu_0}{4\pi\hbar} g_1 g_2 \beta_e^2 \left[\frac{\mathbf{S}_1 \cdot \mathbf{S}_2}{r^3} - \frac{3(\mathbf{S}_1 \cdot \mathbf{r})\mathbf{S}_2 \cdot \mathbf{r})}{r^5} \right]$$

with the g-values of the interacting spins g_1 and g_2. The angular dependence of this interaction can be expressed by the coupling constant d (Eqn. (2.13)):

$$d = -\frac{\mu_0 g_1 g_2 \beta_e^2}{4\pi\hbar r^3} (3\cos^2\theta - 1)$$

as described in Sec. 2.1.2 which becomes

$$d_\perp = 2\pi\nu_\perp = \frac{\mu_0 g_1 g_2 \beta_e^2}{4\pi\hbar r^3}$$

for $\theta = 90°$.

The investigated solar cells are considered as powder samples so that in general EPR powder spectra are measured. Hence, the electron dipolar interaction gives rise to a powder spectrum as well. This is called Pake pat-

tern [147]. The Pake pattern of a weakly coupled spin pair is shown in Fig. 5.19 a). Since such distinct patterns are not resolved in the EDMR spectra, we cannot deduce precise values of inter-spin distances. Nevertheless, we will calculate mean distances based on two assumptions:
First, we consider the mean dipolar splitting $\langle d \rangle$ in the Pake pattern. This is determined by calculating the splitting of the centers of the positive and negative branches symbolized by the shaded areas in Fig. 5.19 a). This is obtained by calculating

$$\langle d \rangle = \int_0^{\pi} \sqrt{d(\theta)^2} \cdot p(\theta) d\theta$$

where $d(\theta)$ is the dipolar interaction function and $p(\theta)d\theta$ the weight function which describes the fraction of spin-spin coupling axes occurring between the angles θ and $\theta + d\theta$ in a powder sample. Integrating over all values of θ yields

$$\begin{aligned} \langle d \rangle &= \int_0^{\pi} \sqrt{(d_{\perp}(3\cos^2\theta - 1))^2} \cdot \frac{1}{2} \sin\theta d\theta \\ &= 0.75 d_{\perp} = 0.75 \frac{\mu_0}{4\pi\hbar} \frac{g_1 g_2 \beta_e^2}{r^3} \end{aligned} \tag{5.3}$$

[148] as shown in Fig. 5.19 b). Thus, the spectrum consists only of a doublet $D(r, \langle d \rangle)$ instead of a complete Pake spectrum.
Second, we assume a distribution of inter-spin distances r which can be described by the weighted sum $M(\langle d \rangle)$ of the doublet spectra $D(r, \langle d \rangle)$ over the distribution of distances $P(r)$:

$$M(\langle d \rangle) = \sum_r P(r) D(r, \langle d \rangle). \tag{5.4}$$

In first approximation we will assume that the distribution of distances $P(r)$ results in a Gaussian shape of $M(\langle d \rangle)$ as shown in Fig. 5.19 c). The line width $\langle d \rangle_{\mathrm{av}}$ of the Gaussian profile is used to calculate an average distance $\langle r \rangle_{\mathrm{av}}$ of the interacting spins by

$$\langle r \rangle_{\mathrm{av}} = \left(0.75 \frac{\mu_0}{4\pi\hbar} \frac{g_1 g_2 \beta_e^2}{\langle d \rangle_{\mathrm{av}}} \right)^{1/3}. \tag{5.5}$$

We use the FWHM values $\Delta\nu_i^{\mathrm{FI}} = \frac{\beta_e g_i}{h} \Delta B_i^{\mathrm{FI}}$ of the line width evaluation as

$\Delta\nu_{\mathrm{i}}^{\mathrm{FI}} = \langle d \rangle_{\mathrm{av}}/2\pi$, so that finally

$$\langle r \rangle_{\mathrm{av}}/\mathrm{nm} = \left(\frac{9.735 \cdot g_1 \cdot g_2}{\Delta\nu_{\mathrm{i}}^{\mathrm{FI}}/\mathrm{MHz}} \right)^{1/3}. \tag{5.6}$$

Strong coupling case In this strong coupling (sc) regime ($|J - \frac{1}{2}d| \gg |\omega_1 - \omega_2|$) a distance determination is possible, since the exchange coupling does not affect the allowed EPR transitions. The splitting of the resonance lines $\Delta\omega$ depends on the dipolar coupling only. Under strong coupling conditions the doublet is split by $\frac{3}{2}d$ (see Sec. 2.1.2) so that:

$$d^{\mathrm{sc}} = \frac{3}{2}d = -\frac{3}{2}\frac{\mu_0}{4\pi\hbar}\frac{g^2\beta_{\mathrm{e}}^2}{r^3}(3\cos^2\theta - 1) \tag{5.7}$$

with $g_1 \approx g_2 = g$. Average distances can be estimated from the width of dipolar couplings, as already presented for the weak coupling case:

$$\langle r \rangle_{\mathrm{av}} = \left(\frac{9}{8}\frac{\mu_0}{4\pi\hbar}\frac{g^2\beta_{\mathrm{e}}^2}{\langle d_{\mathrm{av}}^{\mathrm{sc}} \rangle} \right)^{1/3}. \tag{5.8}$$

We obtain

$$\langle r \rangle_{\mathrm{av}}/\mathrm{nm} = \left(\frac{14.60 \cdot g^2}{\Delta\nu_{\mathrm{i}}^{\mathrm{FI}}/\mathrm{MHz}} \right)^{1/3}. \tag{5.9}$$

Mean inter-spin distances of interacting db, h and CE centers We obtain $\langle r \rangle_{\mathrm{av}} \approx 1.5 - 1.8$ nm and $1.7 - 2.1$ nm as rough values for average inter-spin distances of CE and db centers, respectively. For g_{i} we took the CE or db g-values, since the spin-spin interaction is assumed to take place between neighboring centers of the same kind. The inter-spin distances of interacting spin in h centers range between $\langle r \rangle_{\mathrm{av}} \approx 0.9$ and 1.1 nm.

Mean inter-spin distance of strongly coupled spins in a V complex Using the FWHM values $\Delta\nu_{\mathrm{V}}^{\mathrm{FI}} = \frac{\beta_{\mathrm{e}} g_{\mathrm{V}}}{h}\Delta B_{\mathrm{V}}^{\mathrm{FI}} = \langle d_{\mathrm{av}}^{\mathrm{sc}} \rangle/2\pi \approx 280 - 560$ MHz (corresponding to $10 - 20$ mT) of the line width evaluation and the g-value

parameter	CE signal	db signal	h signal	V signal
Δg_i	0.0070(5)	0.0059(5)	0.0063(5)	<0.014(1)
ΔB_i^{FI} / mT	≈ 0.4	≈ 0.25	2 - 3	10 - 20
$\langle r \rangle_{av}$ / nm	$\approx$ 1.5-1.8	$\approx$ 1.7-2.1	0.8-1.1	0.47 - 0.60

Table 5.3: Summary of the field-dependent (Δg_i) and field-independent (ΔB_i^{FI}) line width contributions of the samples S_{28} and S_{nat}. Furthermore, the estimated mean inter-spin distances $\langle r \rangle_{av}$ are given. The results of the V line are based on measurements of sample S_{nat}.

g_V results in

$$\langle r \rangle_{av} = \left(\frac{14.60 \cdot g_V^2}{\Delta \nu_V^{FI} / \text{MHz}} \right)^{1/3} = 0.47 \ - \ 0.60 \, \text{nm} \tag{5.10}$$

which is in range of the c-Si lattice constant of $a = 0.543$ nm. For the estimation of a lower limit of spin-spin distances we go back to Eqn. (5.7) and assume the case of $\theta = 0$. Then $(3\cos^2\theta - 1) = 2$ and we obtain

$$r = \left(3 \frac{\mu_0}{4\pi\hbar} \frac{g_V^2 \beta_e^2}{d^{sc}} \right)^{1/3} = \left(\frac{38.94 \cdot g_V^2}{\Delta \nu / \text{MHz}} \right)^{1/3} . \tag{5.11}$$

Under these conditions the largest splittings are observed in the spectrum which determine the outermost wings of the broad V line. In Fig. 5.21 we can estimate a total width of the V line between $\Delta B = 30$ and 60 mT ($\Delta \nu = 840 - 1680$ MHz) at S- and X-band. This yields inter-spin distances of

$$r = \left(\frac{38.94 \cdot g_V^2}{\Delta \nu / \text{MHz}} \right)^{1/3} = 0.46 \ - \ 0.58 \, \text{nm} \tag{5.12}$$

which is exactly the inter-spin distance found above.

Discussion

The CE and db lines The CE as well as the db EDMR signals are dominated by field-dependent line widths. Only at S- and X-band a small deviation from the linearity in ν_0 points to a convolution of the field-dependent line with field-independent broadening effects. This is supported by the reduced spectral resolution when going from X- to S-band (Fig. 5.12 and Fig.

5.13).
The CE line broadening based on the Zeeman interaction was already analyzed in chapter 4. The revealed asymmetric profiles were incorporate in the present fit procedures and lead to consistent results. The origin of the field-dependent CE line profile connected with its asymmetry was suggested to be a size distribution of Si crystallites accommodating the CE centers. These crystallites affect the g-value of individual CE centers via confinement effects and lead to an asymmetric g-value distribution in the spectra.
The db defects are assumed to be located in rather disordered parts of the microcrystalline material, e.g. at grain boundaries [129–131]. Thus, the field-dependence of the db line is caused by g-strain, that means by a distribution of g-values arising from an inhomogeneity in the local environment of the individual paramagnetic defect. It can be said, that the db line only consists of line widths based on Zeeman interaction at Q-band frequencies and above. However, at Q-band no g-anisotropy of the db resonance is resolved within SNR, because the g-strain of 0.0059(5) is the major effect washing out any anisotropy. Here a detailed EPR study as performed on the amorphous Si dangling bond [15] would finally answer the question if g-anisotropy of the μc-Si:H db can be resolved.
The field-independent part of the db and CE lines was shown to be insensitive to a change of the Si isotope composition of the solar cell i-layer. This allows to draw two conclusions.
First, the line broadening due to unresolved hyperfine interactions between CE and db centers and ^{29}Si nuclei is smaller than ≈ 0.1 mT. This value describes the threshold of widths which can be deduced reliably from the spectra. Such small and unresolved HFI are an indication of wide spread electron wave functions in disordered systems. In such a case the spin density is distributed over several nuclei. The smaller the isotropic hyperfine constants $a_0 = \frac{8\pi}{3} g g_n \beta_e \beta_n |\psi(0)|$ [149] is, the more delocalized is the spin density. Clearly visible satellites due to large HFI were not found in the EDMR spectra of both resonances. However, regarding the db resonance EPR X-band studies of μc-Si:H powder samples revealed ^{29}Si hyperfine satellites split by ≈ 10 mT [150].
We conclude that the CE center which is a light-activated center near the conduction band is connected with a delocalized wave function, whereas the db centers are rather located paramagnetic states.
Second, the main contribution of the field-independent line width is caused by weakly interacting electron spins in the material. These spins are sepa-

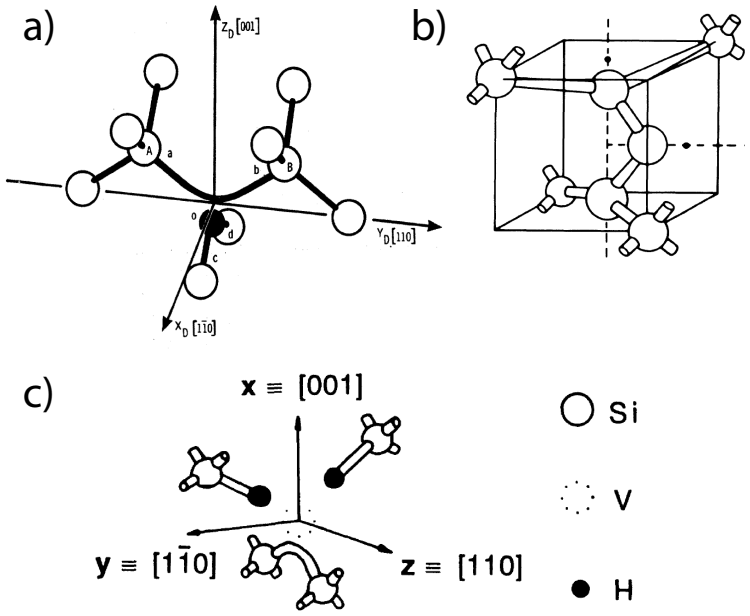

Figure 5.20: Models of three different defect complexes are shown. a) Electronic structure of the one-vacancy-oxygen center. The scheme is taken from Ref. [151], b) Defect model of the two-interstitialcy complex. Illustration from Ref. [152], c) Model of the HVH center from Ref. [153].

rated by calculated average distances of $\langle r \rangle_{\mathrm{av}} \approx 1.5 - 1.8$ nm for interacting CE centers and $\langle r \rangle_{\mathrm{av}} \approx 1.7 - 2.1$ nm for interacting db centers when neglecting exchange interaction. The observation of spin-spin interaction is plausible, since the spins interact in spin-dependent processes which give rise to the observed resonant changes of the sample conductivity. A further possibility to demonstrate the existence of spin-spin processes is the measurement of EDMR spin Rabi nutation as shown later.

The h and V lines The h and V signals show line width developments clearly deviating from a linear behavior contrary to the narrow resonances discussed above. Considerable field-independent line width contributions were found which were assigned to electron spin-spin interaction. Although the field-independent line width of the h signal is negligible at 263 GHz, no g-anisotropy could be detected because the resonance is strongly overlapping with EDMR lines nearby (see Fig. 5.14) and is strongly affected by the influence of g-strain.
The field-independent interaction of the V signal is especially large, so that even at 263 GHz a significant influence occurs. Hence, a possible g-

defect model	spin state	detection	(g_x, g_y, g_z) or $(g_\parallel, g_\perp)$	(D_x, D_y, D_z) or $(D_\parallel, D_\perp)$ or D	Ref.
VO	$S = 1$	EPR	(2.0058, 2.0076, 2.0102)	(-657.6, 350.4, 307.2) MHz	[151, 154]
VO	$S = 1$	ODMR	(2.013, 2.015, 2.011)	(339.0, 290.4, -629.2) MHz	[155]
HVH	$S = 1$	ODMR	(2.002, 2.005, 2.002)	(-348.5, 302.5, 651.0) MHz	[153, 156]
Si_iSi_i	$S = 1$	EPR	(2.0064, 2.0066)	(57.0, 28.2) MHz	[152, 157]
V_4	$S = 1$	EPR	(2.0009, 2.0101, 2.0099)	(-45.7, 23.3, 22.4) MHz	[152, 154, 158]
C_s-Si_i-C_s	$S = 1$	SDR	(2.0076, 2.0030)	1207 MHz	[159, 160]
2C+2V	$S = 1$	SDR	(2.005, 2.012, 2.027)	($\pm$ 984, $\mp$ 286, $\mp$698) MHz	[159, 160]
VP	$S = 1/2$	EPR	(2.0005, 2.0112, 2.0096)	-	[161]
VB	$S = 1/2$	EPR	(2.0011, 2.0052, 2.0090)	-	[162]

Table 5.4: Examples of defect states in irradiated crystalline silicon. Their g-principal values and dipolar coupling parameters are given. The names of the defect models are VO: vacancy-oxygen complex, HVH: di-hydrogen-vacancy complex, Si_iSi_i: two-interstitialcy complex, V_4: planar tetra vacancy chain, C_s-Si_i-C_s: substitutional carbon-interstitial silicon-substitutional carbon complex, 2C+2V: di-carbon + di-vacancy complex, VP: lattice vacancy adjacent to a substitutional phosphorus, VB: vacancy trapped by substitutional boron. SDR = spin-dependent recombination.

anisotropy of the V line is hard to resolve.
The line broadening of the h signal is due to the interaction of neighboring spins in h centers which are separated by $\langle r \rangle_{\mathrm{av}} \approx 0.8 - 1.1$ nm. We point out that this is an estimated value, as information about the influence of exchange coupling are missing.
Coupling strengths of $\approx 10 - 20$ mT as found for the V signal are a consequence of very strong spin-spin interactions, much stronger than the coupling strengths observed for the other narrow EDMR resonances. We think that this is connected with a marked structural difference of this paramagnetic center. Findings in the literature regarding EPR investigations on microcrystalline silicon which report about such broad signals are rare. Only Boulitrop et al. [135, 136] report about ODMR measurements of μc-Si:H samples and resolved a signal at g = 2.016 of 10 mT width at X-band to the best of our knowledge. It was assigned to triplet excitons formed of strongly coupled electron spins.
Extending the search for explanations to EPR studies of induced defects in electron- and neutron-irradiated crystalline silicon reveals a large variety of paramagnetic structural sites which show properties of $S = 1$ states [163]. Such lattice defects could, of course, be part of μc-Si:H material, as the sample deposition process from the gas phase will produce amorphous Si as well as crystallites containing arbitrary lattice imperfections. A collection of such defects is given in Tab. 5.4. The so-called *VO center*, for example, belongs to the group of (oxygen plus vacancy)-type defects [151, 163, 164]. Two of four Si atoms of this complex are bridged via an oxygen atom, whereas the remaining two atoms are vacancy-brigded as shown in Fig. 5.20 a). This photo-excited triplet center shows a large angular-dependent zero-field splitting which could give rise to a resonance of line width in the range of 10-20 mT, when measured in powder samples. In addition, Wang et al. derived a g-matrix with principal values around $g = 2.013$ from ODMR data [155] which is in quite good agreement with the g-value found here ($g_{\mathrm{V}} = 2.017$).
The *HVH complexes* (di-hydrogen-vacancy complexes) in c-Si, where H atoms passivate two of the four dangling bonds, show ODMR spectra dominated by the characteristic zero-field splitting [153, 156]. The zero-field splitting parameters are nearly identical to that of VO centers underlining that they provide a unique fingerprint of a triplet state's geometry. This is apparent when comparing the vacancy structures in Fig. 5.20 a) and c). The HVH complex could be of special relevance, because hydrogen is part of many

gases used for the deposition, so that dangling bonds can be passivated by hydrogen atoms.
An example for $S = 1$ triplets with small zero-field coupling parameters are Si_iSi_i *complexes* (two-interstitialcy complexes) [158]. Here the splittings are in the range of 1-2 mT. A scheme of this site is given in Fig. 5.20 b).
These three defect complexes constitute possible candidates for the broad triplet signal which is called *V signal* here, referring to the suggested *vacancy* complexes. This interpretation is further corroborated by the following points: ODMR studies on the VO and HVH centers illustrate the participation of these sites in spin-dependent processes [153, 155] which is necessary for the observation in ODMR and EDMR experiments. In all these cited studies the EPR spectra show narrow lines because of the crystalline structure of the samples. In the microcrystalline samples investigated here an overall crystalline structure is substituted by an agglomeration of randomly oriented crystallites which give rise to EPR powder patterns. Hence, the broad signal at $g = 2.017(1)$ observed here can be caused by different structural defects in their $S = 1$ triplet state. Their random orientation and the site-to-site variation of zero-field splitting parameters lead to the broad featureless EDMR line. The derived inter-spin distances of the V center lie in the region of distances calculated for VO centers ($\approx 0.4 - 0.6$ nm) [158] as well as for HVH centers due to the similar structure [153, 156]. The distances are in range of the second nearest neighbors which is immediately clear when taking a look on the structures in Fig. 5.20. Which types of vacancies are involved could be further investigated with the help of ESEEM experiments. They allow an access to information about HFI of nuclei which are part of the complex and could help to identify its structure.

Spectral Resolution All these insights taken together, allows to evaluate the spectral resolution of the complete EDMR spectrum. The line profiles of the db, CE and h signals are mainly characterized by field-dependent effects at Q-band and above. This means that no further gain in resolution and, connected with this, information gain regarding magnetic parameters is achieved when going to higher mw frequencies.
Including the broad V signal into the EDMR spectrum results in wide-range changes of the spectrum as function of ν_0 due to its large field-independent line width. This is illustrated in Fig. 5.21. At S- and X-band frequencies (3.5 and 9.7 GHz) the broad V signal defines the high and low field wings of the spectrum. The other resonances appear as sharp needles in the center.

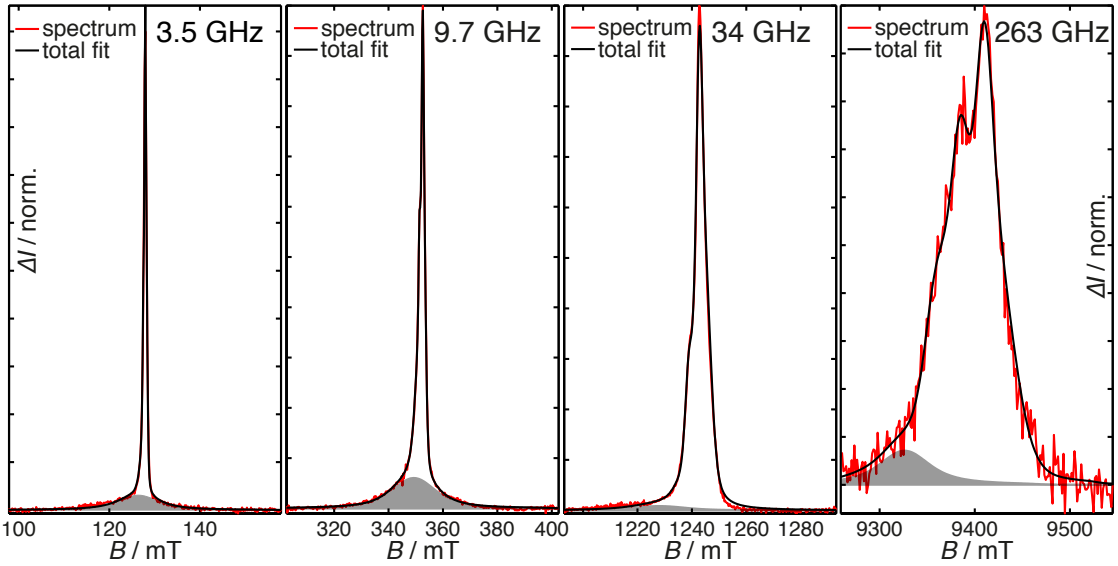

Figure 5.21: The field dependence of the V signal within the EDMR spectrum is illustrated at $\nu_0 = 3.5$, 9.7, 34 and 263 GHz. The fit of this broad line is highlighted by the gray shaded area. The total fit is plotted as a black line.

At Q-band, one a shift of the V resonance is observed to the low field side of the spectrum caused by the reduction of the relative part of $\Delta B_{\mathrm{V}}^{\mathrm{FI}}$ in the total line width compared to $\Delta B_{\mathrm{V}}^{\mathrm{FD}}$. Finally, all four lines show comparable widths determined by the field-dependent interactions at 263 GHz. The V line still spreads out to the center of the spectrum, but has only a small overlap with the CE line.

High-frequency EDMR constitutes a promising approach when hyperfine interactions and spin-spin interactions in form of unresolved broadening effects or as clearly resolved split lines limit the spectral resolution of neighboring resonances or hamper the access to g-anisotropies at low fields. If g-strain, g-anisotropy or other effects based on Zeeman interaction dominate already at moderate mw frequencies no further gain in information is expected at higher mw bands.

Multi-frequency EDMR is especially helpful to decompose the spectra into the different subspectra, which can be due to field-dependent and field-independent interactions.

Summary

We have applied the promising approach of multi-frequency EDMR measurements to μc-Si:H p-i-n solar cells of two different silicon isotope compositions. On the one hand, the intrinsic layer of the cells was made of μc-Si:H material with natural Si isotope abundance. On the other hand, the i-layer consisted of ^{28}Si-enriched μc-Si:H material.
The EDMR measurements at different mw frequencies between 3.5 to 263 GHz together with the characteristic signal dynamics allowed the separation of all four signals and their field-independent and field-dependent line width contributions. It could be shown, that all signals are strongly influenced by *g*-strain so that no *g*-anisotropy or line asymmetry could be resolved except for the CE line as already shown in chapter 4.
The major contribution of the detected field-independent line widths was unambiguously assigned to electron spin-spin interactions by studying samples of μc-Si:H material with and without the nuclear spin carrying isotope ^{29}Si. A line broadening due to unresolved ^{29}Si HFI could not be found within the achievable SNR. But we assume that small hyperfine couplings to neighboring ^{29}Si nuclei exist.
The analysis of the widths of the spin-spin couplings yielded detailed insights into the microscopic structure of the centers: The dipolar broadening of the CE and db lines was utilized for the calculation of inter-spin distances between neighboring centers delivering $1.5 - 1.8$ nm and $1.7 - 2.1$ nm, respectively. The dipolar broadening of interacting h centers yielded $0.8 - 1.1$ nm. Furthermore, the V signal was assigned to paramagnetic vacancy complexes in $S = 1$ triplet states based on the large line widths. In this strong coupling regime an inter-spin distance of ≈ 0.5 nm was estimated and related to inter-spin distances of the suggested vacancy centers. Finally, the development of the four-component spectrum between 3.5 GHz and 263 GHz was analyzed in terms of spectral resolution.
Despite the strong overlap of four different resonances in all spectra which are, in addition, considerably affected by broadening effects, detailed information about the individual paramagnetic centers could be gained. This fact elucidates the great advantage of a combined study of multi-frequency experiments applied to isotopically controlled samples.

5.3 Field-Dependent Electrically Detected ESEEM

The application of different EDMR techniques allowed us in the previous sections to decompose the complex multi-component spectra of the μc-Si:H thin-film solar cells into the individual spectral contributions comprising conduction band tail (CE) states ($g_{\mathrm{CE}} = 1.9978$) in the crystalline regions, dangling bond (db) defects ($g_{\mathrm{db}} = 2.0046$) and holes in valence band tail (h) states ($g_{\mathrm{h}} = 2.0105$) in the disordered parts as well as the vacancy (V) center ($g_{\mathrm{V}} = 2.017$).
The question about the microscopic structures accommodating the different defect states is addressed in the following section. The simple cw and π-pulse experiments so far were not capable to deliver details about the nuclear environment of the paramagnetic centers. Thus, we make use of the electron spin echo envelope modulation (ESEEM) method which gives information about the spin-carrying nuclei in the vicinity of the defect states via the modulation of the echo amplitude. This ESEEM experiment will be applied to the complete spectral range so that structural insights regarding all paramagnetic center are obtained. On the background of the previous sections we will address the following questions:
First, which centers can be assigned to amorphous regions and which to crystalline regions? ESEEM can help to distinguish between both regions by looking for proton frequencies, since protons are believed to be part of disordered lattice structures whereas they are not found in crystalline structures of the μc-Si:H material [113]. On the basis of this approach the CE center was ascribed to the crystalline part of the material [25, 116].
Second, how does the microscopic environment of the V center look like? Is it possible to descriminate between the suggested VO as well as HVH vacancies via the detection of proton frequencies in the ESEEM data?
Third, which signal shows indications of doping atoms? Both elements phosphorus and boron used for the n- and p-doping, respectively, have a high abundance of spin-carrying isotopes (see Tab. 2.1) which should give rise to ESEEM signals. This question is of special interest, since no phosphorus hyperfine signals were found in the EDMR spectra of the current sample (n-μc-Si:H layer), whereas these signals were clearly measured in the spectra of the sample studied in chapter 4 (n-a-Si:H layer). In various EPR studies dealing with n-μc-Si:H [110, 113, 130] no phosphorus signals

were found.

Experiment

All measurements within this ESEEM study are performed at $T = 5$ K. The solar cell is operated under reverse bias conditions ($U = 1$ V) delivering $I_{ph} \approx 20$ µA. At first, field spectra of the sample between 330 and 370 mT as well as 300 and 400 mT are measured by means of a field-swept echo (FSE) experiment to display narrow and broad resonances (see Fig. 5.22 a)). The spin echo is excited by the Hahn echo pulse sequence $\pi/2 - \tau_1 - \pi - \tau_2 -$ echo with $\pi/2$- and π-pulses of 10 and 20 ns length, respectively. The inter-pulse delay is $\tau_1 = 60$ ns. For the electrical detection a $\pi/2$ read out pulse is added at the time τ_2 of echo formation ($\tau_2 = 70$ ns). 50 µs of the transient current response after this pulse sequence are detected. Since the width of the echo (≈ 25 ns FWHM) is broader than the detection pulse ($t_p = 10$ ns), effects of line broadening are observed (see Sec. 3.3). Nevertheless, it is important to perform the field-swept echo experiment with these pulse lengths, since the following field-swept ESEEM experiment makes use of the same pulse sequence. In this way, we are able to compare line widths from the FSE and from the ESEEM experiment.
Afterwards, ESEEM traces are recorded in the central range of the field spectrum between 342.2 and 354.2 mT. In addition, a trace at 330.5 mT is recorded, as here only the broad V signal contributes. The ranges are indicated by the gray shaded regions in Fig. 5.22 a). The applied pulse sequence is, again, the Hahn echo sequence. The $\pi/2$- and π-pulse lengths are the same as in the FSE experiment. The inter-pulse delay τ_1 is incremented between 0.06 µs and 4.06 µs to scan the echo modulations. Therefore the detection pulse delay $\tau_2 = \tau_1 + 10$ ns is shifted accordingly. For the data acquisition the transient current response after the pulse sequence is directly integrated in a time interval of $2 - 6$ µs and detected as function of τ_1. This integration window is chosen to yield the highest signal quality. Further details about the performed experiments are given in Sec. 3.3.

Postprocessing

In this study we direct our attention to the investigation of the nuclear environment of the paramagnetic defects via the detection of echo modulations.

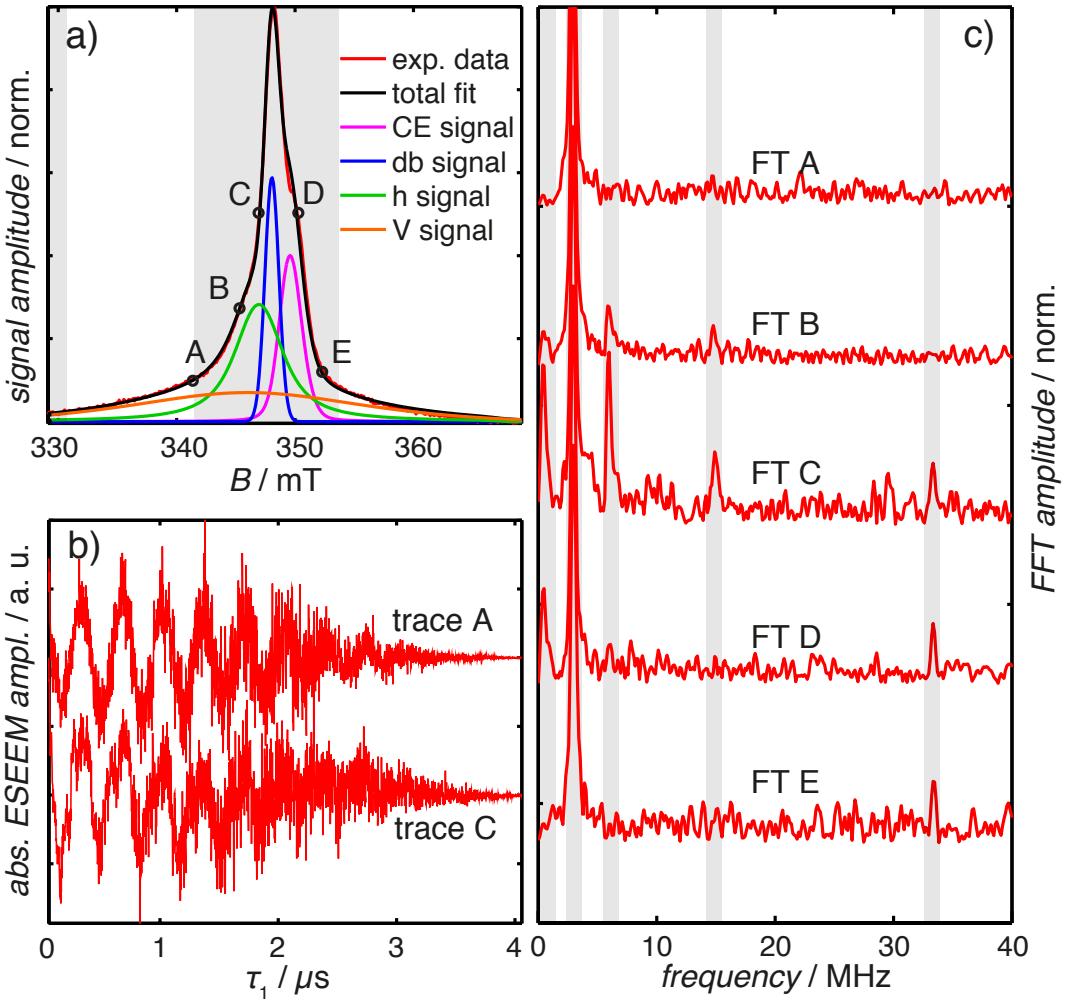

Figure 5.22: a) The echo-detected EDMR spectrum is shown together with the fit results. The gray regions indicate the field intervals for the ESEEM experiment. At the field positions labelled with capital letters A to E ESEEM spectra are shown in b) and c). b) Post processed ESEEM time traces at the field positions A and C are displayed (data are vertically shifted). The traces are dominated by an oscillation of $\approx$ 300 ns period. Trace C shows additional fast and slow modulations. c) FT spectra of the traces measured at field positions A to E are illustrated. The spectra are normalized and vertically shifted for the sake of clarity. The gray shaded vertical bars mark positions of detected frequency contributions. The dominant oscillation is observed at a frequency of $\approx$ 3 MHz.

Hence, we want to assign the nuclear frequencies in the ESEEM traces to the signals in the field spectra. For this it is necessary to know positions and widths of the individual signals. This knowledge can be obtained by decomposing the field-swept echo spectrum with the help of the signal dy-

namics. The decomposition strategy already employed in Sec. 5.1.2 consists of two steps.
In the first step, the EDMR spectrum at a fixed time after the pulse sequence is fitted to obtain a set of line parameters. The fit functions comprise three symmetric Voigtian lines for the h, db and V signals as well as the asymmetric CE profile. These four functions are centered at the field positions defined by the signals' g-values (see Tab. 5.3). The line widths extracted in Sec. 5.1.2 are used as starting parameters. In the fit procedure, the line positions are restricted to small intervals of $\approx$ 0.1 mT width, whereas the line widths are allowed to vary within larger ranges due to the broadening effects of the echo experiment. The signal amplitudes are free parameters. As a result we get a parameter set describing the EDMR spectrum.
In the second step, the fit procedure based on this set is repeated for spectra at various times after the pulse sequence. All parameters except for the amplitudes are fixed in this step. This helps to crosscheck the found line widths.
Fig. 5.22 a) shows the FSE reference spectrum. It was obtained by integrating the transient current response in a time interval of $2 - 6$ µs. This integration interval is used, since the ESEEM data were acquired in the same time window. The results of the fit are illustrated and fully describe the spectrum.
Before evaluating the ESEEM data it is necessary to post process the time traces. All traces are dominated by an exponential echo decay due to spin-spin-relaxation. The echo modulation is only visible as a rather small effect on top of this decay. First, the time traces are fitted with a biexponential function yielding reliable results. Then, the traces are divided point by point by this fit function to remove the echo decay background. Polynomial functions are often employed to remove the non-modulating background. We reject to use a polynomial for the fit, since it can create artifacts or suppress low frequency contributions. The remaining offset is subtracted so that the oscillation takes place around zero. Due to the division step the data noise is strongly enhanced for times larger 2.5 µs in the traces. This would lead to perturbing side-bands in the FT spectra. Hence, we apodize the traces by a Kaiser window function to damp the noise level at times $>$ 2.5 µs. Zero filling of the time traces is not necessary. Two examples of ESEEM traces post processed in that way are shown in Fig. 5.22 b). Finally, fast-Fourier transformation (FFT) is applied to all traces.

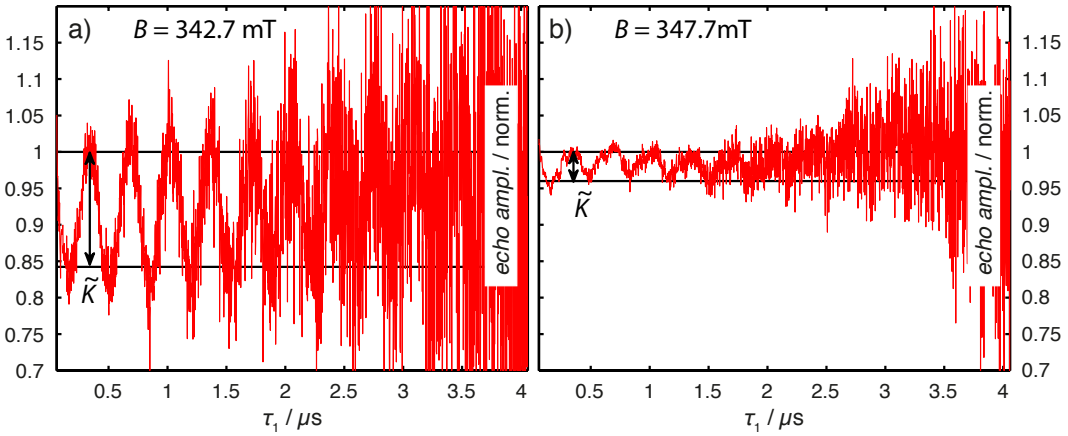

Figure 5.23: The ESEEM time traces measured at 342.7 mT and 347.7 mT are shown. The non-modulating background was removed by biexponentially fitting the traces in the time intervals of modulation maxima and dividing the traces by the fit result. Hence, they show the normalized echo amplitudes. The echo maxima and minima are marked by horizontal lines. The illustrations allow to read off the detected modulation depth parameter $\tilde{K}$ at both field positions as indicated. The echo noise levels at both fields differ because of the large echo amplitude differences between center and marginal regions of the spectrum.

Results

5 out of 26 FT spectra from different field positions are illustrated in Fig. 5.22 c). All FT spectra show a strong signal at $\approx$ 3 MHz. Further contributions at $\approx$ 6 and $\approx$ 14 MHz appear in the central field range. These three signals are in range of the Larmor frequencies of the $I = 1/2$ nuclei ^{1}H (14.9 MHz at 350 mT), ^{29}Si (2.96 MHz at 350 mT) and ^{31}P (6.04 MHz at 350 mT) which are typical elements of P-doped and undoped μc-Si:H. Further lines at high and low frequencies appear in distinct field ranges. At a first glance we see that a field-dependence of the ESEEM spectra exists which means that the different paramagnetic centers which give rise to the signals in the EDMR spectrum do not interact with the same nuclei.
The assignment of the different features in the ESEEM frequency spectra to the four detected EDMR resonances is realized with the help of a concept consisting of two parts. At first, the FT spectra below 343 mT and above 353 mT are studied, because at these fields the V signal dominates. Thus, its ESEEM fingerprint is not perturbed by other frequency contributions and can be analyzed. Since the V signal extends over the complete spectral range, its ESEEM spectrum constitutes a kind of background which

has to be considered when evaluating the spectra at other field positions. Afterwards, the ESEEM frequencies in the central field range are considered. Their field-dependent amplitudes are compared with the line shapes of the signals from the FSE spectrum. In this way the defects are assigned to individual nuclear environments.

The Fig. 5.22 b) shows an ESEEM time trace (trace A) measured at the low field side of the spectrum. The corresponding FT spectrum (FT A) is given in Fig. 5.22 c). It is characterized by only one frequency contribution at $\approx$ 3 MHz. Traces with exactly the same modulation characteristics are measured at high fields (e.g. FT E) and very low fields ($B = 330.5$ mT). In these field ranges the V signal dominates. Hence, these traces and FT spectra are solely due to the broad V line.
As we found out in the previous section, the V resonance is due to a paramagnetic center in the $S = 1$ triplet state. The characteristic feature of triplet ESEEM powder spectra is the detection of intense and sharp lines at nuclear Zeeman frequencies ω_I (see Sec. 2.2.3). Thus, the 3 MHz line is unambiguously assigned to ^{29}Si nuclei in the vicinity of the defect. Signals connected with additional nuclei are not observed.
The analysis of these triplet ESEEM spectra reduces to an evaluation of the modulation depth K, because the line at ω_I is the only detected spectral contribution but does not allow to deduce any information about the hyperfine coupling constants. In Fig. 5.23 a) the normalized ESEEM trace measured at 342.7 mT is displayed. It shows a *detected* modulation depth $\tilde{K}$ of $\approx$ 15%. This visible depth $\tilde{K}$ (which results from a superposition of all non-modulating and modulating sub-traces) can strongly deviate from the *intrinsic* modulation depth K (of a specific electron-nuclear system with distinct coupling parameters) and is, thus, hard to interpret in the present case due to several reasons:
The natural abundance of ^{29}Si is 4.67%. This significantly reduces the fraction of echo intensity which is influenced by ESEEM effects. Let's, further, assume a system of an electron spin coupled to a single nucleus of the ordered Si lattice. Then, the probability of finding an identical nucleus coupling to the electron spin is increased by the number of equivalent sites. This number is defined by the lattice structure. In rather disordered lattice structures the number of equivalent or nearly equivalent sites can only be estimated for nuclei close to the electron spin. Furthermore, the intrinsic modulation depth K of the modulation with frequency ω_I is hard to extract for a specific nucleus, when additional distant nuclei couple to the electron

spin. They will as well give rise to a contribution at ω_I in the frequency spectrum with individual modulation depths.

The EDMR signals in the center of the spectrum comprising especially the db and CE resonance are due to rather weakly coupled electron spins, since they show only small effects of dipolar broadening (see Sec. 5.2). Therefore, it is plausible to expect ESEEM spectra of weakly coupled spin pairs. They are of comparable structure as those of single electron spins coupled to a nucleus (see Sec. 2.1.5 and Fig. 2.9). Typical ESEEM frequency characteristics for powder samples in the hyperfine weak coupling case ($|A/2| < |\omega_I|$) are a sharp line at $2\omega_I$ (due to the transition $\omega_\alpha + \omega_\beta$), a broader line at ω_I (transitions ω_α and ω_β) as well as a line at small frequencies based on $\omega_\alpha - \omega_\beta$. For very small hyperfine coupling conditions all lines are rather sharp and can be detected.
In Fig. 5.24 a) the ESEEM frequency spectra between 346.2 mT and 349.2 mT are given. All spectra show lines at $\omega_I^{Si} \approx 3$ MHz (the larger part belongs to the V signal), at $2\omega_I^{Si} \approx 6$ MHz as well as at < 1 MHz. This set of three lines can be summarized to a ^{29}Si-ESEEM spectrum. The 6 MHz line is probably not due to ^{31}P, since the $2\omega_I^P$-line at ≈ 12 MHz is missing. But a small ω_I^P-contribution with a line at $2\omega_I^P$ below the noise level cannot be excluded.
A detailed evaluation of the FT spectra allows to draw conclusions about the hyperfine coupling constants of the contributing ^{29}Si nuclei. Simulated ^{29}Si-ESEEM spectra are shown in Fig. 5.25 a) which were calculated for a spin system consisting of a single electron coupled to one nucleus in dependence on the hyperfine parameters A_{iso} and T. We applied the EPR toolbox *easyspin* [33] for the simulations. The spectra were post processed using the same conditions and evaluation methods as for the experimental data. The results are compared to an experimental spectrum measured at 347.3 mT. The frequency ranges around 1 MHz and around $\omega_I^{Si} = 3$ MHz are most interesting, as the shape of these signals is indicative for the hyperfine coupling parameters. Increasing A_{iso} and T up to 0.8 and 0.4 MHz, respectively, leads to a splitting of the 3 MHz line and a shift of the 1 MHz line towards higher frequencies. Since the signal at ω_I^{Si} in the experimental data is part of the $S = 1$ ESEEM spectrum (V signal) as well as of the $S = 1/2$ ESEEM spectra (CE, db and h signal), it is hard to interpret its line width in view of hyperfine parameters of the narrow EDMR signals. But a significant broadening of the line in the center of the EDMR spectrum is not observed. The low frequency line which is clearly measured in the experiment appears in the simulation when assuming A_{iso} and T below 0.4 MHz. Hence, the major

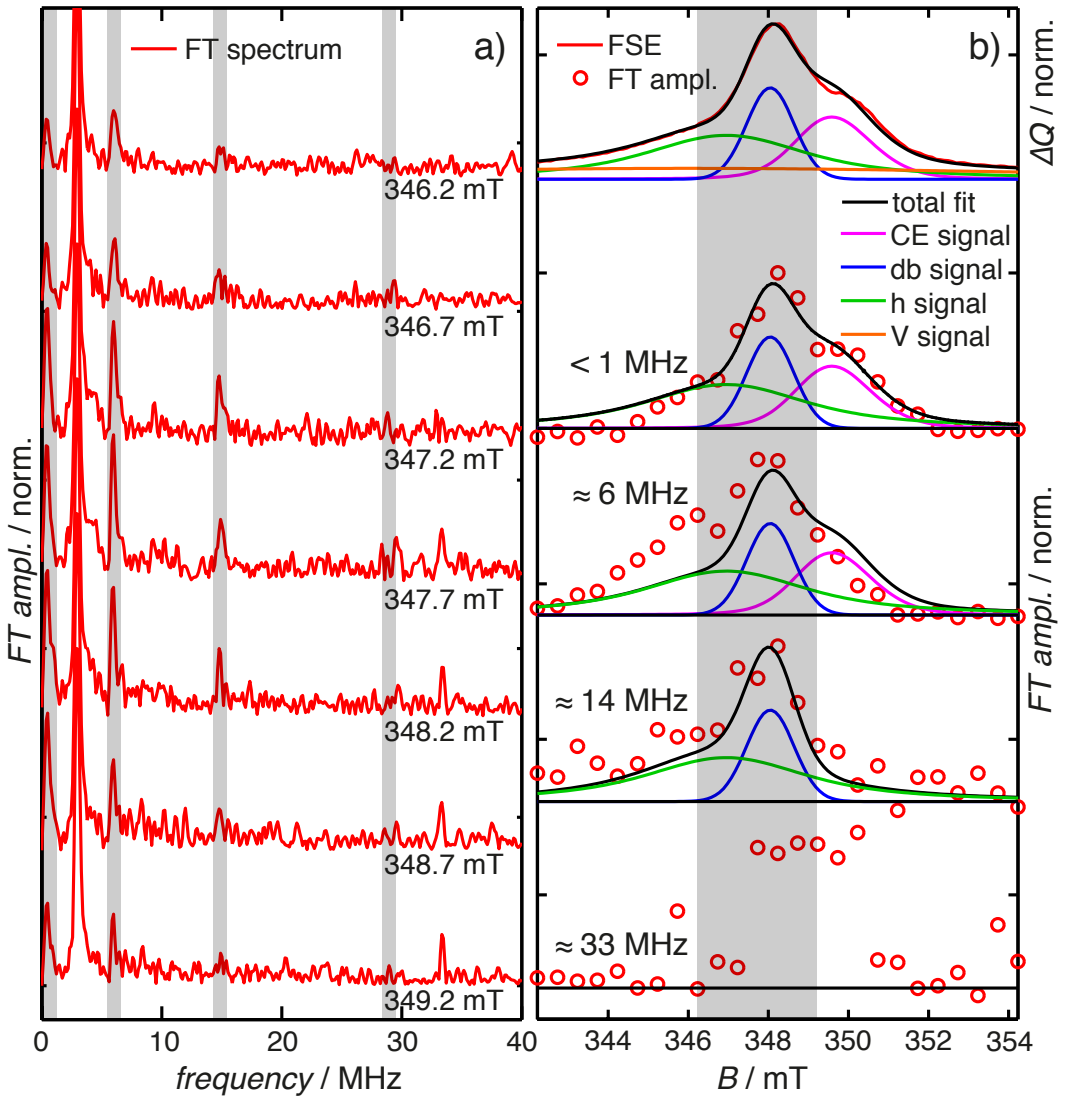

Figure 5.24: a) ESEEM FT spectra between $B = 346.2$ mT and 349.2 mT. This field interval is marked in grey in part b). They show different spectral contributions which are assigned to the narrow EDMR signals. b) At the top of the figure the FSE spectrum of the sample is shown together with the fit functions of the individual signals. Below the intensities of the ESEEM frequency contributions are shown as function of the field B at < 1 MHz, 6 MHz, 14 MHz and ≈ 33 MHz. The spectra were integrated in the intervals $0.1 - 1.1$ MHz, $5.7 - 6.6$ MHz, $14.6 - 15.0$ MHz and $33.1 - 33.6$ MHz to increase the SNR. In addition, the resulting line shapes at < 1 MHz and 6 MHz are compared to a spectral profile consisting of the CE, db and h lines. The 14 MHz profile is compared to a spectrum including the h and db signals.

part of the nuclei is weakly coupled to the electron spin.

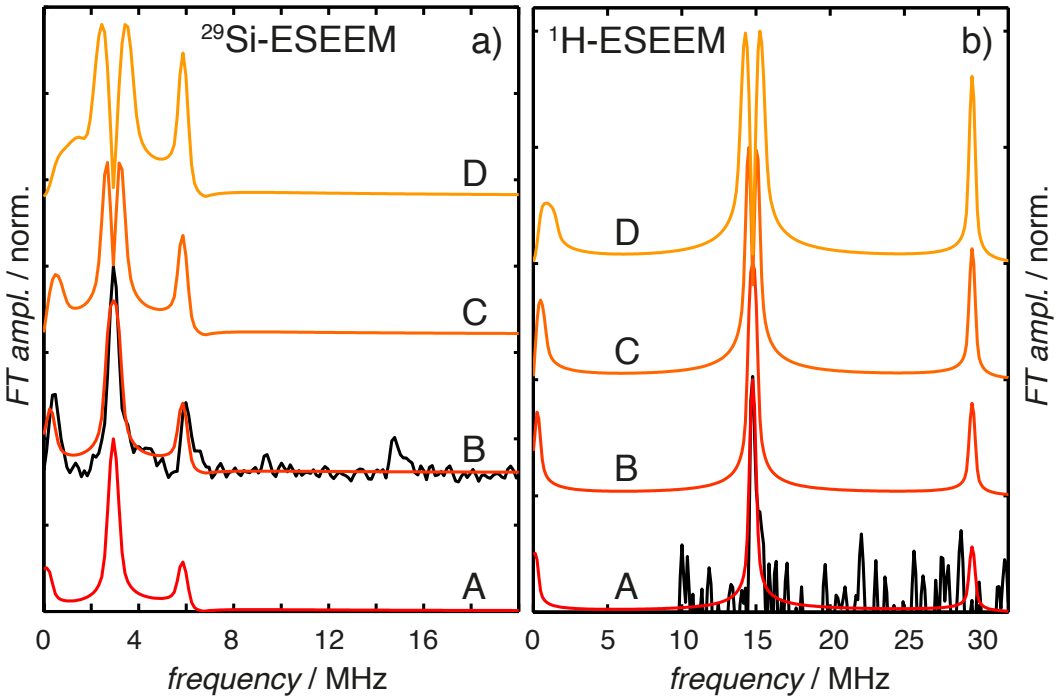

Figure 5.25: Simulated ^{29}Si-ESEEM (a) and ^{1}H-ESEEM (b) powder spectra. The spectra were calculated based on a spin system consisting of a single electron coupled to one nuclei for different hyperfine parameters: spectrum A: $A_{\mathrm{iso}} = 0.1$ MHz, $T = 0.05$ MHz. Spectrum B: $A_{\mathrm{iso}} = 0.2$ MHz, $T = 0.1$ MHz. Spectrum C: $A_{\mathrm{iso}} = 0.4$ MHz, $T = 0.2$ MHz. Spectrum D: $A_{\mathrm{iso}} = 0.8$ MHz, $T = 0.4$ MHz. The simulations are compared to the experimental data measured at $B = 347.2$ mT.

Furthermore, at 14.8 MHz the single Zeeman frequency $\omega_{\mathrm{I}}^{\mathrm{H}}$ of protons is measured. The line at $2\omega_{\mathrm{I}}^{\mathrm{H}}$ is buried in the noise. It is possible that a part of the line at frequencies < 1 MHz belongs to this ^{1}H-ESEEM spectrum as well. The simulations of ^{1}H-ESEEM spectra for different values of A_{iso} and T are shown in Fig. 5.25 b) to estimate proton-electron hyperfine coupling strengths. The experimental spectrum fits to the simulations based on hyperfine parameters < 0.2 MHz. Smaller coupling constants are not resolved in the spectra, since the line width of the ESEEM signals is limited by the spin-spin relaxation times of the system. We conclude, that the majority of the nuclei is weakly coupled to the electron spin.
An indication for boron which would give rise to signals at $\omega_{\mathrm{I}}^{\mathrm{B}} = 4.8$ MHz and $2\omega_{\mathrm{I}}^{\mathrm{B}} = 9.5$ MHz is not found.

For the assignment of these ^{29}Si- and ^{1}H-ESEEM sub-spectra to the three narrow EDMR resonances we consider the amplitudes of the ESEEM

frequencies. The modulation amplitudes are proportional to the amplitudes of the ESEEM frequency signals, since the non-modulating part of the traces was only removed before Fourier transformation, whereas the modulations were left untouched. They, in turn, reflect the amplitude of the respective EDMR signal at the current field position. This assignment is possible, as we assume a modulation depth K that does not vary within a narrow signal's profile. The amplitude of the line at ≈ 3 MHz cannot be considered here, because a large fraction is connected with the broad V signal. It is not possible to subtract this background signal by using a FSE-V-signal weighted amplitude, because this approach delivers inconsistent results. The percental modulation depth of the V signal is not constant in the complete field range. Hence, we concentrate our frequency analysis on the remaining contributions.
In Fig. 5.24 b) the amplitudes of the ESEEM frequency lines are displayed as function of the magnetic field. Results for frequency intervals around 1 MHz, 6 MHz, 14 MHz as well as 33 MHz are shown. The FSE spectrum allows a direct comparison of line shapes. The 6 MHz line is found in field range of the h, db and CE signal. Its profile can be roughly described by a spectral shape consisting of the line shapes of these three signals from the FSE spectrum. The relative amplitudes of the signals are the same as in the FSE. In the range of the h signal the 6 MHz line is too large. The reason is not clear. The 1 MHz line profile fits very well to the profile of the h, db and CE lines. The line shape of the 14 MHz ESEEM signal is affected by noise, since the line in general carries only a small intensity. Nevertheless, the profile can be described by a profile consisting of the h and db lines from the decomposed FSE spectrum. The contribution at 33 MHz appearing between 347.7 and 350.2 mT with constant amplitude is due to an artifact, because no ESEEM frequencies are expected here.

Discussion

With the help of the field-dependent ED-ESEEM study we were able to decompose the ESEEM spectra into three different ESEEM sub-sets which, furthermore, could be assigned to the different EDMR signals. The interpretation of the ESEEM data delivers important details about the nuclear environment of the paramagnetic centers in the microcrystalline Si material.
The ^{29}Si-ESEEM spectrum of an electron spin $S = 1$ is connected with the

broad V signal. This conclusion could be drawn, as the spectrum with the single line at $\omega_{\mathrm{I}}^{\mathrm{Si}}$ is accessible in a pure form in the marginal regions of the EDMR field spectrum. The fact that only $\omega_{\mathrm{I}}^{\mathrm{Si}}$ is found in the spectra can be interpreted in the following way: Either silicon is the only element in the surrounding of the V center (in addition to elements with negligible concentration of nuclear spin-carrying isotopes which cannot be defected) or other spin-carrying nuclei close to the V center are strongly coupled to it and therefore cannot give rise to ESEEM signals. In Sec. 5.2 we suggested the di-hydrogen- (HVH) and oxygen-vacancies (VO) as possible candidates for the V center. In the case of the HVH vacancy two protons passivate two of the four broken bonds of the vacancy complex [153]. Chen et al. determined its ^{1}H-hyperfine coupling matrix to be $\mathbf{A} = (A_{11}, A_{22}, A_{33}) = (5.8, 5.3, 6.3)$ MHz. These coupling strengths can be detected by ESEEM methods but are not found in our spectra. This means that we do not have protons near the vacancy sites. Hence, the HVH vacancy is excluded as a possible vacancy site in μc-Si:H. In the case of the VO site two dangling bonds are bridged by an oxygen atom. The oxygen nucleus cannot be detected in the ESEEM spectra, because of negligible abundance of ^{17}O ($I = 5/2$). Hence, only Si nuclei should give rise to ESEEM signals. An EPR study of the photo excited triplet state of the VO center supports our interpretation [165]. In that study ESEEM experiments were applied to VO defects created by high-energy electron beam irradiation of crystalline silicon. The crystal spectra reveal only signals connected with silicon. Particularly, the line at $\omega_{\mathrm{I}}^{\mathrm{Si}}$ is visible. The existence of VO centers in microcrystalline silicon is further supported by reports about oxygen impurities in μc-Si:H thin-film solar cells [166]. Under comparable deposition conditions impurity levels of $[\mathrm{O}] = 3 \times 10^{18}$ cm^{-3} are reported so that oxygen atoms can be part of vacancy complexes. This allows us to conclude, that the observed vacancy center is probably the VO center. Furthermore, this centers is located inside crystalline grains, owing to missing signals of distant protons.

The ESEEM spectra which belong to the h, db and CE resonances consist of two sub-spectra due to ^{29}Si as well as ^{1}H nuclei coupled to a single spin $S = 1/2$. This means that the spin pair consistuents which give rise to the narrow EDMR lines are bound via weak spin-spin interactions. The hydrogen ESEEM spectrum is observed in the field range of the db and h signal. The majority of nuclei is weakly coupled to the electron spin and, thus, gives rise to narrow matrix peaks in the ESEEM spectra. Precise infor-

mation about coupling parameters or distances cannot be delivered. Disordered material in microcrystalline Si are rich of hydrogen [113]. Thus, we assign the h and db centers to disordered regions in the μc-Si:H material.
The ^{29}Si ESEEM spectrum is detected in the field range of all three narrow resonances. Again, narrow matrix peaks are observed. Based on the ESEEM results it is, nevertheless, hard to extract any information about the localization of the wave functions or the distance of the coupled silicon nuclei. Here, an ENDOR experiment could deliver answers, because this technique allows access to the full bandwidth of hyperfine couplings which is not possible with ESEEM experiments. The distribution of hyperfine coupling strengths then allows to estimate the degree of localization of the respective defect wave function.
The CE centers are only affected by Si nuclei, whereas the environment is completely lacking in protons. This observation was already made in previous ESEEM studies [25, 116]. Based on this, can be concluded that the CE centers are located in crystalline regions within the μc-Si:H material.

Summary

Field-dependent electrically detected ESEEM was applied to a thin-film μc-Si:H solar cell to investigate the microscopic structure of all paramagnetic centers contributing to the EDMR spectrum. By comparing the line shapes of the EDMR signals with the profiles of the different ESEEM lines it was possible to determine which nuclei exist in the environment of the defects centers. In this way we are able to answer the questions raised at the start of this section:
The db and h defects were assigned to the disordered phase of the material based on the influence of distant hydrogen nuclei. The V and CE centers are located in the crystalline region of μc-Si:H, as only ^{29}Si nuclei left marks in the ESEEM traces. The $S = 1$ spin state of the vacancy center was corroborated by the single frequency ESEEM spectrum which is typical for powder samples. Furthermore, is was possible to expel the HVH complex as a candidate for the V center, since no indication for hydrogen in the vicinity of the defect was found. Surprisingly, signals of the doping atoms boron and phosphorus were not found in the ESEEM spectra. Taking the current study and the multi-frequency investigations from the last section together, the doping atoms stay completely invisible.

This field-dependent ESEEM experiment turned out to be a very convenient approach to get information about the local environment of defects from multi-component EDMR spectra. This is especially interesting, since electrically detected ENDOR is still technically demanding and lacks application to disordered systems which give rise to broad hyperfine coupling distributions.

5.4 Rabi Nutation Experiments

In a continuous wave (cw) EDMR experiment the sample is continuously subjected to microwave (mw) radiation while the current change is detected as function of the magnetic field, resulting in the EDMR spectrum. The g-values and line shapes identify the paramagnetic centers participating in current-determining processes in EDMR, as in conventional EPR, nevertheless often different processes may lead to indistinguishable EDMR spectra. In this case pulsed (p) EDMR employing short mw pulses [18] can help to pinpoint the microscopic process and the participating paramagnetic centers in two different ways. First, the time behavior of EDMR signals can reveal which paramagnetic centers are connected via a transport process. This was demonstrated by Behrends et al. [20] and used for the spectral disentanglement in chapter 4 and sections 5.1.2 and 5.2. Second, coherent effects can be harnessed in a similar way like in pulsed EPR [167, 168]. These coherence effects were recently utilized to identify spin-dependent transport and recombination mechanisms in organic semiconductors based on the frequency components observed in electrically detected Rabi oscillations [169–171]. We apply a similar strategy in section 5.4.1 to investigate spin-dependent charge carrier hopping via conduction band tail states, referred to as *CE centers*, in μc-Si:H. This study was recently published in the *Journal of Molecular Physics* (see Ref. [172]). Furthermore, the investigation of coherent effects provides access to information about the spin quantum numbers of the studied paramagnetic center as the nutation frequencies depend on the transition matrix elements of the excited resonance line [37, 173]. This was e.g. successfully applied to samples containing different transition metal ions, each with $S > 1/2$ [173]. With the help of the nutation frequencies of the different resonance lines the respective quantum numbers were determined unambiguously so that an assignment to the contained metal ions was possible. We take advantage of this approach

and determine the spin quantum number of the V center in section 5.4.2.

5.4.1 Investigation of Spin-Dependent Processes via CE Centers

An EDMR signal attributed to CE states is frequently found in the low-temperature transport properties of μc-Si:H films [17, 111] and μc-Si:H-based solar cells [21]. The CE center is of particular technological relevance because it can influence the photocurrent through trapping and thus affects the charge carrier collection efficiency in thin-film solar cells. Since each spin-dependent transition involves two CE center, the transport-limiting hopping transition is governed by the properties of a doublet pair [32]. Provided sufficient mw power is available and the g-values of both CE centers are similar, the collective manipulation of both spin partners should result in *spin-locking* behavior, i.e., in Rabi oscillations with the frequency $\Omega_2 = 2\gamma B_1$ with γ being the gyromagnetic ratio and B_1 the amplitude of the magnetic field induced by the mw radiation [174]. However, previous X-band EDMR experiments showed that the coherent oscillations observed for CE hopping transport are rather dominated by the Rabi frequency $\Omega_1 = \gamma B_1$ as expected for a single $S = 1/2$ center [21]. A similar behavior was found for hopping transport through a-Si:H conduction band tail states [175] and for spin-dependent recombination in a-Si:H films [176]. This raises the question whether a significant Ω_2 component can be detected at all in EDMR experiments on thin-film silicon devices. It further gives rise to the question if disorder [177] or strong broadening of the EDMR signature of one spin partner may lead to an effective suppression of the Ω_2 Rabi frequency. Here we report the application of coherent pEDMR spectroscopy using X- and S-band resonance frequencies to study the mw-power dependence of the Rabi oscillations in combination with simulations of the dynamics of weakly-coupled CE spin pairs in order to address these questions.

Experiment

Low temperature ($T = 5$ K) Rabi and π-pulse experiments were carried out at S- and X-band. With the help of a 1 kW TWT mw amplifier at X-band and a 40 W solid-state amplifier at S-band short π pulses of $t_p = 20$ ns and 60 ns (excitation bandwidth $\Delta\nu \approx 1/t_p = 50$ and 17 MHz, which

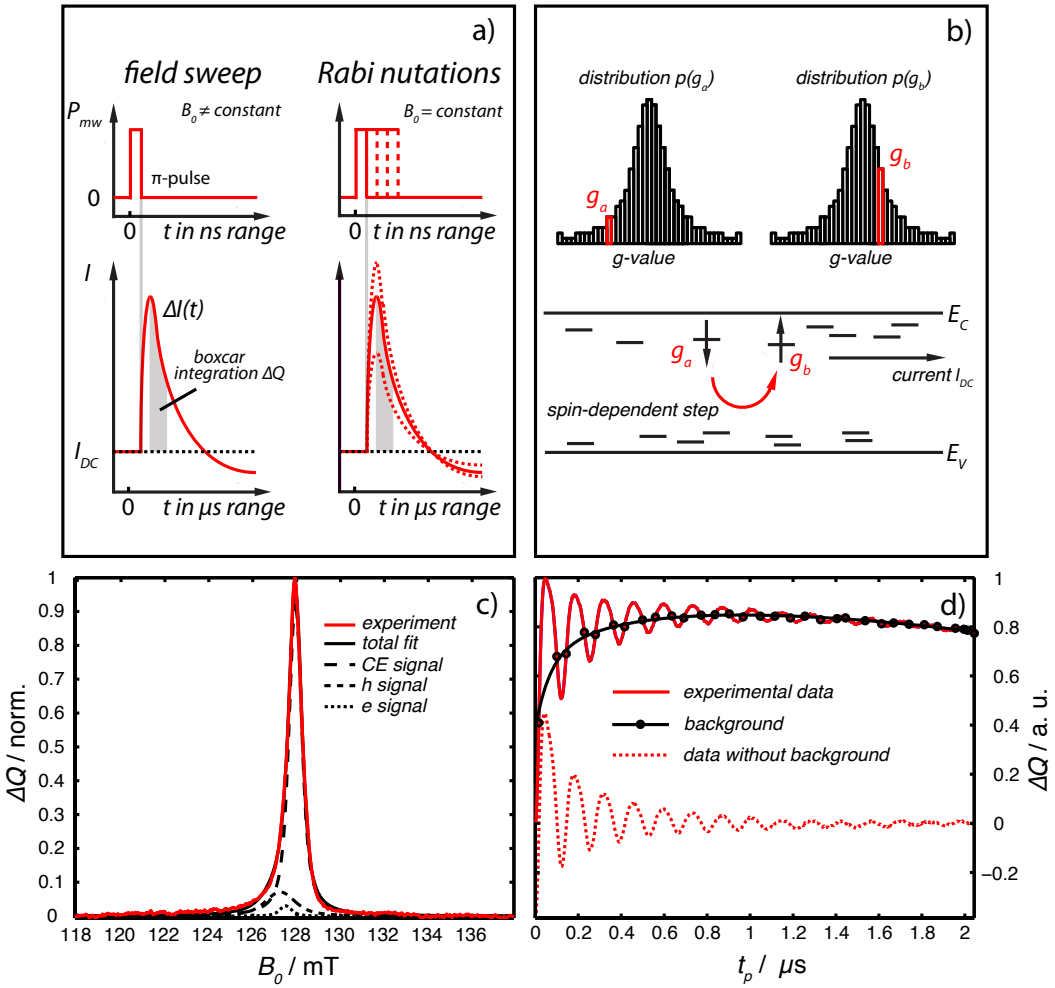

Figure 5.26: a) Field sweep experiment: At a constant time after the mw π-pulse the current response $\Delta I(t)$ is integrated (yielding ΔQ) and detected as a function of B_0. Rabi experiment: At constant B_0 the pulse length t_p is incremented. At a constant waiting time after the pulse $\Delta I(t)$ is integrated and measured as a function of t_p. b) A scheme of the µc-Si:H band structure with two spins (with g-values g_a and g_b) in localized CE centers near the conduction band (E_C). A spin-dependent process between both spins leads to the EDMR signal. For the simulations both spin-pair constituents are assumed to have g-values g_a and g_b taken from g-distributions $p(g_a)$ and $p(g_b)$. c) Field sweep spectrum measured at S-band showing three EDMR signals. d) Rabi oscillations for $B_1 = 0.26$ mT measured on the maximum of the S-band spectrum.

corresponds to 1.4 mT and 0.5 mT, respectively) were generated. The solar cell was operated in reverse direction ($U = 1$ V) under illumination with a halogen cold light source (150 W). Illumination through the optical window

in the resonator at X-band resulted in a photocurrent of 7.2 μA. At S-band the sample was irradiated via an optical fibre and a small micro-prism delivering 5.5 μA. For all Rabi experiments the current response $\Delta I(t)$ after the mw pulse excitation was boxcar integrated from 3 to 7 μs at S- and from 5 to 9 μs at X-band yielding ΔQ with a high signal-to-noise-ratio.

Simulation of Coherent Spin Motion

The coherent evolution of the doublet pairs with two $S = 1/2$ during a mw pulse was modeled by integrating the Liouville-von Neumann equation

$$\frac{d\rho}{dt} = -i\,[H(t), \rho(t)] \tag{5.13}$$

using the spin-pair Hamiltonian

$$\begin{aligned} H(t) &= H_0 + H_1(t) \\ &= \frac{\mu_B B_0}{\hbar}\left(g_a S_a^z + g_b S_b^z\right) + \frac{\mu_B B_1}{\hbar}\cos(\omega t)\left(g_a S_a^x + g_b S_b^x\right) \end{aligned} \tag{5.14}$$

including only the electron Zeeman interaction of both spins as well as the interaction with the mw-induced magnetic field. The spin-pair Hamiltonian consists of a static part, H_0, and a time-dependent part, H_1 (caused by the mw magnetic field). Further, ρ represents the density matrix describing the spin-pair ensemble, $g_{a,b}$ denote the g-values of the spin-pair constituents a and b with spin operators $S_{a,b}$, B_0 is the amplitude of the static magnetic field, and B_1 is the amplitude of the mw field with frequency $\omega/2\pi$ (μ_B: Bohr magneton, $\hbar$: Planck's constant). We assume weakly coupled spin pairs and thus do not take mutual spin-spin interactions (exchange and dipolar coupling) into account. Loss of spin pairs (due to recombination or dissociation) is neglected during the mw pulse and included later by an exponential damping of the simulated EDMR signal.
To account for the finite line width of the CE EDMR signal, which results in a distribution of resonance frequencies, we replaced the g-values in Eqn. (5.14) by g-distributions determined from fits to the S-band pEDMR spectrum. Note that the application of this procedure is not restricted to inhomogeneously broadened resonances due to a true distribution of g-values as a consequence of g-strain. It is also valid for line broadening due to un-

resolved hyperfine interactions. In both cases inhomogeneous broadening leads to a distribution of resonance frequencies that can be covered by the numerical treatment based on a distribution of g-values.
The S-band EDMR spectrum of the CE center can be approximated by a Lorentzian line profile with a line width (FWHM) of $\Delta B_{1/2} = \Delta B^{\mathrm{S}}_{\mathrm{CE}} =$ 0.7 mT. Surprisingly, the line shape is much better approximated by a Lorentzian line than a Gaussian. However, this Lorentzian line shape is not related to a homogeneous lifetime broadening. We thus included the following distribution of g-values

$$p(g_a) = \frac{2}{\pi}\frac{1}{\Delta g_a}\left[1 + 4\left(\frac{g_a - \bar{g}_a}{\Delta g_a}\right)^2\right]^{-1} \quad \text{with } \bar{g}_a = 1.99729 \text{ and } \Delta g_a = 0.0111 \tag{5.15}$$

with Δg_a being the width (FWHM) of the g-distribution centerd at $\bar{g}_a$. The g-distribution is illustrated in Fig. 5.26 b). We assume that the g-distribution for the other constituent of the spin pair, i.e. $p(g_b)$, is identical to $p(g_a)$ except for the central g-value which was set to $\bar{g}_b = 1.99731$. The marginal offset between $\bar{g}_a$ and $\bar{g}_b$ was introduced because pairs of spins with identical g-values may cause numerical instabilities.
To model the spin-pair dynamics we form spin pairs by taking one spin from $p(g_a)$ and one spin from $p(g_b)$ and calculated the spin pair evolution as a function of the mw pulse length t_{p} by numerically integrating Eqn. (5.13) using easyspin's propint function [33]. For 9×10^4 spin pairs with varying g-values (taken from the distributions $p(g_a)$ and $p(g_b)$ consisting of 300 points each) we determine the population of the product states $|\uparrow\downarrow\rangle$ and $|\downarrow\uparrow\rangle$ with antiparallel spin alignment at the end of the resonant mw pulse under the assumption that all spin pairs are initially ($t_{\mathrm{p}} = 0$) in a configuration with parallel spins (pure triplet states). We consider the g-values of both paramagnetic centers forming a spin pair to be uncorrelated, meaning any spin from $p(g_a)$ can form a pair with any other spin from $p(g_b)$. The results for all 9×10^4 spin pairs are added up, yielding the ensemble average. The initial condition is based on the premise that pairs with parallel spins live longer than those in pure triplet states [19].
We assume that the pEDMR signal (i.e. the resonant change in conductivity) is proportional to the combined population of the states $|\uparrow\downarrow\rangle$ and $|\downarrow\uparrow\rangle$ after the mw pulse. This corresponds to the sum of the populations of the states $|S\rangle$ and $|T^0\rangle$ in the case of strong intersystem crossing between these states and is thus independent of the chosen basis. Damping of the Rabi oscilla-

tions due to gradual loss of spin pairs during the excitation is accounted for by including exponential damping of the oscillation amplitude from the experimental data. Damping due to de-phasing of spin pairs is automatically incorporated in the simulation by including g-value distributions. Depending on the ratio between the width of the g-distributions and the mw power, the Rabi oscillations obtained by averaging over the contributions from all spin pairs are dominated either by the frequency Ω_1 (selective excitation at low mw power) or Ω_2 (spin locking at high mw power).

Measurements and Evaluation

The field sweep EDMR spectra were measured using low power π-pulses of $t_p = 300$ ns length in a field range of 20 mT at S- and 40 mT at X-band. The S-band spectrum in Fig. 5.26 c) shows one slightly asymmetric peak near $B_0 = 128$ mT. Application of decomposition techniques making use of the transient dynamics [20, 106] reveals three overlapping resonances. The dominant contribution at $g_{CE} \approx 1.998$ (83 % of the integrated spectral intensity and Voigtian line width (FWHM) $\Delta B^S_{CE} = 0.70(3)$ mT) is assigned to conduction band tail states (CE centers) participating in spin-dependent hopping transport in the crystalline regions of the material [20, 21]. Furthermore two minor contributions are found: a Voigtian line at $g_{db} \approx 2.004$ with $\Delta B^S_{db} = 0.65(5)$ mT (relative contribution: 2.5 %) which is attributed to dangling bond centers (db states) in the amorphous regions as well as a broad Voigtian line at $g_h \approx 2.010$ with $\Delta B^S_h = 1.63(5)$ mT (relative contribution: 14.5 %) due to valence band tail states (h states) [21]. From S- to X-band the line widths of the contributing signals grow by a factor of ≈ 3 and the line intensities change slightly due to different illumination conditions. Nevertheless we can assume that the EDMR signal is predominantly governed by the CE signal when the magnetic field is set to $B_0 = h\nu / g_{CE}\mu_B$ in the Rabi oscillation measurements.
Rabi oscillations were measured in the center of these field sweep EDMR spectra. The applied mw pulse is incremented in time steps of 2 ns up to a length of 2 and 0.5 µs at S- and X-band, respectively, and the integral of the current response is detected (Fig. 5.26 a), right side). An example of Rabi oscillations is shown in Fig. 5.26 d) measured at S-band. For the analysis of the obtained data advanced fitting routines were used, implemented in MATLAB (The Mathworks, Natick, MA, USA). First the non-modulating background of the Rabi data is removed. Afterwards the time traces were

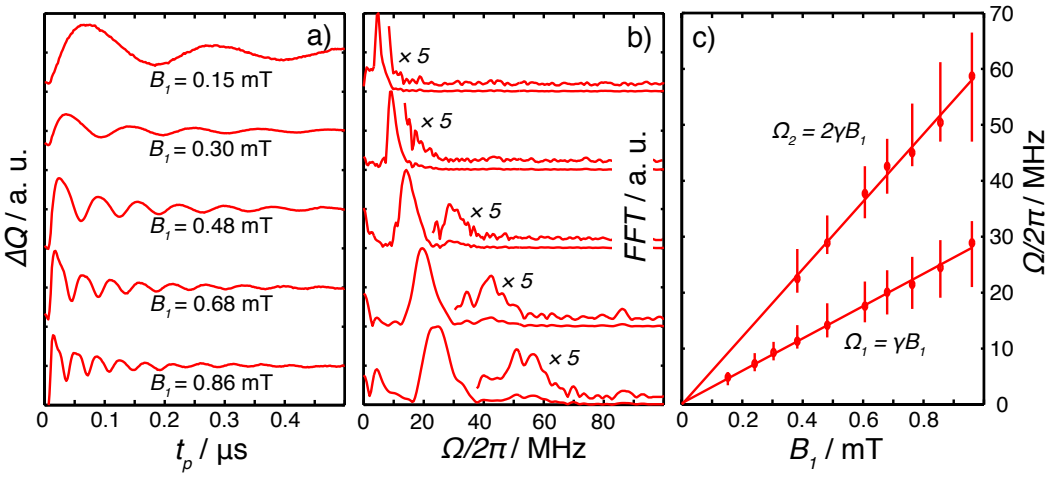

Figure 5.27: a) and b): Background-free X-band Rabi oscillations for different B_1 field strengths and corresponding FT spectra. c) Oscillation frequencies Ω_1 and Ω_2 deduced from the FT spectra in dependence on B_1. The vertical lines at each frequency point indicate the line widths in the FT spectrum (FWHM).

apodized by a Hamming window to obtain a high side-band suppression before fast-Fourier transformation (FFT). The resulting frequency spectra are given in Fig. 5.27 b) and 5.28 b).

X-band Rabi Oscillations

In Fig. 5.27 a) Rabi oscillations at X-band are shown for different mw B_1 fields. In dependence on B_1 the oscillation frequency Ω_1 increases. At high B_1 values the shape of the oscillating signal changes notably. In the FT spectra (Fig. 5.27 b)) this results in a second component Ω_2, which is hardly visible as a broad line. Strong mw background signals at high B_1 fields reduce the quality of the measurement and lead to broadened lines in the frequency domain. Evaluation of both frequency contributions of all measured Rabi oscillations with B_1 values up to 0.96 mT delivers a linear B_1-dependence for Ω_1 and Ω_2 differing by a factor of 2, which means that $\Omega_2 = 2\Omega_1$ (Fig. 5.27 c)).
The frequency Ω_1 apparent in all time traces is due to the coherent spin motion of a single CE center in resonance. The frequency component at Ω_2 measured at high mw field strengths is predicted in the case of small Larmor separation of the two coupled spin partners [19, 178]. This means, we detect a contribution of coupled spin pairs to the EDMR signal. However,

the intensity is too weak to allow a more detailed analysis.

S-band Rabi Oscillations and Simulations

The detection of the second oscillation frequency Ω_2 in Rabi experiments of spin pairs with partners of similar g-values can be further improved by reduction of their Larmor separation. This is achieved at lower mw frequencies. As the CE line width decreases by a factor of 2.6 going from X- to S-band frequencies we have performed Rabi experiments at this lower frequency band. B_1 fields of only up to 0.29 mT are reached in our setup (reduction by a factor of 3.3 in comparison to X-band), nevertheless the quality of the experimental data is enhanced, because the smaller B_1 fields lead to a reduction of the disturbing high power background signals.
The S-band Rabi oscillations for different B_1 fields are shown in Fig. 5.28 a). The data (red lines) show a high signal-to-noise-ratio revealing the Ω_2 component as a narrow peak in the FT spectra (Fig. 5.28 b)). The frequencies found show a linear behavior with slopes differing by a factor of 2 as already found at X-band. For three mw field strengths (B_1 = 0.05, 0.18 and 0.29 mT) Rabi oscillations were calculated by numerical simulation (shown in black) and post-processed to allow a direct comparison with the experimental data. In addition a damped sine function was simulated and evaluated in the same way to show the influence of possible artifacts from the post-processing. For the damped sine function, only a broadened line at the basic frequency arises, showing that the second harmonic is not generated by the post-processing. The simulated Rabi oscillations and their FT spectra are in very good agreement with the experiment. Taking a closer look, the contribution of the Ω_2 component appears weaker in the simulations in comparison to the experimental spectra. To evaluate this aspect, further simulations were performed for B_1 fields up to 1.1 mT. Afterwards both frequency components at Ω_1 and Ω_2 were approximated with symmetric lines for a good fit of all FT spectra and to obtain their line intensities S_{Ω_1} and S_{Ω_2}. The line intensity ratio $r = S_{\Omega_2}/S_{\Omega_1}$ was compared as a function of B_1. The results are displayed in Fig. 5.28 c). With decreasing B_1 fields the relative Ω_2 contribution becomes smaller in experiment and simulation, as the reduced excitation bandwidth reduces the probability to excite both spin partners with different g-values in the g-distributions. However, the relative contribution of the higher frequency found in the measured data exceeds the contribution deduced from the simulated data by a factor of roughly 2. This

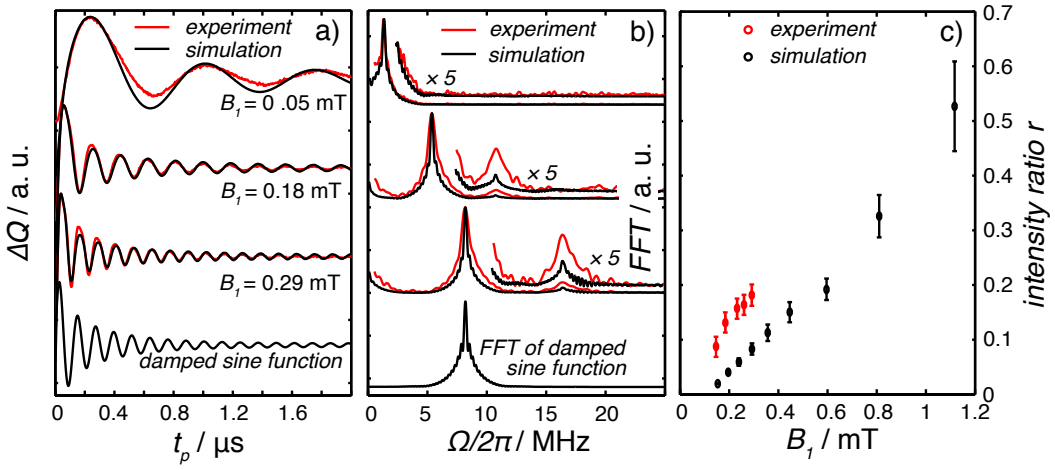

Figure 5.28: a) Three examples of background-free S-band Rabi oscillations (red) and corresponding simulations (black) for three B_1 fields strengths. A damped sine function is added and evaluated with the same methods to exclude that the Ω_2 signal is due to a numerical artifact. b) FT spectra of experiments, simulated data and sine function. c) Ratio r comparing the intensities S_{Ω_2} and S_{Ω_1} of the two frequency contributions deduced from the experimental and simulated FT spectra as a function of B_1.

high proportion of the Ω_2 line allows to answer the question regarding the spin partner of the CE center. As the db and h signals contribute by less than 5% to the EDMR spectrum (Fig. 5.26 c)) at the field position where the Rabi oscillations were recorded, one would expect a strong reduction of the Ω_2 component. Hence these states can be excluded as partners of the CE center. Thus we conclude that the EDMR signal at $g_{\mathrm{CE}} \approx 1.998$ is due to spin-dependent transport via neighboring CE centers. A possible origin of the discrepancy between $r = S_{\Omega_2}/S_{\Omega_1}$ in experiment and simulation will be analyzed in the following.

Influence of the Line Width

Even though the experimental proportion of the Ω_2 component in the time traces is roughly a factor 2 larger than in the simulation, its intensity is too low to show a discernible frequency component directly in the Rabi oscillations traces and shows up clearly only in the FT (Fig. 5.28 b)). This is in contrast to electrically detected Rabi oscillations measured on devices made from organic semiconductors such as Zinc phthalocyanine [169], polymers [170] or polymer:fullerene blends [171], where the Ω_2 component is

already evident from the Rabi oscillation signal in the time domain. This can be attributed to the line width of the paramagnetic centers causing the EDMR signals in these materials, which is considerably smaller than for the CE line width in μc-Si:H. In consequence, the mw power typically available for X-band EDMR is sufficient to obtain a substantial spin-locking signal for organic semiconductor devices.
In order to study the influence of the EDMR line width on the Rabi oscillations we varied the width of the g-distributions used in the simulation. Fig. 5.29 b) shows the simulation results for $B_1 = 0.29$ mT (the highest B_1 available in our S-band setup) assuming different line widths as illustrated in Fig. 5.29 a). The uppermost trace corresponds to a CE line width of $\Delta B_{1/2} = \Delta B_{\mathrm{CE}}^{\mathrm{S}} = 0.7$ mT extracted from the S-band EDMR spectrum. Upon decreasing the width of the g-distribution in the simulation, the shape of the maxima of the time domain signal exhibit notable changes until the spin-locking component becomes clearly visible for $p(g_{a,b})$ equivalent to $\Delta B_{1/2} = 0.3$ mT (lowermost curve in Fig. 5.29). The results show that it is indeed the relatively broad resonance line of the CE center which impairs the detection of a clear spin-locking feature in the time domain signal for the mw power available in our S-band EDMR setup.
One possibility to increase the intensity of the Ω_2 component is certainly the use of more intense mw pulses without changing the resonance frequency. Another appealing option is to perform EDMR measurements on a high-power EPR spectrometer operating at W-band frequency [179]. Although substantial g-strain will cause the CE line width to be much larger than in S-band, the use of a kilowatt W-band mw amplifier can overcompensate this effect. In addition, the better spectral resolution of the CE signal will provide the possibility to check whether all parts of the g-distribution contribute to the Ω_1 and Ω_2 components in the same way or give rise to different Ω_2/Ω_1 ratios.

Conclusions

The comparison between the results of coherent S-band EDMR measurements and numerical simulations indicates that a spin-dependent transition between two paramagnetic centers taken from an inhomogeneously broadened g-value distribution can lead to selective-excitation behavior in the Rabi oscillation signal, even though the g-value distribution is assumed to be identical for both centers. The intensity ratio between the Ω_1 and Ω_2

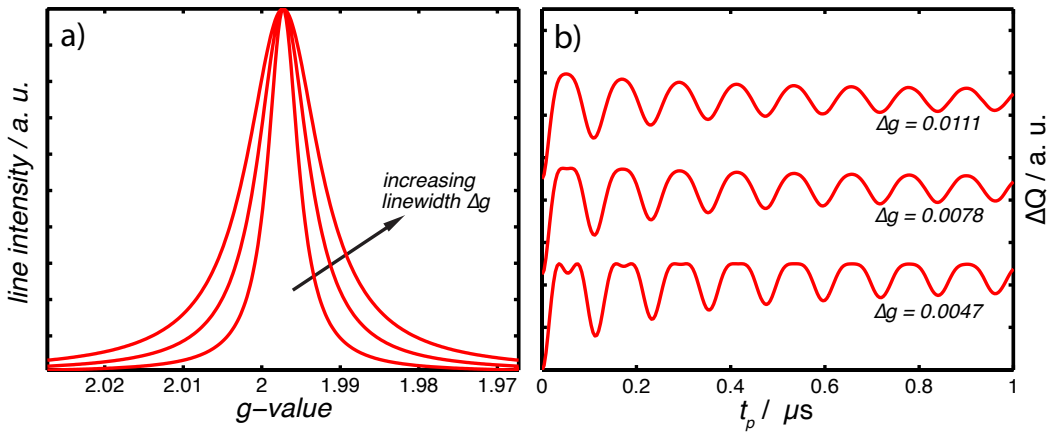

Figure 5.29: a) Three g-distributions with line widths of $\Delta g = 0.0047$, 0.0078 and 0.0111 (FWHM) are shown. These values correspond to $\Delta B_{1/2} = 0.3$, 0.5 and 0.7 mT, respectively. b) Simulations of Rabi oscillations for these three line widths.

Rabi frequency components as shown in Fig. 5.28 c) agrees well with the simulation results for uncorrelated spin pairs, corroborating our hypothesis that g_b is independent of g_a for the vast majority of the doublet pairs. However, the experimental values exhibit a systematically stronger spin-locking component than predicted by the simulations for all chosen values of B_1. This may be explained by the following scenario based on the coexistence of two different types of spin pairs.

Most doublet pairs (A) are uncorrelated and lead to the Ω_2/Ω_1 ratio in agreement with the simulation results. Additionally, a second kind of pairs (B) consisting of paramagnetic centers with similar g-values may give rise to a second contribution that is dominated by Rabi oscillations with frequency Ω_2 and thus increases the intensity of this frequency component in the total EDMR signal.

Such a two-component nature of the EDMR signal could be related to the microscopic structure of μc-Si:H [94, 117]. A previous study has shown that the environment of the EDMR-active CE centers is depleted from hydrogen, i.e. the CE centers are located inside crystalline grains [25]. It has recently been suggested that the asymmetric CE EDMR line shape, which is particularly pronounced in Q- and W-band spectra, results from the size distribution of the Si crystallites in μc-Si:H due to a correlation between crystal diameter and CE g-value as a signature of a quantum size effect [106]. Following this idea and further assuming that the diameters of neighboring Si crystals are not correlated, this model readily explains the fact that the spin-

dependent hopping transition between adjacent CE centers localized in two different grains (forming a spin pair of type A) can be attributed to doublet pairs with uncorrelated g-values. On the other hand, Si crystallites with a diameter above a certain threshold may accommodate several CE centers. An intra-grain hopping transition between two such paramagnetic centers (forming a spin pair of type B) produces a spin-locking Rabi oscillation signal. In total, the combined contributions from A and B pairs result in the Ω_2/Ω_1 ratio found in the experiment.
While this model provides a credible explanation for experimental results, other effects can equally affect the behavior of the Rabi oscillation signals. We note that dipolar and exchange coupling between the spin-pair constituents can severely affect the Ω_2/Ω_1 ratio [180–182]. Since spin-spin couplings are not field-dependent, we believe that coherent EDMR experiments using higher resonance frequencies (Q- and W-band and possibly even higher frequencies) can be applied to distinguish between effects due to g-value distributions and those arising from the presence of spin-spin couplings.

5.4.2 Investigation of the V Signal Rabi Frequencies

The EDMR spectra of the μc-Si:H thin-film solar cell investigated in this work reveal a line (called *V signal*) which is much broader than the other spectral contributions. It is centered around a g-value of ≈ 2.017. With the help of the multi-frequency study in Sec. 5.2 we found the origin of the line width to be a field-independent broadening due to spin-spin interaction. Although this is a signature of strongly interacting spins or even of a paramagnetic system with an effective spin $S > 1/2$, precise information of the spin state is still missing. A possibility to determine the spin quantum number of the V signal is the application of Rabi oscillation experiments as the nutation frequency is directly dependent on the spin quantum number of the excited transition.

Experiment and Evaluation

X-band field sweep spectra and Rabi nutation were measured at 5 K. The solar cell was operated at $U = 1$ V reverse bias under illumination ($I = 11.8$ μA). The experimental conditions and the equipment are described in

Sec. 5.4.1. The field sweep EDMR spectrum was measured in the range between 300 and 400 mT ($t_p = 300$ ns π-pulse length for $S = 1/2$) to detect the complete width of the V signal ($\Delta B = 19(1)$ mT width (FWHM) at X-band). The spectrum is shown in Fig. 5.30 a).
For the Rabi experiments we used the maximum mw power available to excite a high number of nutations before the coherent signal decays due to relaxation processes. The current response $\Delta I(t)$ after the mw pulse excitation was boxcar integrated from 4 to 8 μs yielding ΔQ with a high signal-to-noise-ratio.
A transient nutation trace of 1 μs was detected in the center of the EDMR spectrum ($B = 349.3$ mT, $g = 1.998$). At this position the CE signal clearly dominates, which provides a reference Rabi frequency for a spin $S = 1/2$ system as described above (Sec. 5.4.1). This frequency will be used for a calibration of the B_1 field strength later on. Measurements at 336 mT ($g = 2.078$) and 356 mT ($g = 1.962$) were performed to detect the Rabi frequencies of the V signal. Traces of 0.4 μs length could be measured. The narrow signals in the center of the spectrum do not influence the Rabi experiments at the chosen field positions in the marginal regions of the broad V signal. The post-processing of the data is described in Sec. 5.4.1.

Results and Conclusion

The post-processed Rabi nutations at the chosen field positions in the EDMR spectrum are shown in Fig. 5.30 b). The respective FFT spectra are given in Fig. 5.30 c). The trace in the middle (CE signal) reveals nutations of lower frequency in comparison to the traces of the V signal. Furthermore, the narrow minima in the time domain are indicative of a second, high frequency component of the CE Rabi nutation, which is indeed visible in the FFT data. The basic frequency is described by

$$\Omega = 2\pi\nu = \gamma_{CE} B_1 = g_{CE}\beta_e B_1 \tag{5.16}$$

of a spin $S = 1/2$ system. It is used here to determine the strength of the B_1 field. For $\nu = 23.46$ MHz (maximum of the basic frequency peak in Fig. 5.30 c)) and $g_{CE} = 1.9978$ we obtain $B_1 = 0.84$ mT. In addition, a small fraction of the spin-locking frequency $\Omega = 2\gamma B_1$ is detected. This frequency is twice as large and is found under experimental conditions that allow a simultaneous manipulation of both spins of the weakly coupled spin pair.

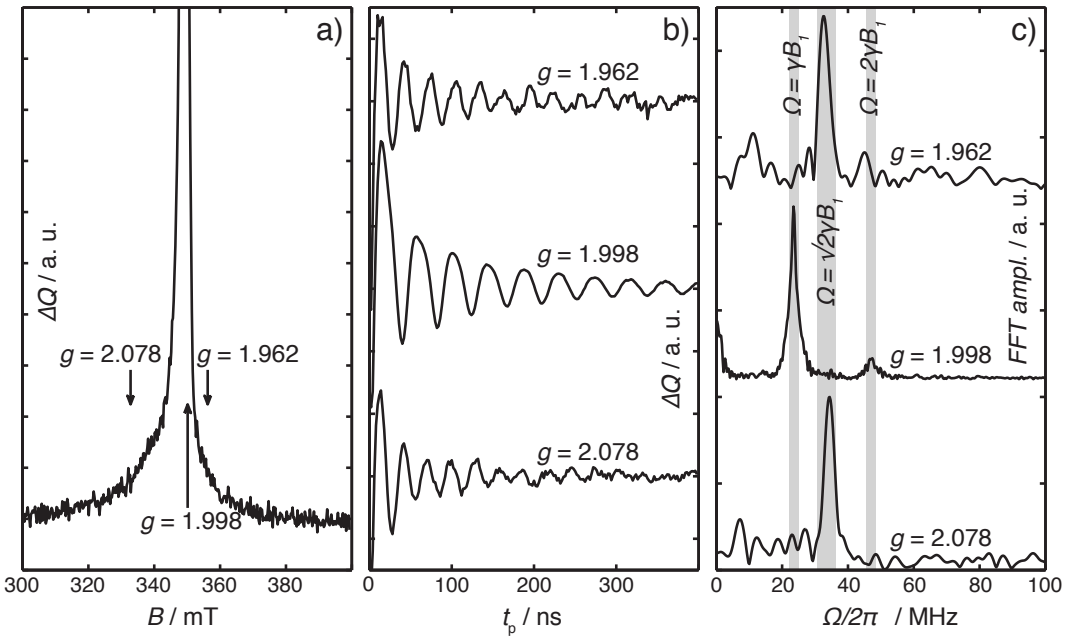

Figure 5.30: a) The 100 mT broad field sweep spectrum measured at X-band. The illustration focusses on the low intensity part to emphasize the V signal, which nearly covers the complete field range. The arrows indicate the field positions for the Rabi experiments. b) The post-processed transient nutations at the chosen field positions are shown between 0 and 400 ns. c) FFT of the time traces. Gray bars mark the frequencies $\Omega = \gamma B_1$ ($S = 1/2$ system), $\Omega = \sqrt{2}\gamma B_1$ ($S = 1$ system) and $\Omega = 2\gamma B_1$ (spin locking frequency of pair of interacting spins $S = 1/2$).

This contribution is clearly visible at $\nu \approx 47$ MHz in the frequency domain (Fig. 5.30 c)).
The Rabi frequencies at $B = 336$ mT and $B = 356$ mT deviate from the frequency expected for a spin $S = 1/2$ system. This can happen in case of off-resonant excitation, which leads to frequencies

$$\Omega_{\text{eff}} = \sqrt{(\gamma_{\text{CE}} B_1)^2 + \Omega_{\text{off}}^2} \tag{5.17}$$

[37, 42] with $\Omega_{\text{off}} = \omega_L - \omega_0$ describing the difference between Larmor ω_L and mw frequency ω_0. The field positions of the V signal Rabi nutations are ≈ 7 and ≈ 13 mT apart from $B_{\text{CE}} = 349.3$ mT which would lead to values of $\nu_{\text{eff}} > 190$ MHz. This is not observed. The big line widths of all signals would, furthermore, average this effect to zero.This means that the V signal could be connected with a spin state $S > 1/2$. To calculate the spin quantum number S we use the dependency of the nutation frequency Ω on the spin

quantum numbers (S, m_S):

$$\Omega = 2\pi\nu = \Omega(m_S, m_S + 1) = \frac{g_i \beta_e B_1}{\hbar} \sqrt{S(S+1) - m_S(m_S+1)} \qquad (5.18)$$

[37]. For $S = 1$ and both allowed transitions ($m_S = -1 \rightarrow m_S = 0$) and ($m_S = 0 \rightarrow m_S = +1$) the Rabi frequency Ω becomes

$$\Omega = 2\pi\nu = \frac{g_i \beta_e B_1}{\hbar} \sqrt{2}. \qquad (5.19)$$

We obtain expected values of $\nu_{th}^{g=1.962} = 32.6$ MHz and $\nu_{th}^{g=2.078} = 34.5$ MHz which are in excellent agreement with the experimental results of $\nu_{exp}^{g=1.962} = 32.5$ MHz and $\nu_{exp}^{g=2.078} = 34.5$ MHz, respectively. The slight shift of the Rabi frequency caused by the differing g-values is directly seen in Fig. 5.30 c). The V center which gives rise to the ≈ 20 mT broad EDMR line can thus be assigned to a paramagnetic center in the triplet $S = 1$ state. The observation of the $S = 1$ transient nutation frequency is in consistence with the large field-independent broadening found in Sec. 5.2 as well as with findings of ODMR triplet signals in microcrystalline silicon in the literature [135, 136]. The considerable number of paramagnetic defects and defect complexes appearing in their light-excited triplet $S = 1$ state which are found in irradiated crystalline silicon can thus be responsible for the V signal in microcrystalline silicon.

5.4.3 Summary

In a first part, the microscopic structure of the light-activated paramagnetic CE center and its participation in spin-dependent hopping transport was studied in a microcrystalline silicon thin-film solar cell. Application of X- and S-band EDMR experiments in combination with numerical simulations of Rabi oscillations indicate that the spin-dependent process takes place between two neighboring CE centers. For sufficiently high microwave power two Rabi frequencies Ω_1 and $\Omega_2 = 2\Omega_1$ show up in the coherent EDMR signals. An analysis of their relative contributions to the Rabi traces suggests that the g-values of both CE spin partners are not correlated for the majority of the EDMR-active pairs. A small fraction of doublet pairs with similar g-values may explain the appearance of a larger Ω_2 contribution than predicted by the simulations.

In a second study the spin quantum number of the center giving rise to the broad V line could be determined unambiguously by the analysis of its Rabi nutation frequency. In comparison to the characteristic frequencies found for weakly coupled spins in neighboring CE centers, we found $\Omega = \sqrt{2}\gamma B_1$ for the V center which is the nutation frequency of a system in its triplet $S = 1$ state.

5.5 Summary

A microcrystalline Si thin-film solar cell was investigated in this chapter with the help of electrically detected magnetic resonance (EDMR) and various applied techniques. In this way the light-activated paramagnetic centers were studied at low temperatures which have influence on charge transport processes in the working device. These centers comprise dangling bonds (db defects, $g_{\mathrm{db}} = 2.0046$) and hole states (h centers, $g_{\mathrm{h}} = 2.0105$) from disordered regions of the material as well as conduction band tail states (CE centers, $g_{\mathrm{CE}} = 1.9978$) and vacancy states (V centers, $g_{\mathrm{V}} = 2.017$) from crystalline grains.
The modulation phase and temperatures dependent cw experiments together with the utilization of the transient current response in pulse experiments allowed a reliable decomposition of the multi-component EDMR spectrum. The extracted characteristic g-values were fully confirmed by measurements at different mw frequencies. The established multi-frequency EDMR was successfully applied and combined with studies of samples made of controlled silicon isotope concentration. Thus, broadening effects based on Zeeman interactions, on hyperfine interactions and on spin-dipolar interaction were distinguished and interpreted with respect to the nature of the defects. ED-ESEEM measurements allowed an assignment of the paramagnetic centers to hydrogen-rich amorphous and hydrogen-poor crystalline regions. Finally, measuring Rabi nutations revealed further details of the transport channels via neighboring CE centers as well as details about the V center spin quantum numbers.
All these studies delivered a variety of related pieces of a puzzle which describes the EDMR-active defect centers in microcrystalline Si. The task of the following chapter will be the combination of these pieces.

6

CONCLUSIONS AND OUTLOOK

6.1 Light-activated Centers and Band Diagram of μc-Si:H

The EDMR studies of the last chapter revealed four completely different paramagnetic centers which are part of different transport channels in the microcrystalline material. The interesting properties of these centers are summarized and discussed in the following. Afterwards, we will draw conclusions about the transport paths via these localized states and will present a schematic band diagram which includes the collected findings about light-activated centers in μc-Si:H thin-film solar cells.

6.1.1 Paramagnetic Centers in Disordered μc-Si:H Regions

The db Center

The microcrystalline Si dangling bond defect (*db center*) was identified by its magnetic parameters g-value ($g_{\mathrm{db}} = 2.0046(3)$) and line width. It is located in the disordered phase, since ESEEM results showed that this defect is influenced by hydrogen in the environment. In addition, measurements at $T = 80$ K showed a strong quenching signal with the identical g-value and line width. This points to a recombination process via dangling bonds. This recombination channel exists at 5 K as well. Nevertheless the transient cur-

rent response shows differences. We suppose that the recombination signal is overlapping with an additional enhancing signal. Possibilities for such processes will be elucidated in Sec. 6.1.3.

The h Center

At the g-value $g_{\mathrm{h}} = 2.0105(5)$ valence band tail states (*h centers*) from the disordered regions within the μc-Si:H material give rise to an EDMR signal. This assignment could be made, because g-value and line widths as well as the modulation phase behavior of the signal in cw experiments agree with the properties of holes in amorphous silicon [100]. The holes interact with distant hydrogen nuclei. This supports the attribution of the h states to the amorphous phase, since bonded hydrogen is incorporated in disordered, but not in crystalline regions [130]. Spin-dependent hopping transport of holes via these localized states is responsible for the EDMR signal. The dipolar coupling between the two spin pair constituents in h centers is quite large compared to the dipolar coupling constants between spins of other transport channels. Mean inter-spin distances between 0.8 and 1.1 nm were found. Aspects of the transport path via h states will be further discussed in the context of the μc-Si:H band diagram in Sec. 6.1.3.

6.1.2 Paramagnetic Centers in Crystalline μc-Si:H Regions

The CE Center

The *conduction electron (CE) center*, named after its initial interpretation [13, 110], gives rise to a resonance at $g_{\mathrm{CE}} \approx 1.998$ in the μc-Si:H EDMR spectra. Spin-dependent hopping of electrons via neighboring CE centers is assumed to constitute the main underlying transport process. Multi-frequency measurements revealed an asymmetric line shape. This particular line shape led us to the suggestion that a size distribution of crystallites accommodating light-activated CE centers is responsible for a g-value distribution and hence for the CE resonance asymmetry. This interpretation is founded on the following points:

1. The value of g_{CE} deviates markedly from the g-value of light-activated conduction band tail states in a-Si:H (*e centers*, $g_{\mathrm{e}} \approx 2.0047$, see chapter 4). Hence, the CE center is assumed to be hosted in regions of different

energetic structure compared to the e center, so that deviations in g can appear.

2. Many silicon-based quantum systems give rise to narrow EPR/EDMR signals possessing g-values at ≈ 1.999 (see Tab. 6.1). In all cases confined electrons in conduction band minima at interfaces (inversion layers) [30, 104, 115, 183, 184] as well as in quantum well and quantum dot structures [119, 185, 186] are the origin of these resonances. It is worth noting that the variation of the g-values among these model systems is remarkably small.

3. Furthermore, different studies show a dependence of g-value and hyperfine couplings of the confined electron spin on the size of the confining particle or quantum well [120, 187–189]. Pereira et al. [120] found a clear change of the phosphorus hyperfine splitting of donors in phosphorus-doped c-Si nanocrystals in dependence of the particle size up to diameters > 10 nm due to dielectric confinement. Baranov et al. studied size-selective samples of ZnO quantum dots (QD diameters between 1.17 and 3 nm) and found an influence on the g-value of the EPR line [187]. In both cases this is a consequence of the modified donor wavefunction localization.

4. n-a-Si:H/p-c-Si structures possess a highly conductive inversion layer inside c-Si at the interface, that is induced by the conduction band mismatch ΔE_C between a-Si:H and c-Si [190]. Numerical calculations showed that for $\Delta E_C > 0.1$ eV this inversion layer occurs. Other studies report about values of $\Delta E_C \approx 0.2$ eV at the n-a-Si:H/p-c-Si interface [191]. EDMR studies of a-Si:H/c-Si solar cells show a resonance line at $g \approx 1.998$ [115], which is likely due to electrons in the inversion layer. Due to the doping of these layers band bending plays an important role, but ΔE_C would lead to a potential well inside the c-Si phase even without doping.

The results of the above mentioned EPR/ EDMR studies on model systems can be combined with the knowledge about μc-Si:H as a composite material of c-Si and a-Si:H [94, 117, 192] and with the results of the EDMR studies of this thesis. This allows to draw the following conclusions:
The CE states are localized within c-Si potential wells and in inversion layers on the c-Si side of a-Si/c-Si interfaces. We believe that CE states are not shallow localized electronic states induced by lattice distortions or crystal

defects as suggested in Ref. [25]. The inversion layers in undoped μc-Si:H are probably formed by band bending effects between crystallites and amorphous regions due to Fermi-level pinning in the middle of the mobility gap [193]. This pinning is caused by the high defect concentration in the disordered films [191, 194, 195]. These CE states act as traps for electrons. When singly occupied, they give rise to the EDMR signal at $g \approx 1.999$. When the electron wave function is restricted to the thin inversions layers at the interfaces or to only some nm small crystallites, confinement effects play a significant role.
The resonances of all model systems mentioned above show symmetric line profiles of significantly smaller widths in comparison to the CE resonance in μc-Si:H (see Tab. 6.1). These devices have perfect crystal structures [196] or distinct layer thicknesses and energy band offsets [104, 115, 119, 186] which results in narrow resonance lines. Transferring these facts to the heterogeneous μc-Si:H material, we conclude that the superposition of such narrow lines with differing magnetic resonance positions can result in a broad asymmetric line profile as found for the CE resonance in microcrystalline Si. Considering the CE resonance g-values of both investigated μc-Si:H solar cells, one can find a difference of $\Delta g = 0.0008$. The CE signal of the μc-Si:H p-i-n cell with n-a-Si:H layer stems from the intrinsic μc-Si:H and is connected with a g-value of $g_{\mathrm{CE}} = 1.9986(3)$. The CE signal of the cell with n-μc-Si:H layer stems from the intrinsic and from the n-μc-Si:H layer and is connected with $g_{\mathrm{CE}} = 1.9978(3)$. This is consistent with the report of Müller et al. [13] in which $g_{\mathrm{CE}} > 1.9980$ is found in undoped microcrystalline material, whereas g_{CE} decreases to values < 1.9980 in n-doped material. This means that the detected discrepancy is not connected with sample-to-sample variations of the g-value but with the different doping conditions of the microcrystalline Si.

The V Center

A very broad resonance called *vacancy (V) signal* at a g-value of roughly $g_{\mathrm{V}} = 2.017$ was found in the EDMR spectra of the μc-Si:H solar cell. The paramagnetic center behind the signal consists of a strongly interacting spin pair giving rise to large unresolved dipolar broadening of $10 - 20$ mT. This corresponds to a mean interspin distance of only ≈ 0.5 nm. The spin pair acts as an $S = 1$ particle which was found out with the help of Rabi nutation studies. Comparing V resonances of samples with isotopically controlled

structure	g-value	ΔB	Ref.
CB electrons in c-Si	1.9995(1)	0.1 mT	[196]
CE centers in a-Si:H/c-Si SC	1.998(1)	0.5 mT	[115]
2DEGs in aFETs	1.9999	< 0.5 mT	[104]
electrons in Si/SiGe NS	≈ 1.9993	< 0.1 mT	[186]
2DEG in $Si/Si_{1-y}C_y$ HS	$\approx 1.9995(1)$	< 0.1 mT	[119]
µc-Si:H p-i-n SC with n-a-Si:H	1.9986(3)	1.4 mT	chapter 4
µc-Si:H p-i-n SC	1.9978(3)	1.4 mT	chapter 5

Table 6.1: X-band line parameters g-value and line width ΔB of EPR and EDMR resonances from Si-based model structures which show g-values at $\approx$ 1.999. In addition, the CE line parameters of both studied solar cells are given. (NS = nanostructure, HS = heterostructure, SC = solar cell).

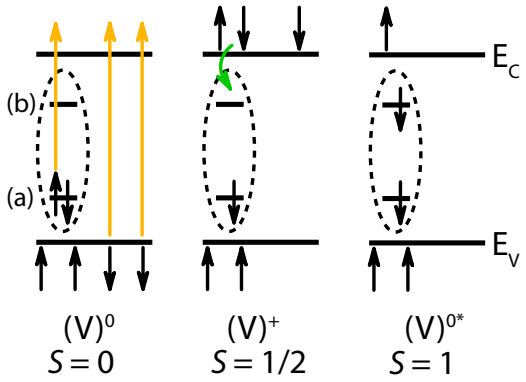

Figure 6.1: Schematic c-Si band diagram with a V center is displayed. Black arrows symbolize the spins in their current states. Colored arrows are used to indicate the subsequent changes: Yellow: optical excitation of charge carriers; green: capture of charge carriers from the conduction band. Further details are given in the text.

^{28}Si concentrations revealed different line shapes. Satellites due to large hyperfine couplings of close Si nuclei could be responsible for this.
Two different vacancy complexes in their photo-excited $S = 1$ triplet state were found as possible candidates for the V centers. Their g-values, dipolar and hyperfine coupling constants correspond to the magnetic parameters of the V center in µc-Si:H. On the one hand, the vacancy-oxygen complex where two of the four broken Si bonds are bridged by an oxygen atom [155]. On the other hand, the vacancy-dihydrogen complex involving two hydrogen atoms passivating two broken bonds [153]. The latter complex could be excluded because of the absence of hydrogen in the center's environment. Because of *natural* oxygen impurities in the material [166], the V centers can

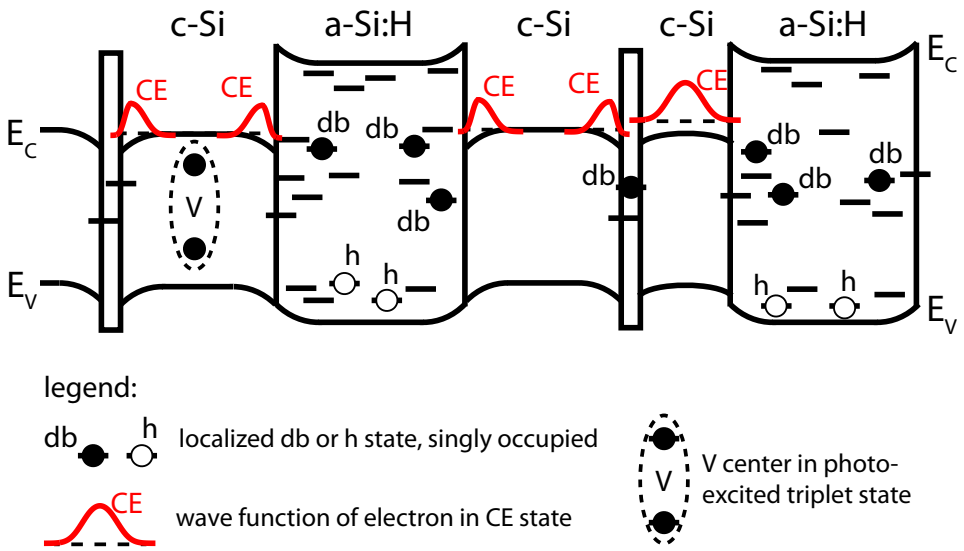

Figure 6.2: Schematic band diagram of microcrystalline silicon. It consists of crystalline (c-Si) and amorphous (a-Si:H) phases. Further details in the text.

probably be identified as the vacancy-oxygen complex.
In the EDMR spectra the V center is observed in its $S = 1$ triplet state. This triplet state has to be formed. As shown in Fig. 6.1 the ground state of this complex V^0 is assumed to be diamagnetic ($S = 0$) and thus EPR-silent. Illumination ionized the V center (V^+). The subsequent capture of an electron from the conduction band can result in formation of an EPR-active triplet state V^{0*} ($S = 1$). The underlying spin-dependent transport process which allows the detection with EDMR is supposed to involve three spins and will be addressed in Sec. 6.1.3.

6.1.3 Band Diagram of μc-Si:H and Spin-Dependent Transport Processes

Schematic Band Diagram of μc-Si:H

In the following, a schematic μc-Si:H band diagram is presented (shown in Fig. 6.2) which is constructed on the basis of the concept given by Finger et al. [130]. It is intended to serve as an illustrative tool for summarizing and discussing the results of this thesis. Here, the defects' location within the heterogeneous material and their energetic positions are of special relevance.

This band diagram includes crystalline (c-Si) regions as well as disordered (a-Si:H) regions. For the c-Si regions the band gap of crystalline Si with a gap energy of 1.1 eV is used. For the a-Si:H regions a density-of-states picture of a-Si:H with a mobility gap of 1.75 eV and tail states near the energy band edges as well as deep defects is utilized [197]. A large band offset between both regions was chosen in the conduction bands. Band bending effects at the a-Si/c-Si interfaces are included in the scheme as discussed regarding the CE center in Sec. 6.1.2. Hence, inversion layers appear at the interfaces. Thin disordered layers between neighboring crystallites are as well included in the scheme. They might give rise to deep defects.
Based on the results of the EDMR studies on μc-Si:H p-i-n solar cells under illumination in Ref. [21, 25] as well as of this work we can include the paramagnetic centers in μc-Si:H into this band diagram as follows:

1. CE states are located in inversion layers and quantum wells of the c-Si phase. Illumination can excite electrons into these states.
2. V complexes are localized in the c-Si band gap. They can occur in an excited triplet state.
3. Dangling bonds are found in the middle of the a-Si:H mobility gap.
4. Holes occupy a-Si:H valence band tail (h) states under illumination conditions.
5. Furthermore, we assume that conduction band tail states (*e states*) as well as localized phosphorus donor (*P states*) and boron acceptor (*B states*) states are all part of the disordered regions. This assumption is explained later.

In the following we will draw conclusions about the transport paths these paramagnetic centers participate in. The schematic band diagram will help to illustrate these conclusions. In turn, we will see that the experimental results can be consistently explained within this model.

Spin-Dependent Transport Channels via CE and V Centers

Strongly coupled spin pairs have only a very small probability to change from the triplet manifold to the singlet manifold and vice versa, since this transition is forbidden. Hence, only transitions within the triplet manifold can give rise to EPR. EDMR signals are not expected when they are solely

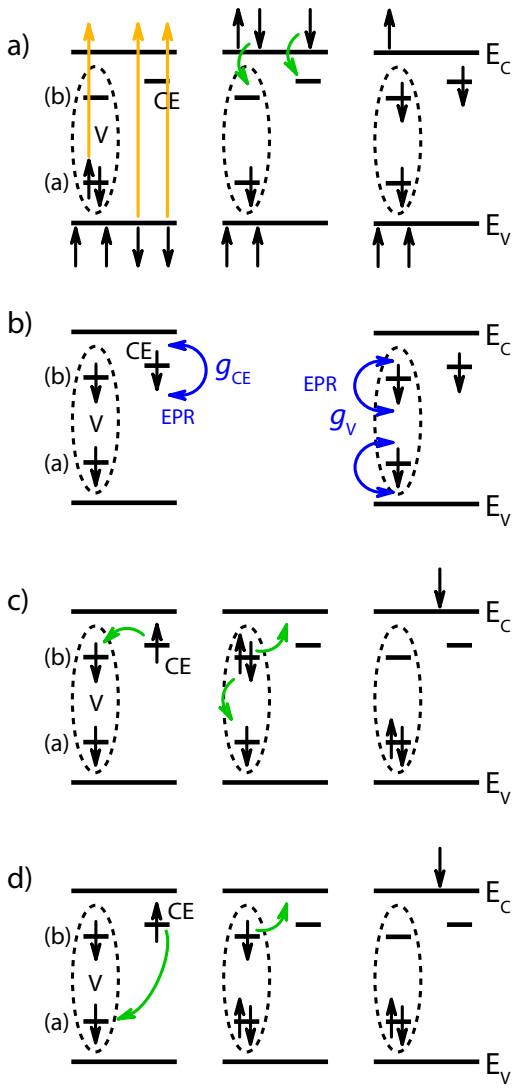

Figure 6.3: Spin-dependent processes involving the V center in its photo-excited $S = 1$ state and the singly occupied CE center. Schematic c-Si band diagrams are displayed. Black arrows symbolize the spins in their current states. Colored arrows are used to indicate the subsequent modification: Yellow: optical excitation of charge carriers; green: spin transitions between different states; blue: EPR manipulation. a) Formation of the starting situation b) The spin states of the V and CE centers can be individually altered by EPR. c) and d) Spin-dependent processes involving the V and CE centers. Details are given in the text.

based on a strongly coupled spin pair, since here the signal intensity depends on the amount of singlet pairs created by spin manipulation. Therefore, it is surprising to find EDMR signals of the photo-excited V center

which clearly acts as an $S = 1$ system. The spin-dependent process behind the signal cannot be based on the two strongly interacting spins only. Hence we will introduce a spin-dependent transport model which involves an additional third spin.
The model is based on the approach of Vranch et al. and Behrends [43, 83], as described in Sec. 2.3.3. Assuming a center in its $S = 1$ triplet state spatially sufficiently close to an additional singly occupied localized center ($S = 1/2$), a three spin system is formed. In the present example the V center in its photo-excited $S = 1$ triplet state is located in the crystalline phase. Thus, the only additional paramagnetic center at hand is the CE center. This three spin system can exist in different spin configurations. Some of them constitute the basis for spin-dependent processes which, in turn, are necessary for detecting EDMR.
Fig. 6.3 a) shows the initial configuration. Light excites charge carriers into the conduction band. The V center is ionized by illumination. Subsequently, a charge carrier is trapped in the localized CE state near the conduction band. The ionized V center captures a spin creating an excited $S = 1$ triplet state V^{0*}. In the final configuration all spins are parallel so that no spin pair out of the three possible pairs is in a singlet configuration. No spin-dependent transition can take place and, thus, no EDMR signal in detected. This three spin configuration constitutes the starting point for the following considerations.
Spin manipulation of either the CE center in its $S = 1/2$ state or of the V center in its $S = 1$ state comes into play now as illustrated in Fig. 6.3 b). The three-spin configurations are changed, so that spin-dependent processes take place with larger probability. In Fig. 6.3 c) and d) the spin configuration resulting after the spin manipulation of the CE center is given in place of all equivalent three-spin configurations. Starting from here, two possibilities of spin-dependent processes exist.
In Fig. 6.3 c) the spin in the CE state passes over into state (b) of the V center. Subsequently, the V center is converted into its $S = 0$ ground state in two steps. One spin from state (b) returns to the energetically lower state (a). The excess energy that is released by this recombination step might be transferred through an Auger process to the third spin which is still in the high energy level (b) of the V center. The third spin is thereby excited to the conduction band and participates in charge transport.
Fig. 6.3 d) shows the same starting situation, but here the spin of the CE center passes over into state (a) of the V center. The released energy can be

transferred to the remaining spin in state (b). This spin is emitted into the conduction band and contributes to the conductivity.
In principle the weakly allowed $\Delta m_S = \pm 2$ transition of the V center should as well give rise to an EDMR signal within this model. However, this signal at $g \approx 4$ was not found until now. This might be due to the strong dependence of the signal intensity on the dipolar coupling parameters D and E. When these parameters are too small, the transition is forbidden and no signal is detected. Even when a resonance of small intensity should be detected, it will be broadened by various strain effects and finally become undetectable.
In both sequences described above, the transition of the V center from its excited triplet state back to its singlet ground state leads to an additional electron in the conduction band which contributes to the current through the sample. This might be connected with a positive EDMR signal, which is indeed observed (see Fig. 5.9 c)). This positive transient current response is furthermore connected with time constants which are fast compared to the other signals' time constants. It indicates the excitation of the third spin into states in or very close to the conduction band where it efficiently contributes to the current.
As reported by Boulitrop et al. the V resonance in μc-Si:H can be detected in ODMR measurements [136]. The signal is found when observing the photoluminescence (PL) intensity at an energy of 0.75 eV as function of the magnetic field. Interestingly, the CE resonance is found under the same ODMR conditions. At other PL energies both resonances cannot be detected, which means that the observed spin-dependent process involves V and CE centers and is connected with PL energies around 0.75 eV.
These findings fit well into the presented model, since the excess energy from the transition of the V center from its excited triplet state V^{0*} back to its singlet ground state V^0 can, of course, be emitted in form of a photon. Conclusively, the energy of 0.75 eV would be the energy difference between the states V^{0*} and V^0. This emission of photons will be observed whenever the CE or the V center is in spin resonance and thereby activates the recombination step. This additional photon should give rise to an enhancing ODMR signal (PL intensity change $\Delta I > 0$). It is observed as illustrated in Ref. [136]. These results are further corroborated by ODMR studies of the VO complex which show PL energies in the same range [155].

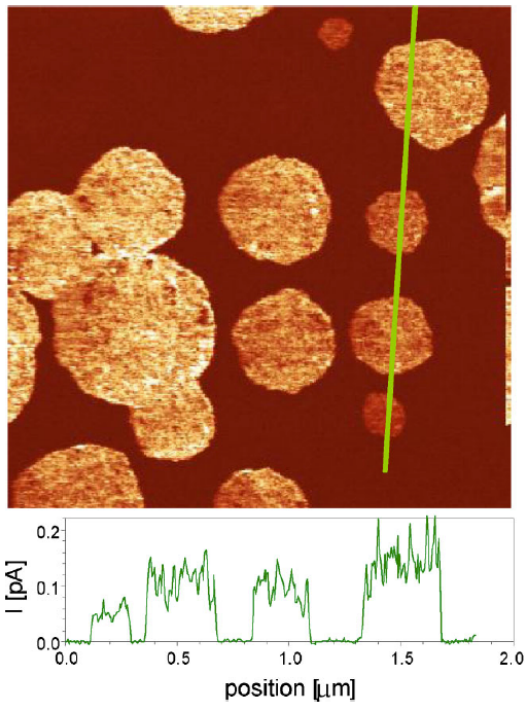

Figure 6.4: Local current map of a μc-Si:H sample (2×2 μm^2) measured with the Conductive (C)-AFM (-0.7 V bias). Conductive (white) crystalline Si grains are observed in non-conductive a-Si:H based tissue. The plot shows the current flow along the line in the map. The images are from Ref. [198].

Spin-Dependent Transport Channels via CE Centers

The EDMR spectra show a CE signal which is connected with an enhancement of the sample conductivity under spin resonance conditions. A spin-dependent hopping transport between neighboring CE centers is responsible for this EDMR signal, which could be shown with Rabi nutation measurements (see Sec. 5.4.1). The spin pairs can consist of CE centers from different crystallites, but also of centers from the same crystallite.
These centers are located in c-Si quantum wells and inversion layers (see Sec. 6.1.2). They are considered to be highly conductive [190]. Thus, it is probable that the transport path via the crystalline grains contributes a significant part to the sample conductivity at low temperatures. This is consistent with the increase of the μc-Si:H conductivity as function of the crystalline volume fraction I_c [195] as well as with the increase of the EPR CE signal intensity as function of the conductivity [113].
The question where the current flow takes place within the heterogeneous

μc-Si:H material is still frequently discussed. Several groups carried out conductive atomic force microscopy (C-AFM) measurements on undoped μc-Si:H samples with different values of I_c to study this phenomenon [198–201].
Interestingly, Kočka et al. [198, 200] could show that in μc-Si:H samples the current flows predominantly inside the Si crystallites. The a-Si:H matrix is characterized by low conductivities. Fig. 6.4 showing C-AFM images from Ref. [198] illustrates this very well. On the contrary, other studies showed that the amorphous tissue and grain boundaries are conductive and dominate the transport based on the observation of conductive rings at the grain boundaries [199]. But this observation was assigned to an oxidation effects during a C-AFM measurement with high bias voltages and does not reflect the natural conductivity conditions in μc-Si:H films at low voltages [200].
Hence, the C-AFM results of conductive grains within the non-conductive a-Si:H matrix constitute a confirmation of the EDMR results of previous studies [21, 25] and of the present work.

Spin-Dependent Transport Channels involving db Centers

The dangling bond defect which is localized in the disordered phase of μc-Si:H is a deep defect and, thus, acts as an effective charge carrier recombination center, as we clearly saw in the 80 K EDMR spectra (Fig. 5.10 b)). However, at $T = 5$ K the transient current response of the db center seems to consist of two contributions (see Fig. 5.9 b)): a positive and relatively fast response (enhancing signal) as well as a negative but slow current response (quenching signal). This slow contribution is observed at $T = 80$ K as well. Further, we see that both 5 K contributions are quite independent, since the negative part dominates at high light intensities, whereas the positive part dominates at low illumination strengths. This can be interpreted in the following way: The db defect participates in two spin-dependent processes at low temperatures. On the one side, it is part of charge carrier recombination processes connected with a quenching signal. On the other side, it is part of hopping processes between CE and db centers, giving rise to an enhancing signal. This interpretation is based on several reasons.
For samples with crystalline volume fractions I_c below $\approx 70\%$ current routes partly pass through regions which are characterized by isolated crystallites

embedded in the relatively insulating and db-rich a-Si:H matrix [202].
According to our EDMR results, low temperature transport through a-Si:H regions involves localized states in the a-Si:H mobility gap comprising db and h centers. Conduction band tail states (e centers) are not involved.
Furthermore, in different studies CE as well as db resonances were simultaneously measured in EPR spectra of unlighted undoped and n-doped μc-Si:H powder samples [110, 111, 113, 130, 203]. Finger et al. argued [130] that both the db and CE states are, hence, found near the Fermi level so that they are singly occupied and paramagnetic with high probability.
Different studies show that the defect concentration in μc-Si:H increases as function of I_c [191, 194], which means that the disordered layers and regions are overproportionally rich in defects. Finally, hopping transport via neighboring db defects was already found in a-Si:H [71]. These three facts support the argumentation for transport via localized db centers. Hence, we assign the enhancing signal of the db current transient to the hopping process via CE and db centers. A major part of the enhancing signal can indeed be due to spin-dependent hopping between CE centers in the crystalline grains and db defects at the a-Si:H/c-Si interface or in the a-Si:H regions, since the enhancing signals of both resonances show comparable times constants. If this transport path via CE and db centers crosses only thin db-rich disordered layers between crystallites or includes larger amorphous regions, cannot be said on the basis of the EDMR results.

Spin-Dependent Transport Channels via h Centers

The h signal in the EDMR spectra is an enhancing signal. It is assumed to be caused by a spin-dependent hopping transport of holes via localized valence band tail states [21]. The time constants of the transient current response in the present study (see Fig. 5.9) deviate significantly from those of the other signals and are thus characteristic for the h signal. This means, the h centers are probably not involved in other spin-dependent transport paths. The long time constants are indicative for a process in the a-Si:H matrix owing to the smaller conductivity of this material compared to c-Si. If the transport path via the a-Si valence band tail states crosses crystalline parts cannot be answered. This critically depends on the valence band energy offset between both material.

Conduction Band Tail States and Phosphorus Donor States in n-Doped μc-Si:H

We saw that the main transport paths via localized states at low temperatures include CE, db and h centers. However, the EDMR measurements on p-i-n μc-Si:H solar cells gave no indication for a-Si:H conduction band tail states (e centers) and phosphorus donor states (P centers), although they are expected to exist in amorphous regions and phosphorus doped layers. EPR experiments on n-doped μc-Si:H samples [110, 113, 130] resolved db and CE signals only, but did not reveal tail state signals and ^{31}P hyperfine satellites. On the contrary, both centers are found in n-a-Si:H samples (see chapter 4 and Ref. [197]).
A possible explanation is found when considering the Fermi level E_F in the material. The schematic band structure in Fig. 6.2 shows a band offset between amorphous and crystalline Si conduction bands. Such an offset was already applied for a qualitative model of μc-Si:H by Finger et al. [130] and justified by the simultaneous detection of db and CE resonances in undoped and n-doped samples.
In undoped μc-Si:H E_F is found in the middle of the mobility gap which gives rise to the dangling bond EPR signal. Negative doping introduces additional electrons and should results in a significant shift of E_F towards higher energies. For higher phosphorus doping concentrations the CE signal appears and its intensity increases [13, 110, 113, 130]. The P donor signal does not appear together with the CE line. This means that the P atoms cannot be located in the crystalline phase, because P donor states near the c-Si conduction band and hyperfine satellites split by 4.2 mT in the EPR and EDMR spectra would be expected [168]. Hence, the P atoms are part of the amorphous phase.
In principle, conduction band tails states and P donor states in the a-Si:H regions should be detected in the n-doped μc-Si:H material when the doping concentration is sufficiently high. But the shift of E_F in μc-Si:H is small, even for high doping concentrations. Probably, the high defect and CE state density in this material pins the Fermi level close to the middle of the gap. Korte et al. could show [191], that strong phosphorus doping leads to a minimum achievable distance between E_F and the amorphous Si conduction band E_C of $\approx$ 360 meV in a-Si:H/c-Si structures. Since tail states and P donor states in a-Si:H are located $0.0 - 0.2$ eV below E_C, these states stay probably unoccupied and P donor states remain ionized. Following this idea they cannot

be detected with EPR and EDMR. Even under illumination, when charge carriers are excited into these states, they cannot be observed with EDMR, because they do not participate in spin-dependent transport through the material. In addition, there was no indication for distant P nuclei in the environment of h and db centers from a-Si:H. This is likely justified by the limited detection radius of < 1 nm for ED-ESEEM experiments.

6.2 Summary and Outlook

In the present thesis paramagnetic centers in thin-film solar cells made of microcrystalline silicon were investigated. Therefore, we combined the electron paramagnetic resonance spectroscopy (EPR) with the photo current measurement of the device yielding electrically detected magnetic resonance (*EDMR*). Furthermore, we carried out experiments at microwave frequencies ranging over two orders of magnitude (*multi-frequency EDMR*). Together with techniques like ESEEM and Rabi nutation experiments we had a powerful tool at hand to study the defects in microcrystalline silicon. The experiments at low temperatures and under illumination conditions revealed four different paramagnetic species which contribute to spin-dependent transport processes in μc-Si:H. The combination of sensitive current measurement and selective EPR spectroscopy allowed insights about the microscopic structure of the defects' environment and the character of the transport channels they are part of. In the end, we were able to present a schematic band diagram of microcrystalline Si which is consistent with all results regarding the microscopic structure of the defects, their energetic position and their transport processes. The most relevant conclusions of the overall evaluation are:

1. CE and V center are assigned to crystalline regions, whereas db and h centers are found in the amorphous regions of the microcrystalline Si composite material.

2. Mean inter-spin distances of $\approx$ 0.5 nm for the V center and of $\approx 1-2$ nm for the remaining centers were estimated from dipolar line broadening effects.

3. From the particular properties of the CE line it was concluded that the corresponding states are located in inversion layers and potential wells close to the c-Si conduction band.

4. Vacancy complexes (called *V centers*) in the c-Si regions are EPR-active when photo-excited in the triplet state. They show strong analogy to so-called vacancy-oxygen (VO) centers in irradiated c-Si. V centers participate in spin-dependent transport together with CE centers close by.

5. CE centers are involved in three-spin processes together with V complexes, in transport processes including db defects as well as in hopping transport via neighboring CE centers.

6. Dangling bond defects in μc-Si:H can act as recombination centers. Charge transport processes via db and CE centers are possible as well.

7. Conduction band tail (e) states and P donor states in the a-Si:H phase are not involved in transport, since they are not occupied. Hence, they are EDMR-inactive.

The results regarding the CE center as well as the V complex are of particular relevance for the further development of thin-film solar cells based on μc-Si:H and for new approaches of PV technology.
The result that CE centers are accommodated in inversion layer and quantum well/ quantum dot structures extends the understanding of microcrystalline silicon as a composite material and the charge carrier transport therein. The two-phase model shown in Fig. 6.2, which was already presented in earlier studies [130], gets new support. Hence, μc-Si:H can be seen as a material with two band gaps, in which the charge carrier transport takes place predominantly in the crystalline regions. But transport paths can even cross disordered, less conductive regions as could be shown by the example of CE-db transport. These are important details for a further development of percolation models for composite materials like microcrystalline silicon [202, 204, 205].
New solar cell concepts have the aim to use tailor-made band gap materials for additional layers in tandem solar cells to facilitate a more efficient usage of the solar spectrum. This band gap engineering makes use of energy confinement of e.g. Si based quantum dot nanostructures in oxide or nitride matrices [2, 206]. Here the knowledge about CE centers and their properties in μc-Si:H can be helpful for a research of these quite similar taylor-made material.
The vacancy (V) complex in the crystalline zones shows strong analogy to the oxygen-vacancy (VO) centers found in irradiated c-Si which raises new

questions: How does the V center influence the conductivity of microcrystalline silicon? Does it act as a trap of photo-excited charger carriers? Furthermore, the V center can possibly help to answer the question of the role of oxygen impurities in microcrystalline Si [166, 200].
Finally, we turn to the relevance of the multi-frequency EDMR approach chosen here. It could be shown in the framework of this work, that particularly the pulse EDMR experiments carried out at various mw frequencies delivered many information about the studied defects in the device. The extraordinary advantage of this method is the ability to decompose multi-component spectra, to resolve g-anisotropy, to identify hyperfine and spin-spin interactions and to separate between different line broadening effects within one series of EDMR measurements at appropriate mw frequencies. The application of sophisticated detection schemes like ENDOR or ESEEM allows even further insights. Despite some requirements regarding the sample design to be compatible with the EDMR setups, this technique will be of importance in the field of semiconductor devices. Fortunately, there are many possibilities of multi-frequency EDMR applications within this field.
Two possible candidates in the new field of emerging PV should be mentioned here. Both solar cells concepts are especially appropriate, since they utilize materials made of light elements like silicon, carbon and hydrogen. These elements give rise to only small influence of spin-orbit coupling which allows an access to the magnetic parameters of the spins in the device.
First, organic solar cells. There are already reports about multi-frequency EPR on different polymer and fullerene materials [207] which are used in form of blends in organic solar cells. Hence, a next step would be the investigation of fully processes OPV devices with multi-frequency EDMR to study the charge carrier separation and loss processes. Second, we like to mention hydrid solar cells consisting of blends of inorganic nanocrystals and polymers [206, 208] in the field of quantum dot cells. Here, especially systems involving Si nanocrystals are of interest [209, 210] for the investigation with multi-frequency EDMR.

This work about multi-frequency EDMR applied to thin-film microcrystalline Si solar cells should make a contribution to the further development of this versatile technique to aim for a more detailed device investigation.

7

APPENDIX

7.1 Coherent Spin Motion of a Spin $S = 1$

In section 2.2.2 the results of Rabi frequency calculations of different spin ensembles were briefly summarized. They were obtained with the help of the density matrix approach [37, 42]. Detailed calculations of Rabi oscillations including selective and non-selective excitation of weakly coupled spin pairs against the background of EDMR were already presented in a recent thesis [43]. As a counterpart of uncoupled spin pairs ($S_1 = 1/2, S_2 = 1/2$), whose properties well describe weakly coupled spin pairs observed in EPR, an $S = 1$ system is appropriate to describe spin pairs in the strong coupling limit. Beside weakly coupled spin pairs, pairs showing $S = 1$ characteristics (e.g. via nutation frequencies) are observed in the solar cells investigated here. Taking this up, the density matrix formalism is utilized here to calculate Rabi frequencies regarding selective transitions $\Delta m_S = \pm 1$ of a spin $S = 1$. The mw manipulation can be described by the interaction of the spin system with the spin operator S_x assuming $\mathbf{B}_1$ to be parallel to the **x**-axis. The rotation operator representation $R_x(\phi)$ of the S_x operator is used to calculate the evolution of the initial density matrix ρ^i under the influence of mw radiation. Here $\phi = \omega_1 t$ stands for the rotation angle. The density matrix transforms as

$$\rho^f = R_x(\phi)\rho^i R_x(\phi)^\dagger = R_x(\phi)\rho^i R_x(-\phi) \tag{7.1}$$

delivering the final density matrix ρ^f. For the initial state of the spin ensemble we define

$$\rho^i = \begin{pmatrix} 0 & 0 & 0 \\ 0 & 0 & 0 \\ 0 & 0 & 1 \end{pmatrix} \tag{7.2}$$

which means that all spins are in the triplet $|\downarrow\downarrow\rangle$ state. To consider only the transition $m_S = -1 \leftrightarrow m_S = 0$ the matrix of S_x

$$S_x = \frac{1}{2} \begin{pmatrix} 0 & \sqrt{2} & 0 \\ \sqrt{2} & 0 & \sqrt{2} \\ 0 & \sqrt{2} & 0 \end{pmatrix} \tag{7.3}$$

must be truncated yielding

$$S_x^{m_S=-1\leftrightarrow 0} = S_x^{tr} = \frac{1}{2} \begin{pmatrix} 0 & 0 & 0 \\ 0 & 0 & \sqrt{2} \\ 0 & \sqrt{2} & 0 \end{pmatrix} \tag{7.4}$$

The rotation matrix is obtained by

$$\begin{aligned} R_x^{tr}(\omega_1 t) &= \sum_{n=0}^{\infty} \frac{(i\phi S_x^{tr})^n}{n!} \\ &= \begin{pmatrix} 1 & 0 & 0 \\ 0 & 1 & 0 \\ 0 & 0 & 1 \end{pmatrix} + i \sum_{n=0}^{\infty} \frac{(-1)^n \left(\frac{\phi}{\sqrt{2}}\right)^{2n+1}}{(2n+1)!} \begin{pmatrix} 0 & 0 & 0 \\ 0 & 0 & 1 \\ 0 & 1 & 0 \end{pmatrix} \\ &\quad + \sum_{n=1}^{\infty} \frac{(-1)^n \left(\frac{\phi}{\sqrt{2}}\right)^{2n}}{(2n)!} \begin{pmatrix} 0 & 0 & 0 \\ 0 & 1 & 0 \\ 0 & 0 & 1 \end{pmatrix} \\ &= \begin{pmatrix} 1 & 0 & 0 \\ 0 & 1 & 0 \\ 0 & 0 & 1 \end{pmatrix} + i \sin\left(\frac{\phi}{\sqrt{2}}\right) \begin{pmatrix} 0 & 0 & 0 \\ 0 & 0 & 1 \\ 0 & 1 & 0 \end{pmatrix} + \left(\cos\left(\frac{\phi}{\sqrt{2}}\right) - 1\right) \begin{pmatrix} 0 & 0 & 0 \\ 0 & 1 & 0 \\ 0 & 0 & 1 \end{pmatrix} \\ &= \begin{pmatrix} 1 & 0 & 0 \\ 0 & \cos\left(\frac{\phi}{\sqrt{2}}\right) & i\sin\left(\frac{\phi}{\sqrt{2}}\right) \\ 0 & i\sin\left(\frac{\phi}{\sqrt{2}}\right) & \cos\left(\frac{\phi}{\sqrt{2}}\right) \end{pmatrix} \end{aligned}$$

Now we can determine the evolution of the density matrix under rotation of an angle ϕ:

$$\begin{aligned}
\rho^f &= R_x^{\mathrm{tr}}(\phi)\rho^i R_x^{\mathrm{tr}}(-\phi) \\
&= \begin{pmatrix} 1 & 0 & 0 \\ 0 & \cos\left(\frac{\phi}{\sqrt{2}}\right) & i\sin\left(\frac{\phi}{\sqrt{2}}\right) \\ 0 & i\sin\left(\frac{\phi}{\sqrt{2}}\right) & \cos\left(\frac{\phi}{\sqrt{2}}\right) \end{pmatrix} \cdot \begin{pmatrix} 0 & 0 & 0 \\ 0 & 0 & 0 \\ 0 & 0 & 1 \end{pmatrix} \cdot \begin{pmatrix} 1 & 0 & 0 \\ 0 & \cos\left(\frac{\phi}{\sqrt{2}}\right) & -i\sin\left(\frac{\phi}{\sqrt{2}}\right) \\ 0 & -i\sin\left(\frac{\phi}{\sqrt{2}}\right) & \cos\left(\frac{\phi}{\sqrt{2}}\right) \end{pmatrix} \\
&= \begin{pmatrix} 0 & 0 & 0 \\ 0 & \sin^2\left(\frac{\phi}{\sqrt{2}}\right) & i\cos\left(\frac{\phi}{\sqrt{2}}\right)\sin\left(\frac{\phi}{\sqrt{2}}\right) \\ 0 & -i\cos\left(\frac{\phi}{\sqrt{2}}\right)\sin\left(\frac{\phi}{\sqrt{2}}\right) & \cos^2\left(\frac{\phi}{\sqrt{2}}\right) \end{pmatrix}.
\end{aligned}$$

We can see that the population of the triplet state $|\downarrow\downarrow\rangle$ under the influence of mw radiation ($\phi = \omega_1 t$) oscillates regarding the transition $m_S = -1 \leftrightarrow m_S = 0$ with

$$\rho_{33}^f = \cos^2\left(\frac{\omega_1 t}{\sqrt{2}}\right) = \frac{1}{2}(1 + \cos(\sqrt{2}\omega_1 t)). \tag{7.5}$$

The same Rabi frequency $\Omega = \sqrt{2}\omega_1$ is obtained when exciting the transition $m_S = 0 \leftrightarrow m_S = +1$. Thus, the Rabi frequency of the $S = 1$ system is a factor of $\sqrt{2}$ larger than the Rabi frequency of a spin $S = 1/2$.

BIBLIOGRAPHY

[1] L. El Chaar, L. A. Lamont, and N. El Zein: *Review of photovoltaic technologies*. Renewable & Sustainable Energy Reviews **15**, 2165–2175 (2011).

[2] G. Conibeer, M. Green, R. Corkish, Y. Cho, E. C. Cho, C. W. Jiang, T. Fangsuwannarak, E. Pink, Y. D. Huang, T. Puzzer, T. Trupke, B. Richards, A. Shalav, and K. L. Lin: *Silicon nanostructures for third generation photovoltaic solar cells*. Thin Solid Films **511**, EMRS (2006).

[3] J. Meier, R. Flückiger, H. Keppner, and A. Shah: *Complete Microcrystalline p-i-n Solar Cell - Crystalline or Amorphous Cell Behavior*. Appl. Phys. Lett. **65**, 860-862 (1994).

[4] A. Shah, P. Torres, R. Tscharner, N. Wyrsch, and H. Keppner: *Photovoltaic technology: The case for thin-film solar cells*. Science **285**, 692-698 (1999).

[5] O. Vetterl, F. Finger, R. Carius, P. Hapke, L. Houben, O. Kluth, A. Lambertz, A. Muck, B. Rech, and H. Wagner: *Intrinsic microcrystalline silicon: A new material for photovoltaics*. Solar Energy Materials and Solar Cells **62**, 97–108 (2000).

[6] Y. Mai, S. Klein, R. Carius, H. Stiebig, X. Geng, and F. Finger: *Open circuit voltage improvement of high-deposition-rate microcrystalline silicon solar cells by hot wire interface layers*. Applied Physics Letters **87**, 073503 (2005).

[7] D. E. Carlson and C. R. Wronski: *Amorphous Silicon Solar Cell*. Appl. Phys. Lett. **28**, 671-673 (1976).

[8] V. Smirnov, A. Lambertz, B. Grootoonk, R. Carius, and F. Finger: *Microcrystalline silicon oxide (μc-SiO_x:H) alloys: A versatile material for application in thin film silicon single and tandem junction solar cells*. Journal of Non-crystalline Solids **358**, 1954-1957 (2012).

[9] Fanny Meillaud, Adrian Billet, Corsin Battaglia, Mathieu Boccard, Grègory Bugnon, Peter Cuony, Mathieu Charrière, Matthieu Despeisse, Laura Ding, JordiEscarre-Palou, Simon Hänni, Linus Löfgren, Sylvain Nicolay, Gaetano

Parascandolo, Michael E. Stückelberger, and Christophe Ballif: *Latest Developments of High-Efficiency Micromorph Tandem Silicon Solar Cells Implementing Innovative Substrate Materials and Improved Cell Design*. IEEE Journal of Photovoltaics **2**, 236-240 (2012).

[10] Martin A. Green, Keith Emery, Yoshihiro Hishikawa, Wilhelm Warta, and Ewan D. Dunlop: *Solar cell efficiency tables (version 42)*. Progress In Photovoltaics **21**, 827–837 (2013).

[11] F. Finger, L. B. Neto, R. Carius, T. Dylla, and S. Klein: *Paramagnetic defects in undoped microcrystalline silicon*. phys. stat. sol. (c) **1**, 1248-1254 (2004).

[12] T. Umeda, S. Yamasaki, J. Isoya, and K. Tanaka: *Electron spin-resonance center of dangling bonds in undoped a-Si:H*. Phys. Rev. B **59**, 4849-4857 (1999).

[13] J. Müller, F. Finger, R. Carius, and H. Wagner: *Electron spin resonance investigation of electronic states in hydrogenated microcrystalline silicon*. Phys. Rev. B **60**, 11666-11677 (1999).

[14] W. Fuhs: *Recombination and transport through localized states in hydrogenated amorphous and microcrystalline silicon*. J. Non-Cryst. Solids **354**, 2067-2078 (2008).

[15] M. Fehr, A. Schnegg, B. Rech, K. Lips, O. Astakhov, F. Finger, G. Pfanner, C. Freysoldt, J. Neugebauer, R. Bittl, and C. Teutloff: *Combined multifrequency EPR and DFT study of dangling bonds in a-Si:H*. Phys. Rev. B **84**, 245203 (2011).

[16] J. Schmidt and I. Solomon: *Modulation De La Photoconductivite Dans Le Silicium a Basse Temperature Par Resonance Magnetique Electronique Des Impuretes Peu Profondes*. Compt. Rend. Acad. Sci. B **263**, 169 (1966).

[17] M. Stutzmann, M. S. Brandt, and Bayerl M. W.: *Spin-dependent processes in amorphous and microcrystalline silicon: A survey*. J. Non-Cryst. Solids **266-269**, 1 (2000).

[18] C. Boehme and K. Lips: *Time domain measurement of spin-dependent recombination*. Appl. Phys. Lett. **79**, 4363 (2001).

[19] C. Boehme and K. Lips: *Theory of time-domain measurement of spin-dependent recombination with pulsed electrically detected magnetic resonance*. Phys. Rev. B **68**, 245105 (2003).

[20] J. Behrends, A. Schnegg, C. Boehme, S. Haas, H. Stiebig, F. Finger, B. Rech, and K. Lips: *Recombination and transport in microcrystalline pin solar cells studied with pulsed electrically detected magnetic resonance*. Journal of Non-crystalline Solids **354**, 2411–2415 (2008).

[21] J. Behrends, A. Schnegg, M. Fehr, A. Lambertz, S. Haas, F. Finger, B. Rech, and K. Lips: *Electrical detection of electron spin resonance in microcrystalline silicon pin solar cells*. Philosophical Magazine **89**, 2655–2676 (2009).

[22] H. Huebl, F. Hoehne, B. Grolik, A. R. Stegner, M. Stutzmann, and M. S. Brandt: *Spin echoes in the charge transport through phosphorus donors in silicon*. Phys. Rev. Lett. **100**, 177602 (2008).

[23] F. Hoehne, H. Huebl, B. Galler, M. Stutzmann, and M. S. Brandt: *Spin-Dependent Recombination between Phosphorus Donors in Silicon and Si/SiO_2 Interface States Investigated with Pulsed Electrically Detected Electron Double Resonance*. Phys. Rev. Lett. **104**, 046402 (2010).

[24] F. Hoehne, L. Dreher, H. Huebl, M. Stutzmann, and M. S. Brandt: *Electrical Detection of Coherent Nuclear Spin Oscillations in Phosphorus-Doped Silicon using Pulsed ENDOR*. Phys. Rev. Lett. **106**, 187601 (2011).

[25] M. Fehr, J. Behrends, S. Haas, B. Rech, K. Lips, and A. Schnegg: *Electrical detection of electron-spin-echo envelope modulations in thin-film silicon solar cells*. Physical Review B **84**, 193202 (2011).

[26] Max Suckert, Felix Hoehne, Lukas Dreher, Markus Kuenzl, Hans Huebl, Martin Stutzmann, and Martin S. Brandt: *Electrically detected double electron-electron resonance: exchange interaction of ^{3}1P donors and P_{b0} defects at the Si/SiO_2 interface*. Molecular Physics **111**, (2013).

[27] D. R. McCamey, H. Huebl, M. S. Brandt, W. D. Hutchison, J. C. McCallum, R. G. Clark, and A. R. Hamilton: *Electrically detected magnetic resonance in ion-implanted Si:P nanostructures*. Applied Physics Letters **89**, 182115 (2006).

[28] G. B. Silva, L. F. Santos, R. M. Faria, and C. F. O. Graeff: *EDMR of MEH-PPV LEDs*. Physica B-condensed Matter **308**, 1078–1080 (2001).

[29] M. S. Brandt, S. T. B. Goennenwein, T. Graf, H. Huebl, S. Lauterbach, and M. Stutzmann: *Spin-dependent transport in elemental and compound semiconductors and nanostructures*. Phys. stat. sol. (c) **1**, 2056–2078 (2004).

[30] W. J. Wallace and R. H. Silsbee: *Spin Resonance of Inversion-Layer Electrons in Silicon*. Physical Review B **44**, 12964–12968 (1991).

[31] I. Solomon: *Spin-dependent Recombination in a Silicon Para-Normal Junction*. Solid State Communications **20**, 215–217 (1976).

[32] D. Kaplan, I. Solomon, and Mott N. F.: *Explanation of Large Spin-Dependent Recombination Effect in Semiconductors*. Journ. de Phys. Lettr. **39**, L51 (1978).

[33] S. Stoll and A. Schweiger: *EasySpin, a comprehensive software package for spectral simulation and analysis in EPR*. Journal of Magnetic Resonance **178**, 42–55 (2006).

[34] A. Carrington and A. D. McLachlan: *Introduction to Magnetic Resonance*. John Wiley & Sons, Inc. New York (1979).

[35] John A. Weil and James R. Bolton: *Electron Paramagnetic Resonance - Elementary Theory and Practical Applications*. John Wiley & Sons, Inc. Hoboken, New Jersey (2007).

[36] A. Abragam: *Principles of Nuclear Magnetism*. Oxford University Press Inc., New York (2011).

[37] A. Schweiger and G. Jeschke: *Principles of Pulse Electron Paramagnetic Resonance*. Oxford University Press (2001).

[38] J. D. Jackson: *Classical Electrodynamics*. John Wiley and Sons, Inc., New York (1962).

[39] C. Kittel: *Introduction to Solid State Physics*. John Wiley & Sons, Inc. (2005).

[40] G. Zwanenburg and P. J. Hore: *Analytical Theory of Electron Spin Echo Modulations in Correlated Radical Pairs*. Journal of Magnetic Resonance Series A **114**, 139–146 (1995).

[41] G. Zwanenburg and P. J. Hore: *EPR of Spin-Correlated Radical Pairs - Analytical Treatment of Selective Excitation Including Zero-Quantum Coherence*. Chemical Physics Letters **203**, 65–74 (1993).

[42] Malcolm H. Levitt: *Spin Dynamics - Basics of Nuclear Magnetic Resonance*. John Wiley & Sons, Ltd (2007).

[43] J. Behrends: *Spin-dependent Transport and Recombination in Solar Cells studied by Pulsed Electrically Detected Magnetic Resonance*. Freie Universität Berlin, Diss. (2009).

[44] E. L. Hahn: *Spin Echoes*. Physical Review **80**, 580–594 (1950).

[45] R. J. Blume: *Electron Spin Relaxation Times In Sodium-ammonia Solutions*. Physical Review **109**, 1867–1873 (1958).

[46] W. B. Mims: *Envelope Modulation In Spin Echo Experiments*. Physical Review B-solid State **5**, 2409 (1972).

[47] W. B. Mims, K. Nassau, and J. D. McGee: *Spectral Diffusion In Electron Resonance Lines*. Physical Review **123**, 2059 (1961).

[48] Alex De Groot, Rob Evelo, and Arnold J Hoff: *Electron spin-echo envelope modulation in randomly oriented doublet and triplet systems*. Journal of Magnetic Resonance (1969) **66**, 331 - 343 (1986).

[49] D. J. Sloop, H. L. Yu, T. S. Lin, and S. I. Weissman: *Electron Spin Echoes of a Photo-Excited Triplet - Pentacene in Para-Terphenyl Crystals*. Journal of Chemical Physics **75**, 3746–3757 (1981).

[50] E. Abe, K. M. Itoh, J. Isoya, and S. Yamasaki: *Electron-spin phase relaxation of phosphorus donors in nuclear-spin-enriched silicon*. Physical Review B **70**, 033204 (2004).

[51] J. Isoya, M. K. Bowman, J. R. Norris, and J. A. Weil: *An Electron Spin Echo Envelope Modulation Study of Lithium Nuclear Hyperfine and Quadrupole Coupling in the A(Ti-Li) Center of Alpha-quartz*. Journal of Chemical Physics **78**, 1735–1746 (1983).

[52] F. Bitter: *The Optical Detection of Radiofrequency Resonance*. Physical Review **76**, 833–835 (1949).

[53] S. Geschwind, R. J. Collins, and A. L. Schawlow: *Optical Detection of Paramagnetic Resonance in an Excited State of* ^{3+}Cr *in* Al_2O_3. Physical Review Letters **3**, 545–548 (1959).

[54] J. Brossel, S. Geschwind, and A. L. Schawlow: *Optical Detection of Paramagnetic Resonance in Crystals at Low Temperatures*. Physical Review Letters **3**, 548–549 (1959).

[55] J. Schmidt and J. H. Van Der Waals: *Optical detection of zero-field transitions in phosphorescent triplet states*. Chemical Physics Letters **2**, 640–642 (1968).

[56] R. H. Clarke: *Triplet State ODMR Spectrocopy*. John Wiley & Sons, New York (1982).

[57] S. I. Kurarev and E. A. Pshenich: *Effect of High-frequency Magnetic-fields On Recombination of Radicals*. Chemical Physics Letters **28**, 66–67 (1974).

[58] E. L. Frankevich and S. I. Kubarev: *"Spectroscopy of Reaction-Yield Detected Magetic Resonance", in "Triplet State ODMR Spectrocopy"*. John Wiley & Sons (1982).

[59] R. Maxwell and A. Honig: *Neutral-Impurity Scattering Experiments in Silicon with Highly Spin-Polarized Electrons*. Phys. Rev. Lett. **17**, 188 (1966).

[60] A. Honig: *Neutral-Impurity Scattering and Impurity Zeeman Spectroscopy in Semiconductors Using Highly Spin-Polarized Carriers*. Phys. Rev. Lett. **17**, 186 (1966).

[61] D. J. Lepine: *Spin-Dependent Recombination on Silicon Surface*. Phys. Rev. B **6**, 436 (1972).

[62] I. Solomon, D. Biegelsen, and J. C. Knights: *Spin-dependent Photoconductivity in N-type and P-type Amorphous Silicon*. Solid State Communications **22**, 505–508 (1977).

[63] V. S. Lvov, O. V. Tretyak, and I. A. Kolomiets: *Spin-dependent Carrier Recombination on a Silicon Surface*. Soviet Physics Semiconductors-USSR **11**, 661–664 (1977).

[64] G. Mendz, D. J. Miller, and D. Haneman: *Photoconductive Resonance In Silicon - Theory and Experiment*. Physical Review B **20**, 5246–5251 (1979).

[65] G. Mendz and D. Haneman: *A New Model of Spin-dependent Resonance at Si Surfaces*. Journal of Physics C-solid State Physics **13**, 6737–6759 (1980).

[66] C. Boehme: *Dynamics of spin-dependent charge carrier recombination*. Philipps Universität Marburg, Diss. (2002).

[67] C. Boehme and K. Lips: *The investigation of charge carrier recombination and hopping transport with pulsed electrically detected magnetic resonance techniques*. Chichester, England; Hoboken, NJ: Wiley (2006).

[68] W. Pauli: *Über den Zusammenhang des Abschlusses der Elektronengruppen im Atom mit der Komplexstruktur der Spektren*. Zeitschrift für Physik **31**, 765-783 (1925).

[69] R. A. Street: *Hydrogenated amorphous silicon*. Cambridge University Press (2005).

[70] R. Haberkorn and W. Dietz: *Theory of Spin-dependent Recombination In Semiconductors*. Solid State Communications **35**, 505–508 (1980).

[71] N. Kishimoto, K. Morigaki, and K. Murakami: *Conductivity Change due to Electron Spin Resonance in Amorphous Si-Au Systems*. Journal of the Physical Society of Japan **50**, 1970–1977 (1981).

[72] K. Lips, C. Boehme, and W. Fuhs: *Recombination in silicon thin-film solar cells: a study of electrically detected magnetic resonance*. IEE Proceedings-circuits Devices and Systems **150**, 309–315 (2003).

[73] J. Stuke: *Recent Results on Hydrogenated Amorphous Silicon*. Annual Review of Materials Science **15**, 79–102 (1985).

[74] D. Ephron, M. R. Beasley, H. Bahlouli, and K. A. Matveev: *Correlated hopping through thin disordered insulators*. Phys. Rev. B **49**, 2989–2992 (1994).

[75] Pratik Desai, P. Shakya, T. Kreouzis, W. P. Gillin, N. A. Morley, and M. R. J. Gibbs: *Magnetoresistance and efficiency measurements of* Alq_3*-based OLEDs*. Phys. Rev. B **75**, 094423 (2007).

[76] V. Ern and R.E. Merrifield: *Magnetic Field Effect on Triplet Exciton Quenching in Organic Crystals*. Physical Review Letters **21**, 609 (1968).

[77] P. Janssen, M. Cox, S.H.W. Wouters, M. Kemerink, M.M. Wienk, and B. Koopmans: *Tuning organic magnetoresistance in polymer-fullerene blends by controlling spin reaction pathways*. Nature Communications **4**, 1–8 (2013).

[78] U. E. Steiner and T. Ulrich: *Magnetic Field Effects in Chemical Kinetics and Related Phenomena*. Chemical Reviews **89**, 51–147 (1989).

[79] F. J. Wang, Heinz Bässler, and Z. Valy Vardeny: *Magnetic Field Effects in π-Conjugated Polymer-Fullerene Blends: Evidence for Multiple Components*. Phys. Rev. Lett. **101**, 236805 (2008).

[80] L. S. Swanson, J. Shinar, A. R. Brown, D. D. C Bradley, R. H. Friend, P. L. Burn, A. Kraft, and A. B. Holmes: *Electroluminescence-Detected Magnetic Resonance Study of Polyparaphenylenevinylene (PPV)-Based Light-Emitting Diodes*. Phys. Rev. B **46**, 15072–15077 (1992).

[81] Thomas D. Pawlik, Marina E. Kondakova, David J. Giesen, Joseph C. Deaton, and Denis Y. Kondakov: *Charge carriers and triplets in OLED devices studied by electrically detected electron paramagnetic resonance*. Journal of the Society For Information Display **17**, 279–286 (2009).

[82] W. J. Baker, D. R. McCamey, K. J. van Schooten, J. M. Lupton, and C. Boehme: *Differentiation between polaron-pair and triplet-exciton polaron spin-dependent mechanisms in organic light-emitting diodes by coherent spin beating*. Phys. Rev. B **84**, 165205 (2011).

[83] R. L. Vranch, B. Henderson, and M. Pepper: *Spin-Dependent Pair Generation at* Si/SiO_2 *Interfaces*. Applied Physics Letters **53**, 1299–1301 (1988).

[84] W. Rehm and R. Fischer: *Fast Radiationless Recombination in Amorphous Silicon*. Physica Status Solidi B-basic Research **94**, 595–602 (1979).

[85] R. A. Street: *Recombination in a-Si:H - Auger Effects and Non-Geminate Recombination*. Physical Review B **23**, 861–868 (1981).

[86] W. Schmid: *Auger Lifetimes for Excitons Bound to Neutral Donors and Acceptors in Si*. Physica Status Solidi B-basic Research **84**, 529–540 (1977).

[87] Jinming Lu, Felix Hoehne, Andre R. Stegner, Lukas Dreher, Martin Stutzmann, Martin S. Brandt, and Hans Huebl: *High-resolution electrical detection of free*

induction decay and Hahn echoes in phosphorus-doped silicon. Physical Review B **83**, 235201 (2011).

[88] Felix Hoehne, Jinming Lu, Andre R. Stegner, Martin Stutzmann, Martin S. Brandt, Martin Rohrmueller, Wolf Gero Schmidt, and Uwe Gerstmann: *Electrically Detected Electron-Spin-Echo Envelope Modulation: A Highly Sensitive Technique for Resolving Complex Interface Structures*. Physical Review Letters **106**, 196101 (2011).

[89] F. Meillaud, A. Feltrin, M. Despeisse, F-J. Haug, D. Domine, M. Python, T. Soderstrom, P. Cuony, M. Boccard, S. Nicolay, and C. Ballif: *Realization of high efficiency micromorph tandem silicon solar cells on glass and plastic substrates: Issues and potential*. Solar Energy Materials and Solar Cells **95**, 127 - 130 (2011).

[90] M. Matsumoto, Y. Aya, A. Kuroda, H. Katayama, T. Kunii, K. Murata, M. Hishida, W. Shinohara, I. Yoshida, A. Kitahara, H. Yoneda, A. Terakawa, M. Iseki, and M. Tanaka: *The Development of High-Rate Deposition Technology for Microcrystalline Silicon for High-Efficiency a-Si/µc-Si Tandem Solar Module*. Photovoltaics, IEEE Journal of, 35-40 (2013).

[91] B. Rech, O. Kluth, T. Repmann, T. Roschek, J. Springer, J. Muller, F. Finger, H. Stiebig, and H. Wagner: *New materials and deposition techniques for highly efficient silicon thin film solar cells*. Solar Energy Materials and Solar Cells **74**, (2002).

[92] Stefan Haas, Aad Gordijn, and Helmut Stiebig: *High speed laser processing for monolithical series connection of silicon thin-film modules*. Progress In Photovoltaics **16**, 195–203 (2008).

[93] B. Rech, T. Roschek, T. Repmann, J. Müller, R. Schmitz, and W. Appenzeller: *Microcrystalline silicon for large area thin film solar cells*. Thin Solid Films **427**, (2003).

[94] M. Luysberg, P. Hapke, R. Carius, and F. Finger: *Structure and growth of hydrogenated microcrystalline silicon: Investigation by transmission electron microscopy and Raman spectroscopy of films grown at different plasma excitation frequencies*. Philosophical Magazine A-physics of Condensed Matter Structure Defects and Mechanical Properties **75**, 31–47 (1997).

[95] R. T. Weber: *Elexsys E580 User's Manual*. (2000).

[96] A. Stesmans and G. Vangorp: *Novel Method for Accurate g-Measurements in Electron Spin Resonance*. Review of Scientific Instruments **60**, 2949–2952 (1989).

[97] M. Pflüger: *Endohedral Atomic Nitrogen ($N@C_{60}$) as a Field Standard in Electron*

Paramagnetic Resonance Spectrocopy. Freie Universität Berlin, Bachelor thesis (2012).

[98] V. Lang, C. C. Lo, R. E. George, S. A. Lyon, J. Bokor, T. Schenkel, A. Ardavan, and J. J. L. Morton: *Electrically detected magnetic resonance in a W-band microwave cavity*. Review of Scientific Instruments **82**, 034704 (2011).

[99] Eric L. Dane, Thorsten Maly, Galia T. Debelouchina, Robert G. Griffin, and Timothy M. Swager: *Synthesis of a BDPA-TEMPO Biradical*. Organic Letters **11**, 1871–1874 (2009).

[100] H. Dersch, L. Schweitzer, and J. Stuke: *Recombination Processes in a-Si:H - Spin-dependent Photoconductivity*. Physical Review B **28**, 4678–4684 (1983).

[101] M. Bennati and T. F. Prisner: *New developments in high field electron paramagnetic resonance with applications in structural biology*. Reports On Progress In Physics **68**, 411–448 (2005).

[102] G. W. Morley, D. R. McCamey, H. A. Seipel, L. C. Brunel, J. van Tol, and C. Boehme: *Long-Lived Spin Coherence in Silicon with an Electrical Spin Trap Readout*. Phys. Rev. Lett. **101**, 207602 (2008).

[103] C. C. Lo, J. Bokor, T. Schenkel, A. M. Tyryshkin, and S. A. Lyon: *Spin-dependent scattering of neutral antimony donors in ^{28}Si field-effect transistors*. Appl. Phys. Lett. **91**, 242106 (2007).

[104] C. C. Lo, V. Lang, R. E. George, J. J. L. Morton, A. M. Tyryshkin, S. A. Lyon, J. Bokor, and T. Schenkel: *Electrically Detected Magnetic Resonance of Neutral Donors Interacting with a Two-Dimensional Electron Gas*. Physical Review Letters **106**, 207601 (2011).

[105] M. Fehr: *Paramagnetic Defects in hydrogenated amorphous silicon: an advanced Electron Paramagnetic Resonance study*. Freie Universität Berlin, Diss. (2011).

[106] Christoph Meier, Jan Behrends, Christian Teutloff, Oleksandr Astakhov, Alexander Schnegg, Klaus Lips, and Robert Bittl: *Multi-frequency EDMR applied to microcrystalline thin-film silicon solar cells*. Journal of Magnetic Resonance **234**, 1 - 9 (2013).

[107] C. Boehme and K. Lips: *The ultra-sensitive electrical detection of spin-Rabi oscillation at paramagnetic defects*. Physica B-condensed Matter **376**, 930–935 (2006).

[108] J. R. Knutson, D. G. Walbridge, and L. Brand: *Decay-associated Fluorescence Spectra and the Heterogeneous Emission of Alcohol-dehydrogenase*. Biochemistry **21**, 4671–4679 (1982).

[109] S. Hasegawa, S. Narikawa, and Y. Kurata: *Electron-spin-resonance and Electrical-properties of P-doped Microcrystalline Si*. Philosophical Magazine B-physics of Condensed Matter Statistical Mechanics Electronic Optical and Magnetic Properties **48**, 431–447 (1983).

[110] F. Finger, C. Malten, P. Hapke, R. Carius, R. Flückiger, and H. Wagner: *Free-electrons and Defects in Microcrystalline Silicon Studied by Electron Spin Resonance*. Philosophical Magazine Letters **70**, 247–254 (1994).

[111] W. Fuhs, P. Kanschat, and K. Lips: *Bandtails and defects in microcrystalline silicon (μc-Si:H)*. Journal of Vacuum Science & Technology B **18**, 1792–1795 (2000).

[112] M. Kondo, T. Nishimiya, K. Saito, and A. Matsuda: *Light induced phenomena in microcrystalline silicon*. Journal of Non-crystalline Solids **227**, 1031–1035 (1998).

[113] F. Finger, J. Müller, C. Malten, R. Carius, and H. Wagner: *Electronic properties of microcrystalline silicon investigated by electron spin resonance and transport measurements*. Journal of Non-crystalline Solids **266**, 511–518 (2000).

[114] M. M. de Lima, P. C. Taylor, S. Morrison, A. LeGeune, and F. C. Marques: *ESR observations of paramagnetic centers in intrinsic hydrogenated microcrystalline silicon*. Physical Review B **65**, 235324 (2002).

[115] B. M. George, J. Behrends, A. Schnegg, T. F. Schulze, M. Fehr, L. Korte, B. Rech, K. Lips, M. Rohrmüller, E. Rauls, W. G. Schmidt, and U. Gerstmann: *Atomic Structure of Interface States in Silicon Heterojunction Solar Cells*. Phys. Rev. Lett. **110**, 136803 (2013).

[116] J. H. Zhou, S. D. Baranovskii, S. Yamasaki, K. Ikuta, M. Kondo, A. Matsuda, and K. Tanaka: *Transport properties of microcrystalline silicon at low temperatures*. Semiconductors **32**, 807–811 (1998).

[117] L. Houben, M. Luysberg, P. Hapke, R. Carius, F. Finger, and H. Wagner: *Structural properties of microcrystalline silicon in the transition from highly crystalline to amorphous growth*. Philosophical Magazine A-physics of Condensed Matter Structure Defects and Mechanical Properties **77**, 1447–1460 (1998).

[118] Q. Y. Ye, R. Tsu, and E. H. Nicollian: *Resonant Tunneling via Microcrystalline Silicon Quantum Confinement*. Physical Review B **44**, 1806–1811 (1991).

[119] N. Nestle, G. Denninger, M. Vidal, C. Weinzierl, K. Brunner, K. Eberl, and K. von Klitzing: *Electron spin resonance on a two-dimensional electron gas*. Physical Review B **56**, R4359–R4362 (1997).

[120] R. N. Pereira, A. R. Stegner, T. Andlauer, K. Klein, H. Wiggers, M. S. Brandt, and M. Stutzmann: *Dielectric screening versus quantum confinement of phosphorus*

donors in silicon nanocrystals investigated by magnetic resonance. Physical Review B **79**, 161304 (2009).

[121] Christoph Freysoldt, Gernot Pfanner, and Jörg Neugebauer: *The dangling-bond defect in amorphous silicon: Statistical random versus kinetically driven defect geometries*. Journal of Non-crystalline Solids **358**, 2063,Äì2066 (2012).

[122] U. Gerstmann, M. Rohrmüller, F. Mauri, and W.G. Schmidt: *Ab initio g-tensor calculation for paramagnetic surface states: hydrogen adsorption at Si surfaces*. Phys. Status Solidi C **7**, 157,Äì160 (2010).

[123] W. R. Hagen, D. O. Hearshen, R. H. Sands, and W. R. Dunham: *A Statistical Theory for Powder Electron Paramagnetic Resonance in Distributed Systems*. Journal of Magnetic Resonance **61**, 220–232 (1985).

[124] J. R. Pilbrow: *Lineshapes in frequency-swept and field-swept EPR for Spin 1/2*. Journal of Magnetic Resonance **58**, 186–203 (1984).

[125] D. R. McCamey, G. W. Morley, H. A. Seipel, L. C. Brunel, J. van Tol, and C. Boehme: *Spin-dependent processes at the crystalline Si-SiO_2 interface at high magnetic fields*. Physical Review B **78**, 045303 (2008).

[126] K. Lips, S. Schütte, and W. Fuhs: *Microwave-Induced Resonant Changes in Transport and Recombination in Hydrogenated Amorphous Silicon*. Philosophical Magazine B-physics of Condensed Matter Statistical Mechanics Electronic Optical and Magnetic Properties **65**, 945–959 (1992).

[127] H. Dersch, J. Stuke, and J. Beichler: *Electron Spin Resonance of Doped Glow Discharge Amorphous Silicon*. Physica Status Solidi B-basic Research **105**, 265–274 (1981).

[128] T. Umeda, S. Yamasaki, J. Isoya, A. Matsuda, and K. Tanaka: *Electronic structure of band-tail electrons in a-Si:H*. Physical Review Letters **77**, 4600–4603 (1996).

[129] K. Lips, P. Kanschat, and W. Fuhs: *Defects and recombination in microcrystalline silicon*. Solar Energy Materials and Solar Cells **78**, 513–541 (2003).

[130] F. Finger, J. Müller, C. Malten, and H. Wagner: *Electronic states in hydrogenated microcrystalline silicon*. Philosophical Magazine B-physics of Condensed Matter Statistical Mechanics Electronic Optical and Magnetic Properties **77**, 805–830 (1998).

[131] T. Ehara: *Nanocrystalline Silicon: Electron Spin Resonance*. Encycl. Nanosci. Nanotechnol. **6**, 495-503 (2004).

[132] A. L. B. Neto, T. Dylla, S. Klein, T. Repmann, A. Lambertz, R. Carius, and F. Finger: *Defects and structure of hydrogenated microcrystalline silicon films de-*

posited by different techniques. Journal of Non-crystalline Solids **338**, 168–172 (2004).

[133] C. Malten, J. Muller, and F. Finger: *Pulsed ESR studies on doped microcrystalline silicon*. Physica Status Solidi B-basic Solid State Physics **201**, R15–R16 (1997).

[134] G. Feher, J. C. Hensel, and E. A. Gere: *Paramagnetic Resonance Absorption from Acceptors in Silicon*. Physical Review Letters **5**, 309–311 (1960).

[135] F. Boulitrop, A. Chenevaspaule, and D. J. Dunstan: *Luminescence and Magnetic-resonance In Post-hydrogenated Microcrystalline Silicon*. Solid State Communications **48**, 181–184 (1983).

[136] F. Boulitrop and A. Chenevaspaule: *Radiative Recombination and Spin Effects in Plasma Post-hydrogenated Monocrystalline Silicon*. Journal De Physique **43**, 153–157 (1982).

[137] F. Boulitrop: *Recombination Processes in a-Si:H - A Study by Optically Detected Magnetic Resonance*. Physical Review B **28**, 6192–6208 (1983).

[138] K. Morigaki and M. Yoshida: *Triplet Exciton Recombination in a-Si:H*. Journal of Non-crystalline Solids **90**, 139–146 (1987).

[139] S. Liedtke and W. Fuhs: *Optically Detected Magnetic Resonance (ODMR) in a-Si:H*. Journal of Non-crystalline Solids **137**, 583–586 (1991).

[140] M. S. Brandt and M. Stutzmann: *Excitons and Light-induced Degradation of Amorphous Hydrogenated Silicon*. Applied Physics Letters **58**, 1620–1622 (1991).

[141] M. S. Brandt and M. Stutzmann: *Triplet Excitons in Porous Silicon and Siloxene*. Solid State Communications **93**, 473–477 (1995).

[142] W. R. Hagen: *"g-strain: Inhomogeneous Broadening in Metalloprotein EPR", in Advanced EPR: Application in Biology and Biochemistry*. Elsevier Science Publishers B. V. (1989).

[143] Wilfred R. Hagen: *Broadband Transmission EPR Spectroscopy*. PLoS ONE **8**, (2013).

[144] R. Narkowicz, D. Suter, and I. Niemeyer: *Scaling of sensitivity and efficiency in planar microresonators for electron spin resonance*. Review of Scientific Instruments **79**, 084702 (2008).

[145] P. W. Anderson and P. R. Weiss: *Exchange Narrowing In Paramagnetic Resonance*. Reviews of Modern Physics **25**, 269–276 (1953).

[146] J. H. VanVleck: *The Dipolar Broadening of Magnetic Resonance Lines in Crystals*. Physical Review **74**, 1168–1183 (1948).

[147] G. E. Pake: *Nuclear Resonance Absorption In Hydrated Crystals - Fine Structure of the Proton Line*. Journal of Chemical Physics **16**, 327–336 (1948).

[148] M. D. Rabenstein and Y. K. Shin: *Determination of the Distance Between 2 Spin Labels Attached To A Macromolecule*. Proceedings of the National Academy of Sciences of the United States of America **92**, 8239–8243 (1995).

[149] N. M. Atherton: *Electron Spin Resonance - Theory and Applications*. John Wiley & Sons, Inc. (1973).

[150] B. George: *private communication*. .

[151] K. L. Brower: *Electron Paramagnetic Resonance of Neutral (S=1) One-vacancy-oxygen Center in Irradiated Silicon*. Physical Review B **4**, 1968 (1971).

[152] Y. H. Lee, N. N. Gerasimenko, and J. W. Corbett: *EPR Study of Neutron-Irradiated Silicon - Positive Charge State of (100) Split Di-Interstitial*. Physical Review B **14**, 4506–4520 (1976).

[153] W. M. Chen, O. O. Awadelkarim, B. Monemar, J. L. Lindström, and G. S. Oehrlein: *Microscopic Identification and Electronic Structure of a Di-hydrogen Vacancy Complex in Silicon by Optical Detection of Magnetic Resonance*. Physical Review Letters **64**, 3042–3045 (1990).

[154] K. L. Brower: *Structure of multiple-vacancy (oxygen) centers in irradiated silicon*. Radiation Effects **8**, 213-219 (1971).

[155] F. P. Wang and B. Monemar: *Spin-Dependent Electron Transition Processes Related to Excited Triplet Spin States of Neutral Complex Defects in Silicon Studied by Optically Detected Magnetic Resonance*. Physical Review B **42**, 7576–7579 (1990).

[156] W. M. Chen and B. Monemar: *Role of Free-carriers in the Application of Optically Detected Magnetic Resonance for Studies of Defects in Silicon*. Applied Physics A-materials Science & Processing **53**, 130–135 (1991).

[157] Y. H. Lee, Y. M. Kim, and J. W. Corbett: *New EPR spectra in neutron-irradiated silicon*. Radiation Effects **15**, 77-84 (1972).

[158] Y. H. Lee and J. W. Corbett: *EPR Studies of Defects in Electron-irradiated Silicon - Triplet-state of Vacancy-oxygen Complexes*. Physical Review B **13**, 2653–2666 (1976).

[159] L. S. Vlasenko, Y. V. Martynov, T. Gregorkiewicz, and C. A. J. Ammerlaan: *Electron Paramagnetic Resonance versus Spin-Dependent Recombination - Excited Triplet-States of Structural Defects in Irradiated Silicon*. Physical Review B **52**, 1144–1151 (1995).

[160] L. S. Vlasenko: *Photoelectrically detected magnetic resonance spectroscopy of the excited triplet states of point defects silicon*. Physics of the Solid State **41**, 697–700 (1999).

[161] G. D. Watkins and J. W. Corbett: *Defects in Irradiated Silicon - Electron Paramagnetic Resonance + Electron-Nuclear Double Resonance of Si-E Centers*. Physical Review A-general Physics **134**, 1359 (1964).

[162] G. D. Watkins: *EPR of a Trapped Vacancy in Boron-Doped Silicon*. Physical Review B **13**, 2511–2518 (1976).

[163] E. G. Sieverts: *Classification of Defects in Silicon after their g-Values*. Physica Status Solidi B-basic Research **120**, 11–29 (1983).

[164] G. D. Watkins, J. W. Corbett, and R. M. Walker: *Spin Resonance in Electron Irradiated Silicon*. Journal of Applied Physics **30**, 1198–1203 (1959).

[165] Waseem Akhtar, Takeharu Sekiguchi, Tatsumasa Itahashi, Vasileia Filidou, John J. L. Morton, Leonid Vlasenko, and Kohei M. Itoh: *Rabi oscillation and electron-spin-echo envelope modulation of the photoexcited triplet spin system in silicon*. Physical Review B **86**, 115206 (2012).

[166] T. Kilper, W. Beyer, G. Braeuer, T. Bronger, R. Carius, M. N. van den Donker, D. Hrunski, A. Lambertz, T. Merdzhanova, A. Mueck, B. Rech, W. Reetz, R. Schmitz, U. Zastrow, and A. Gordijn: *Oxygen and nitrogen impurities in microcrystalline silicon deposited under optimized conditions: Influence on material properties and solar cell performance*. Journal of Applied Physics **105**, 074509 (2009).

[167] C. Boehme and K. Lips: *Electrical detection of spin coherence in silicon*. Physical Review Letters **91**, 246603 (2003).

[168] A. R. Stegner, C. Boehme, H. Huebl, M. Stutzmann, K. Lips, and M. S. Brandt: *Electrical detection of coherent ^{31}P spin quantum states*. Nature Phys. **2**, 835 (2006).

[169] S. Schaefer, S. Saremi, K. Fostiropoulos, J. Behrends, K. Lips, and W. Harneit: *Electrical detection of coherent spin pair oscillations in ZnPc devices*. Physica Status Solidi B-basic Solid State Physics **245**, 2120–2123 (2008).

[170] D. R. McCamey, K. J. van Schooten, W. J. Baker, S. . Y. Lee, S. . Y. Paik, J. M. Lupton, and C. Boehme: *Hyperfine-Field-Mediated Spin Beating in Electrostatically Bound Charge Carrier Pairs*. Physical Review Letters **104**, 017601 (2010).

[171] J. Behrends, A. Schnegg, K. Lips, E. A. Thomsen, A. K. Pandey, I. D. W. Samuel, and D. J. Keeble: *Bipolaron Formation in Organic Solar Cells Observed by Pulsed Electrically Detected Magnetic Resonance*. Phys. Rev. Lett. **105**, 176601 (2010).

[172] C. Meier, J. Behrends, and R. Bittl: *Electrical detection of Rabi oscillations in microcrystalline silicon thin-film solar cells*. Molecular Physics **111**, 2683-2689 (2013).

[173] A.V. Astashkin and A. Schweiger: *Electron-spin transient nutation: a new approach to simplify the interpretation of ESR spectra*. Chemical Physics Letters **174**, 595 - 602 (1990).

[174] Y. N. Molin, O. A. Anisimov, Grigoryants V. M., Molchanov V. K., and Salikhov K. M.: *Optical Detection of ESR Spectra of Short-Lived Ion-Radical Pairs Produced in Solution by Ionizing Radiation*. J. Phys. Chem. **84**, 1853 (1980).

[175] C. Boehme, J. Behrends, K. von Maydell, M. Schmidt, and K. Lips: *Investigation of hopping transport in n-a-Si:H/µc-Si solar cells with pulsed electrically detected magnetic resonance*. Journal of Non-crystalline Solids **352**, 1113–1116 (2006).

[176] T. W. Herring, S. . Y. Lee, D. R. McCamey, P. C. Taylor, K. Lips, J. Hu, F. Zhu, A. Madan, and C. Boehme: *Experimental discrimination of geminate and non-geminate recombination in a-Si:H*. Phys. Rev. B **79**, 195205 (2009).

[177] C. Michel, A. Gliesche, Baranovskii S. D., Lips K., Gebhard F., and Boehme C.: *Influence of disorder on electrically and optically detected electron spin nutation*. Phys. Rev. B **79**, 052201 (2009).

[178] Y. Araki, K. Maeda, and H. Murai: *Observation of two-spin controlling of a radical pair by pulsed irradiation of microwave monitored by absorption detected magnetic resonance*. Chemical Physics Letters **332**, 515–520 (2000).

[179] P. A. S. Cruickshank, D. R. Bolton, D. A. Robertson, R. I. Hunter, R. J. Wylde, and G. M. Smith: *A kilowatt pulsed 94 GHz electron paramagnetic resonance spectrometer with high concentration sensitivity, high instantaneous bandwidth, and low dead time*. Rev. Sci. Instrum. **80**, 103102 (2009).

[180] M. Gierer, A. van der Est, and D. Stehlik: *Transient EPR of Weakly Coupled Spin-Correlated Radical Pairs in Photosynthetic Reaction Centers - Increased Spectral Resolution from Nutation Analysis*. Chem. Phys. Lett. **186**, 238 (1991).

[181] M. E. Limes, J. Wang, W. J. Baker, S. . Y. Lee, B. Saam, and C. Boehme: *Numerical study of spin-dependent transition rates within pairs of dipolar and exchange coupled spins with $S = 1/2$ during magnetic resonant excitation*. Physical Review B **87**, 165204 (2013).

[182] R. Glenn, M. E. Limes, B. Saam, C. Boehme, and M. E. Raikh: *Analytical study of spin-dependent transition rates within pairs of dipolar and strongly exchange coupled spins with $S = 1/2$ during magnetic resonant excitation*. Physical Review B **87**, 165205 (2013).

[183] Z. Wilamowski, W. Jantsch, H. Malissa, and U. Rossler: *Evidence and evaluation of the Bychkov-Rashba effect in SiGe/Si/SiGe quantum wells*. Physical Review B **66**, 195315 (2002).

[184] C. F. O. Graeff, M. S. Brandt, M. Stutzmann, M. Holzmann, G. Abstreiter, and F. Schaffler: *Electrically detected magnetic resonance of two-dimensional electron gases in Si/SiGe heterostructures*. Physical Review B **59**, 13242–13250 (1999).

[185] H. J. Kümmerer, K. Hüftle, C. Weinzierl, G. Denninger, N. Nestle, and K. Eberl: *Spin exchange between a quantum well and the donor layer in* $Si/Si_{1-x}C_x$. Physical Review B **59**, 12568–12572 (1999).

[186] F. Lipps, F. Pezzoli, M. Stoffel, C. Deneke, J. Thomas, A. Rastelli, V. Kataev, O. G. Schmidt, and B. Buechner: *Electron spin resonance study of Si/SiGe quantum dots*. Physical Review B **81**, 125312 (2010).

[187] Pavel G. Baranov, Sergei B. Orlinskii, Celso de Mello Donega, and Jan Schmidt: *High-Frequency EPR and ENDOR Spectroscopy on Semiconductor Quantum Dots*. Applied Magnetic Resonance **39**, 151–183 (2010).

[188] E. R. Glaser, W. E. Carlos, G. C. B. Braga, J. A. Freitas, W. J. Moore, B. V. Shanabrook, A. E. Wickenden, D. D. Koleske, R. L. Henry, M. W. Bayerl, M. S. Brandt, H. Obloh, P. Kozodoy, S. P. DenBaars, U. K. Mishra, S. Nakamura, E. Haus, J. S. Speck, J. E. Van Nostrand, M. A. Sanchez, E. Calleja, A. J. Ptak, T. H. Myers, and R. J. Molnar: *Characterization of nitrides by electron paramagnetic resonance (EPR) and optically detected magnetic resonance (ODMR)*. Materials Science and Engineering B-solid State Materials For Advanced Technology **93**, (2002).

[189] M. J. Snelling, G. P. Flinn, A. S. Plaut, R. T. Harley, A. C. Tropper, R. Eccleston, and C. C. Phillips: *Magnetic g-Factor of Electrons in GaAs* $Al_xGa_{1-x}As$ *Quantum Wells*. Physical Review B **44**, 11345–11352 (1991).

[190] J. P. Kleider, Y. M. Soro, R. Chouffot, A. S. Gudovskikh, P. Roca i Cabarrocas Cabarrocas, J. Damon-Lacoste, D. Eon, and P.-J. Ribeyron: *High interfacial conductivity at amorphous silicon/crystalline silicon heterojunctions*. Journal of Non-crystalline Solids **354**, (2008).

[191] L. Korte and M. Schmidt: *Investigation of gap states in phosphorous-doped ultra-thin a-Si:H by near-UV photoelectron spectroscopy*. Journal of Non-crystalline Solids **354**, (2008).

[192] M. Tzolov, F. Finger, R. Carius, and P. Hapke: *Optical and transport studies on thin microcrystalline silicon films prepared by very high frequency glow discharge for solar cell applications*. Journal of Applied Physics **81**, 7376–7385 (1997).

[193] H. Jungblut H.-J. Lewerenz: *Photovoltaik*. Springer-Verlag Berlin Heidelberg New York (1995).

[194] O. Astakhov, R. Carius, Yu. Petrusenko, V. Borysenk, D. Barankov, and F. Finger: *Defects in thin film silicon at the transition from amorphous to microcrystalline structure*. Physica Status Solidi-rapid Research Letters **1**, R77–R79 (2007).

[195] A. L. B. Neto, A. Lambertz, R. Carius, and F. Finger: *Relationships between structure, spin density and electronic transport in 'solar-grade' microcrystalline silicon films*. Journal of Non-crystalline Solids **299**, 274–279 (2002).

[196] C. F. Young, E. H. Poindexter, G. J. Gerardi, W. L. Warren, and D. J. Keeble: *Electron paramagnetic resonance of conduction-band electrons in silicon*. Physical Review B **55**, 16245–16248 (1997).

[197] M. Stutzmann, D. K. Biegelsen, and R. A. Street: *Detailed investigation of doping in hydrogenated amorphous silicon and germanium*. Phys. Rev. B **35**, 5666–5701 (1987).

[198] A. Fejfar, A. Vetushka, V. Kalusova, O. Certik, M. Ledinsky, B. Rezek, J. Stuchlik, and J. Kocka: *Relation of nanoscale and macroscopic properties of mixed-phase silicon thin films*. Physica Status Solidi A-applications and Materials Science **207**, 582–586 (2010).

[199] D. Azulay, I. Balberg, V. Chu, J. P. Conde, and O. Millo: *Current routes in hydrogenated microcrystalline silicon*. Physical Review B **71**, 113304 (2005).

[200] Jan Kocka: *Relation of defects and grain boundaries to transport and phototransport: Solved and unsolved problems in microcrystalline silicon*. Journal of Non-crystalline Solids **358**, (2012).

[201] B. Rezek, J. Stuchlik, A. Fejfar, and J. Kocka: *Microcrystalline silicon thin films studied by atomic force microscopy with electrical current detection*. Journal of Applied Physics **92**, 587–593 (2002).

[202] I. Balberg, D. Azulay, D. Toker, and O. Millo: *Percolation and tunneling in composite materials*. International Journal of Modern Physics B **18**, 2091–2121 (2004).

[203] K. Lips, P. Kanschat, S. Brehme, and W. Fuhs: *An ESR study of bandtail states in phosphorus doped micro crystalline silicon*. Journal of Non-crystalline Solids **299**, (2002).

[204] H. Overhof, M. Otte, M. Schmidtke, U. Backhausen, and R. Carius: *The transport mechanism in micro-crystalline silicon*. Journal of Non-crystalline Solids **227**, 992–995 (1998).

[205] K. Shimakawa: *Percolation-controlled electronic properties in microcrystalline silicon: effective medium approach*. Journal of Non-crystalline Solids **266**, (2000).

[206] D. Di, I. Perez-Wurfl, G. Conibeer, and M. A. Green: *Formation and photoluminescence of Si quantum dots in SiO2/Si3N4 hybrid matrix for all-Si tandem solar cells*. Solar Energy Materials and Solar Cells **94**, 2238–2243 (2010).

[207] Jens Niklas, Kristy L. Mardis, Brian P. Banks, Gregory M. Grooms, Andreas Sperlich, Vladimir Dyakonov, Serge Beaupre, Mario Leclerc, Tao Xu, Luping Yu, and Oleg G. Poluektov: *Highly-efficient charge separation and polaron delocalization in polymer-fullerene bulk-heterojunctions: a comparative multi-frequency EPR and DFT study*. Physical Chemistry Chemical Physics **15**, 9562–9574 (2013).

[208] Dmitri V. Talapin, Jong-Soo Lee, Maksym V. Kovalenko, and Elena V. Shevchenko: *Prospects of Colloidal Nanocrystals for Electronic and Optoelectronic Applications*. Chemical Reviews **110**, 389–458 (2010).

[209] Chin-Y Liu, Zachary C. Holman, and Uwe R. Kortshagen: *Hybrid Solar Cells from P3HT and Silicon Nanocrystals*. Nano Letters **9**, 449–452 (2009).

[210] F. D. Rodrigues, M. Cunha, L. Hilliou, L. Rino, M. R. Correia, T. Busani, G. Bernardo, H. Wiggers, S. A. Filonovich, and R. N. Pereira: *Impact of composition and morphology on the optical properties of Si-NC/P3HT thin films processed from solution*. Applied Physics A-materials Science & Processing **113**, 439–446 (2013).

List of Abbreviations

a-Si:H hydrogenated amorphous silicon

C-AFM conductive atomic force microscopy

c-Si crystalline silicon

cwEDMR continuous wave EDMR

DAS decay-associated spectra

DFT density functional theory

(p)EDMR (pulsed) electrically detected magnetic resonance

(ED-)ELDOR (electrically detected) electron electron double resonance

(ED-)ENDOR (electrically detected) electron nuclear double resonance

EPR electron paramagnetic resonance

(ED-)ESEEM (electrically detected) electron spin echo envelope modulation

(F)FT (fast-)Fourier transformation

FID free induction decay

(ED-)FSE (electrically detected) field swept echo

FWHM full width half maximum

HFI hyperfine interaction

HVH center di-hydrogen-vacancy center

KSM model Kaplan Solomon Mott model

μc-Si:H hydrogenated microcrystalline silicon

mw microwave

NMR nuclear magnetic resonance

ODMR optically detected magnetic resonance

(O)PV (organic) photovoltaic

PECVD plasma enhanced chemical vapor deposition

PL photoluminescence

RYDMR reaction-yield detected magnetic resonance

SNR signal-to-noise ratio

TCO transparent conductive oxide

VO center vacancy-oxygen center

DANKSAGUNG

Ich möchte mich gern bei den Leuten bedanken, die einen besonderen Anteil an dieser Arbeit haben.

Ich beginne dazu ungewöhnlich früh. Im zweiten Semester des Meteorologiestudiums haben mich mein Kommilitone Alex Krüger und meine damalige Tutorin Nicole Helbig davon überzeugt, dass ich in der Physik besser aufgehoben bin als in der Meteorologie. Für diese fundamentale Weichenstellung will ich beiden sehr danken!

Es hat sich schließlich gelohnt. Das liegt zu einem sehr großen Teil daran, dass es mir viel Spaß gemacht hat, in der Arbeitsgruppe Bittl zu arbeiten. Ich möchte daher allen voran Robert Bittl danken für die Gelegenheit, hier zu arbeiten, obwohl Wetterfrösche im Allgemeinen zu nichts taugen! Die vielen Anregungen und vor allem die Gestaltungsfreiheit haben sehr zum Erfolg dieser Arbeit beigetragen.

Jan Behrends und Christian Teutloff habe durch ihre Unterstützung, wertvolle Diskussionen und ein ungebrochenes Interesse ein großes Dankeschön verdient! Die Laufrunden im Grunewald mit euch und zusammen mit der AG im Team haben viel Freude gemacht.

Bei Bernd Rech, Klaus Lips, Alexander Schnegg und Matthias Fehr vom Helmholtz-Zentrum Berlin (HZB) möchte ich mich ebenfalls bedanken. Bernd, danke für die Bereitschaft, die Zweitbegutachtung zu übernehmen. Klaus, Deine Begeisterung für die Themen hat mich sehr motiviert. Alexander, Dir danke ich für die Unterstützung beim Aufbau der W-band EDMR und für die Messungen bei 263 GHz. Matthias, danke für die Hilfe

auf dem Weg zu meiner ersten EDMR-Messung.

Für die Herstellung der μc-Si:H Solarzellen möchte ich Friedhelm Finger und Oleksandr Astakhov vom Forschungszentrum Jülich ganz herzlich danken. Hier seien auch Stefan Common und Martin Muske vom HZB erwähnt, die sich um die Weiterverarbeitung der Proben gekümmert haben.

Allen Mitgliedern der Arbeitsgruppe in dieser Zeit ein Dankeschön für die gute Arbeitsatmosphäre und die Hilfsbereitschaft! Ich möchte hier besonders Klaus-Peter Dinse für wertvolle Diskussionen, Jana und Susanne für die gemeinsame Bürozeit, Richard, Julia, Christopher und Felix für viele Gespräche und Unterstützung sowie Roswitha für den Service in der Gruppe aber vor allem für die ganz besonderen Ratschläge Danke sagen. Richard und Susanne, ich erinnere mich gern an viele hilfreiche Gespräche, mind mapping und Magic zurück.

Abschließend bedanke ich mich bei meiner Familie, bei Florian und Mathias für das Zuhören und Motivieren und ganz besonders bei Björn für die tolle Zeit fern der Physik.

ERKLÄRUNG

Ich erkläre ehrenwörtlich, dass ich die dem Fachbereich Physik der Freien Universität Berlin zur Promotionsprüfung eingereichte Arbeit ohne sonstige Hilfe selbst durchgeführt und bei der Abfassung der Arbeit keine anderen als die in der Dissertation aufgeführten Hilfsmittel benutzt habe.

Ort, Datum, Unterschrift